2D Elastic Full-Waveform Tomography of Vibro-Seismic Data in Crystalline Host Rock at the GFZ-Underground-Lab, Freiberg

Zur Erlangung des akademischen Grades eines

DOKTORS DER NATURWISSENSCHAFTEN

von der Fakultät für Physik des
Karlsruher Instituts für Technologie (KIT)

genehmigte

DISSERTATION

von

Dipl.-Geophys. Sven Heider
aus Bamberg

Tag der mündlichen Prüfung:	17. Juli 2014
Referent:	Prof. Dr. Thomas Bohlen
Korreferent:	Prof. Dr. Friedemann Wenzel

Für T.

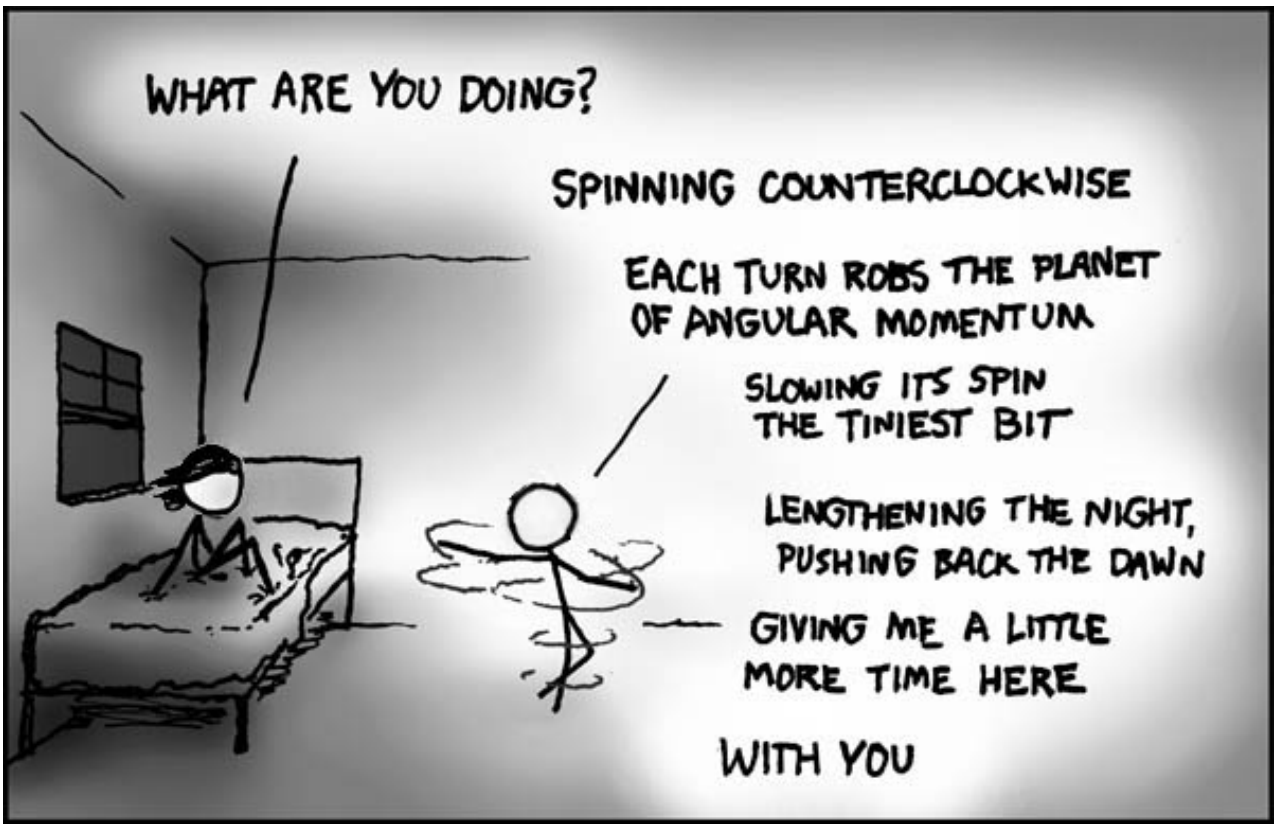

Modifiziert von http://xkcd.com/162/ 23.07.2014

Abstract

In the past decades, the progress in tunnelling and underground developments has been increased rapidly. In this context high-resolution exploration of the geology in the vicinity of the construction site can lead to a minimisation of the construction period, to a reduction of the investment costs and can improve the reliability and safety of the construction phase.

We performed a 2D elastic full-waveform inversion (FWI) in a crystalline rock environment below ground in the GFZ-Underground Laboratory in which the geological situation is quite well known. The source and receiver positions are in transmission geometry and surround a Freiberger grey gneiss block. We used a high frequency magnetostrictive vibrator source to excite a sweep signal from 300 - 3000 Hz. The data preprocessing prior to the FWI consists of a rotation of receiver orientation, a spreading transformation and a time-windowing of the first arrival P-wave.

The influence of the different preprocessing parameters, the resolution potential and strategies for a better convergence of the FWI are investigated in synthetic studies by using the same geometry and the same source wavelet as in the field survey with a random distributed velocity model which represents crystalline rock. The studies give information about the range of the parameters we could use in the field data inversion.

A semblance analysis which is sensitive to differences in the waveforms showed that the field data is less influenced by ghost reflections at the gallery walls than the 2D synthetic data. Thus, we invert the field data with a gallery-free model, i. e., without the rock-air interface which fits the behaviour of the field data best.

In the field data inversion we used a multi-scale inversion by starting at 400 Hz and by increasing the frequency in steps of 100 Hz until we reached 900 Hz. The source time function is recomputed at each frequency range. The general velocity distribution of the P-wave velocity model is consistent for all frequency ranges. We could achieve a small-scale velocity distribution of the gneiss which is in agreement with the former known geological characteristics.

The work presents a first successful application of the FWI to field data in a hard rock regime. The resolution of the inverted velocity structures could be increased by using the FWI in contrast to a classical travel time tomography. Nevertheless, further work has to be done to be able to invert later arriving phases, like the S-wave, too.

Although the FWI is a complex multi-parameter problem, we recommend its application in hard rock regimes, e. g., for seismic imaging around a tunnel to identify rock changes during the construction period or to monitor the rock conditions between two tunnels to obtain a high resolution image.

Contents

1 Introduction

In the past decades, a rapid progress in tunnelling and underground developments can be noticed all over the world. Large-scale projects are currently planned or realised, such as the Gotthard Base Tunnel through the Alps with a length of 57 km. Many of these projects are often located in complex geological environments. Such projects as well as smaller underground developments in urban areas require technologies for a high-resolution exploration of the geology in the vicinity of the construction site. This can be realised by seismic tomography. The knowledge of the geological conditions leads to a minimisation of the construction period, reduction of the investment costs and can improve for the reliability and safety during as well as after the construction phase.
In this thesis, we focus on a seismic survey in a hard rock regime under laboratory conditions. We record real data, investigate preprocessing steps, the influence of various parameters and finally apply a full-waveform inversion (FWI) to determine the geological structures of the hard rock. The major developments in hard rock regimes are tunnel constructions (Kolymbas, 1998). In the past, mainly travel-time based methods were applied to determine the geology, such as structural changes in the host rock (Dickmann and Sanders, 1996; Kneib et al., 2000; Giese et al., 2005; Lüth et al., 2006; Jetschny, 2010). The resulting resolution were limited because of two reasons: First, the measurement conditions are very challenging in the underground and second, the travel-time based methods have a lack in terms of the resolution. Latter can be significantly improved with the use of the FWI which has the potential for high-resolution images.
In the 1980s, the FWI approach was suggested by Tarantola (1984) and Mora (1987). Due to the high computational costs, the benefit of the method could not be exploited until the last decade. Many field applications in seismology (Fichtner et al., 2009), in marine seismics (Boonyasiriwat et al., 2010) and for onshore wide-aperture surveys (Bleibinhaus et al., 2009) are published in the last years.

In our survey we use a transmission geometry which is rather similar to a crosshole geometry. In the following, some crosshole seismic data examples recorded with hydrophones which are mostly processed with the acoustic approximation are mentioned. Although the application purpose may differ, we are focusing on some interesting facts, such as the data preprocessing for the FWI. Zhou et al. (1997) performed an elastic wave equation travel-time and waveform inversion (WTW) and could invert the P- and the S-wave velocity model in synthetic tests as well as for field data. However, they need high-quality direct P- and S-wave arrivals for an appropriate starting model and a well estimated source wavelet. In a publication of Pratt (1999), first the necessary preprocessing steps, e. g., time windowing or the source signature estimation are introduced with synthetic examples and measurements on a physical scale model. Subsequently, Pratt and Shipp (1999) carried out a viscoacoustic FWI with a static anisotropy. The FWI provides a significantly improved image of the velocity structures when comparing with the original travel-time tomography results. Bauer et al. (2005) and Pratt et al. (2005) acquired data with a vibrator source for a crosswell seismic experiment with a time-lapse approach. Again, a preprocessing workflow for the data was

applied including tube-wave suppression, low-pass frequency filtering and time windowing of the data. They gained detailed information on the distribution of the P-wave velocity and attenuation properties at the survey area for one data set. Recently, a time-lapse inversion was performed by Zhang et al. (2012) who use almost the same preprocessing as suggested by Pratt and Shipp (1999).
In contrast to our survey, most of the former publications use hydrophones as receivers. Nevertheless, the mentioned preprocessing steps are applicable to both, acoustic and elastic measurements. Manukyan (2011) used, besides of hydrophones, also multi-component geophones within a clay formation as host rock in the Mont Terri Rock Laboratory, Switzerland. The aim is to monitor high-level radioactive waste disposals regarding the water saturation with an elastic full-waveform inversion. Amongst other things, they figured out that the coupling effects of the hydrophones overwhelm possible long-term changes in the repository. In contrast to the hydrophones, grouted geophones yield coherent recordings over time. This is of interest for our work as we use geophones mounted with anchors in the host rock. Further elastic crosshole inversion results including anisotropy are published by Barnes et al. (2008).

We want to perform a 2D elastic full-waveform inversion in a crystalline rock environment below ground under laboratory conditions. As a test site, we chose GFZ-Underground-Laboratory (GFZ U-Lab) operated by the German Research Centre for Geosciences (GFZ) in the research and education mine *Reiche Zeche* of the Freiberg University of Mining and Technology (TU BAF). This facility provides the necessary equipment for performing elastic seismic measurements and has stable environmental conditions which gives the possibility for repeating-measurements (Krauss et al., 2014). The measurement area is already well characterised by travel-time based methods (Richter, 2010; Krauss, 2013) and by a geological mapping (Kopf et al., 2008). With the FWI, we expect a higher resolution of the velocity distribution in contrast to the travel-time tomography.

A block of crystalline rock (*Freiberger Greygneiss*) almost 50 m wide and 80 m long, is surrounded by three galleries in a depth of approximately 150 m. The geological mapping provides no material changes in the host rock, except of two major fault zones where hydrothermal mineralisation occur. Depending on the characteristics of the faults, seismic measurement are sensitive to the fault zones in the host rock and can be identified as heterogeneities within the rock. These changes in the elastic properties are assumed to be visible in the inverted image in order to locate fault zones.

The source and receiver positions are in transmission geometry and are located in an almost ideally horizontal plane. Mostly, in underground measurements an impulsive pneumatic hammer or the signal of the cutting wheel of a tunnel boring machine act as seismic sources (Petronio et al., 2007). However, the disadvantage of both is that the sources are poorly reproducible and the frequency content is not clearly defined. Therefore, we use a highly regulated magnetostrictive double vibrator which can excite sweep signals, in our case from 300 Hz to 3000 Hz (Borm and Giese, 2003). The source wavelet is well-defined and reproducible (Borm et al., 2008b). Apart from the actual rock conditions, also long-term changes in the host rock are measurable by repeating-measurements.
As receivers, we used 30 three-component (3C) geophone anchors which are horizontally drilled into the hard rock. The depth of the boreholes varies between 1 m and 2 m. The varying depth is an important fact for the further analysis because first, the behaviour of the reflections from the rock-air interface differs for the different depths. And second, since

we use a 2D inversion code, the characteristic of the modelled reflections differs to the field observations. Due to the extremely expensive computational effort of an elastic 3D inversion (Butzer et al., 2013) and the intention to study the influence of various parameters in synthetic tests, we have to find a compromise between the measurement in 3D and an inversion in 2D. Anyhow, the galleries act like a 3D object which cannot be approximated by a 2D model. The discrepancy is investigated within the scope of this thesis.

The overall aim of the thesis is to invert the acquired field data with the full-waveform inversion approach by solving several issues concerning the measurement and the implemented algorithms. The thesis first leads to a future application of the elastic FWI in hard rock conditions to be able to characterise the geology by proposing solutions for the acquisition geometry and equipment, the data preprocessing and the inversion strategy. And second, we want to characterise the elastic properties of the gneiss block within the U-Lab more explicitly, e. g., to be able to validate the properties of newly developed seismic sources and receivers for underground applications more precisely.
The thesis is written within the framework of the project Seismic Observations for UNderground Development (SOUND, Appendix F).

In the following, the content of the chapters is briefly introduced.
In **Chapter 2 - Methodology**, we explain the basics of the elastic wave equation which is solved by a finite-difference scheme (Virieux, 1986; Levander, 1988; Bohlen, 2002). The theory of the full-waveform inversion, in particular, the adjoint approach, which was first formulated in time domain by Tarantola (1984) and Mora (1987) is introduced.
In **Chapter 3 - Field Survey in Freiberg**, the focus lies on the performed seismic measurement in hard rock conditions at the GFZ-Underground-Laboratory in the research and education mine *Reiche Zeche* of the TU BAF. The already known facts about the survey area are described as well as the measurement equipment, such as the characteristics of the source and receivers, is specified.
In **Chapter 4 - Model Geometry and Data Characteristics**, the specifics of the source wavelet is evaluated and the acquired data is characterised regarding, e. g., the first-arrival times and by applying a 3D/2D transformation. In addition, we analyse the data in terms of the frequency content, possible anisotropy effects and the similarity of waveforms for neighbouring sources and receivers.
In **Chapter 5 - Synthetic Case Studies**, we illustrate the application of the full-waveform inversion with synthetic data by adopting the geometry of the field data. We use a random distributed seismic velocity model which should represent the crystalline rock and a checkerboard model. The influence of different preconditioning parameters, the resolution potential and strategies for a better convergence of the FWI are tested.
In **Chapter 6 - Application to Field Data**, the FWI is applied to the field data introduced in Chapter 3. We first perform a travel-time tomography of the first-arrival times to obtain an appropriate starting model and subsequent estimate the source wavelet. The FWI is applied to the preprocessed field data using a multi-scale approach.
In **Chapter 7 - Summary and Conclusion**, the content of the thesis is summarised and the conclusion is drawn.

2 Methodology

In this chapter we explain and describe the theory behind the methods which are used in the thesis. At first, the general elastic wave equation is derived from the equation of motion and Hooke's law (Section 2.1). An approach to solve the wave equation for complex media is the finite-difference scheme (FD scheme) which is briefly introduced in Section 2.2. As we use an already available code, we concentrate on the further implementations which are necessary for our purpose. In the next section, the general approach of the full-waveform inversion (FWI) is introduced (Section 2.3). The theoretical background of the adjoint approach - a conjugate gradient method - which is the basis of the FWI is explained in detail as well as the gradient for different parametrisations are shown. Further, for different misfit definitions the adjoint sources are explicitly formulated. Additional steps, such as the preconditioning and the scaling of the gradient, are explained. The overall workflow of the FWI algorithm which is implemented in a code called DENISE is afterwards presented with emphasising the most important steps. Also, we apply strategies, such as frequency filtering, to increase the convergence of the gradient method. In addition, the source time function has to be determined to use it as the source wavelet in the inversion (Section 2.4). At last, we performed a travel-time tomography to obtain a sufficient starting model (Section 2.5).

2.1 Elastic Wave Equation

In this section, we follow the work of Lay and Wallace (1995) which explain very clearly the necessary steps to obtain the elastic wave equation.
The most fundamental equation in seismic is the equation of motion. It describes the relation between forces in a medium to the measurable displacements or how a wave propagates through a continuum:

$$\rho \frac{\partial^2 u_i}{\partial t^2} = \frac{\partial \sigma_{ij}}{\partial x_j} + f_i \tag{2.1}$$

This is a system of three second order partial differential equations in the so-called stress-displacement formulation for the equation of motion in a three-dimensional medium, where the vector x is the position vector in space, ρ denotes the density, u_i the ith-component of the particle displacement vector, σ_{ij} the stress tensor and f_i are external body forces.

We now introduce the relation between stress and strain (Hooke's law). If steady and small stresses are applied to a medium for a long time, almost all materials act ductile. That means they are deformed permanently. We are interested in short and small stresses as this is typical for seismic or seismology. For measurements under laboratory conditions a linear relation between stress and strain could be found. The principles for the relation are that they are linear and elastic. Elastic means "that reducing the small stress restores the medium

to its original state" (Lay and Wallace, 1995, p. 48). The relation can be expressed by

$$\sigma_{ij} = C_{ijkl}\epsilon_{kl}. \tag{2.2}$$

The constants of proportionality C_{ijkl} are the so-called elastic moduli. C_{ijkl} is a tensor with 81 components which describes the properties of the medium and connects the stress tensor σ_{ij} and the strain tensor ϵ_{kl}, both with nine components. Due to symmetrical reasons, the number of independent components is reduced to 36. Because the elastic energy for deformation is a state function, the tensor can further be reduced to 21 components. If we consider isotropic media, that means, the properties of the media do not depend on the direction, only the two Lamé parameters λ and μ remain. We can rewrite C_{ijkl} to

$$C_{ijkl} = \lambda\delta_{ij}\delta_{kl} + \mu(\delta_{ik}\delta_{jl} + \delta_{il}\delta_{jk}) \tag{2.3}$$

with

$$\delta_{ij} = \begin{cases} 1 & \text{if } i = j \\ 0 & \text{if } i \neq j \end{cases}. \tag{2.4}$$

δ_{ij} is called the Kronecker delta. Equation (2.2) can be rewritten to

$$\sigma_{ij} = \lambda\theta\delta_{ij} + 2\mu\epsilon_{ij} \tag{2.5}$$

with

$$\theta = \epsilon_{11} + \epsilon_{22} + \epsilon_{33}. \tag{2.6}$$

The Equations (2.1) and (2.5) and the strain relationship

$$\epsilon_{ij} = \frac{1}{2}\left(\frac{\partial u_i}{\partial x_j} + \frac{\partial u_j}{\partial x_i}\right) \tag{2.7}$$

are a system of second order partial differential equations in the so-called stress-displacement formulation. By taking the time derivative of the stress-strain relationship and the strain tensor and by using $v_i = {}^{\partial u_i}/_{\partial t}$, we can rewrite the equations to

$$\begin{aligned} \rho\frac{\partial v_i}{\partial 2} &= f_i + \frac{\partial \sigma_{ij}}{\partial x_j}, \\ \frac{\partial \sigma_{ij}}{\partial t} &= \lambda\frac{\partial \theta}{\partial t}\delta_{ij} + 2\mu\frac{\partial \epsilon_{ij}}{\partial t} \quad \text{and} \\ \frac{\partial \epsilon_{ij}}{\partial t} &= \frac{1}{2}\left(\frac{\partial v_i}{\partial x_j} + \frac{\partial v_j}{\partial x_i}\right). \end{aligned} \tag{2.8}$$

This is the so-called stress-velocity formulation. To solve the equations, we use the finite-difference scheme explained in the following section.
The relation between the Lamé parameters and the density to the seismic velocities for P-

and S-wave (v_P and v_S) are following (Lay and Wallace, 1995):

$$v_P = \sqrt{\frac{\lambda + 2\mu}{\rho}}, \qquad v_S = \sqrt{\frac{\mu}{\rho}}. \tag{2.9}$$

2.2 Forward Modelling

The used FWI code is based on a 2D P-SV finite-difference time-domain implementation originally developed by Bohlen (2002). The extensive theory for elastic and viscoelastic media is described in Bohlen (1998). The corresponding forward modelling codes SOFI2D and SOFI3D (Seismic mOdelling with Finite-dIfferences) are available from `http://www.gpi.kit.edu/Software.php` under the terms of the GNU General Public License.
In this work we want to give a brief introduction to finite-difference modelling. We focus on the explanation of necessary features required for a general understanding within the scope of the FWI. Later, the inversion code DENISE is presented, where the 2D forward modelling code is included.

2.2.1 Finite-Difference Scheme

For modelling seismic waves in an elastic and isotropic medium, that is, in order to solve Equation (2.8), we have to discretise the space on a regular and rectangular grid as well as the time in regular time steps. At every grid point the elastic parameters λ and μ as well as the particle displacement u and the stresses σ_{ij} are assigned. The grid spacing dh is the spatial distance between two adjacent grid points and dt is the increment of discrete time steps. The indexes m and n indicate the discrete local dependence in space with $x = m \cdot dh$ and $y = n \cdot dh$ and the index p indicates the discrete time step with $t = p \cdot dt$. Now, the partial derivatives are replaced by finite-differences. For the spatial derivatives only second order Taylor operators are used due to the expected strong discontinuities at the rock-air interface (Cunha, 1993). For the time derivatives only second order operators are used, too. The finite-difference operators for a function $u(x,t)$ can be written as

$$\frac{\partial u(x)}{\partial x} = \frac{u(m + dh) - u(m)}{dh} \tag{2.10}$$

and

$$\frac{\partial u(t)}{\partial t} = \frac{u(p + dt) - u(p)}{dt}, \tag{2.11}$$

respectively.
Furthermore, we have to introduce the standard staggered grid (SSG) proposed by Virieux (1986) and Levander (1988). It ensures that the partial derivatives are calculated at the correct positions in space and time. The corresponding illustration of the distribution of the wavefield variables and material properties can be seen in Köhn (2011, Figure 2.5). Due to the staggered grid, the Lamé parameter μ and the density ρ have to be averaged

harmonically and arithmetically, respectively.
A source time function which represents the source wavelet is applied at one grid point. Afterwards the elastic fields of the wave propagation are updated for each grid point after each time step. By saving the wavefield variables, such as the particle velocity field at one grid point, we obtain a seismogram which is sampled with dt.

2.2.2 Required Accuracy of the FD-Parameters

On the one hand, the computational costs strongly depend on the number of both, grid points and time steps and thus, on the discretisations dh and dt, respectively. On the other hand, a stable finite-difference scheme and seismograms without numerical artefacts are requested. With Equation (2.12) and (2.13) we can calculate the necessary spatial and temporal sampling. For second order Taylor operators we need at least 12 grid points per minimum wavelength to avoid numerical artefacts caused by grid dispersion (Köhn, 2011, Table 2.2). This leads to

$$dh \leq \frac{\lambda_{\min}}{n} \quad \text{with} \quad \lambda_{\min} = \frac{c_{\min}(f_{\max})}{f_{\max}} \tag{2.12}$$

where n is the number of grid points per minimum wavelength, $\lambda_{\min}$ is the smallest occurring wavelength which depends on the minimum velocity $c_{\min}$ in the model and the maximum frequency $f_{\max}$ of the source. The minimum velocity $c_{\min}$ is usually determined with the v_S model.

The second crucial parameter is the temporal sampling dt. The so-called Courant-Friedrichs-Lewy criterion ensures the stability of the simulation and is given by

$$dt \leq \frac{dh}{\sqrt{D}c_{\max}} \tag{2.13}$$

with $D \in \{1,2,3\}$ the dimension of the FD scheme for a second order Taylor operator (Courant et al., 1928; Courant et al., 1967). $c_{\max}$ is the maximum occurring velocity usually determined by the v_P model.

In Section 5.2, the two described parameters are defined for our purpose so that both criteria are satisfied.

2.2.3 Additional Features

We shortly introduce the new implementations in the finite-difference code which are necessary due to the performed survey (Chapter 3).

Rotated Sources

As we will see in Chapter 3, the direction of the sources in the field measurement has an arbitrary angel with respect to the x- and y-axis of the coordinate system. To model the effect of the radiation pattern of the source correctly, we have to split the force density on the x- and y-direction, respectively. This is done with the sine and cosine functions and the corresponding angle β (Figure 2.1a). For a detailed description how the force density is

implemented in the FD-scheme, we refer to (Groos, 2013, Section 3.3).
For testing the implementation, we used a homogeneous velocity model with $v_P = 3500\,\mathrm{m/s}$, $v_S = 2000\,\mathrm{m/s}$ and a density of $\rho = 2000\,\mathrm{kg/m^3}$ and a grid size of NX = NY = 800 grid points. The source wavelet has a $\sin^3(t)$ shape with a centre frequency of 5 Hz. To satisfy the required accuracy of FD-modelling we set DH = 12.5 m and DT = 0.001 s (Section 2.2.2). The source was located in the middle of the grid. In Figure 2.1b, the P- and S-wave can be seen, respectively, for two different points in time (T1 and T2) and for four different angles β. In all figures, for a better visualisation, the pure P- and S-wave contribution to the wavefield and not the particle velocity or displacement is shown. How to separate the wave types, we refer to (Bohlen, 1998, Section 3.3.4). The clip of the colour scales are equal for T1 and T2 to illustrate the effect of geometrical spreading which leads to an amplitude decay but differs for the P- and S-wave. In T1 and in T2, for $\beta = 0\,^\circ$, the leading phase of the P-wave has in terms of the compression (black colour) its highest amplitude in the direction of the positive y-axis and in terms of dilatation (white colour) its lowest amplitude in the direction of the negative y-axis. In x-direction, the P-wave excites no energy, as the radiation pattern is symmetrical. The radiation pattern of the S-wave is rotated by $90\,^\circ$. In the direction of the x-axis, the highest and lowest amplitudes occur, whereas at the y-direction, the amplitude is zero. For $\beta = 30\,^\circ$ (Figure 2.1a), the axis of the maximal amplitude is also rotated with the desired angle for the P- and S-wave, respectively. For $\beta = 90\,^\circ$ and $\beta = 270\,^\circ$ we can observe a reversed polarity of both wave types which we expected. Please note that we are directly looking at the compression and dilatation of the P- and S-wave and not at the particle velocities on the x- and y-component in used coordinate system. Comparing the P-wave of $\beta = 90\,^\circ$ and $\beta = 270\,^\circ$, both have the same polarity in the direction of the force because in both, the material is compressed first. In terms of the polarity regarding particle velocity, we would observe a change in the polarity because the particle movement for $\beta = 90\,^\circ$ is along the positive x-axis and for $\beta = 270\,^\circ$ along the negative x-axis.

CPML Boundaries

A numerical problem in modelling seismic waves using a finite grid are waves that are reflected at the edge of the grid back into the model. This leads to artefacts in the seismograms which makes them usually hard to interpret. By extending the grid the reflections would occur at a later time after the wanted main phases, but this also increases the computational cost and the memory requirements. In the used FWI code the convolutionary perfectly matched layers (CPMLs) are implemented which damp the waves near the boundaries very effectively. For more details, we refer to Komatitsch and Martin (2007). All synthetic tests as well as the field data results in this thesis are calculated with the CPMLs.

2.3 Full-Waveform Inversion

The full-waveform inversion (FWI) uses the entire wavefield and, thus, the full information content of the seismic waves, to be able to reconstruct the model with a sub-wavelength resolution. A very good overview over the full-waveform inversion is given by Virieux and Operto (2009) and Fichtner (2011). In this section we will only introduce the approaches which are requires in this thesis.
The used FWI code DENISE is developed by Köhn (2011) and is an acronym for sub-wavelength DEtail resolving Nonlinear Iterative SEismic inversion. It is a 2D time-domain code which is based on the adjoint method (Tarantola, 1984; Mora, 1987). For forward

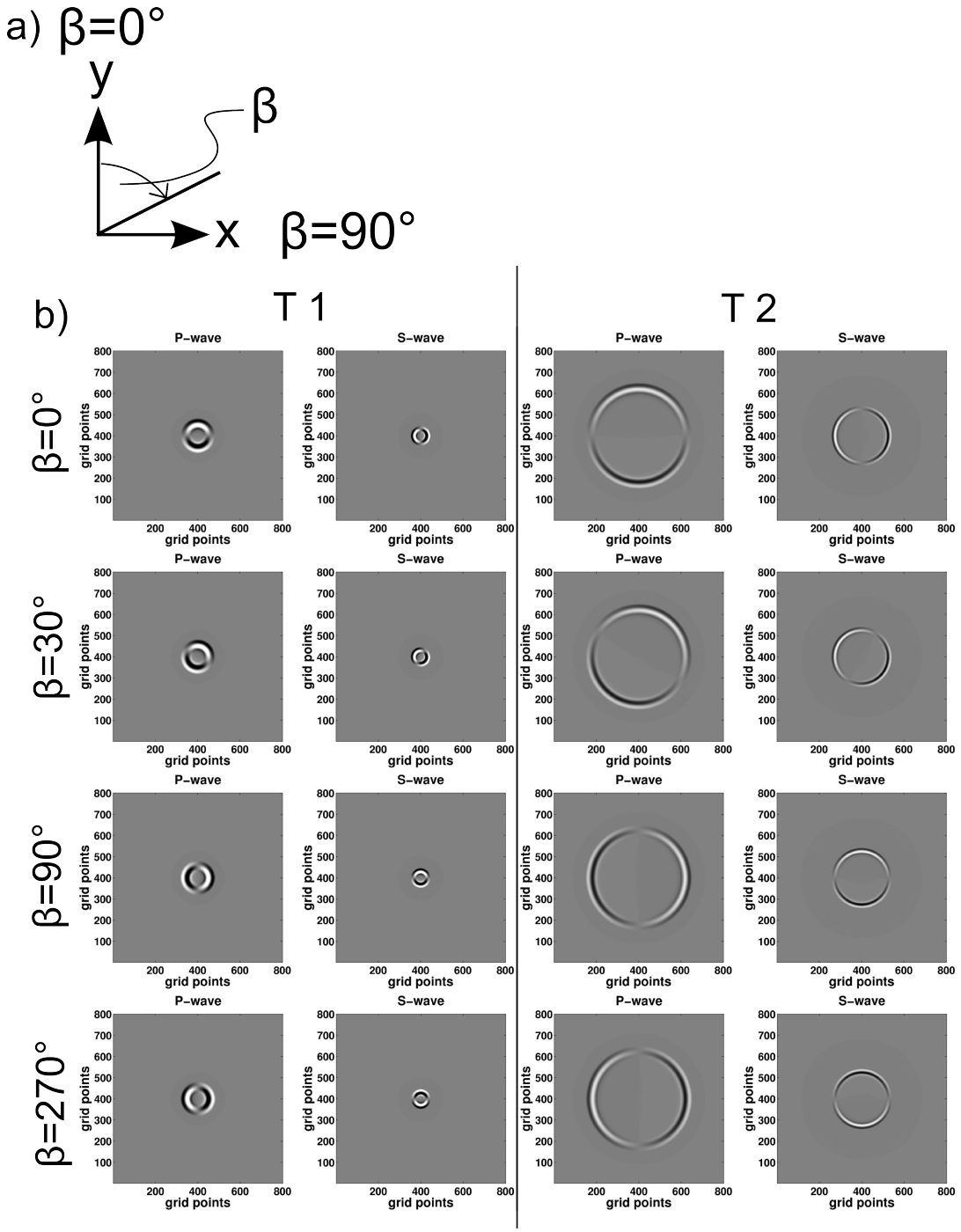

Figure 2.1: Scheme for the rotated sources. a) β denotes the angle between the y- and x-axis. For $\beta = 0^\circ$ the force is in accordance with a force in y-direction and for $\beta = 90^\circ$ with a force in x-direction, respectively. b) Snapshots of the P- and S-wave for a homogeneous velocity model for different points in time (T1 and T2) and for different values of β. The wavefield is separated into the appearing wave types (Bohlen, 1998, Section 3.3.4). We do not look directly at the spatial displacement or velocity. The colour scale for P- and S-waves differs.

modelling of the source wavefield and back-propagation of the data residuals, a finite-differences stress-velocity scheme is applied (Section 2.2). With the adjoint approach, a gradient of a predefined misfit function can be calculated numerical efficiently. Further, the conjugate gradient method is used to improve the convergence of the iterative algorithm. In the following, the theory of the adjoint approach and important implemented features are explained. For more details of DENISE, we refer to Köhn (2011) and Groos (2013). The code is available from `http://www.gpi.kit.edu/Software.php` under the terms of the GNU General Public License.

2.3.1 The FWI with the Adjoint Approach

In general, the FWI as an inverse method wants to find a model which explains the observed data. In the case of the FWI this is not only related to first-arrival times or amplitudes of specific phases, but also to the whole waveform which should be explained. In seismic, the shape of the waveform depends on the used source wavelet and on the elastic properties. In latter we are interested in. The relation between the unknown elastic parameters of the model and the behaviour of the seismic waves are strongly non-linear.
At a first step, the properties of the model have to be parametrised. In the case of seismic or seismology the typical parameters are the seismic velocities or the Lamé parameters and the density. The next step is to describe the physics as good as possible with appropriate equations which are then used to calculate synthetic data $\mathbf{d}_{synth}(\mathbf{m})$ based on the model parameters $\mathbf{m}$. This can be written as

$$\mathbf{d}_{synth}(\mathbf{m}) = f(\mathbf{m}) \tag{2.14}$$

with f as a non-linear forward operator.
In the last step, the observed data $\mathbf{d}_{obs}$ are taken into account. The model parameters $\mathbf{m}$ are updated until the predicted synthetic data $\mathbf{d}_{synth}$ fits to the observed data $\mathbf{d}_{obs}$. Usually, this is not done in one step. Basically, the FWI is an iterative method.

Model Optimisation

The inversion wants to find a model which fits the predicted synthetic data $\mathbf{d}_{synth}(\mathbf{m})$ best to the observed data $\mathbf{d}_{obs}$. As a measure how good the model parameters $\mathbf{m}$ can explain the observed data, the data residual or misfit $\delta\mathbf{d}$ is introduced:

$$\delta\mathbf{d} = \mathbf{d}_{synth} - \mathbf{d}_{obs} = f(\mathbf{m}) - \mathbf{d}_{obs}. \tag{2.15}$$

A widely-used criterion to measure the residual is the squared L2-norm:

$$E(\mathbf{m}) = \frac{1}{2}\delta\mathbf{d}^T\delta\mathbf{d} \tag{2.16}$$

where $E(\mathbf{m})$ is the objective function or misfit function, respectively, and the superscript ^{T} is the transpose operator. In general, the residuals are summed up over the number of components, the number of source-receivers pairs and the number of time samples. At once, it has a special physical meaning: It is the elastic energy $E(\mathbf{m})$ which is not adapted to the model. So, the aim is to minimise the energy, or in other words, to fit the synthetic data to the observed data.

By assuming only low non-linearities between the data and the model, one solution to linearise a problem is called the Born approximation. We would like to find an updated model $\mathbf{m}$ which fits the data best in the vicinity of the starting model $\mathbf{m_0}$ with a small perturbation $\delta\mathbf{m}$:

$$\mathbf{m} = \mathbf{m_0} + \delta\mathbf{m}. \tag{2.17}$$

We expand the residual energy of Equation (2.16) in a Taylor series and neglect higher-order terms such that

$$E(\mathbf{m}) = E(\mathbf{m_0} + \delta\mathbf{m}) = E(\mathbf{m_0}) + \delta\mathbf{m}\left(\frac{\partial E(\mathbf{m_0})}{\partial \mathbf{m}}\right) + \mathcal{O}(\mathbf{m}^2). \tag{2.18}$$

To find the minimum of Equation (2.18), we calculate the derivative with respect to the model parameters and set the equation zero:

$$\frac{\partial E(\mathbf{m})}{\partial \mathbf{m}} = \frac{\partial E(\mathbf{m_0})}{\partial \mathbf{m}} + \delta\mathbf{m}\left(\frac{\partial^2 E(\mathbf{m_0})}{\partial \mathbf{m}^2}\right) = 0, \tag{2.19}$$

which leads to

$$\delta\mathbf{m} = -\left(\frac{\partial^2 E(\mathbf{m_0})}{\partial \mathbf{m}^2}\right)^{-1} \frac{\partial E(\mathbf{m_0})}{\partial \mathbf{m}}. \tag{2.20}$$

The second factor of the objective function $-\frac{\partial E(\mathbf{m_0})}{\partial \mathbf{m}}$ denotes the steepest descent of the objective function and can be written as

$$\frac{\partial E(\mathbf{m_0})}{\partial \mathbf{m}} = \left(\frac{\partial \mathbf{d}_{synth}(\mathbf{m}_0)}{\partial \mathbf{m}}\right)^T (\mathbf{d}_{synth}(\mathbf{m}_0) - \mathbf{d}_{obs}) = \mathbf{J}_0^T\, \delta\mathbf{d}. \tag{2.21}$$

$\mathbf{J}$ denotes the Jacobian matrix. $\mathbf{J}^T$ is also called Fréchet derivative matrix:

$$J_{ij} = \frac{\partial d_{synth_i}}{\partial m_j} \quad (i = 1, 2, \ldots, K), (j = 1, 2, \ldots, L) \tag{2.22}$$

where K is the length of the vector $\mathbf{d}_{synth}$ and L the length of the model vector $\mathbf{m}$.

The first factor of the objective function, $\mathbf{H}^{-1}$, is called the inverse Hessian matrix. It represents the curvature of the objective function and has the dimension $L \times L$.

$$\frac{\partial^2 E(\mathbf{m_0})}{\partial \mathbf{m}^2} = \mathbf{H}_0 = \mathbf{J}_0^T\, \mathbf{J}_0 + \left(\frac{\partial \mathbf{J}_0}{\partial \mathbf{m}}\right)^T \delta\mathbf{d}. \tag{2.23}$$

The calculation of $\mathbf{H}^{-1}$ is very time-consuming. Often, the Hessian is approximated by a preconditioning operator $\mathbf{P}$. As there is no general rule how to choose the preconditioning, we designed our own preconditioning operators $\mathbf{P}$ with respect to the survey and experience we made (Section 2.3.3).

Equation (2.20) can now be rewritten as

$$\delta\mathbf{m} = -\mathbf{H}_0^{-1}\, \mathbf{J}_0^T\, \delta\mathbf{d} \tag{2.24}$$

or

$$\delta \mathbf{m} \approx -\mathbf{P}\, \mathbf{J}_0^T\, \delta \mathbf{d} = -\mathbf{P}\, \frac{\partial E}{\partial \mathbf{m}}. \tag{2.25}$$

Finally, the model is updated iteratively with the conjugate gradient method. The model is updated in the opposite direction of the gradient of the objective function by a multiplication with an appropriate step length κ (Section 2.3.4). At iteration n we get:

$$\mathbf{m}_{n+1} = \mathbf{m}_n - \kappa_n \mathbf{P}_n \left(\frac{\partial E}{\partial \mathbf{m}} \right)_n. \tag{2.26}$$

The step length κ has to be recalculated after each iteration step (Section 2.3.4).

The Adjoint Approach

In the previous section, Equation (2.21) can be described as follows: A small change in the data space is related to a change in the model space and vice versa. As we intend to minimise the misfit between synthetic and observed data, we have to perturb the parameters of the model. The calculation of the Fréchet derivative matrix $\mathbf{J}$ explicitly would require L forward modellings because every single model parameter has to be changed separately. The full-waveform inversion uses the adjoint approach proposed by Tarantola (1984) and Mora (1987) which calculates the direction of the gradient by a cross-correlation of the forward modelled synthetic data with the back-propagated residual data. That means, for every source only two modellings are required. Below, we follow the work of Mora (1987) closely, although for more details the reader is refer to Tromp et al. (2005) and Bozdağ et al. (2011).

We start with Equation (2.14) and add a perturbation $\delta \mathbf{m}$ to the background model $\mathbf{m_0}$:

$$\mathbf{d}_{synth}(\mathbf{m}) = f(\mathbf{m}) = f(\mathbf{m}_0 + \delta \mathbf{m}). \tag{2.27}$$

The initial non-linear operator f is approximated with the Taylor series expansion similar to Equation (2.18), again neglecting higher-order terms:

$$f(\mathbf{m}_0 + \delta \mathbf{m}) = f(\mathbf{m}_0) + \frac{\partial f(\mathbf{m}_0)}{\partial \mathbf{m}} \delta \mathbf{m} + \mathcal{O}(\mathbf{m}^2). \tag{2.28}$$

To express a small perturbation in the model space $\delta \mathbf{m}$ which results in perturbation of the data space $\delta \mathbf{d}$, we use

$$\delta \mathbf{d} = f(\mathbf{m}_0 + \delta \mathbf{m}) - f(\mathbf{m}_0). \tag{2.29}$$

With Equation (2.28), Equation (2.29) leads to

$$\delta \mathbf{d} = f(\mathbf{m}_0) + \frac{\partial f(\mathbf{m}_0)}{\partial \mathbf{m}} \delta \mathbf{m} - f(\mathbf{m}_0) = \frac{\partial f(\mathbf{m}_0)}{\partial \mathbf{m}} \delta \mathbf{m}, \tag{2.30}$$

thus, that the deviation can be identified to

$$\delta \mathbf{d} = \mathbf{J}_0\, \delta \mathbf{m}, \tag{2.31}$$

where $\delta \mathbf{d}$ are the data residuals between synthetic and observed data (Equation (2.16)). The equation states that the data residuals $\delta \mathbf{d}$ act linearly to a perturbation in the model space

$\delta\mathbf{m}$. After Mora (1987), we can rewrite Equation (2.31) in a continuous form:

$$\delta\mathbf{d}(D) = \int_M \frac{\partial\mathbf{d}(D)}{\partial\mathbf{m}}\delta\mathbf{m}(M)\,dM, \tag{2.32}$$

where M indicates the model space and D the data space, respectively. By integrating over the model space M, that means a small perturbation in the model parameter $\partial\mathbf{m}$ multiplied with the Fréchet derivative matrix, the resulting perturbations in the data space $\delta\mathbf{d}$ can be calculated.
Finally, also the gradient of the objective function in Equation (2.25) can be addressed in a continuous form:

$$\delta\hat{\mathbf{m}}(M) = \int_D \left[\frac{\partial\mathbf{d}(D)}{\partial\mathbf{m}}\right]^* \delta\mathbf{d}(D)\,dD, \tag{2.33}$$

where the superscript * denotes the adjoint. The circumflex is used to make clear that $\delta\hat{\mathbf{m}}$ and $\delta\mathbf{m}$ are not the same.

The displacement u for a given model $\mathbf{m}$, a source location $\mathbf{x}_s$ and a receiver location $\mathbf{x}_r$ at time t can be defined as $u_i(\mathbf{x}_r, \mathbf{x}_s, t) = f(\mathbf{m}) = u(\mathbf{x}_r, t; \mathbf{x}_s)$. With Equation (2.32) and (2.33), this leads to

$$\delta d_i(\mathbf{x}_r, \mathbf{x}_s, t) = \int_V \frac{\partial d_i(\mathbf{x}_r, \mathbf{x}_s, t)}{\partial\mathbf{m}(\mathbf{x})}\delta\mathbf{m}(\mathbf{x})\,dV(\mathbf{x}), \tag{2.34}$$

and

$$\delta\hat{\mathbf{m}}(\mathbf{x}) = \sum_s \int \sum_r \frac{\partial d_i(\mathbf{x}_r, \mathbf{x}_s, t)}{\partial\mathbf{m}(\mathbf{x})}\delta d_i(\mathbf{x}_r, \mathbf{x}_s, t)\,dt, \tag{2.35}$$

where the second equation denotes the adjoint problem and represents the integral over the data space of the Fréchet derivative matrix multiplied with the data residuals. In addition, we have to sum up over all sources and receivers. To obtain the adjoint operation in Equation (2.35), we only need the integral expression of Equation (2.34) for the forward problem which gives the perturbation of the displacement δd_i. This corresponds to some perturbations in the model parameters $\delta\mathbf{m}$. A linearised approximation of Equation (2.8) regarding the Green's functions supplies afterwards the desired integral as we will see later on. This is a proper way to to solve a linear differential equation.

For the full derivation of the adjoint method in the elastic case, we again refer to Mora (1987). The gradients for the Lamé parameters λ and μ and for the density ρ in the 2D case as we use it in this thesis can be written as:

$$\delta\lambda = -\sum_s \int_t \left(\frac{\partial u_x}{\partial x} + \frac{\partial u_y}{\partial y}\right)\left(\frac{\partial u_x^\dagger}{\partial x} + \frac{\partial u_y^\dagger}{\partial y}\right) dt, \tag{2.36}$$

$$\delta\mu = -\sum_s \int_t \left(\frac{\partial u_x}{\partial y} + \frac{\partial u_y}{\partial x}\right)\left(\frac{\partial u_x^\dagger}{\partial y} + \frac{\partial u_y^\dagger}{\partial x}\right) + 2\left(\frac{\partial u_x}{\partial x}\frac{\partial u_x^\dagger}{\partial x} + \frac{\partial u_y}{\partial y}\frac{\partial u_y^\dagger}{\partial y}\right) dt, \tag{2.37}$$

$$\delta\rho = \sum_s \int_t \left(\frac{\partial u_x}{\partial t}\frac{\partial u_x^\dagger}{\partial t}\right) + \left(\frac{\partial u_y}{\partial t}\frac{\partial u_y^\dagger}{\partial t}\right) dt \tag{2.38}$$

where the wavefield variable u denotes the displacement wavefield which was excited

by a source $s(\mathbf{x}, t; \mathbf{x}_s)$ in the current model and $u^\dagger$ denotes the back-propagated residual wavefield. Please note that both u and $u^\dagger$ depend on the source location $\mathbf{x}_s$. The gradient of the objective function can be calculated by a zero-lag cross-correlation of the forward propagated wavefield u and the adjoint wavefield $u^\dagger$ with

$$u(\mathbf{x}, t; \mathbf{x}_s) = \int_V G(\mathbf{x}, t; \mathbf{x}_s, 0) * s(\mathbf{x}, t; \mathbf{x}_s)\, dV \tag{2.39}$$

and

$$u^\dagger(\mathbf{x}, t; \mathbf{x}_s) = \sum_r G(\mathbf{x}, -t; \mathbf{x}_r, 0) * \delta d_i(\mathbf{x}_r, \mathbf{x}_s, t) \tag{2.40}$$

where the $*$ denotes a convolution and G denotes the Green's function associated with Equation (2.8).

$u^\dagger$ is calculated by back-propagating the residual wavefield in reverse time direction. The residuals are applied in the FD scheme at every receiver point that corresponds to the original source. The residual wavefield is interpreted as the missing diffracted energy of the current model compared to the "true" model. The gradient of the objective function can be calculated by a zero-lag cross-correlation of the forward modelled wavefield and the back-propagated residuals or adjoint wavefield, respectively. To obtain the final gradient, all individual gradients for all sources are summed up.
With DENISE it is possible to choose whether the gradient is parametrised by the density and the Lamé parameters or the density and the seismic velocities for the P- and S-wave. Köhn et al. (2012) investigated the reconstruction potential with synthetic tests by using different parametrisation on reflection geometry. They concluded that the reconstructed model for the density and the P- and S-waves are more accurate than for the density and the Lamé parameters. As the scope of this thesis is to characterise the velocity distribution within an area of interest, for all synthetic tests as well as for the field data we use the density and the seismic velocities as the parametrisation. The relation between the Lamé parameters and the density to the seismic velocities for P- and S-waves (v_P and v_S) are stated in Equation (2.9). With

$$\begin{aligned} \rho' &= \rho, \\ \lambda = \rho'\,(v_\mathrm{P}^2 - 2v_\mathrm{S}^2) \quad &\text{and} \\ \mu &= \rho'\, v_\mathrm{S}^2 \end{aligned} \tag{2.41}$$

the gradients could be rewritten by using the chain rule (Mora, 1987) to

$$\delta v_\mathrm{P} = 2\rho' v_\mathrm{P} \delta\lambda, \tag{2.42}$$

$$\delta v_\mathrm{S} = -4\rho' v_\mathrm{S} \delta\lambda + 2\rho' v_\mathrm{S} \delta\mu \tag{2.43}$$

and

$$\delta\rho' = (v_\mathrm{P}^2 - 2v_\mathrm{S}^2)\delta\lambda + v_\mathrm{S}^2 \delta\mu + \delta\rho, \tag{2.44}$$

respectively.

2.3.2 Misfit Definition - Objective Function

In this thesis two different objective functions are used to define the misfit which are explained in the following.
In general, the objective function influences the shape of the gradient or the derivative of the objective function with respect to the model parameters, respectively. By using the chain rule, we obtain

$$\frac{\partial E(\mathbf{m})}{\partial \mathbf{m}} = \frac{\partial E_{\text{misfit}}(f(\mathbf{m}))}{\partial \mathbf{m}} = \frac{\partial E_{\text{misfit}}(f(\mathbf{m}))}{\partial f(\mathbf{m})} \frac{\partial f(\mathbf{m})}{\partial \mathbf{m}} = \mathbf{J}^T \mathbf{r} \tag{2.45}$$

where E_{misfit} is the used objective function in the inversion, $\mathbf{J}$ denotes the Jacobian matrix and $\mathbf{r}$ represent the residual seismograms. The Jacobian matrix does not depend on the used objective function, in contrast to the residual seismograms $\mathbf{r}$ which are defined as $\partial E_{\text{misfit}}(f(\mathbf{m}))/\partial f(\mathbf{m})$. The residual wavefield is calculated by back-propagating the residual seismograms back in time from the corresponding receiver positions (Section 2.3).

Least-Squares Norm

A common objective function is the L2 norm or least-squares norm which is defined as

$$E = ||\delta \mathbf{d}||_2^2 = ||\mathbf{d}_{synth} - \mathbf{d}_{obs}||_2^2 = (f(\mathbf{m}) - \mathbf{d}_{obs})^2. \tag{2.46}$$

E is summed up over all time samples, source-receiver combinations and components.
The residual seismograms or adjoint sources, respectively, for the least-squares norm are

$$\mathbf{r} = 2\,\delta \mathbf{d}. \tag{2.47}$$

Global Correlation Norm

The global correlation norm was suggested by Choi and Alkhalifah (2012). The objective function is defined with wavefields which are normalised trace by trace with its RMS value. The advantage of the misfit definition is being not sensitive to the geometrical spreading and, thus, having no offset dependency. Furthermore, the definition can handle differences in the energy levels between the observed wavefield and the synthetic wavefield.
In DENISE the misfit calculation is slightly different implemented as suggested by Choi and Alkhalifah (2012). In addition, the misfit value is normalised with respect to the energy of the normalised observed seismograms (Groos, 2013, p. 26):

$$E = \frac{\left| \hat{f}(\mathbf{m}) - \hat{\mathbf{d}}_{obs} \right|^2}{|\hat{\mathbf{d}}_{obs}|^2} \tag{2.48}$$

with $\hat{f}(\mathbf{m}) = f(\mathbf{m})/|f(\mathbf{m})|$ and $\hat{\mathbf{d}}_{obs} = \mathbf{d}_{obs}/|\mathbf{d}_{obs}|$ which are the RMS normalised displacement seismograms of the synthetic and observed data. Because of the normalisation to the energy of the normalised observed seismograms, the misfit value is meaningful. For example, $E = 1.5$ means that the energy of the adjoint sources have 1.5 times the energy as the normalised observed seismograms, i. e., 150% of the energy of the observed seismograms are not yet fitted. We will use the misfit values in the field data inversion (Chapter 6) to state how much the misfit has been decreased in the inversion.
With Equation (2.45), the adjoint sources can be calculated which coincide with Choi and

Alkhalifah (2012, Equation (8)):

$$\mathbf{r} = \frac{1}{|f(\mathbf{m})|}\left[\hat{f}(\mathbf{m})\left(\hat{f}(\mathbf{m})\cdot\hat{\mathbf{d}}_{obs}\right) - \hat{\mathbf{d}}_{obs}\right]. \tag{2.49}$$

For the back-propagation, the time has to reversed additionally.

2.3.3 Preconditioning of the Gradient

In Equation (2.26), with the operator P, we can precondition the gradient for our purposes. We use two possibilities. On the one hand, the preconditioning can be applied before the summation of the individual gradients for every single source. On the other hand, the preconditioning can be applied to the summed up gradient.
In the vicinity of the source positions, the gradient has very high values. The reason for this is simple: The amplitude of the propagating wavefield is decreasing with distance because of the geometrical spreading. Around the source positions the amplitude is very high. The cross-correlation of the forward modelled and back-propagated wavefields leads to very high values of the gradient at the source positions (Causse et al., 1999). The velocity model is, thus, only updated around the source positions and no update would occur in other areas of the model, respectively. Therefore, a preconditioning of the individual gradients for each source is applied before the summation over all sources. This ensures that the entire model receives a significant update. As a taper function, the shape of a Gauss error function is used. At the source position, the taper equals zero. The taper coefficients increase continuously until a predefined radius around the source is reached (Groos, 2013, Figure 2.4).
In addition, we used a second taper function after the summation of the gradient. This is common practise in the marine FWI where an update within the water layer is forbidden (Kurzmann, 2012). We used this technique to allow only an update within our measurement area (Chapter 3). The summed up gradient is multiplied with a matrix which consists of ones within the measurement area and zeros for all other grid points.

2.3.4 Scaling of the Gradient

Before updating the model, the gradient has to be scaled with the step length κ (Equation (2.26)). The parameters of the model are the density, the P- and S-wave velocity. In DENISE, each gradient for the three parameters (δv_P, δv_S and $\delta\rho$) is scaled independently without any cross constrains. Let $\mathbf{v}_\mathrm{P}$, $\mathbf{v}_\mathrm{S}$ and ρ be vectors which contain density, P- and S-wave velocities of the current model. Each gradient, which could be also addressed as a vector, is scaled by the maximum of the gradient to the maximum of the current model (Köhn, 2011):

$$\begin{aligned}
\kappa_\mathrm{P} &= \epsilon\frac{\max[\mathbf{v}_\mathrm{P}]}{\max[\delta v_\mathrm{P}]},\\
\kappa_\mathrm{S} &= \epsilon\frac{\max[\mathbf{v}_\mathrm{S}]}{\max[\delta v_\mathrm{S}]},\\
\kappa_\rho &= \epsilon\frac{\max[\rho]}{\max[\delta\rho]}
\end{aligned} \tag{2.50}$$

where ϵ is a scalar factor. That means, that the maximum update in each model parameter $\vec{v}_P$, $\vec{v}_S$ and $\vec{\rho}$ is ϵ times the maximum value of this parameter in the current model (Groos, 2013). The step length κ is a function of the scalar factor ϵ and must be determined before the model can be updated. In the FWI, after Kurzmann et al. (2009), the misfit can be locally approximated by a parabola. For the general theory behind such a line search method, we refer to Nocedal and Wright (1999). For three different test step lengths the corresponding misfit can be calculated and a parabola could be fitted. The minimum of the parabola is the optimal step length. In DENISE an enhanced approach is implemented. For details of the implementation in DENISE, we refer to Köhn et al. (2013).
In order to save computational time, not all sources have to be used for determining the test step length. We only take three test sources in the synthetic tests (Chapter 5) and every fifth source for the field data (Chapter 6) into account. Finally, the model is updated by scaling the gradient with the optimal step length which was found for the current iteration.

2.3.5 Workflow in DENISE

In the following, the workflow of DENISE is presented step by step.
As the input parameters, we first need the observed data and the corresponding acquisition geometry. With the observed data e. g., by picking the first arrivals, we have to calculate an initial model which fits the phases at least within half a wavelength (Section 2.3.6). Otherwise, due to the high non-linearity of the problem, the inversion could not reconstruct the structures of the "true" model. Afterwards, for each source, the forward problem is solved with a loop over all sources and all timesteps. The wavefields for the stresses and particle velocities are saved in the memory. The residual seismograms or the adjoint sources, respectively, are calculated using the synthetic forward modelled data and the observed data (Section 2.3.2). The residual seismograms are then back-propagated from the receiver positions. In practise, this corresponds to a forward modelling where the adjoint sources are reversed in time and act like sources at the receiver positions. The gradient of the misfit function can be calculated by a zero-lag cross-correlation of the forward modelled wavefield and the back-propagated wavefield on the fly during the back-propagation. The next step is to precondition the gradient with an adequate operator (Section 2.3.3) and to calculate the conjugate gradient. With at least three different test step length the optimal step lengths by fitting a parabola to the misfit values can be determined (Section 2.3.4). At last, the model parameters are updated by scaling the gradients with the determined step length. For the next iteration step, the updated model is used as the new initial model. The inversion converged to a minimum if the misfit could not be further reduced.

2.3.6 Non-Linearities of the FWI

The full-waveform inversion is a highly non-linear problem. In consequence, the shape of the misfit function is not linear with one global minimum, rather a complex structure with lots of local minima. To avoid to get stuck in a local minimum, it is important to start with a proper starting model where no cycle-skipping occurs and to apply a multi-scale approach with frequency filtering.

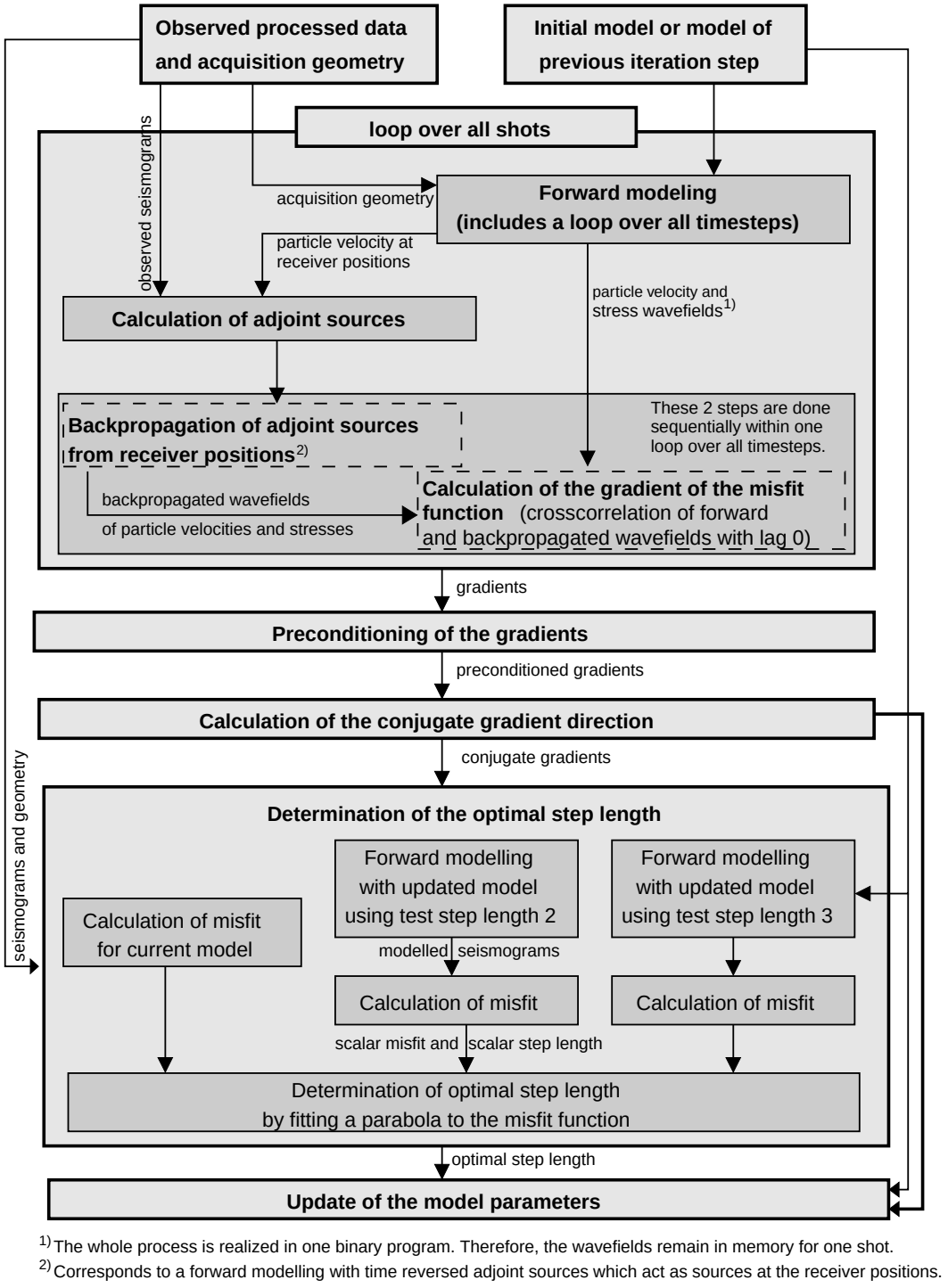

1) The whole process is realized in one binary program. Therefore, the wavefields remain in memory for one shot.
2) Corresponds to a forward modelling with time reversed adjoint sources which act as sources at the receiver positions.

Figure 2.2: Workflow of DENISE for a single iteration step (Groos, 2013, Figure 2.3).

Cycle-skipping

The starting model must be as good as possible, at least it must explain the data within half the wavelength, otherwise cycle-skipping occurs (Virieux and Operto, 2009). The inversion cannot decide which phase of the synthetic data corresponds to the observed data. Therefore, we have to ensure that the phases have a maximum phase shift of half the wavelength. If this is not the case, the inversion fits cycles from synthetic and observed data which actually do not correspond to each other and the FWI ends up in a local minimum.

Multi-Scale Approach with Frequency Filtering

To reduce the non-linearity of the inverse problem and to avoid cycle-skipping, we have to reduce the ambiguities of the misfit function. This is usually done with the so called multi-scale inversion approach (Bunks et al., 1995). The inversion starts with low frequencies of the observed data. This leads to a more linear behaviour of the misfit function and it is easier to avoid cycle-skipping because of the longer wavelength. Higher frequencies are continuously added after the inversion converged for one frequency range. This approach can lead the inversion to the global minimum (Sirgue and Pratt, 2004). In DENISE, the multi-scale approach is implemented by applying a Butterworth low-pass filter to the observed data with a user-defined minimum and maximum corner frequency for the filter as well as a user-defined increment of the corner frequency.

2.4 Source Time Function Inversion

In the synthetic analysis, we always assume to know the source properties and the shape of the source wavelet. For the field data inversion this is not the case. Pratt (1999) suggested an iterative, linear least-squares optimisation inversion which is based on a deconvolution of the observed data with the synthetic data to estimate the source wavelet:

$$s(\omega) = \frac{\mathbf{d}_{synth}^T \cdot \mathbf{d}_{obs}^*}{\mathbf{d}_{synth}^T \cdot \mathbf{d}_{synth}^*} \tag{2.51}$$

where the vector $\mathbf{d}_{synth}$ denotes the synthetic data and the vector $\mathbf{d}_{obs}$ the observed data. The superscript ^{T} is the transpose operator and the superscript * means the complex conjugated (Pratt, 1999, Equation 17). As the inverse problem is formulated in the frequency domain, we have to minimise the least-squares misfit for each frequency ω. For more details how the approach is implemented with a stabilised deconvolution in DENISE, we refer to Groos (2013) and Groos et al. (2014).

The method needs an initial source wavelet as well as an initial velocity model to perform the forward modelling to compute the synthetic data which is compared to the field data. The initial velocity model is the crucial point in the linear inversion. As we use a transmission geometry (Chapter 3), the waveforms are influenced by the velocity structure of the "true" velocity model. If the initial model is not accurate enough, the difference between initial and true velocity model are projected into the wavelet.

To avoid this problem, we repeat the source time function inversion after each frequency range of the multi-scale approach with the updated velocity model and, thus, determine an updated source wavelet (Section 2.3.6). This can serve as a quality check of the inversion, too. If the source wavelet is mostly coherent in its appearance for the different frequency ranges,

this indicates an accurate reconstruction of the velocity model (Brenders, 2011; personal communication: Jean Virieux).

2.5 Travel-Time Tomograhy

As described in the previous section, due to the high non-linearity of the inversion problem and in order to gain robustness, the FWI can only succeed with a sufficiently and accurate starting model. Thus, cycle-skipping is avoided. Pratt and Goulty (1991) showed that starting models obtained from a travel-time tomography are a reasonable choice.
For the performed travel-time tomographies in this thesis we use the software GeoTomCG[1] (Tweeton, 2011). This is a commercial software for both 2D and 3D travel-time tomographies. The hand-picked first-arrival times are inverted using the simultaneous iterative reconstruction technique (SIRT, e. g., Peterson et al., 1985; Lytle and Lawrence Livermore Laboratory, 1978). The SIRT method was former used for medical tomographies but is nowadays also used for seismic tomographies. The advantage of the method lies on the one hand in its computational low costs (Trampert and Leveque, 1990) and on the other hand it is also very suitable for field data by obtaining the most stable results because in the case of noisy data, the noise does not critically deteriorate the reconstructed model (Lehmann, 2007).
The method is an iterative method which repeats the common steps: Perform a forward modelling of the travel times, calculate the residual values for the modelled and picked travel times and update the velocity model in the direction to reduce the residual values. For the starting model, a homogeneous velocity model is used, adopted from the mean and the slowest straight-line velocity (Tweeton, 2011). In addition, the software also provides an initial suggested block size and grid points, respectively, to gain a robust and stable velocity model. After the inversion, the still remaining travel-time residuals for each source-receiver pair as well as the ray density for each block are available. The ray density for each block is used in order to assess the validity of the inversion results (Section 5.1.2 and 6.1). The remaining residuals could be used to determine possible anisotropies in the measurement area (Section 4.4.2).

[1] http://dev.geotom.net/ 25.03.2014

3 Field Survey in Freiberg

After the theory, in this chapter the focus lies on the field survey in Freiberg (Saxony). In an old silver mine, we used the existing infrastructure to perform a seismic survey in hard rock conditions. Such a facility and seismic equipment is almost unique in the world and encouraged us even more in our project.
In the following the formation and the geology of the Ore Mountains are described (Section 3.1). The mining history (Section 3.2) and, as the most important part, the field survey are presented in detail in the Sections 3.3 and 3.4.

3.1 Geology of the Ore Mountains

The geology of the Ore Mountain is very complex, probably one of the most complicated geological structure in the world (Sebastian, 2013). In this section, the formation of this geological structure is described briefly.
In the Paleozoic era, around 540 million to 250 million years ago, the Variscan orogeny was caused by the collision of Gondwana and Laurasia (Gradstein et al., 2012). This time period forms, e. g., gneiss, mica schist, and phyllite. After the intrusion of magma from the earth's interior the solidification of the magma leads to granite which is related to ore deposits. Over the course of millions of years the Variscan mountains were eroded and only undulating hills were left (Figure 3.1a).
In the Tertiary (65 to 30 million years ago) the remaining mountains faced a strong lateral pressure by the North drift of the North American plate (Alpidic orogeny). The massif of the Ore Mountains as they exist today was partially lifted up as one block: on the German side the mountains rise slowly, on the Czech side the mountains have very steep slopes (Figure 3.1b).
Starting from the Cenozoic era, erosion took place. The plateaus were severely eroded, except of the valleys, because basalt is a highly weather resistant stone. This process is known as relief inversion. In the Quaternary the present valleys were formed (Figure 3.1c).

3.2 Mining History of Freiberg

The university and mining town Freiberg in the Free State of Saxony, Germany, is very famous for its mining history. The city is situated in the eastern part of the Ore Mountains, in German *Erzgebirge* (Figure 3.2a). An overview of the geological situation can be found in Figure 3.2b. In 1168 the first silver deposits were found (Bayer, 1999). In the 16th century, the Ore Mountains also received its current name because of its rich ore findings.
After decades of successful operation of the *Himmelfahrt Fundgrube*, with the beginning of

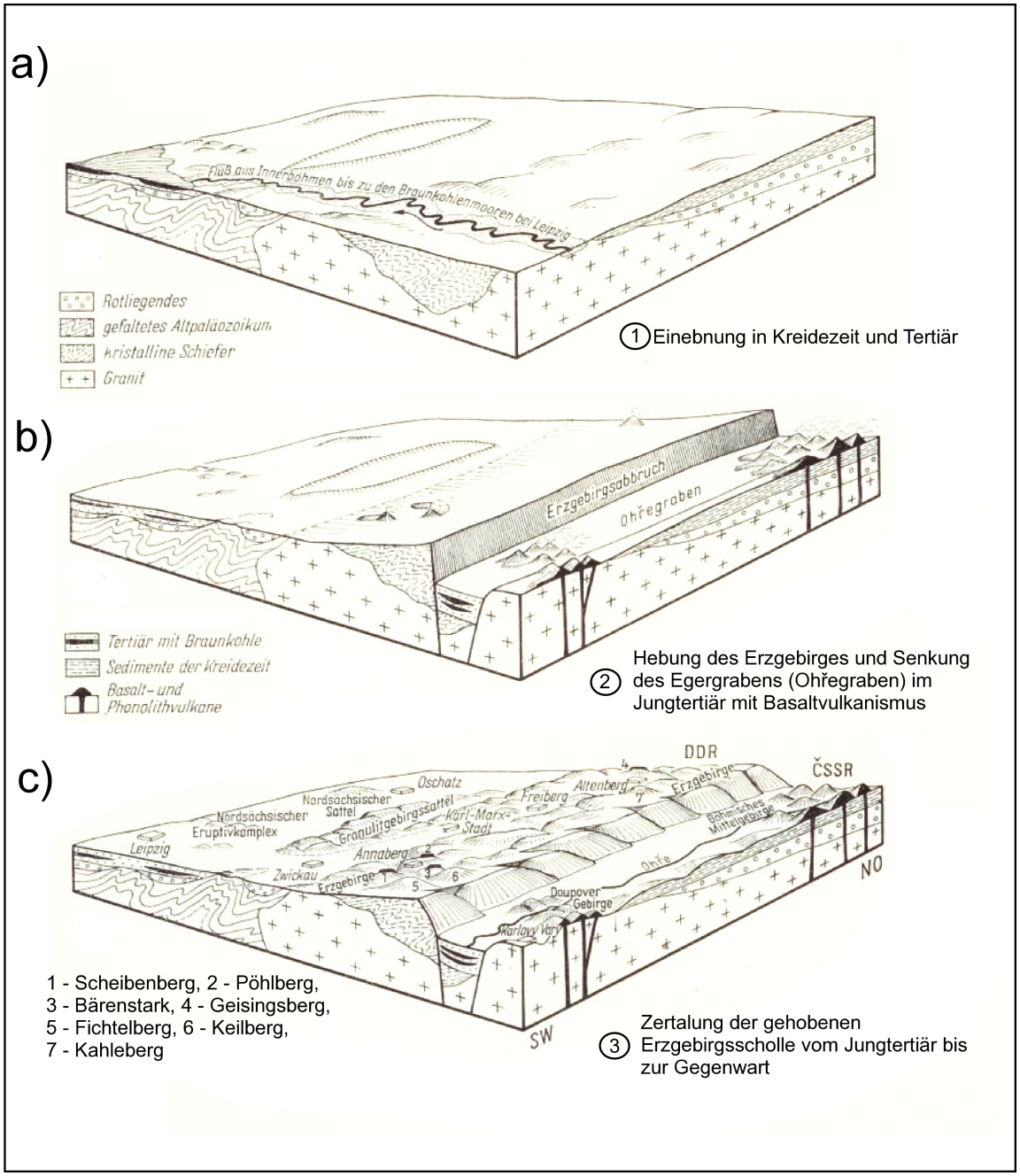

Figure 3.1: a) Denudation in the Cretaceous and Tertiary. b) Uplift in the Upper Tertiary. c) Erosion from the Upper Tertiary to the present (modified from Wagenbreth and Steiner, 1985, p. 135).

1880 the mining in Freiberg was no more cost effective due to the overproduction of silver and other minerals all over the world. As a consequence, mine operations were shut down in 1913. At that time, both the shaft *Reiche Zeche* and the *Alte Elisabeth* were already used for scientific research and education purposes. Again, within a short period of economic use, especially in the 1980s, since then, the mine's infrastructure has been continuously upgraded to improve the research facilities and abilities. The Freiberg University of Mining and Technology (Technische Universität (TU) Bergakadamie Freiberg - TU BAF) is the only university in Germany which has got an own mine for research and education purposes (Bayer, 1999). Since 1992, the *Reiche Zeche* (Figure 3.2c, black circle) is also open to the public who is interested in natural mineral deposit and mining history[2].

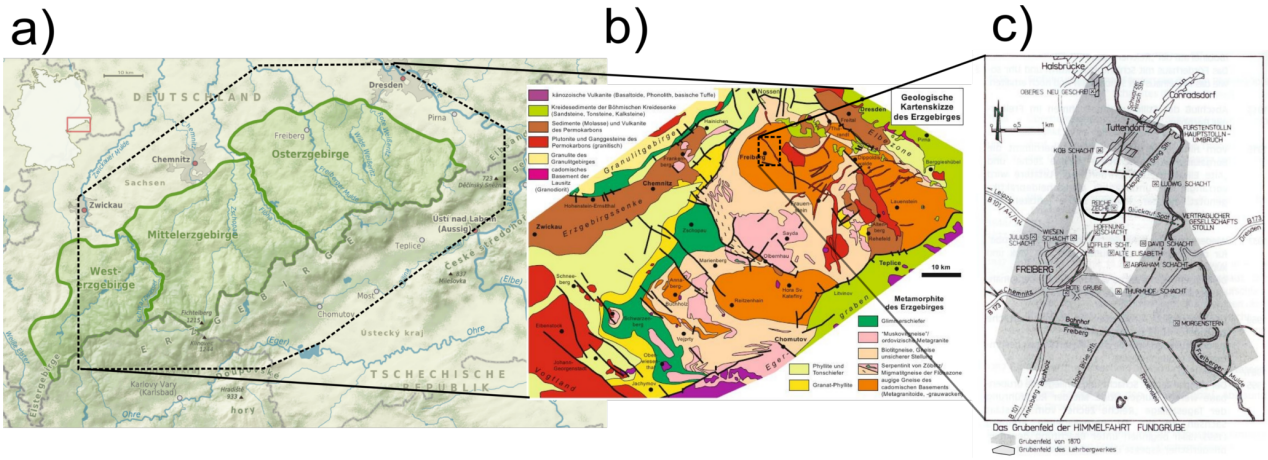

Figure 3.2: a) The location of the Ore Mountains in Germany and the division into its three parts[3]. b) Geological map of the Ore Mountains. Freiberg, in the northeastern part of the Ore Mountains, is located in an area of gneiss (modified from Sebastian, 2013, p. 5). c) Map of Freiberg and its surrounding with the mining fields of 1870 and the entrance to the research and education mine *Reiche Zeche* (encircled shaft).

3.3 GFZ-Underground-Laboratory in Freiberg

3.3.1 Description and Infrastructure

The German Research Centre for Geosciences (GFZ) in Potsdam, Germany, operates the GFZ-Underground-Laboratory (GFZ U-Lab) in the research and education mine *Reiche Zeche* in Freiberg. The geophysical Institute of the TU BAF has been using this facility for geophysical practical courses, especially for seismics in the underground, for many years. Around the year 2008, the GFZ established the U-Lab. It has been gradually upgraded with additional infrastructures and facilities. It is a unique location to test geophysical instruments, their applications as well as evaluation methods in a very defined and well-known geological environment. Especially for the FWI an accurate and reproducible measurement

[2]http://www.besucherbergwerk-freiberg.de/informatives.htm 17.10.2013
[3]http://en.wikipedia.org/wiki/FileErzgebirge_Naturraum_map_de.png 17.10.2013
Author: Alexander Karnstedt

is essential. The necessary infrastructure to perform seismic measurements below ground such as power supplies, Internet connection and electric light are available. Also, heavy equipment can be moved with rail cars on tracks.
With the shaft *Reiche Zeche* one have access to the first floor level at a depth of about 150 m below the surface (Figure 3.3a, red galleries). A block of gneiss, more specifically addressed as *Freiberger Greygneiss* (Hofmann, 1965), almost 50 m wide and 80 m long, is surrounded by three galleries (Figure 3.3b). Please note that the north arrow is turned upside down. The gneiss block will always be shown like this. The cross in the centre of Figure 3.3b is discussed in more detail in Section 4.1.
The western gallery (*Richtstrecke*) and the eastern gallery (*Wilhelm Stehender Süd*) are connected by the *Quergang* in the north. The gneiss block has been geologically mapped carefully (Section 3.3.2). From the mapping the gneiss block can be treated as mostly homogeneous with no expected changes in the host rock. However, there are breaks, fractures and hydrothermal mineralisation in the host rock which can be addressed as material changes and have an impact on seismic measurements. In addition, crystalline rocks are usually anisotropic. From the investigation in Section 4.4.2, we conclude that there is no evidence for anisotropy in the considered gneiss block.

All receivers are situated along the three galleries in almost a single plane (Section 4.1). Anchors can be screwed by a screw thread in a cased borehole. The boreholes are, as far as possible, perpendicular to the gallery walls. At the far end of the anchor, which is in the rock, three geophones are mounted and displaced by 90 ° in space to each other. Hereby, the ground velocities can be recorded in all the three spatial directions. Each anchor can only be inserted to a certain degree, allowing for a constant and well defined spatial orientation of the geophones. The three components are named EW, NS and Z and are specific for each anchor. The design of the anchors has been patented (Borm et al., 2003; Borm et al., 2008b). The anchors are either one or two m long. The receivers are mounted into the rock to avoid the influence of the excavation damage zone (EDZ) which exist around an excavated gallery (Giese et al., 2005). The seismic sources can be applied to the gallery walls around the block in an arbitrary positions, the shot spacing can thus be irregular. The word source and shot is used as a synonym in this work.
For the sake of completeness, the two additional boreholes which are not relevant for this study are mentioned. Two horizontal 8 1/2" boreholes of 20 m and 30 m length were drilled into the test site. The boreholes are open and completely cored. The boreholes can be used to test different kinds of sources and receivers on borehole tools[4].

3.3.2 Known Facts about the Survey Area

In former publications, the average velocity for P-waves, v_P, of the grey-gneiss has be determined to be 5430 m/s with a minimum velocity of 4010 m/s and a maximum velocity of 6070 m/s due to the anisotropy of the gneiss (Hurtig, 1967). The possible influence of the anisotropy is analysed in detail in Section 4.4.2.
The Freiberger gneiss block has been also a test object for seismic measurements for students of the TU BAF as well as a subject in several theses and projects. A geological mapping of the gneiss block was performed in 2008. Both sources of information are presented in the

[4]http://www.gfz-potsdam.de/en/scientific-services/labore/gfz-underground-lab-freiberg/ 28.11.2013
[5]http://www.besucherbergwerk-freiberg.de/grubenrisse/grubenriss.htm 28.11.2013

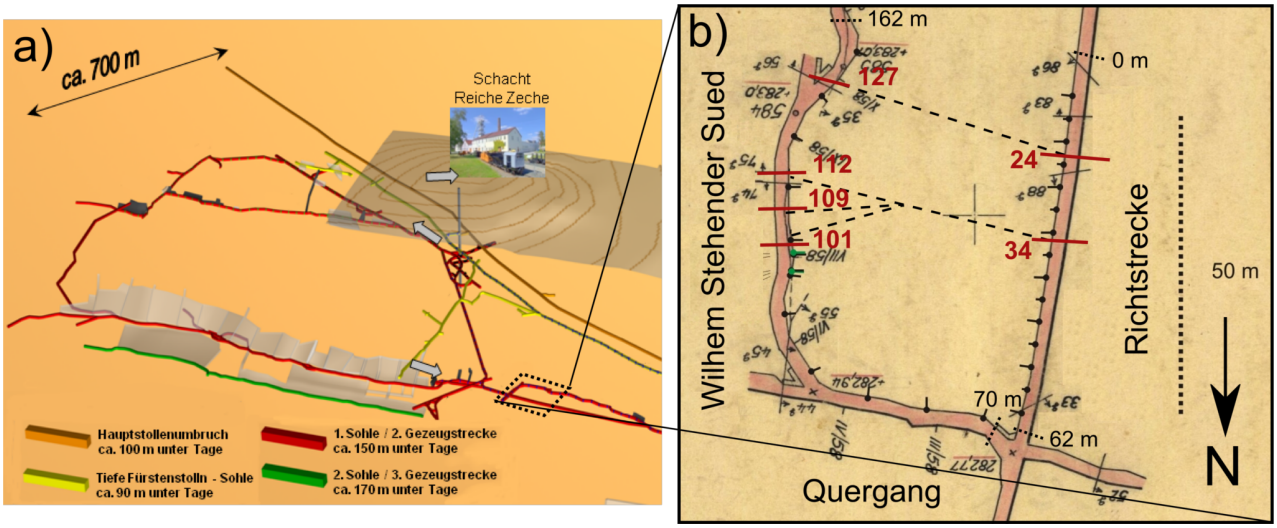

Figure 3.3: a) Part of a mine map: The red galleries on the first floor level are accessible from the *Reiche Zeche* shaft.[5]. b) Section of an old underground map from the year 1962 showing the survey area. Please note that the north arrow is turned downwards. The block is surrounded by three galleries in a depth of 150 m (*Wilhelm Stehender Süd*, *Richtstrecke* and *Quergang*). The red dashes and numbers indicate faults which were mapped from Kopf et al. (2008). The black dashed lines are assumed faults in the gneiss block (modified from Koop, 1962).

following.

3.3.2.1 Geological Mapping

Within the project Seismic Prediction While Drilling (SPWD) a geological mapping has been performed along the three galleries. The aim was to map breaks and faults and evaluate afterwards if a fault system strikes through the whole gneiss block. These faults systems could be possible seismic reflectors or areas with changing seismic velocities. Kopf et al. (2008) mapped beginning at 0 - 62 m along the *Richtstrecke* and from 70 - 162 m along the *Quergang* and *Wilhelm Stehender Süd*. The corner between 62 - 70 m could not be included due to a man-made concrete wall (Figure 3.3b). A total number of 130 structures were recorded and numbered. Most of them are mainly small cracks with a dimension from mm to cm. Also six joints faults could be mapped (Table 3.1). Structures 24, 34 and 112 are broad zones of alteration which usually have fractures or faults in the order of cm to several dm. The altered areas show a yellowish-brownish colour indicating that Fe^{3+} precipitates (Figure 3.4, fault 24). These areas are usually water ways, at least in the past. The density of the *Freiberger Greygneiss* gneiss was determined to 2.5 - 2.6 kg/m^3 (Kopf et al., 2008).
In the next section prior studies are presented which investigated the gneiss block in terms of velocity and attenuation. Afterwards the results are linked with the geological mapping.

3.3.2.2 Former Travel-Time Tomographies

Since the establishment of the U-Lab many students and thesis have been dealt with the gneiss block. Relevant results for this work are presented below and afterwards compared

Table 3.1: The most prominent joints of the geological mapping of Kopf et al. (2008). The joint number and the corresponding faults are shown in Figure 3.3b with a possible geologically interpretation.

Joint number	Position	Corresponding fault
24	Between R 3 and R 4	1
34	Between R 7 and R 8	2
101	At R 26	Maybe 2
109	Between R 26 and R 27	Probably 2
112	At R 27	2
127	Between R 29 and R 30	1

Figure 3.4: Pictures of the geological mapping of Kopf et al. (2008). From 18 - 22 m a large joint occurs which can be distinguished by a yellowish-brownish colour (joint number 24. The scale of the two pictures is almost the same, but only roughly estimated from the 1 m indicators (white dashes) in the pictures. Due to the slightly different perspectives, the images cannot be directly put together.

and evaluated.
Over several years, in the practical courses of the TU BAF, within a transmission geometry between the two almost parallel excavations *Wilhelm Stehender Süd* and the *Richtstrecke* many seismic measurements have been performed. Usually, the evaluation was done by the students with travel-time based methods. An example of a travel-time tomography of the P-wave with 25 shot positions and 23 receivers is shown in Figure 3.5a (modified from Bayer, 1999, p. 66). Please note that at the time of the tomography, no boreholes had been drilled.
The following two examples are based on the data discussed in this thesis. The data is presented in detail in Section 3.4. Within the framework of a diploma thesis, a travel-time tomography was performed (Richter, 2010). With a checkerboard test, the resolution limit was determined. Afterwards a tomography of the first-arrival P-wave was carried out (Figure 3.5b). In another thesis (Krauss, 2013) a quality factor model Q_p has been be calculated with focus on the P-wave. Krauss (2013) uses, amongst others, the logarithmic spectral ratio (LSR) method which operates in the frequency domain. For the calculation of the dimensionless value Q_p, a v_P model is necessary. Now, we can directly compare the three travel-time tomography models. Please note that both the geometry and the colour scale differs for the three examples.
In Figure 3.5a, in general, the v_P value varies from 4800 - 5200 $\mathrm{m/s}$. At the rock-air interface very strong velocity contrasts are visible which correlates with the source and receiver positions. Therefore these areas are treated as artefacts. A zone with little increasing velocity extends almost parallel to the *Richtstrecke*. In Figure 3.5b, please notice the broader range of the colour scale. In the northern part, the mean velocity from $y = 0$ m to $y = 40$ m is estimated to 5500 - 6000 $\mathrm{m/s}$. In the southern part, the velocity may vary very locally. In Richter (2010), a low velocity layer from west to east at about $y = 50$ m was identified. In the southernmost area of the v_P model, the velocities are higher than 8000 $\mathrm{m/s}$. But this area is not taken into account or interpreted, first because of very poor ray coverage, and second, this velocity is, even for hard rock, not physically meaningful. In Figure 3.5c, the average velocity is approximately 6000 $\mathrm{m/s}$ with two significant low-velocity areas. On the one hand, an area strikes from east to west (Figure 3.5b). On the other hand, a second area is again almost parallel to the *Wilhelm Stehender Süd*, however, much more pronounced compared to Figure 3.5a and a low instead of a high velocity zone.
In summary, a low velocity layer in the southern area can be assumed as a result the geological mapping and the travel-time tomography. The velocity is decreased by 500 - 1000 $\mathrm{m/s}$ compared to the northern part. At the southernmost part the interpretation of the travel-time tomography are difficult, since the ray coverage is quite low and since the tomography are in conflict with each other. In the northern area no faults are detected both in the geological mapping and by the travel-time tomography. We can expect a fairly homogeneous rock.
In this work, we performed an additional travel-time tomography. A discussion including picking of travel-times can be found in Section 4.3.2 and 6.1. The obtained velocity model is very crucial because it serves as a starting model for the FWI.

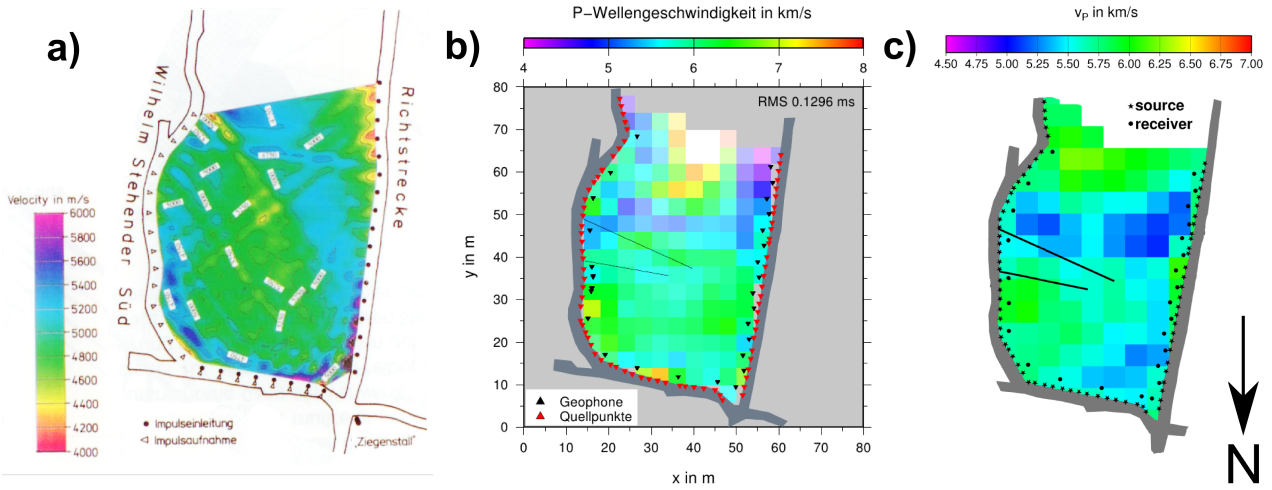

Figure 3.5: Three travel-time tomography results for the first arrivals of the P-wave. b) and c) are based on the same data set as we used in this work. Please note the different used geometries and the different range of the colour scales (a) modified from Bayer, 1999, p. 66, b) Richter, 2010, c) Krauss, 2013).

3.4 Survey

In December 2009, a seismic survey in the GFZ U-Lab was performed. The measurement was done by employees of the GFZ in Potsdam in the frame of the SPWD project. We discuss the used measurement equipment and specifications in the following. The advantage of a transmission geometry and the location in an almost ideal plane, thus, that the data can be compared to crosswell data, have been shown in Zhou et al. (1997).
30 three-component (3-C) geophones have been used as seismic receivers for the measurement (Figure 3.6, R1 to R30). 76 shot positions spaced almost equidistantly (spacing about 2 m) around the block, were recorded (Figure 3.6, S1 to S76). The source was a vibrator which generated a pilot sweep signal from 300 - 3000 Hz (Borm and Giese, 2003). The length of the sweep was 2.9 s, tapered at both ends with the half of a 0.1 s Hanning window to minimise side lobes. As far as possible, we have took care that the orientation of the source is always perpendicular to the wall.
The recording time was 3.008 s with a sampling interval of 0.0625 s respectively 16 kHz. Thus, the listening time was 0.108 s. The stacking varied between three and five shots per shot point. The recording unit consists of a SUMMIT system from the German Montan Technologie (DMT).

The source was a magnetostrictive double vibrator with a distance of 28 cm between the two heads (Figure 3.7a). The motion is generated by the magnetisation of ferromagnetic materials which causes them to change their shape. The frequency of the oscillation is gradually changed over a certain time interval, typically in the range of seconds. In our case, a linear pilot sweep was used, i. e., the frequency increases linearly with time. Seismic waves with different wavelengths propagate through the material under investigation. During the measurement, the vibrators were clamped between two walls in the galleries and pressed with compressed air against the wall. An unregulated sweep excitation leads to unwanted feedback effects (resonances) between the vibrator and the medium, e. g., the tunnel wall, at certain frequencies. Moreover, the maximum amplitude of the excitation

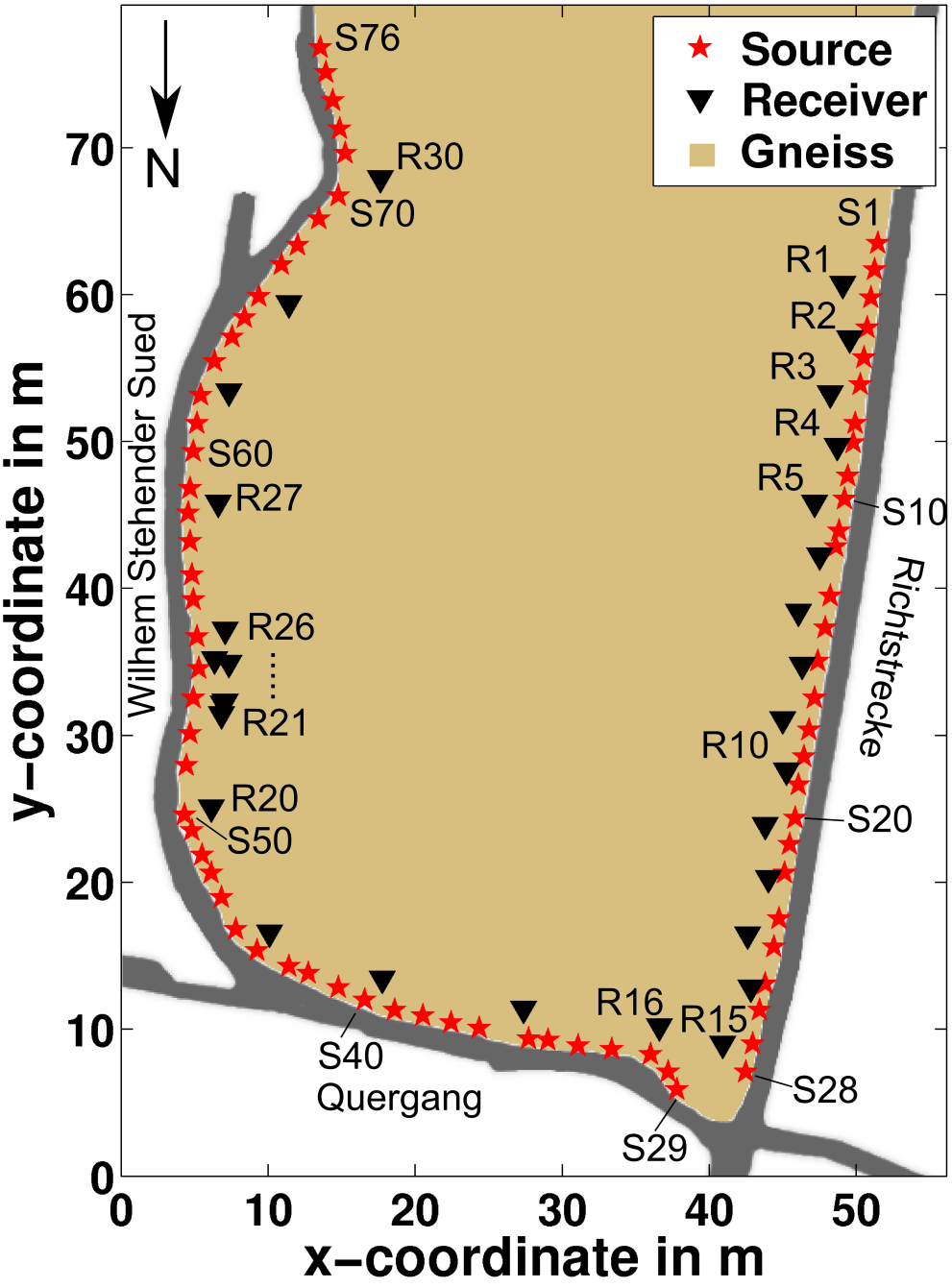

Figure 3.6: Measurement geometry of the survey in Freiberg. The 30 three-component (3-C) receivers are marked with black triangles (R1 to R30), the 76 source positions with red stars (S1 to S30). How the geometry of the block got digitised will be described in Section 4.1. The brownish colour indicates the area under investigation.

(a) Magnetostrictive double vibrator

(b) Heads of vibrator

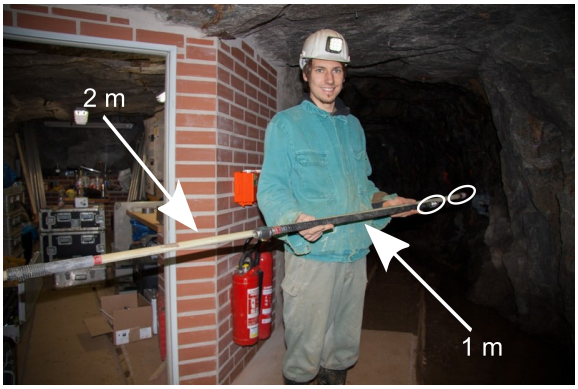

(c) 1 and 2 m long geophone anchors

(d) Parts of the measurement equipment

Figure 3.7: Pictures taken at the survey in the U-Lab in Freiberg. a) Magnetostrictive double vibrator with an air compressors: The source is oriented perpendicular between the two walls of the *Richtstrecke*. b) Close up of the heads of the vibrator: The blue cables leading out directly from the heads are connected to the piezoelectric devices. c) Two different geophone anchors with 1 m length (black) and 2 m length (white): At the one end which is inserted into the borehole, three orthogonal geophones are attached (white circles). At both ends a screw thread is cut in so that the geophones are oriented well-defined. d) Parts of the measuring equipment: The equipment for controlling the source and for the data recording was moved with a rail car on tracks on the ground (Picture a), b) and c) from Stefan Jetschny, d) from Aissa Rechlin).

must be adapted on the resonance amplitudes, which leads to very low signal amplitudes outside the resonance frequencies. Therefore, we use a real-time electronic control, which measures the resultant acceleration signal at the head of the vibrator with a piezoelectric device during the sweep (head signal, Figure 3.7b). At once the excitation amplitude could be reduced when approaching a resonance. This allows a uniform amplitude distribution over a wide frequency range[6]. The two vibrators can be controlled individually. This leads to a very similar amplitude and phase response of both over the entire frequency band. The two vibrators interfere constructively in the selected frequency band and can, thus, be considered as one source. The sources are patented at the German Patent and Trademark Office (Borm et al., 2008a).

As receivers, we used 30 3-C geophone anchors. The receiver spacing is approximately 4 - 9 m to each other (Figure 3.6, R1 to R30). Between Receiver 21 and Receiver 26 a small array is installed with six receivers which are very close to each other. The depth of the boreholes along the *Richtstrecke* is alternating from 1 - 2 m in the host rock. This varying depth is an important fact for the further analysis. In Figure 3.7c two different long anchors can be seen with the screw thread at both ends.

In the next chapter the characteristics of the field data will be investigated.

[6]http://www.gfz-potsdam.de/forschung/ueberblick/wissenschaftliche-infrastrukturen/wissenschaftliches-bohren/projekte/ingenieurgeophysik/isis/seismische-quellen/ (only in German) 14.01.2014

4 Model Geometry and Data Characteristics

In the previous chapter, the overall geology of the Ore Mountains, the measurement area and the survey at the GFZ U-Lab were presented. In this chapter, we focus on the characteristics and quality of the field data and on the necessary preprocessing steps before applying the full-waveform inversion (FWI).
First, the interface of the gneiss block, respectively measuring area have to be digitised and discretised based on two different approaches (Section 4.1). Afterwards, the specifics of a vibroseis source is explained (Section 4.2). The raw data has to be cross-correlated with the excited sweep signal before the further processing. The source wavelet (Klauder wavelet) and its characteristics will be illustrated in more detail. Before applying the FWI, the data have to be preprocessed. The important steps, such as rotating the receiver components, trace muting, time windowing and a 3D/2D transformation of the seismograms are discussed in Section 4.3. After the preprocessing, we investigate the frequency content of the data as it is an important parameter for the inversion strategy (Section 4.4). Also, the data is analysed in terms of a potential predominant anisotropy. Receiver side effects due to the geometry and different coupling issues are discussed at the end of the chapter.

4.1 Interface of the Gneiss

Before working with the field data, we have to discretise the interface of the three galleries. We compare two different approaches to get the most satisfying result. First, we obtained the three dimensional coordinate for the sources and receivers from the GFZ in Potsdam. The x- and y-coordinate denotes the two horizontal and the z-coordinate the vertical direction. The horizontal extension of the coordinates was reduced to have as little as possible grid points in the FD-Scheme later on. This reduces the run-time of the inversion. The x- and y-coordinate of the sources can be seen in Figure 4.1a, red stars. Second, the edge of the gneiss from the underground map as displayed in Figure 3.3b were manually and repeatable picked (Pick 1 and Pick 2). To convert the pixel values in a metrical dimension, two different ways of determine the scaling factor were used. A cross is drawn in the map every 100 m. As in Figure 3.3b only a small sketch of the whole map is shown, we were able to pick four times four crosses in horizontal and vertical direction. Afterwards, the mean value for converting the pixel value into meter was calculated (crosses). Also, a scale on the map was picked to get a second scaling factor (scale).

Pick 1 and Pick 2 were converted with the two different scaling factors (crosses and scale) and were plotted in Figure 4.1a. The edges of all four possibilities were aligned along the *Richtstrecke* to the coordinate of the sources. In general, the edges from the underground map are not distinguishable for Pick 1 and Pick 2 and two different scaling factors. Comparing

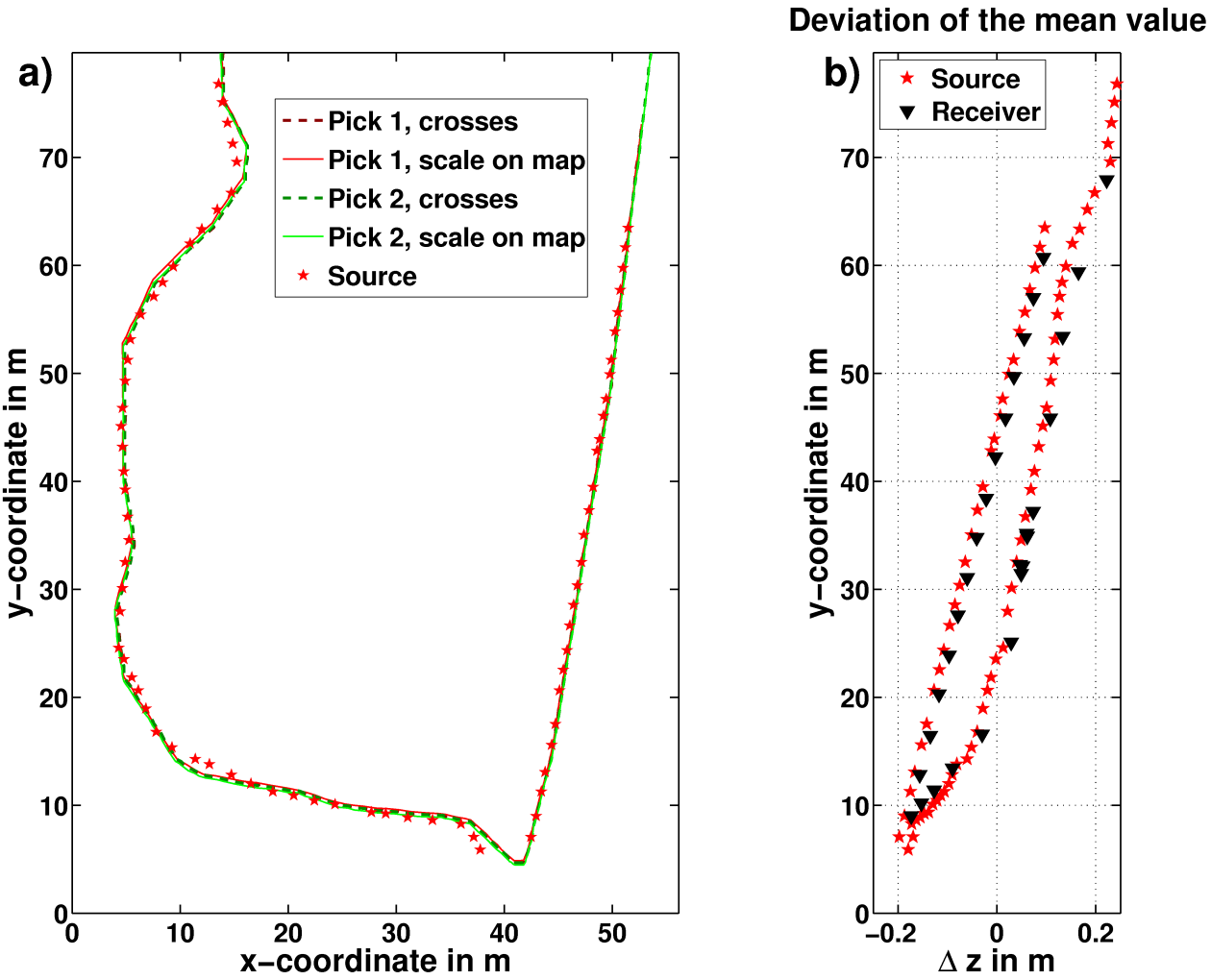

Figure 4.1: Discretised interface around the gneiss. a) The red stars mark the x- and y-coordinate of the sources which we received from the GFZ in Potsdam. The four lines are the picked interface from Figure 3.3b for Pick 1 and Pick 2 and two different scaling factors. b) The deviation of the mean value of Δz for the z-coordinate of sources and receivers as a function of the y-coordinate.

the layout of the lines along the *Wilhelm Stehender Süd* and the *Quergang*, the picked interface differs from the coordinate of the sources at some areas up to 2 m. Unfortunately, we do not know which approach is more accurate. On the one hand, the measuring of the source coordinate was done with a simple metering rule. So, we cannot state the exact error for the coordinate. On the other hand, the map is quite old and hand drawn. We also cannot estimate the accuracy of the drawn interface and the scale. Later on, in Section 5.4.4, we investigate the influence of wrong coordinates regarding the potential resolution potential of the FWI.
We finally decided to take the coordinate of the sources as the interface along the gneiss. We do not want to rely on the accuracy of the map. In addition, because of a lack of information, in the southern direction, the gallery walls along the *Richtstrecke* and the *Wilhelm Stehender Süd* were extended vertically. At the intersection of the *Richtstrecke* and the *Quergang* between S28 and S29, no source could be placed. The rounded corner was inserted manually with two additional points.

Figure 4.1b shows the deviation of the mean value Δz of the z-coordinate of the sources and receivers as a function of their y-coordinate. The maximum deviation is 0.25 m. The overall range covers 0.45 m. Depending on the grid spacing in the FD-scheme, this corresponds to only a few grid points. Our assumption, that the source and receiver positions are in an almost ideal plane is justified and comprehensible and will influence the inversion result only very little (Section 5.4.4).

After the edge of the model is determined, we will now evaluate the characteristics of the field data. The description of the vibroseis source, the preprocessing steps and the analysis of the field data are described in logical order.

4.2 Vibroseis Data

4.2.1 Correlation

As we used a frequency-modulated sweep as a source signal (Section 3.4), the total recording time and hence, the raw seismograms are quite long in time (Kirk, 1981). After recording, the sweep signal and the raw seismograms have to be cross-correlated (Yilmaz, 2001). We can describe this process as a sliding of the sweep signal along the recorded data. If the pilot sweep "sees" a similar version of itself, the correlation is high which leads to a high value of the correlation coefficient (Costain and Coruh, 2004). The length of the correlograms depends on the listening time, the difference in time between the sweep length and the total recording time. In Figure 4.2a, a small part of the sweep signal is shown. The actual length of the sweep was 2.9 s. In the shown window, the frequency is increasing from 600 - 630 Hz. The amplitude spectra of the Fourier transformed for the entire sweep can be seen in Figure 4.2b. The dashed lines indicate the corner frequency of the sweep signal at 300 Hz and 3000 Hz. As expected, the frequency spectra reproduced the excited range and have a flat amplitude spectra, except from the corner frequencies. This is because the sweep is tapered at both ends with the half of a 0.1 s Hanning window to minimise side lobes. The overshoot on the spectra at odd-numbered multiples of 50 Hz which is the electrical power frequency in Germany, are artefacts produced by the sweep-generator unit. In the autocorrelation of the sweep signal, the Klauder wavelet (Section 4.2.2), the artefacts disappear because of

the averaging over all sweeps. In Figure 4.2c and Figure 4.2d, the NS component of Shot 1 for all 30 receivers are shown. As can be seen in Figure 4.2c, nothing can be seen. The raw data, respectively the uncorrelated traces are not interpretable without the correlation with the sweep signal. In Figure 4.2d, the correlated seismograms are shown. In the thesis, seismogram is a synonym for correlogram. Note the shortened time axis. The now visible different wave types are explained in detail in Section 4.3.3. In Appendix A, seismograms for five shots (S1, S20, S40, S60 and S76) for all three components (NW, EW and Z) can be found. This gives an impression of how the wavefield behaves if the source position moves around the gneiss (Figure 3.6).

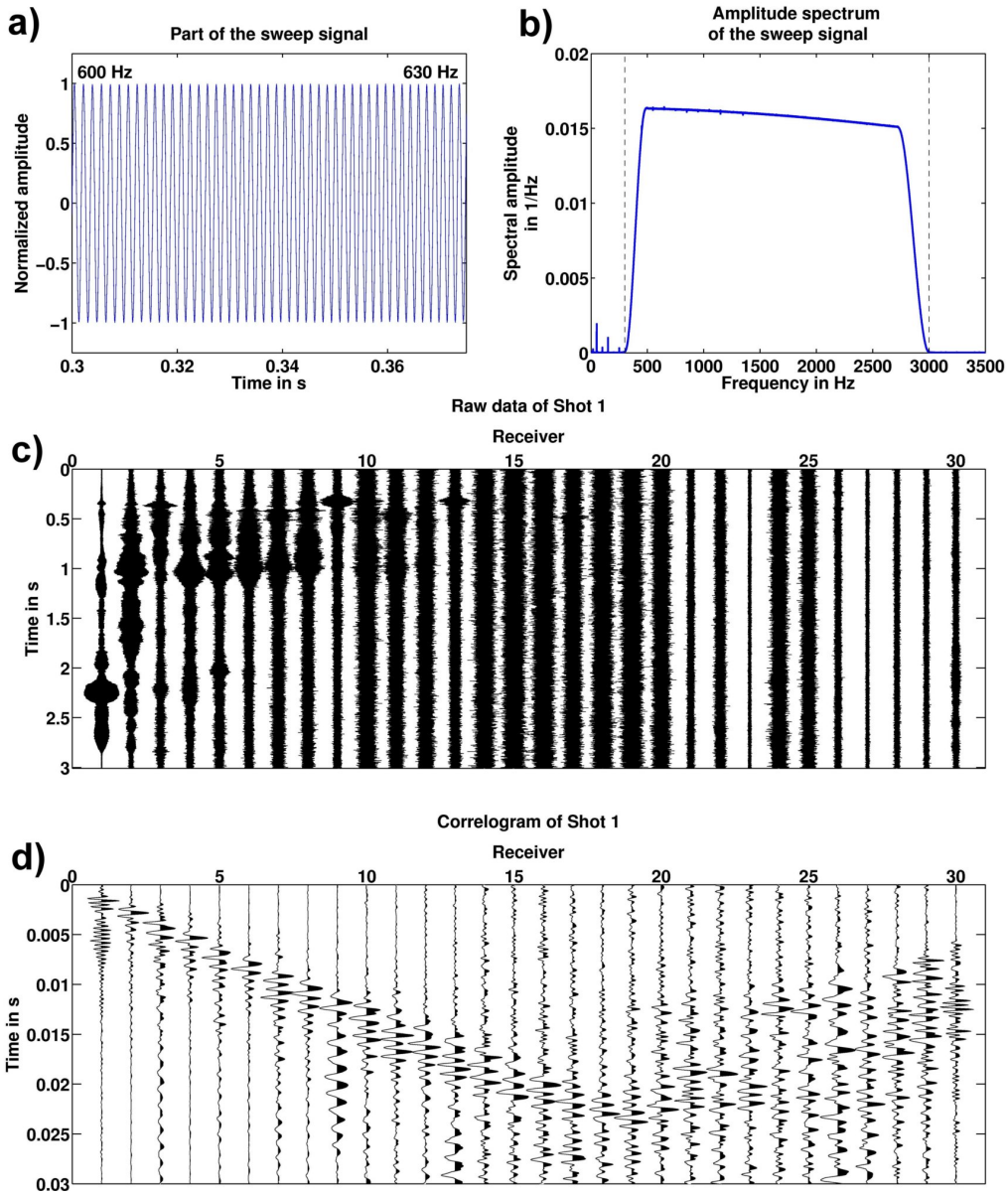

Figure 4.2: a) Short window of the original sweep signal from 600 - 630 Hz. The amplitude is normalised. b) Frequency spectrum of the entire sweep signal. The dashed lines indicate the corner frequencies of the sweep signal at 300 Hz and 3000 Hz. c) Raw common shot gather (NS) of Shot 1 for all 30 receivers. d) The correlated seismograms with shortened time axis.

4.2.2 Klauder Wavelet

For the FWI it is necessary to know the shape of the source wavelets as we intend to explain the entire waveforms.
For a vibroseis, the source wavelet is the autocorrelation of the pilot sweep (Sheriff, 2002). With the linear pilot sweep signal from 300 to 3000 Hz (Section 3.4), we auto-correlate the sweep to obtain to obtain the so called Klauder wavelet (Geyer, 1989). It is a symmetrical and zero-phase wavelet which has its global maximum at time zero. Because our used Finite Differences code cannot model with a negative time, the time-axis was shifted by 0.015 s. After this time period, the amplitude of the Klauder wavelet is practically zero. For this reason, the same time shift of 0.015 s was added to the field data the, i. e., the seismograms were padded with zeros before time zero. In Figure 4.3a, the Klauder wavelet extracted from the field data and additionally, an analytical calculated Klauder wavelet after Costain and Coruh (2004) is plotted. In Figure 4.3b, the corresponding Fourier transform are shown. The frequency content is equal to the original sweep. In both figures, the amplitudes are normalised individually. The equation for one part of the analytical Klauder wavelet can be found in Appendix B. The wavelets match quite nicely, even though the analytical wavelet has more side lobes. This can also be seen in the Fourier domain. The amplitude spectrum is not as stable as for the Klauder wavelet of the field data.

As for synthetic tests and for the field data inversion it is very unusual to use the whole frequency content at once because of the high non-linearity of the inversion scheme, we used different zero-phase Butterworth low-pass filter to neglect high frequencies. In Figure 4.3c three additional wavelets are computed by low-pass filtering. In Figure 4.3d the corresponding amplitude spectra are shown. The amplitude in both the time and frequency domain, are normalised to the original Klauder wavelet. As we used a zero-phase filter, the global maximum remains at the same position. With lower frequencies, the complexity of the wavelet is reduced. Even if the frequency content is strongly truncated at high frequencies, the spectra still begins at 300 Hz as wanted.
If not stated otherwise, the Klauder wavelet is always used as the source signal. Nevertheless, we have to keep in mind that the induced source wavelet also depends on the coupling of the heads of the vibrator to the rock, how precise the source is clamped between the walls and additional influences.

4.2.3 Zero-Phase Investigation

In theory, after the cross-correlation of the raw data with the sweep signal, also the correlograms should be zero-phase (Yilmaz, 2001). That means, e. g., for picking of the first-arrival travel time of the P-wave, the maximum of the correlogram marks the arrival time. With a synthetic study, we want to investigate the characteristics of the correlograms and if yes how the used velocity model influences the waveforms. At best, with the known distance between source and receiver, the known velocity of the model and the known Klauder wavelet, we should be able to predict the time of the maximum amplitude in the seismogram. With this test, we want prove first, if it is equal to use a sweep signal as the source wavelet and correlate the seismograms and the sweep afterwards or to model seismograms with the Klauder wavelet directly. And second, we want to study the shape of the obtained seismograms to gain experiences for picking the first-arrival times of the field data. Accurate

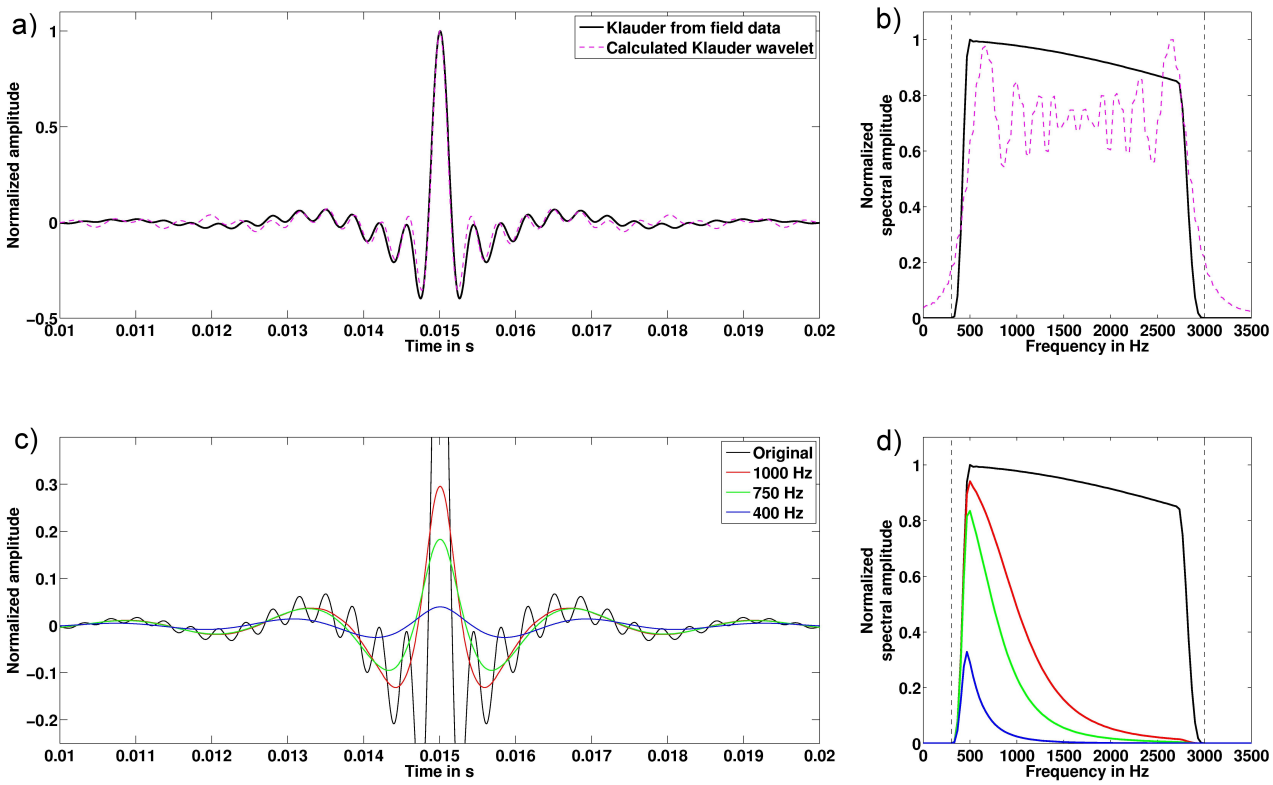

Figure 4.3: Comparison of different Klauder wavelets and its corresponding frequency content. a) The Klauder wavelet extracted from the field data compared to an analytical Klauder wavelet from the equation in Appendix B. b) The corresponding amplitude spectra. The dashed lines indicate the corner frequencies at 300 Hz and 3000 Hz. c) The original Klauder wavelet and filtered versions of the wavelet. We used a zero-phase Butterworth low-pass filter with different corner frequencies. The amplitude is normalised to the original Klauder wavelet. d) The spectral amplitude of the different wavelets normalised to the amplitude of the Klauder wavelet.

travel-time picks will lead to a sufficient starting model for the FWI.

With a FD-modelling (Section 2.2), the principles of a sweep signal respectively a Klauder wavelet as source signals are studied. We used two different velocity models, first a homogeneous model with $v_P = 6000\,\mathrm{m/s}$, $v_S = \frac{v_P}{\sqrt{3}}$ and $\rho = 2550\,\mathrm{kg/m^3}$. In addition, the second model is a random distributed velocity model which is described in more detail in Section 5.1.1. As a source, a single force in y-direction is used. We recorded one single seismogram in a distance of 45 m along the y-direction. This offset represents a typical distance in the field survey. As the source wavelets, we tested both, the sweep signal which we extracted from the field data and its autocorrelation, the Klauder wavelet (Figure 4.3). Both wavelets had the same length of 3.008 s and a frequency content of 300 - 3000 Hz (Section 3.4). The different model setup are summarised in Table 4.1.
In Figure 4.4 the important part of the seismograms with the first-arrival picks is shown. The grey dashed seismogram was modelled with the sweep signal and was cross-correlated with the mentioned sweep signal (S_homo) afterwards, the red seismogram was directly modelled with the Klauder wavelet from the field measurement (K_homo), both with the homogeneous model. The green seismogram was modelled again with the Klauder wavelet but in this case with the random velocity model (K_rand). In all seismograms the typical shape of the Klauder wavelet is recognisable. However, the maximum is no longer the point of symmetry. As expected, the two seismograms for S_homo and K_homo are identical. The red dotted line indicates the theoretical arrival time of the P-wave. The maximum and the arrival time correspond very well. The maximum of the green seismogram (K_rand) has a slight time shift. If we calculate the mean P-wave velocity directly between the source and receiver, again the theoretical arrival time matches with the maximum (green dotted line). So, the maximum is exactly at the predicted arrival time of the P-wave and thus, zero-phase. Looking at the flanks of the seismograms, the amplitude of the second peaks differs. Especially after the global maximum, the amplitude of the seismogram for the random velocity model is larger. This effect could be based on the scattering points in the random distributed model. Due to interference of the waves, the amplitudes become larger. Later on, this effect can also be observed in the field data, e. g., Figure 4.7. Before the first-arrival time, the amplitude of the maximum is increasing. After the first-arrival time, the amplitudes of the secondary maximum are less decreasing. Nevertheless, we could be very confident, that we have to pick the first-arrival time at the maximum value due to the zero-phase characteristics of the seismograms.

Table 4.1: The three different model setup and the corresponding lines style in Figure 4.4.

Name	Model	Wavelet	Line style
S_homo	homogeneous	Sweep	grey dashed
K_homo	homogeneous	Klauder	red solid
K_rand	random	Klauder	green solid

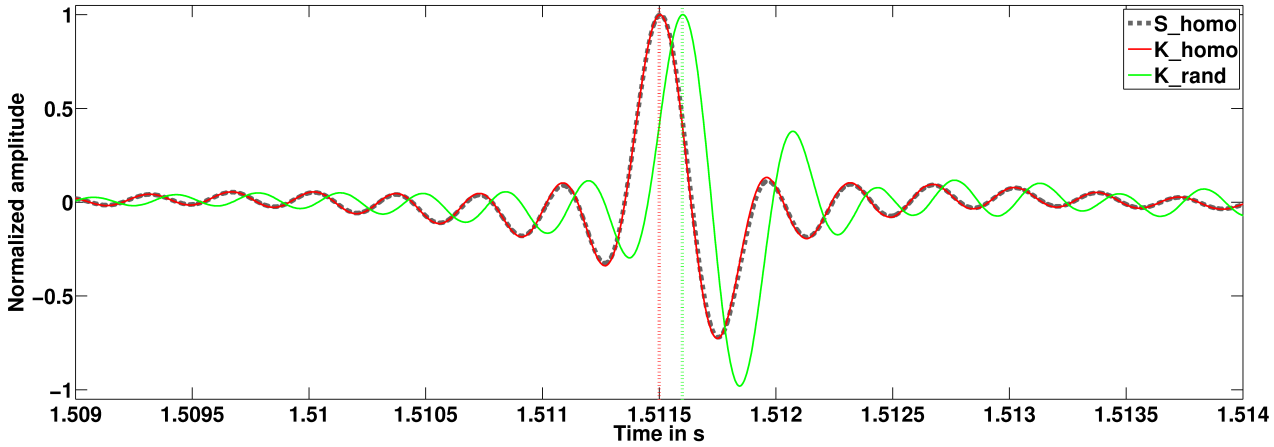

Figure 4.4: Investigation of the zero-phase characteristics. In grey dashed and red solid the modelling for the homogeneous model with the original sweep signal from the field data and the corresponding Klauder wavelet is shown. As expected, both seismograms are almost identical. The calculated arrival time of the P-wave is plotted as a red dotted vertical line and coincident very well with the global maximum. The green seismogram is modelled with the random distributed velocity model. The theoretical calculated arrival time matches very well, too.

4.3 Data Preprocessing

4.3.1 Rotation

Since we use a 2D modelling code, we need to ensure that the individual receiver components of the field data and the synthetic data are uniform and comparable to each other. The modelling code has a global coordinate system in contrast to the field data. Every receiver has its own local coordinate system relative to the gallery wall. So, we have to rotate the field data into the coordinate system of the modelling code.
The GFZ in Potsdam provided the necessary information for the construction, orientation and polarity of the three one component geophones in one anchor. The notation NS, EW and Z for the three components is not related to its orientation. We must assume that the receivers were drilled perpendicular to the gallery wall, but we suppose an error of up to $\pm 5\,^{\circ}$. The EW- and Z-component are the horizontal components. The modelling will take place in this plane. The NS-component is vertical polarised for all receivers and is, thus, not needed in the used 2D-scheme. The Z-component has its orientation always perpendicular to the gallery walls with an equal polarity in the direction of the borehole for the anchor. This can be shown with a simple test. The principle of reciprocity states that it is legal to exchange any source and receiver and still the same seismogram should be recorded. So, we will take two seismograms which travelled straight along the x-axis from the *Richtstrecke* to the *Wilhelm Stehender Süd* and vice versa. The direct raypath differs with less than $2\,^{\circ}$ and the offset deviation is less than 1 m. In Figure 4.5, three examples with the corresponding source and receiver number at the top are plotted. The seismograms are low-pass filtered. The black seismograms travelled from the *Wilhelm Stehender Süd* to the *Richtstrecke* and the red seismograms the other way round. The orientation of the source for the red and black seismograms is in the opposite direction. However, the signals are very coherent and have almost no phase shifts. That means, the Z-component is oppositely polarised (Figure 4.6).

In the FD scheme, the orientation of the receivers are uniform, i. e., we must rotate the 30 receivers in a uniform coordinate system.
In Figure 4.6, for few receivers, the orientation of the EW- and Z-component is shown with

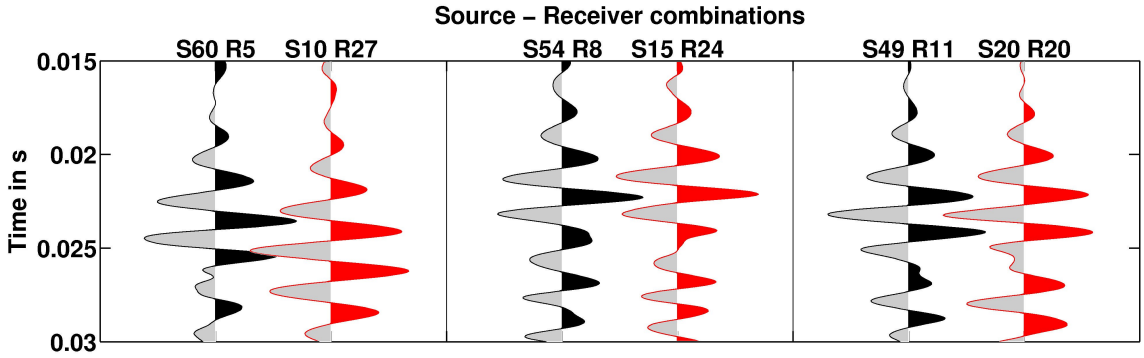

Figure 4.5: Comparison of three examples for the Z-component which nearly have the same raypath. The black seismograms travelled from the *Richtstrecke* to the *Wilhelm Stehender Süd* and the red seismograms vice versa. Above, the source and receiver number is shown. The waves have the same polarity for all examples with only a minor phase shift.

their corresponding rotation angle. All angles can be found in the Appendix C. By equation

$$\mathbf{d} = \mathbf{R_a}\mathbf{u} \tag{4.1}$$

with

$$\mathbf{R_a} = \begin{pmatrix} \cos\alpha & \sin\alpha \\ -\sin\alpha & \cos\alpha \end{pmatrix} \tag{4.2}$$

where $\mathbf{u}$ are the original seismogram vectors (EW- and Z-component), $\mathbf{d}$ are the rotated seismogram vectors (x- and y-component) and α is the rotation angle, we can rotate the EW- and Z-component clockwise. Finally, the EW-component corresponds to the x-coordinate and the Z-component corresponds to the y-coordinate (Figure 4.6, workflow). To make the polarity equal, the Z-component must be multiplied with -1. Also, for R25, we have to reverse the polarity of the x-component (personnel communication: Rüdiger Giese).

4.3.2 First-Arrival Picking

The first-arrival travel times of the P-wave for the present field data have already been picked by Richter (2010) for a travel-time tomography (Section 3.3.2.2).
Based on the zero-phase investigation made in Section 4.2.3, the first-arrival times of the P-wave were picked again. As is it not easy to pick in the unfiltered seismograms because of prevalent noise and other high frequency disturbances, therefore, the data is filtered with a zero-phase low-pass filter with a corner frequency of 400 Hz. Thereby, in a common receiver gather (CRG) the coherency is more apparent after low pass filtering since high frequency "disturbances" are removed. In Figure 4.7, as examples, both, the original and filtered data for Receiver 8 along the *Richtstrecke* and Receiver 24 along the *Wilhem Stehender Süd* are shown. Additionally, as green dots, the picked travel times of Richter (2010) and in red triangles, the new picks made for this thesis are marked. For both receivers, only the

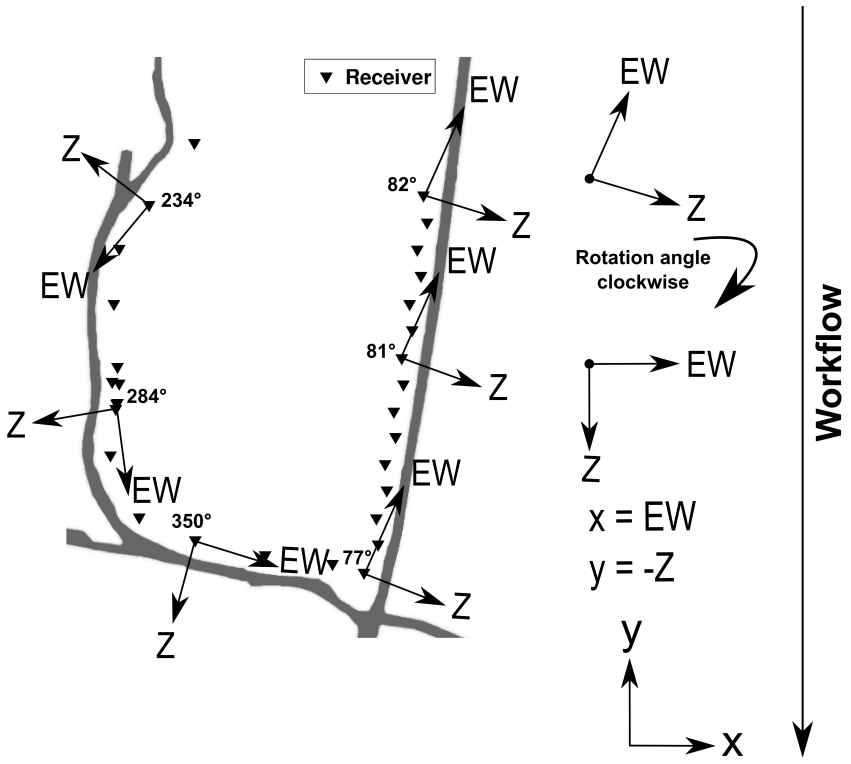

Figure 4.6: The orientation of the EW- and Z-component and the corresponding rotation angle for some exemplary receivers. On the right side the workflow for the rotation in the xy-coordinate system is shown.

parts where we could pick travel times are shown. The new picks were set for the filtered data but also correspond well with the unfiltered. In the seismograms the characteristics of Klauder wavelet is recognizable very nice for many shots, similar to the previous synthetic test in Section 4.2.3. For our chosen coordinate system, the maximum of the correlation for Receiver 8 is positive and for Receiver 24 negative. The picks of Richter (2010) and the new picks differs systematically in the travel time. In our opinion, Richter (2010) estimates rather the first-arrival time than the maximum. Thus, our estimated velocities are approximately up to 500 $^{m}/_{s}$ smaller than the velocities of Richter (2010).
Based on the new picks, a travel-time tomography is performed in Section 6.1 and the resulting velocity model is compared to the already known. For now, the picks are used for another purpose as described in the following section.

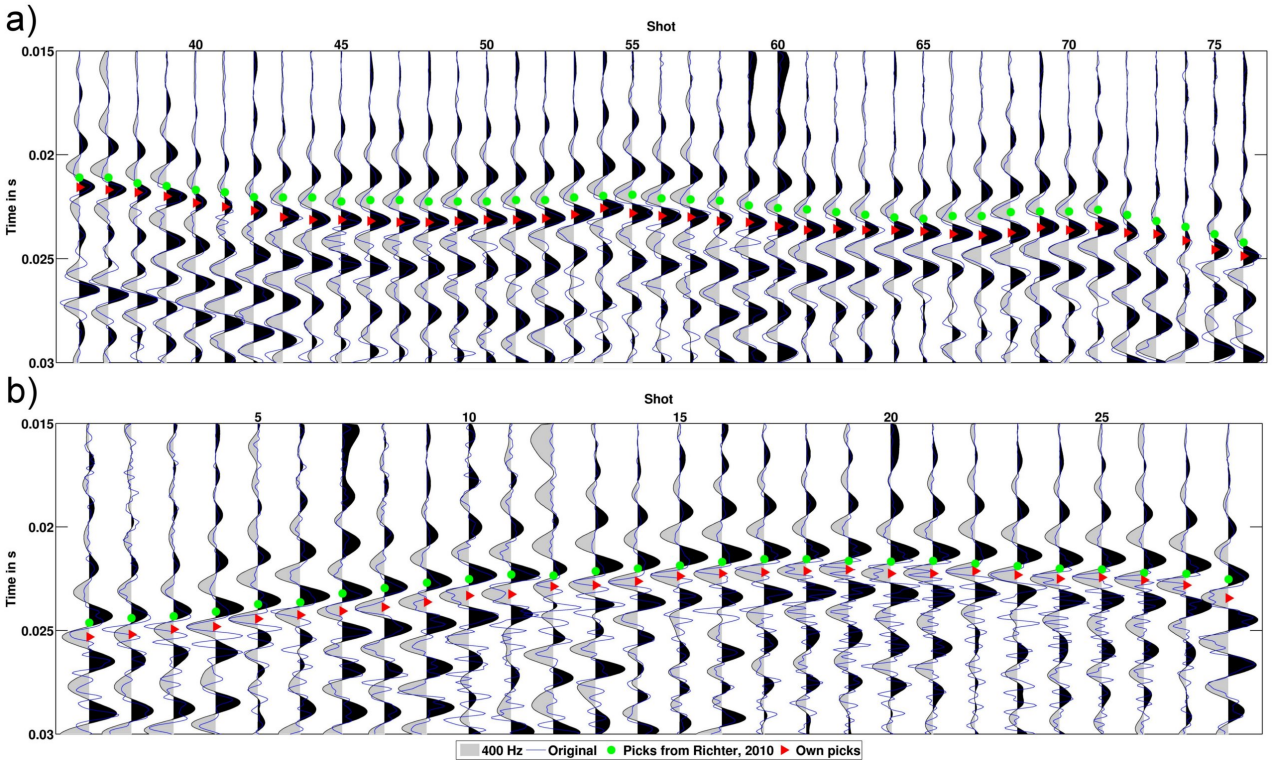

Figure 4.7: Common receiver gather (CRG) with its corresponding picked first-arrival times. a) CRG for Receiver 8 along the *Wilhem Stehender Süd*. The black/grey seismogram in the background are low-pass filtered with a corner frequency of 400 Hz, the blue seismograms are raw data for comparison. The green dots mark the picks from Richter (2010), the red triangles are the new picks for this thesis. b) the same as in a) but for Receiver 24 along the *Richtstrecke*.

4.3.3 Trace Muting and Time Windowing

The previous section provides the first-arrival travel time of the direct P-wave. We will make use of these picks in the following.
By the use of a 2D code and in contrast to the 3D geometry of the galleries, we cannot model some wave types physically correct which are included in the field data. The P- and S-waves propagate similar through the entire hard rock in both the modelling and

the field measurement and are modelled with a sufficient accuracy. The waves which are propagating along the rock-air interface are tunnel surface waves (Lüth et al., 2005). Jetschny (2010) investigated the characteristics of surface waves propagating along the galleries by introducing a factor for the ratio of the wavelength to the tunnel diameter. The mean frequency of the tunnel surface wave f_{TS} is approximately 1000 Hz (Section 4.4.1). The average v_S value is derived from the typical v_P to v_S ratio of $\sqrt{3}$ and with $v_P = 5500\,\frac{m}{s}$:

$$v_S = \frac{v_P}{\sqrt{3}} = \frac{5500\,\frac{m}{s}}{\sqrt{3}} = 3175\,\frac{m}{s}. \tag{4.3}$$

This results in a wavelength $\lambda_{TS} = \frac{v_S}{f_{TS}} = \frac{3175\,\frac{m}{s}}{1000\,Hz} = 3.175\,m$. Although the galleries in the U-Lab have no rounded shape like tunnels but are rather rectangular, from Figure 3.7(a) the extend d_G is estimated to 4 m. The ratio of wavelength to tunnel diameter is, thus, $\omega = \frac{\lambda_{TS}}{d_G} = \frac{3.175\,m}{4\,m} = 0.794$. In the range of $0.6 < \omega < 1.2$ the tunnel surface waves are composed of classical Rayleigh waves and S-waves. Also, the ratio is indicating that we are at the edge to have Rayleigh waves, we have to assume a mixture of both wave types.
In a 2D FD-scheme, the gallery walls are infinitely extended in the third dimension and act like a planar surface. In Figure 4.8, the different basic physics of a 2D and 3D modelling schemes are illustrated. To conclude, the waves travelling along the gallery walls in the field data can only be modelled accurately with a 3D but not with a 2D scheme. Since

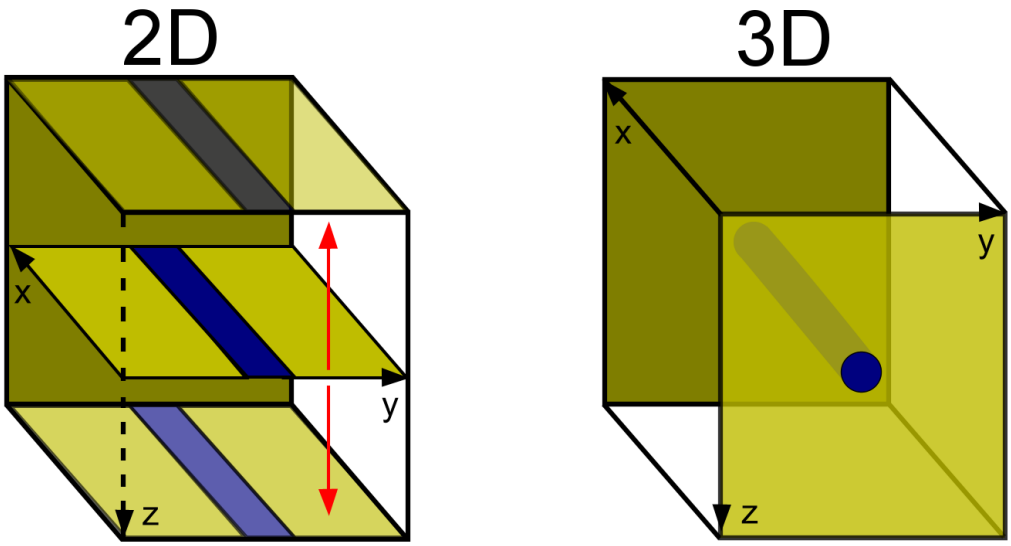

Figure 4.8: Sketch for a 2D and 3D modelling scheme. a) For a 2D modelling code, the third dimension (z-dimension) is expanded infinitely. The boundary in the xy-plane acts like a plane layer. b) In 3D, the tunnel can be modelled realistically (modified from Jetschny, 2010, p. 30).

we are lacking a physically correct modelling of the tunnel surface wave, we also cannot invert for them. We, therefore, have to neglect seismograms where the tunnel surface wave and the P-wave are not separated in time (Heider et al., 2012). In practise, we will use the sources and receivers in the transmission geometry and do not use the traces with a short shot-receiver-distance. We demonstrate the procedure on the basis of a CRG from Receiver 2 in Figure 4.10.
The seismograms of the x- and y-component are shown in Figure 4.10a. All traces are

normalised to their maximum. The P-waves are highlighted by red colour. Especially on the x-component the arrival of the direct P-wave can be easily seen, in particular for Shot 30 - 63. Since the tunnel surface waves, highlighted in green, have a significantly higher amplitude than body waves, P-wave arrivals are not visible in the shot position range from Shot 1 - 28. Because of the different polarisation, the S-wave arrivals are more clearly visible on the y-component after the P-wave, highlighted in blue. Also, due to their polarisation, the tunnel surface wave has only low energy on the y-component. The red stars mark the picked first-arrival time of the P-wave. In Figure 4.9, an overview of the used and muted traces are plotted. The matrix contains both, muted traces because of the used 2D code and muted traces where no pick for the first arrival could be set. Altogether, we use 703 of 2280 possible source-receiver combinations.

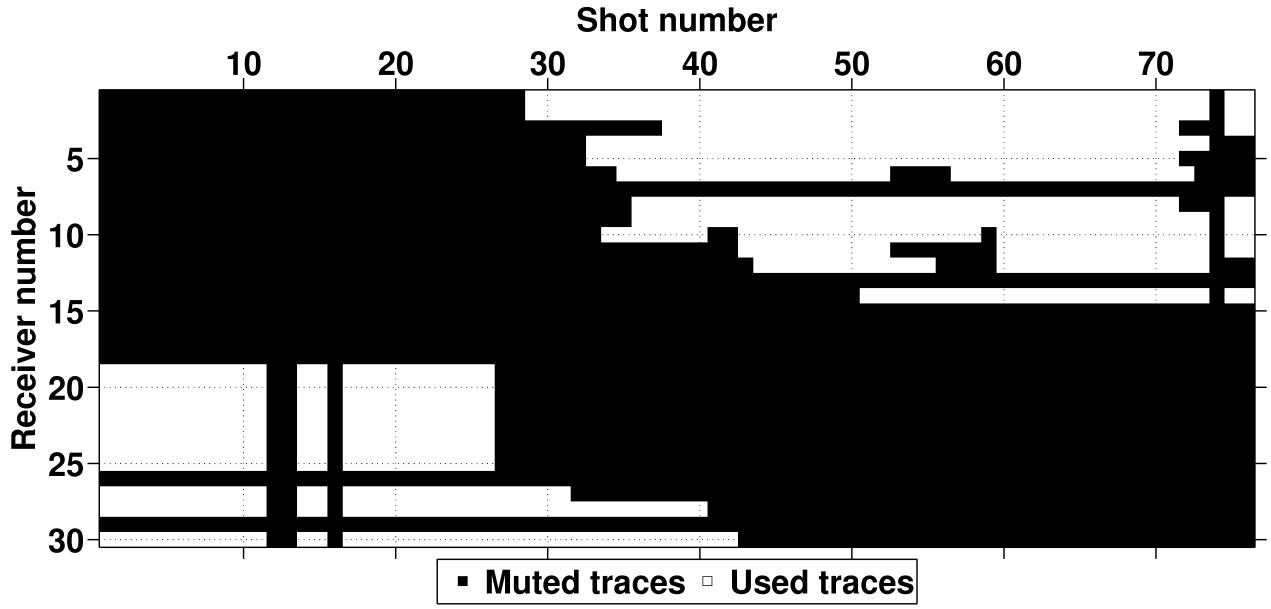

Figure 4.9: Overview of the used and muted traces. Altogether, we use 703 of 2280 possible source-receiver combinations.

From evaluating the seismogram contributions after the P-wave arrival, we cannot observe other phases clearly (Appendix A). The S-wave is often influenced by the P-wave coda. Thus, we decided to only invert for the first-arrival P-wave and cut off all other phases. This reduces the non-linearities of the inversion and is common practise in the FWI (Pratt and Worthington, 1988; Sheng et al., 2006). We call the approach time windowing. We use an exponential function to calculate taper coefficients (Brossier et al., 2009). The slope of the flanks of the taper function can be controlled by the parameter γ. Additionally, we define two time periods before and after the first-arrival pick where the taper coefficients are equal one. The seismograms are then multiplied with the taper function.

In Figure 4.10b, the preprocessed data is shown after trace muting and time windowing. As an example, the taper function for time windowing for Shot 76 is shown in Figure 4.11. Depending on the used frequency, the length of the time window should be chosen adequately, so that one to a few periods of the P-wave are included (Sheng et al., 2006). As we have zero-phase data, the time window has the same length of ($\pm$0.0015s) before and after the first arrival. For the flanks, we have chosen a damping value of $\gamma = 1000000$, which should also be selected in dependence of the frequency. In addition, the near offset

seismograms have been muted, where tunnel surface waves and P-waves are not clearly separated in the time or where corrupt seismograms occur. This is then the actual data we want to invert.

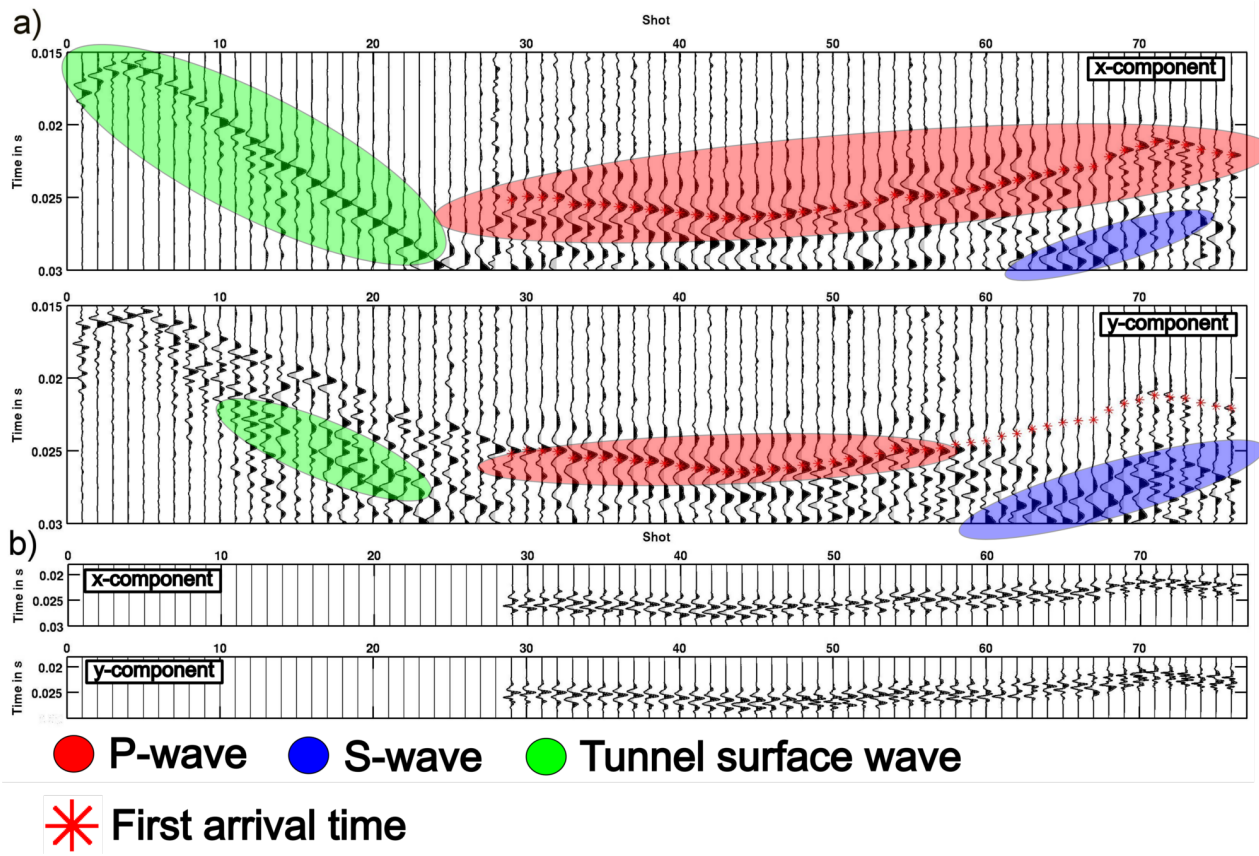

Figure 4.10: CRG of Receiver 2. a) The x- and y-component with the first-arrival times are shown. Different wave types are highlighted with different colours. All traces are normalised to their maximum amplitude separately. b) The preprocessed data of a) is shown. This is the actual data which is used as input for the FWI.

4.3.4 3D/2D Transformation

As we use a 2D code, some problems occur due to the different physical behaviour of the reduced dimensions (Auer et al., 2013), which we will discuss in this section.
In the field measurement, the seismic energy has been induced with a vibrator source at a certain point. This is called point source, as almost all types of artificial sources are point sources. With the given three spatial coordinates, a point source can only be simulated adequately with a 3D code. However, as we use a 2D code by only specifying two spatial coordinates, the third dimension is infinitely extended (Section 4.3.3). That means, that an infinite number of sources are simulated simultaneously along a line in the direction of the not defined coordinate. This is called a line source (Forbriger et al., 2014).

For body waves, as we use them in this work, the difference in phase due to the different source types, can be corrected by a convolution with $\frac{1}{\sqrt{t}}$ (Pica et al., 1990). However, possible 3D effects of the velocity structures cannot be corrected. Thus, we tested the correction for

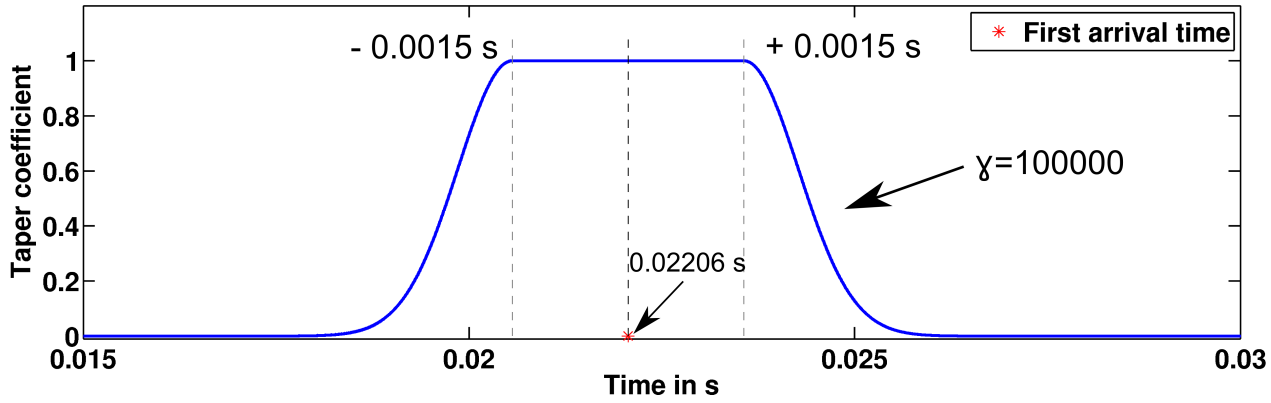

Figure 4.11: Typical taper function. A time window around the first-arrival time can be chosen, for this example ± 0.0015s with a damping value of $\gamma = 1000000$.

a 2.5D media. That means the model is extended into the third spatial direction, but the material parameters do not change along this direction. The different decay of the amplitude in 2D (synthetic) and 3D (field data) is not transformed as suggested by Pica et al. (1990) since, as discussed later, the amplitudes for the inversion are normalised trace by trace (Section 5.3) and only one wave type is taking into account (Section 4.3.3).

The transformation of the phase has been tested synthetically for a 2D and 2.5D random velocity model, which is described in detail in Section 5.1.1. The model also includes the interfaces of the gneiss (Section 4.1). The seismograms for the 2.5D media model were computed with a 3D code. The seismograms for Shot 60 at the *Wilhelm standing Süd* (S60) are preprocessed as described in the previous sections (Section 4.3.2 and 4.3.3). Afterwards, the seismograms of the 2.5D model were convolved with $\frac{1}{\sqrt{t}}$. Figure 4.12 shows the comparison for the receiver along the *Richstrecke* to the seismograms before (Figure 4.12a) and after the transformation (Figure 4.12b). Each trace is normalised. The phase correction works very well for the given scenario. The noticeable different waveforms for neighbouring receivers are discussed in Section 4.4.3. With the used geometry and the recorded data, the assumption that the velocity distribution within the gneiss is also 2D, cannot be verified. Nevertheless, in Section 3.3.2.1, the geological mapping illustrated that the main strike directions of the fault zones are perpendicular to the investigated horizontal xy-plane. Assuming that the strike direction does not change abruptly, the presumed seismic anomalies, respectively the fault zones resemble a 2.5D model. Butzer et al. (2013) showed with synthetic tests, that a 2D cross-section of 2.5D or 3D structures can also be inverted with a 2D geometry and a 2D code, under the loss of resolution. In her work, also a random distributed media is used, which is based on crystalline rock. So, if in my case 3D velocity variations are present, it should still be possible to resolve the structures as a 2D structure.

4.4 Data Evaluation

After the necessary preprocessing of the field data, in the following, we are now concentrating on the evaluation regarding the frequency content, check if a possible anisotropy is present and compare the waveforms with a semblance analysis. These information are important for the performed FWI later on.

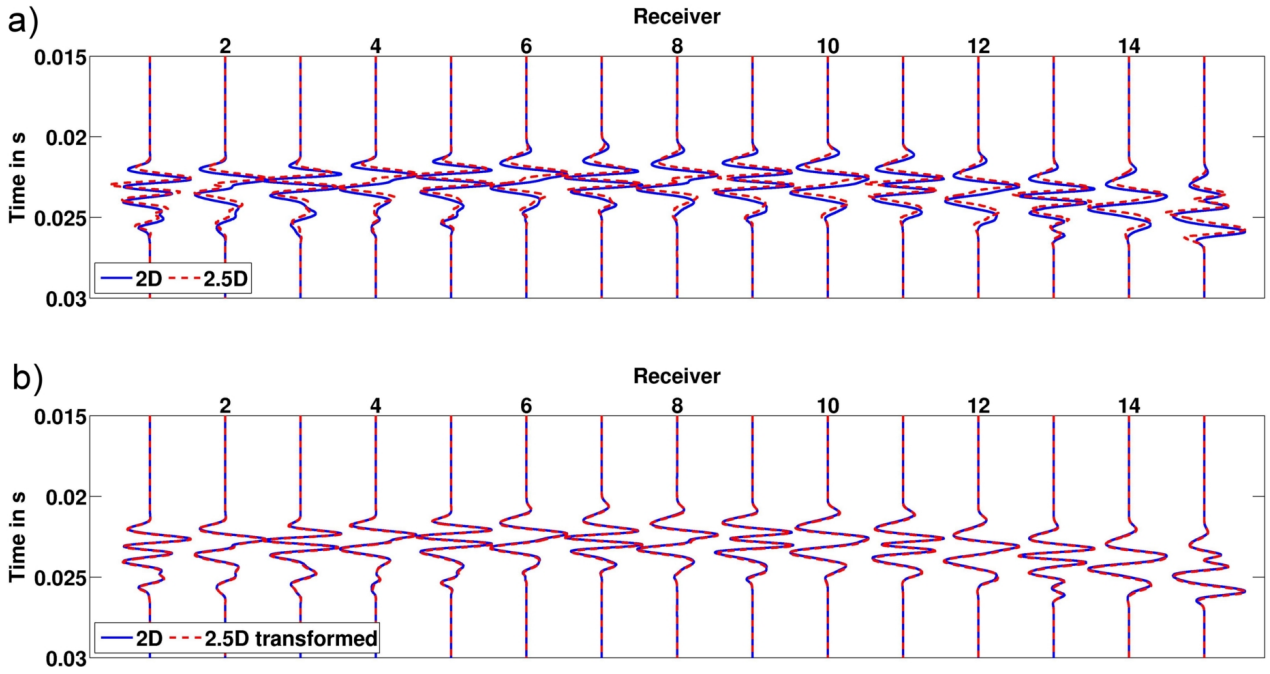

Figure 4.12: a) Synthetic CSG for Shot 60 for a 2D (blue) and 2.5D media (red dashed). The phase shift of both seismograms are due to the different sources in 2D (line source) and 3D (point source). b) Comparison of the seismograms after the 3D/2D transformation.

4.4.1 Frequency Content

First, the frequency content of the data has to be determined. The frequency content is a crucial parameter in later inversion steps because it has a huge influence on the complexity of the misfit function. Also, some parameters in the FD-scheme such as grid spacing and the time step increment, depends on the maximum occurring frequency.
With the excitation of a linear sweep from 300 - 3000 Hz, we expect almost the same frequency range in field data. By a conventional Fourier transformation, the seismograms in the time-domain are transformed to the frequency domain. To obtain a reasonable analysis, we proceeded as follows. In Figure 4.13a, the frequency content of the unprocessed data with true amplitudes of Shot 1 is shown for the x-component. Along the direction of this component, mainly the tunnel surface wave and the P-wave are polarised. The legend shows only four of the 30 receivers which are represented by black (Receiver 1) to light grey (Receiver 30) lines. In all four Figures 4.13a - 4.13d, the amplitude is each time normalised to the global maximum. Due to the very large amplitudes of the tunnel surface wave in the near vicinity of the source, the first three to four receivers have a dominant spectral amplitude which exceeded all other receivers. To remove the effect of different amplitudes, the data from Shot 1 were normalised to an RMS value of one for each seismogram in the time-domain. The corresponding frequency spectrum is shown in Figure 4.13b. Here, a mixture of the frequency content of tunnel surface waves and body waves can be seen. The highest spectral amplitudes are between 400 - 1250 Hz. No single peak occurs. Above 1250 Hz, the spectral amplitude decreases abruptly and stay at a very low level until 3000 Hz. In general, it is not possible to distinguish between tunnel surface waves and body waves. In order to evaluate all shots, the average of all receivers for each shot was calculated. This is shown in Figure 4.13c. The colour gradations are again from black (Shot 1) to light grey

(Shot 76). In general, the frequency content of the different shots is comparable to each other. The largest spectral amplitude are between 400 - 800 Hz with another smaller peak at about 1250 Hz. From 1250 Hz, the amplitude decreases steadily and faints out at 3000 Hz.
In Figure 4.13a - 4.13c the unprocessed data are shown. As we are interested only in the spectra of the P-wave, in Figure 4.13d the preprocessing was applied which is explained in the previous sections. Due to the trace muting, every shot was normalised with the number of used receivers. The general picture is the same as in 4.13c. By only considering the first-arrival phase of the P-wave without noisy parts, the spectrum is much smoother. The main spectral amplitude for all shots is in the range from 400 - 700 Hz with the main peak at 500 Hz. The spectral amplitude differs almost systematically for shots with a low (blackish) and high number (greyish). For shots at the *Richtstrecke* (blackish), the receivers in the transmission geometry which are mainly used, have a uniform depth of 2 m. These leads to receiver ghost reflections at the gallery walls and a doubling of the amplitude of certain frequencies, respectively a cancelling out of other frequencies (Ikelle and Amundsen, 2005). For these shots, two peaks are observable, the main peak at 500 Hz another at about 1200 Hz. For shots along the *Wilhelm Stehender Süd* (greyish), the receivers are in an alternating depth of 1 m and 2 m. So, the ghost effect around the main frequency at 500 Hz only occurs at every second receiver and is, thus, not as good observable as for shots along the *Wilhelm Stehender Süd*. The receiver ghost effect can also be seen in synthetic data, e. g., Figure 4.12b, and is also subject in the Section 4.4.3. Nevertheless, the P-wave contains almost no energy in the range of 1500 - 3000 Hz. Comparing 4.13c and d, the frequency range of the tunnel surface wave could be determined not exactly to one frequency, but in general over the whole frequency range from 400 - 1500 Hz. Without considering the tunnel surface waves, the broadness of the spectra does not change extremely.
Despite an excited frequency band of 300 - 3000 Hz, the largest amplitudes are between 400 - 800 Hz with a peak at 500 Hz. We expected a drop of the spectral amplitude at higher frequencies due to a possible attenuation. But, in general, a more constant frequency content and not one dominant peak within a small frequency band was expected.
Later, in the Section 6.3.1, this study provides suitable frequency parameters for the FWI.

4.4.2 Anisotropy

Gneiss often has an anisotropic characteristic because the structure of the crystalline rock is often aligned parallel (Murawski and Meyer, 2010). Anisotropic means that a crystal structure of the minerals does not behave physically the same in all spatial directions. In our case the propagation velocity depends on the path the wave propagates through the media. In the following, we will investigate whether the anisotropy need to be considered for the FWI. Hurtig (1967) investigated velocity changes due to the anisotropy of the gneiss of $\pm 100\,\mathrm{m/s}$.

For further analysis, the new first-arrival travel-time picks are used (Section 4.3.2). Since the sources and receivers are located an almost ideal plane (Section 4.1), the analysis can only investigate the anisotropy in the horizontal xy-plane. Of course, the rock could have further anisotropy with other orientations, however, we cannot investigate those.

At the beginning, a ray angle from each receiver to each source must be calculated. The range of the values is -90 ° or 90 °. Assume a coordinate system with its origin in the coordinate of each receiver: If the ray path is parallel to the x-axis, the ray angle is 0 ° and consequently, if

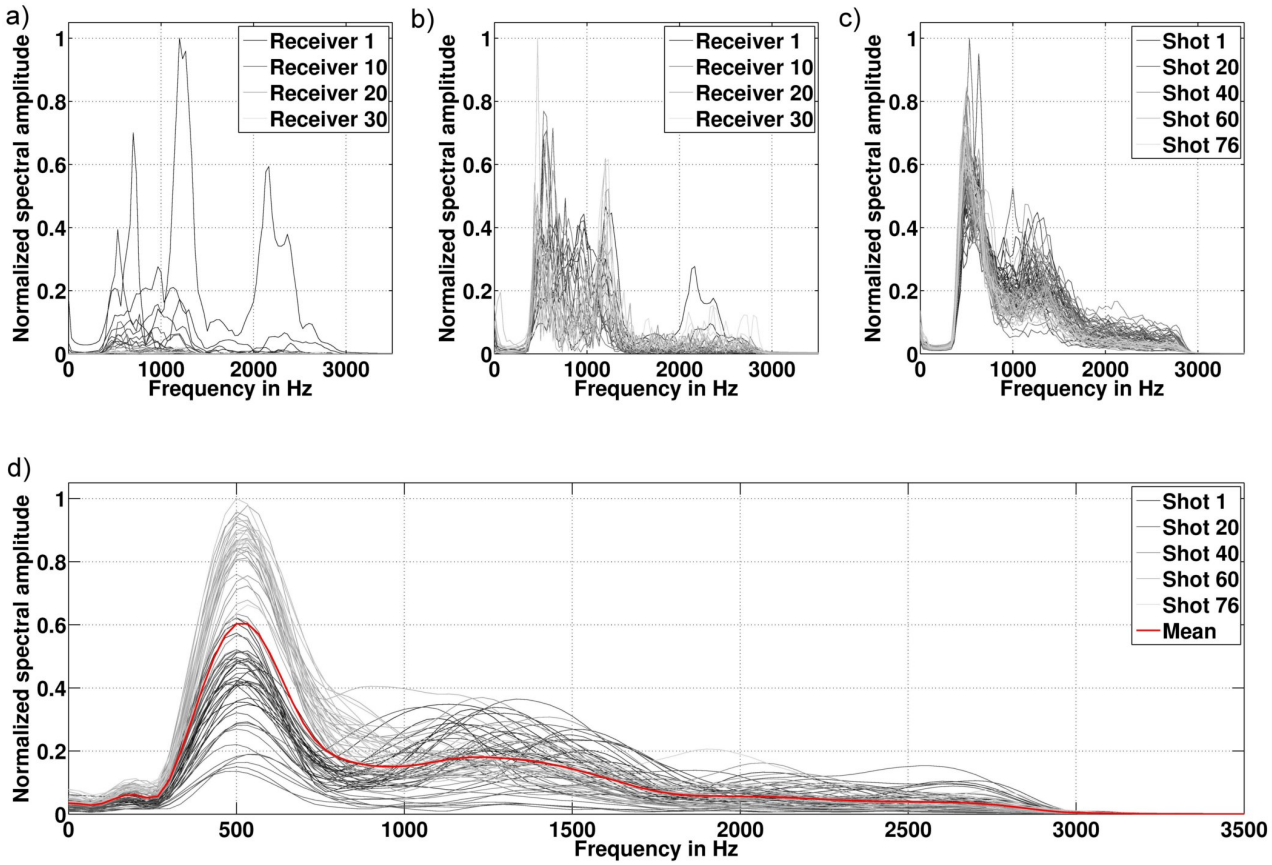

Figure 4.13: Frequency content of the field data. In all four plots, the amplitude is each time normalised to the global maximum. a) The frequency content of Shot 1 for unprocessed field data with true amplitudes for the x-component. The 30 receiver are colour coded from black (Receiver 1) to light grey (Receiver 30). Only the spectra of the receivers in the near vicinity of the source positions can be seen due to their high spectral amplitude. b) The same as in a) but with normalised wavefields due to their RMS value in the time-domain. The tunnel surface wave and the P-wave are threatened equally. c) Mean of all receivers for each shot again with wavefields normalised to their RMS value. The colour range is from black (Shot 1) to light grey (Shot 76). d) Same as c) but with preprocessed data. Only the P-wave is taken into account for the spectral amplitude. The red curve shows the mean value for all shots.

the ray path is perpendicular to the x-axis, the ray angle is -90 ° and 90 °,respectively. The I quadrant and III quadrant include the negative angle, the II and IV quadrants the positive angle. This ensures that ray paths with the same direction also have the same angle value.

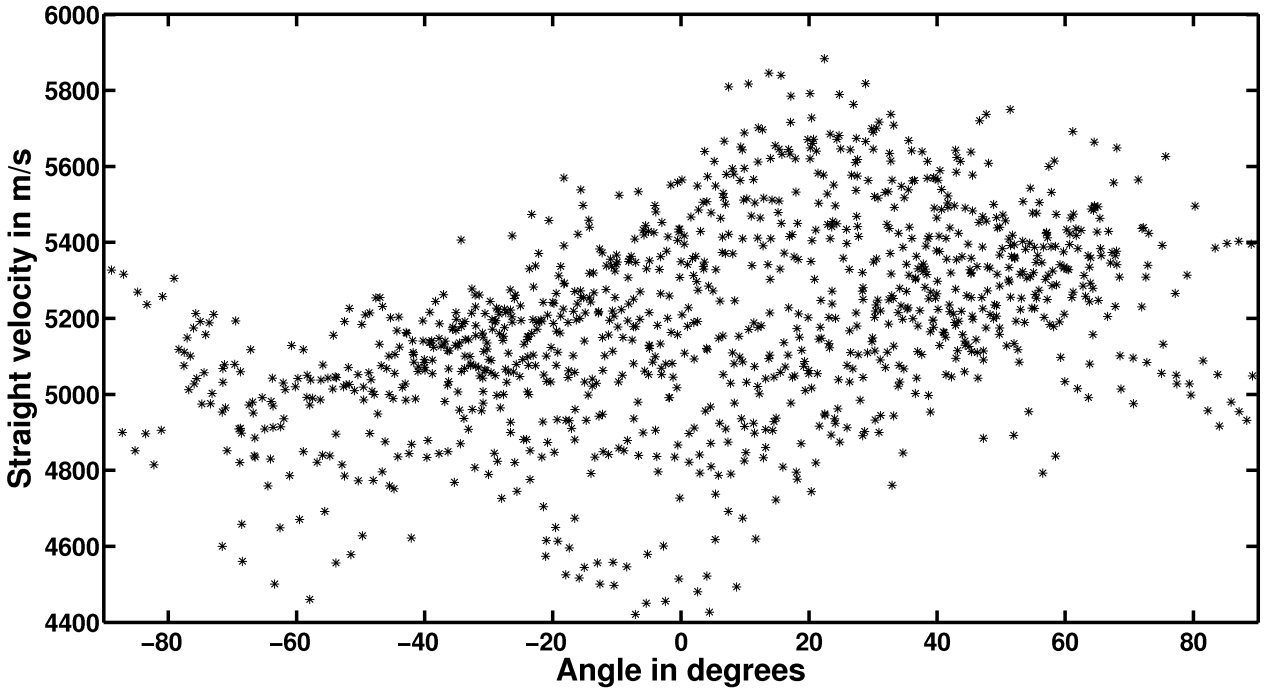

Figure 4.14: The straight velocity overt the ray angle. 0 ° means the ray path is parallel to the x-axis and -90 ° and 90 °, respectively, means the ray angle is parallel to the y-axis. The stars represent the source-receiver combinations. Short offsets are not considered. The pattern of the data points is not symmetric to the y-axis which is the requirement for an anisotropic media in this analysis

.

In Figure 4.14, the straight velocity, that means the linear ray path divided by the first-arrival travel-time picks, versus the ray angle is plotted (Wang, 2011). Short offset combinations were neglected. Due to the irregular geometry the data points are not evenly distributed, mostly appearing between -40 ° and 60 °. Most of the values are in the range of 4800 - 5800 m/s. With a predominant anisotropy the pattern should be symmetrical to the y-axis with two clear minimum and maximum. However, this is not the case. The data points do not have a clear pattern.
With this kind of plot, it is assumed, that the anisotropy is constant distributed over the entire plane. If the ray paths are directly colour-coded plotted with their straight velocity, it can also be possible to recognise small-scale areas of anisotropy (Wang, 2011). Therefore the geometry is divided into two parts. We use the sources along the *Richtstrecke* and the receiver along the *Wilhelm Stehender Süd* for Part 1 (R1 - R15 and S46 - S76) and for Part 2 vice versa (R19 - R30 and S1 - S28). This allows a better overview of the ray path. In Figure 4.15a and 4.15b Part 1) and Part 2) are shown individually. Again, there is no recognizable fast or slow predominant direction. The scattering in Part 1 and Part 2 for different straight velocity depends on the different sources and receivers rather on the direction. Notable is the high velocity zone in the upper part for both. After superimposing all possible source and receiver combinations the impression is confirmed (Figure 4.15c). Also, this figure gives

us a first impression how the velocity distribution after a travel-time tomography looks like.

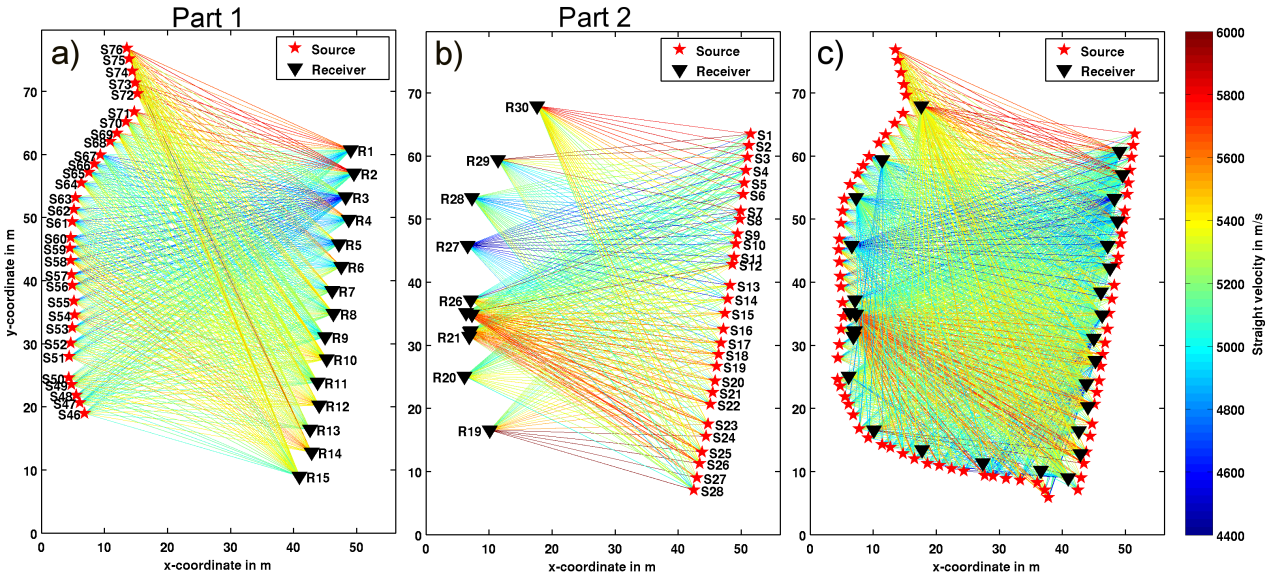

Figure 4.15: The straight velocity colour-coded for all source-receivers pair with three different geometries. In a) only the receivers along the *Richtstrecke* and the sources along the *Wilhelm Stehender Süd* were used (Part 1) and in b) vice versa (Part 2). In both parts no ray angle is preferred. The straight velocities are more influenced by source and receiver anomalies and also some clear travel-time pick inaccuracies. In c) any possible source and receiver combination are shown except with a short offset. Again, a colourful picture results with no clear preferred direction over the entire block.

In the previous analysis, the influence of the velocity changes in the host rock was not considered. In Section 6.1 a travel-time tomography will be calculated with the software GeoTomCG[7]. Although, the inverted velocity model is not introduced at this point, we would like to make use of the information the software provides to us. GeoTomCG exports for each source-receiver pair the travel-time residual which could not adapted to the velocity model. In Figure 4.16a the travel-time residual is plotted versus the ray angle. The data points vary between -0.4 ms and 0.4 ms. Especially in this case, the pattern of the residual values should be axis-symmetrical to the y-axis which would indicate an existing anisotropy because the velocity changes in the host rock are now considered (Rao and Wang, 2011). However, no clear pattern of the straight velocity over the ray angle is observably. Even if we plot the travel-time residual for each individual source-receiver combination, the direction of the residual is almost arbitrary (Figure 4.16b). To sum up, anisotropy could not be identified in the data. The error by not considering this effect is negligible. However, that does not mean that no anisotropy exist, but rather the first-arrival P-wave picks are not accurate enough for the analysis. Also the anisotropy must not be limited to the investigated horizontal xy-plane.

[7]http://dev.geotom.net/ 25.03.2014

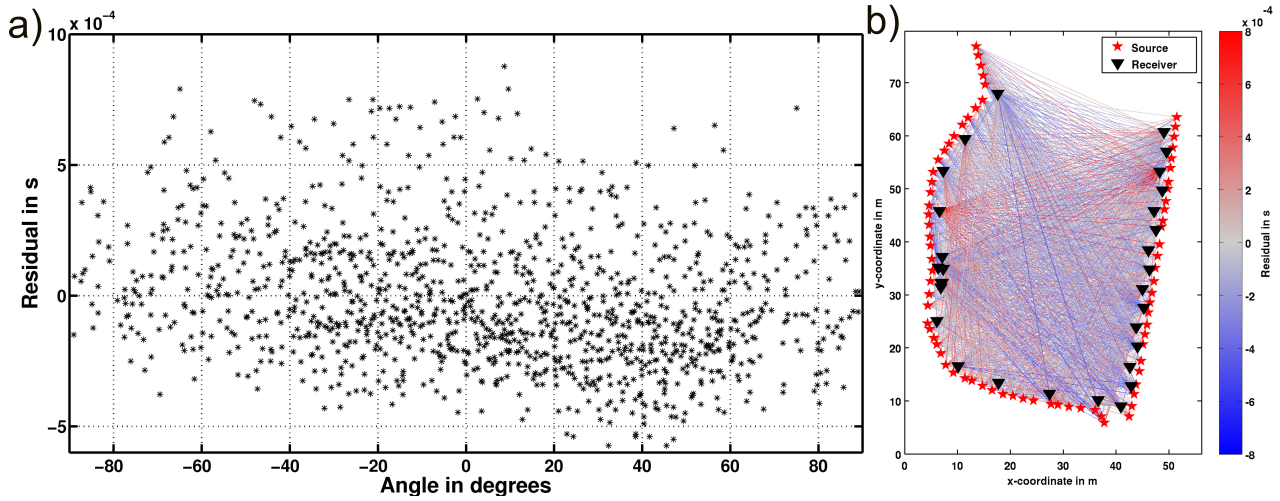

Figure 4.16: Time residuals after the travel-time tomography. In a) the time residuals which could not be adapted by the velocity model versus the ray angle are shown. In b) the travel-time residual for every source-receiver combination is plotted colour-coded. In both, no clear axis-symmetrical pattern and no preferred direction, respectively, is recognizable.

4.4.3 Semblance Analysis

As we want to invert not only for the first-arrival travel times but for whole waveforms, we want to investigate the similarity of waveforms for neighbouring shots and receivers. As a measure of coherence between seismograms we use the semblance. This technique is originally used in reflection seismics to identify reflections which are covered by background noise or interference reflections and, thus, increase the resolution power of the data. We use a modified technique for our purposes.
In the field data, we already observed differences in the waveforms for neighbouring receivers or sources. In hard rock regimes this this is often due to a little different coupling for different receivers or sources (Maurer et al., 2012). We refer to these effects as source and receiver coupling. In the synthetic examples (Chapter 5) we usually assume a known source signal and a uniform and perfect coupling of sources and receivers. To explore the relative contributions of source and receiver effects in the field data, we compare waveforms in the common shot gather (CSG) and common receiver gather (CRG).

For the field data, we consider the semblance analysis for the preprocessed data, i. e., for the first-arrival P-wave for different frequency contents (Section 4.3.2 and 4.3.3). However, we do not use the original matrix for the muting (Figure 4.9), because we should be able to see the corrupt receivers with these analysis anyway. For the semblance analysis the energy of each trace d is normalised, so that effects of the radiation pattern of the source and the offset-dependent amplitude decrease is removed. A semblance based cross-correlation is performed for all possible combinations of sources and receivers. The maximum value of the correlograms is calculated as follows:

$$SEM = \frac{\sum_{n=1}^{n_r} [\max(\frac{\hat{\mathbf{d}}_\mathbf{i} \oplus \hat{\mathbf{d}}_\mathbf{j}}{ns})]_n}{n_r}, \tag{4.4}$$

where SEM is the semblance value for one shot combination and receiver combination, and is in the range between 0 for no coherence and 1 if the waveforms are exactly the same. n_r is the number of possible combinations, $\hat{\mathbf{d}}_\mathbf{i}$ and $\hat{\mathbf{d}}_\mathbf{j}$, respectively, are the energy normalised traces, ns is the number of samples, $\oplus$ denotes the cross-correlation and $i, j = 1, ..., t_{\max}$ the number of traces for each CRG or CSG.

In Figure 4.17 the semblance for unfiltered field data in the CSG domain (Figure 4.17a) and in the CRG domain (Figure 4.17b) is shown. The yellow colour indicates were no semblance could be calculated due to the muting of the traces (Figure 4.9) or the semblance value is smaller than 0.35. The value in the title documents the summed up semblance values and the maximum possible value. The diagonal is equals one because the shots are correlated with itself. The most interesting area is in the vicinity of the diagonal. These shots are very close to each other and, thus, their excited seismic waves are travelling through nearly the same host rock. The apparent crosses in the matrix indicates shots which differs most to every other shot, e. g., Shot 74. We neglect those sources in the later field data inversion application. But in general, the overall reproducibility of the vibroseis signal is very high.
For the CRG in Figure 4.17b also coloured crosses are observable like in the CSG, e. g., Receiver 7 or 26. We neglect those receivers in the later field data inversion application (Chapter 6). Another more crucial effect is visible: For the Receiver 1 - 15 in the CRG, the pattern is like a checkerboard. Only the waveform of every second receiver fits to each other. This checkerboard pattern corresponds to the depth of two adjacent receivers varying from 1 - 2 m or vice versa. The pattern is - most likely - caused by ghost reflections at the gallery walls as the distance to the tunnel surface between neighbouring receivers changes by ± 1 m. All other receivers are in the same depth of 2 m, except of Receiver 25. For those receivers, the coupling effects and the velocity perturbation within the host rock is responsible for the different waveforms. The semblance values in the right upper and left lower part are negligible because they are not comparable due to geometrical reasons. The Receivers 15 - 18 are not used, because they are not in transmission geometry (Figure 4.9).

In Figure 4.18 the CRG are again shown with different corner frequencies for a low-pass filter. The corner frequencies are 1500 Hz, 750 Hz and 400 Hz. For lower frequencies, the semblance values increases. Especially for Receivers 1 - 15, the checkerboard pattern is almost no more observable at 400 Hz due to the increasing wavelength (Figure 4.18(c)). The ghost effect is frequency dependent and more distinct for higher frequencies. Nevertheless, the corrupt receivers, e. g., Receiver 7, are still visible. So, with lower frequencies, the similarity increases.
The same effect can be reproduced in the CSG section. With decreasing corner frequencies of the low-pass filter, the similarity and thus, the semblance is decreasing.

4.5 Chapter Conclusion

In this chapter the general characteristics of the field data have been investigated. First, the interfaces of the measuring area were compared with those of an underground map and the given source positions from the GFZ. Both match pretty well except of some areas. We finally interpolated the coordinates of the sources as the edge of the gneiss block. The 3D expansion of the geometry was merely ± 0.25m.
The source for the field measurement was a magnetostrictive double vibrator which excited

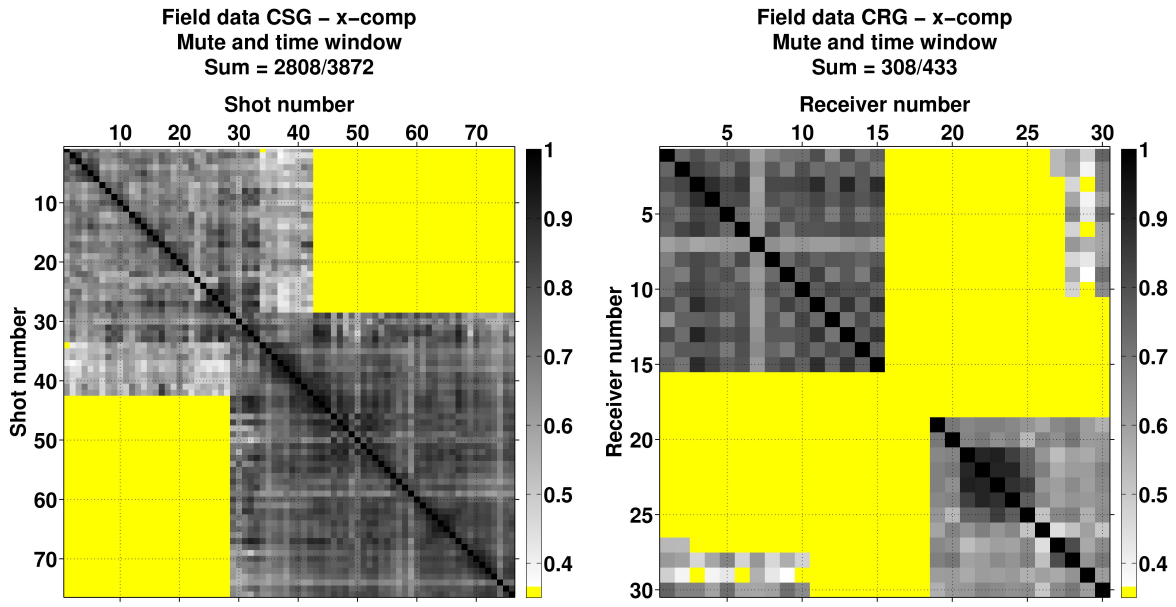

(a) CSG (b) CRG

Figure 4.17: a) Semblance values in the CSG domain for different shot pairs and in b) in the CRG domain for different receiver pairs for the field data (Equation (4.4)). The colour scale is clipped at the semblance value of 0.35. For some shot and receiver pairs no cross-correlation could be calculated (yellow parts) because of muted traces. In the title the summed up SEM value and the maximum possible value is shown.

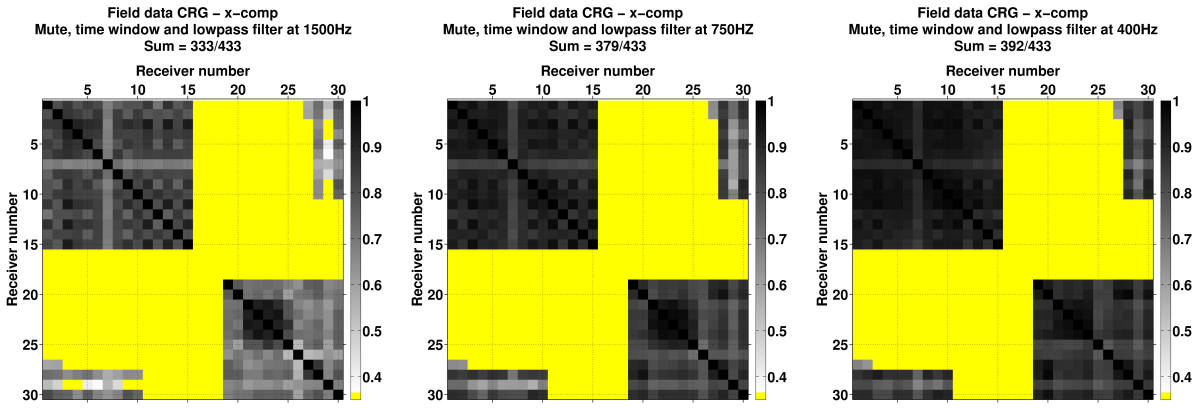

(a) CRG 1500 Hz (b) CRG 750 Hz (c) CRG 400 Hz

Figure 4.18: Semblance values for the field data in the CRG domain for different frequencies. From a) to c) the data is low-pass filtered with corner frequencies of 1500 Hz, 750 Hz and 400 Hz. The colour scale has the same range for all figures. In the title the summed up SEM value and the maximum possible value is shown.

a linear sweep from 300 - 3000 Hz. The raw data had to be correlated with the sweep signal afterwards. The autocorrelation of the sweep signal, the Klauder wavelet, has the same frequency range and has a zero-phase characteristic, as expected. This wavelet is further used for the modelling. With a synthetic test, it could be shown that the synthetic seismograms are equal if we chose either the sweep signal or the Klauder wavelet as the source wavelet.

In order to ensure comparability with simulated waveforms, the entire wavefield were rotated into the coordinate system of the FD-scheme. After a comparison of our own picked travel-times for the first-arrival P-wave and picks from Richter (2010), we decided to use the own picks in the thesis for further investigations, as these account for the zero-phase characteristic of the data. Due to the used 2D code, the tunnel surface waves cannot be included in the inversion because we are not able to model them physically correct. We muted the near offset traces where the P-wave and the tunnel surface wave are not separated. Subsequent, we applied a time windowing around the first-arrival time. Also, a 3D/2D transformation needs to be applied subsequently. The transformation works accurate for synthetic tests.

The preprocessed field data was then analysed for its frequency content, anisotropy and for the similarity of the waveforms. The main frequency range of the raw field data including all wave types lies between 400 - 1250 Hz. After the preprocessing, the maximum frequency is at 500 Hz. For the used horizontal plane in the inversion, no anisotropy is recognizable by investigating the angle dependency of the first-arrival times for the P-wave. The semblance analysis shows a high similarity of the waveforms in the CSG. The shots are reproducible besides of a few exceptions. In the CRG, the geometry of the receivers R1 - R15 are reflected in the semblance values. Due to the alternating depth of the receiver a checkerboard pattern is observable because the reflection at the rock-air interface differs in its effective waveform. By a low-pass frequency filtering and thereby longer wavelengths in the field data, the effect of the ghost reflection can be minimised. In general, the data for low frequencies are quite coherently, for higher frequencies the coherence is strongly decreasing. Also some receivers in the CRG have significantly differences in the waveforms compared to their neighbours. Apparently, this is due to an imperfect coupling of or corrupt receivers. Consequently, we can only use 703 of 2280 possible source-receiver combinations.
In the next chapter, many synthetic tests will light up the influence of some above described parameters.

5 Synthetic Case Studies

In the previous chapter the field data and their characteristics had been explored and described. This chapter primarily deals with the extensive developed synthetic studies based on the experience of the field data. On the one hand, these studies help to investigate features of the field data in a synthetic scenario and, on the other hand, to test the used FWI code for its applicability. We apply the FWI on synthetic modelled data which pretend to be the true, respectively observed data. These synthetic tests can be very helpful to test the resolution potential of the FWI, since we know the true model and we can directly evaluate the reconstructed velocity model. The influence of a single parameter or of different true and starting models, respectively, can be investigated.
For all upcoming inversion tests, we adopted the geometry of field measurement. First the used synthetic models are presented. Afterwards, we obtain the starting models for the FWI with a travel-time tomography for one synthetic model (Section 5.1). To get the inversion running, we need to specify some important parameters first, for the forward modelling (Section 5.2) and second for the inversion (Section 5.3). In the following sections, we investigate the influence by varying different parameters on the inversion results. The reconstruction potential of the FWI is then investigated by using the checkerboard model with different block sizes and different source frequencies. Also the influence of a wrong v_S and density model is shown. A widely-used approach to improve the convergence of the inversion is tested (Section 5.4). At the end, similar to the field data, a semblance analysis for different models with different spatial dimensions and for different frequencies is calculated (Section 5.5).
Most of the synthetic FWI were performed on high-performance-computing (HPC) systems like the Institute Cluster 2 (IC2) at the Karlsruhe Institute of Technology or on JuRoPA at the Jülich Research Centre (Appendix E). The used grid was usually distributed on 96 CPUs. The run-time for one iteration of the FWI was approximately 10 minutes.

5.1 Synthetic Velocity Models

5.1.1 Random Distributed and Checkerboard Velocity Model

Even with the assumption that the bedrock is fairly homogeneous, this is justified up to a certain extent. Due to water leaks or fault zones, the host rock will be quite complex and have heterogeneities at all scales from a few mm to several m (Section 3.3.2). We use two different synthetic velocity models by varying the physical properties, i. e., v_P and v_S and the density, in order to investigate a wide range of the influence on the inversion and features of the field data. Both models have advantages and disadvantages in the evaluation of different aspects.
First, a random distributed velocity model is used to represent the heterogeneities in the

gneiss (Kneib, 1995). A typical description of a model with heterogeneity geological structures is given by the Von Kármán correlation function. It describes a self-similar medium and includes small wavelengths. The full 3D anisotropic function is given by Goff and Jordan (1988). For the major structures in the random model, a correlation length a and a Hurst coefficient H ($0 < H < 1$) must be specified. With a Hurst coefficient of 0.5, the Von Kármán correlation function can be simplified to an exponential correlation function. Then, the correlation length a directly defines the size of the dominant structures in the heterogeneity media. With the standard deviation σ the velocity variations is defined. The average velocity was adapted to $v_P = 6000\,\mathrm{m/s}$. Second, a classical checkerboard model is used based again on a homogeneous model with $v_P = 6000\,\mathrm{m/s}$ (Zhao et al., 1992). Both, the length of the edges and the positive and negative velocity perturbations of the squares can be varied. Of course, this model does not represent the gneiss. It is used for determining the resolution potential of the FWI.

In Figure 5.1a an example of a checkerboard model with an edge length of 4 m, a background v_P value of $6000\,\mathrm{m/s}$ with a perturbation of $\pm 5\,\%$ is shown. There is no continuous transition between the squares of the checkerboard. The border of the gneiss has been determined as described in Section 4.1. The area outside of the gneiss is threaded as air with an v_P value of $300\,\mathrm{m/s}$. In Figure 5.1b the random model is shown. For the Hurst coefficient we used $H = 0.5$, i. e., an exponential autocorrelation function in space. The correlation length was set to $a = 10\,\mathrm{m}$ and the standard deviation to 5 %. In general, the model consists of each two low and high velocity zones. Furthermore, starting from the specified correlation length, the structures are getting smaller and smaller. In Figure 5.1c, the Gaussian distributed seismic velocities are plotted without the areas filled with air. Due to the ratio of the model size to the correlation length, the average velocity (Avg) is not exactly $6000\,\mathrm{m/s}$ with a standard deviation (Std) of $299\,\mathrm{m/s}$. Assuming the given average velocity of $6000\,\mathrm{m/s}$ within the specified standard deviation of $\pm\sigma$ ($5700\,\mathrm{m/s}$ and $6300\,\mathrm{m/s}$) less values than the required 68.27 % can be found (Pro=64.80%).

As we us an elastic code, we also need a v_S and ρ model. For v_S we used the typical ration of $v_P/v_S = \sqrt{3}$. The density ρ is chosen homogeneous with $2550\,\mathrm{kg/m^3}$ which is the mean value of the determined density by Kopf et al. (2008).
In the following, the random model is used, e. g., for investigating the influence of various parameters on the inversion result and the checkerboard pattern to determine the resolution potential for different source frequencies.

5.1.2 Starting Model

As described in Section 2.3.6, we need an accurate starting model for the FWI. For a high similarity between starting model and true model, the inversion has the ability to reconstruct the true model properly.
For the checkerboard model (Figure 5.1a) a homogeneous velocity model of $v_P = 6000\,\mathrm{m/s}$ is used for all checkerboard tests. This makes the comparison between different inversion results more easy and reliable, since a variety of different checkerboard patterns is used. The chosen velocity is exactly in the middle of the positive and negative velocity perturbation.

For the random model (Figure 5.1b) we decided to compute a travel-time tomography for the first-arrival times of the P-wave. Pratt and Goulty (1991) showed that a starting model

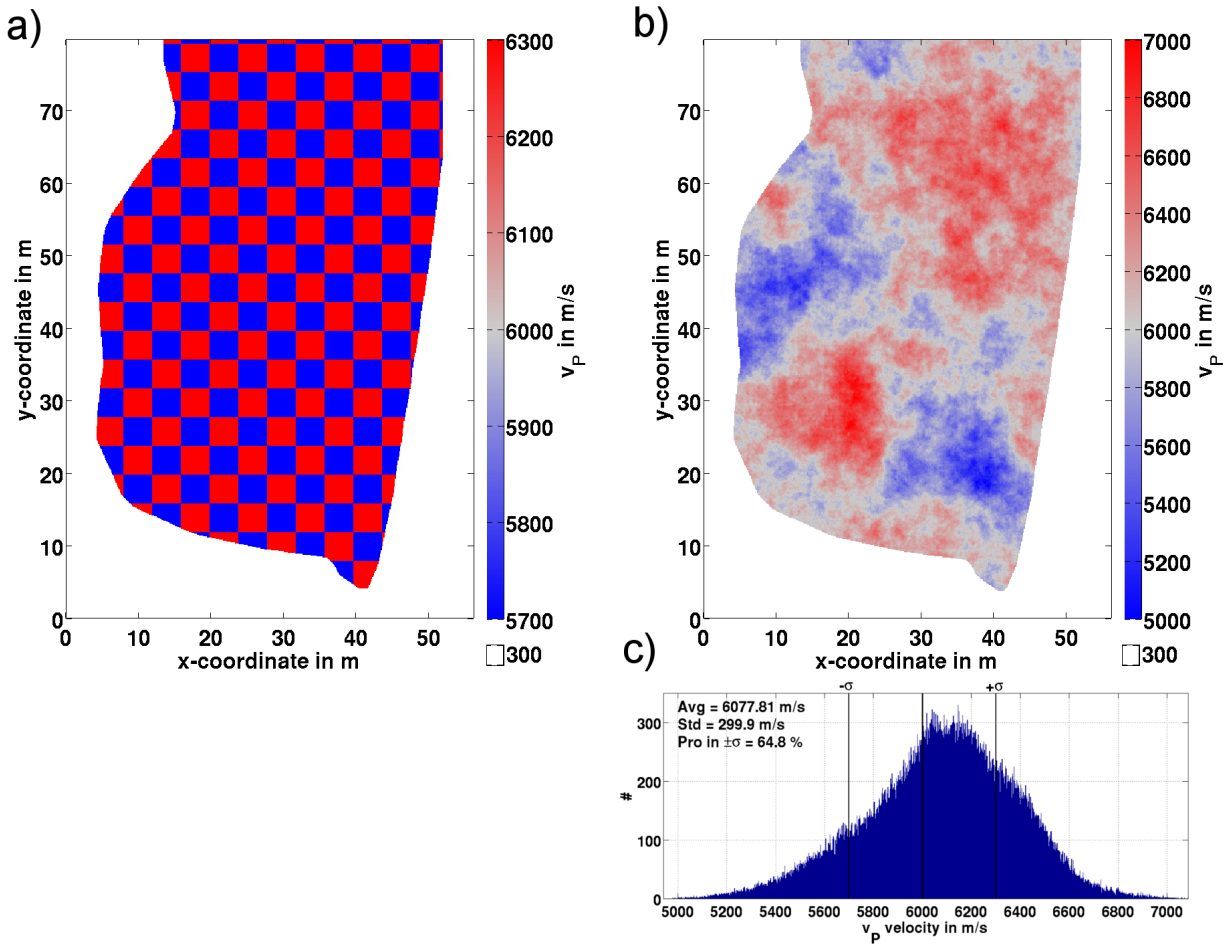

Figure 5.1: a) Checkerboard model with a background v_P value of 6000 m/s, an edge length of 4 m and a positive and negative velocity perturbation of $\pm 5\,\%$. b) Random velocity model generated with a Hurst coefficient H of 0.5 and a correlation length a of 10 m. The same background velocity and perturbation was used as in the checkerboard model. c) The velocity distribution of the random model.

obtained from a travel-time tomography can be sufficient for FWI. The existing transmission geometry also supports us in this decision. Therefore, a forward modelling on the true model with the same geometry as it is used in the field measurement and with the Klauder wavelet as the source wavelet was calculates to obtain the observed data. The first-arrival travel times are then picked. Taking the zerophase characteristic of the Klauder wavelet into account, in our case the first break is the point in time of the maximum amplitude. In the forward modelling we include the gallery walls in the random model. This leads to a clear ghost reflection similar to the field data (Section 4.4.3). For some receivers, therefore, it is hard to pick the maximum amplitude because the reflection creates a second maximum. By comparing seismograms which are modelled without the walls of the galleries (no ghost reflections occur), it was possible to identify the first arrival. The picks were set by hand for seismograms with a clear first arrival.
For the travel-time tomography we use the software GeoTomCG[8]. This is a commercial software for both, 2D and 3D travel-time tomographies based on the simultaneous iterative reconstruction technique (SIRT) (Section 2.5). As an important parameter for the inversion, we can specify the spatial size of the grid points, respectively the blocks size between the grid points. We use five different block sizes to study the influence of the parameter. The initial block size is specified by the program due to the geometry and the occurring velocities, so that the inversion is stable. Since also the travel-time tomography requires a starting model, a homogeneous model with uniform velocity is used, adopted from the mean and the slowest straight-line velocity (Tweeton, 2011). In addition, with the initial suggested block size, we calculate a travel-time tomography by neglecting five receivers from the receiver array R21 - R26 by only using R24 to analyse possible focusing effects and related fingerprints by the geometry.

In Figure 5.2d the true model and the random distributed velocity model, respectively, which was described in Section 5.1.1 is shown for a better comparison. In all other plots in Figure 5.2 the inversion results of the travel-time tomography for different block sizes without the receiver array are shown. In addition, the light grey line shows the galleries for not getting lost in the plots. With the used software we could not make any constraints to account for the gallery walls. The suggested block size of the GeoTomCG software was 2.2 m with a homogeneous velocity of 5700 $^{m}/_{s}$. In Table 5.1 the different used block sizes are summarised. After the inversion, all velocity models are interpolated to 0.12 m. We will use this grid spacing in most of our performed modellings and inversion (Section 5.2). As we know the true model, we can directly compare the results of the travel-time tomographies. Of course, this is the advantage of synthetics tests and is not possible for the field data. In Figure 5.2a and 5.2b, despite of the interpolation, the blocks are still clearly visible. However, the coarse structures of the random model with two low velocity zones can be seen. In Figure 5.2f and 5.2g, some characteristic artefacts for a too small chosen block size are already visible. Especially in 5.2g, individual ray paths are very easily observable. The velocity variations within the models were not originated by the true velocity model and do not resemble these, but by an insufficient ray density per block. At the gallery walls, already little artefacts appear. Also the sources are very dense, a block size of 1 m would be too small.

In Figure 5.2c, approximately the proposed size of the block has been used, 2 m instead of 2.2 m. The high velocity areas are included in the inversion compared to the true model. Also, e. g., smaller structures with high velocity at about $x = 10$ m and $y = 60$ m and other

[8]http://dev.geotom.net/ 25.03.2014

Table 5.1: Overview of the different block sizes of the travel-time tomography.

Figure number	Block size in m	Figure number	Block size in m	Figure number	Block size in m
Fig. 5.2a	6	Fig. 5.2c	2	Fig. 5.2f	1
Fig. 5.2b	3	Fig. 5.2e only R24	2	Fig. 5.2g	0.5

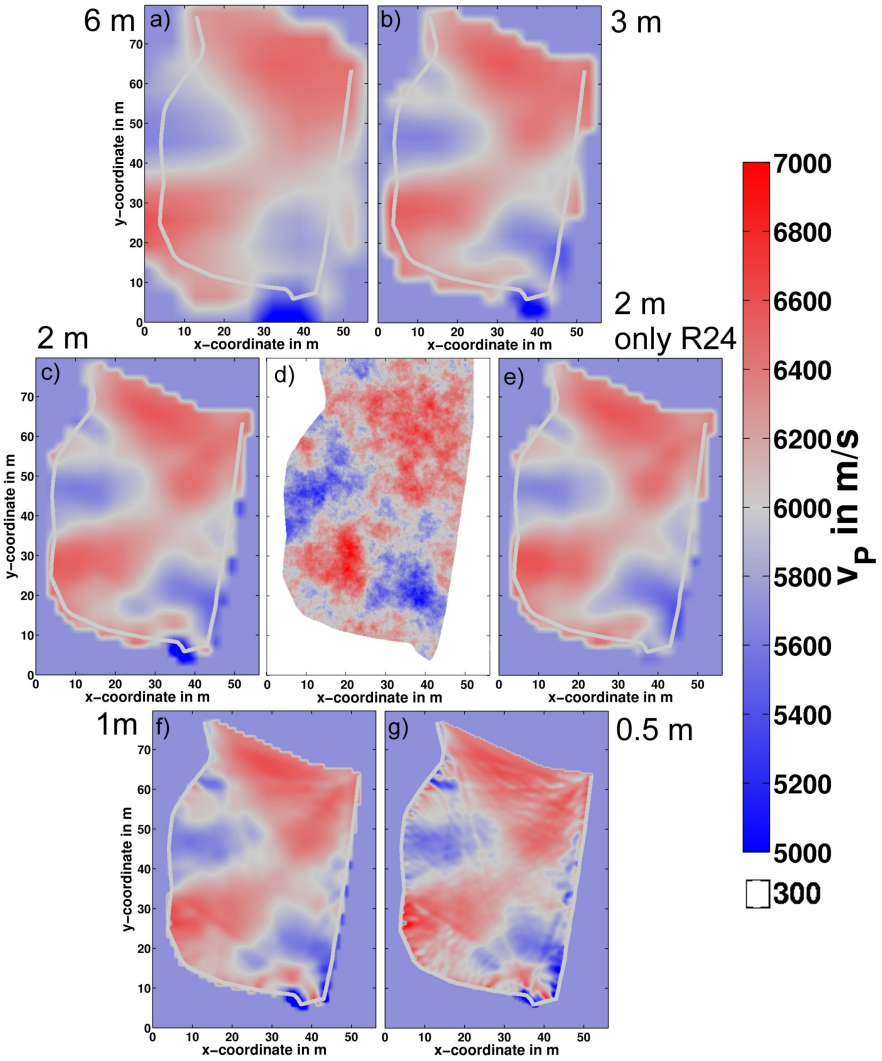

Figure 5.2: Result of the travel-time tomography for different block sizes. The different block sizes are summarised in Table 5.1. All results are interpolated to DH = 0.12 m, the used grid spacing in the modelling (Section 5.2). The grey line represents the three galleries for better orientation. For comparison, in d), the true random distributed velocity model is shown.

areas with low velocity at $x = y = 40\,\text{m}$ already occur in the model. However, no unique ray path are observable at this block size.
In Figure 5.2e, the receiver array at about $x = 10\,\text{m}$ and $y = 30 - 40\,\text{m}$ (Figure 3.6) has been neglected and only one receiver (R24) were used. It should be tested whether the array provides some kind of footprint in the model. For the specified geometry, this is not the case. Figure 5.2c and 5.2e are very similar except for a few small differences such as at $x = 40\,\text{m}$ and $y = 10\,\text{m}$ where the array incorporate a low velocity area, although it does not exist in the true model.

For all travel-time tomography results the upper part of the model has not been updated. Due to the geometry no ray path are running through this area. Also in the FWI, the sensitivity in this area will be very low and we expect no significant velocity changes.
We determine the block size to 2 m because of first, this is the suggested block size of GeoTomCG and second, it is a well acceptable compromise between the sureness not to have single ray paths in the velocity structure and a sufficient resolution. For the travel-time tomography for the field data (Section 6.1) we will do an equivalent analysis. Further, the starting model is smoothed with a median filter of 1.2 m which corresponds to 10 grid points in the used FD-grid. The median filter sorts the velocities within the specified area and takes the middle value. This can especially reduce strong local velocity anomalies as well as by the interpolation arisen geometrically effects of the blocks.
For later analysis we calculate the minimum and maximum velocity difference (-788 m/s and 883 m/s, respectively) and the corresponding mean values for positive and negative velocities (-77 m/s and 103 m/s, respectively) of the true to the starting model. These mean values are in the range of $\pm 2\,\%$ and are later on compared to the differences in other models.

As we are using an elastic code, we also need a v_S and ρ model. The v_S model is calculated by the v_P to v_S ratio of $\sqrt{3}$. The shear wave velocity in air is equals $0\,\text{m/s}$. Outside of the gneiss, we have set v_S to $1 * 10^{-3}\,\text{m/s}$ due to stability reasons in the staggered grid. The density ρ was chosen homogeneous within the gneiss with $2550\,\text{kg/m}^3$. It is the same value as for the true model and is assumed to be known in order to have the possibility to consider other parameters more isolated. Again, for the part of the model filled with air, we choose a realistic density of $1.25\,\text{kg/m}^3$. These values are also used in the field data inversion.
In Section 5.4, with both models, synthetic tests are carried out.

5.2 Modelling Parameters

The theory for the used FD-scheme is explained in detail in Section 2.2. For an accurate modelling with FD, we have to specify some parameters with care. The basic FD-parameters are described in Table 5.2. All input parameters are written in capital letters. Unless nothing else is mentioned, we use these parameters in the synthetic tests or did studies by varying the values. For a stable and accurate modelling, the most important parameters are the grid spacing DH and the time stepping DT. The parameters depend on the largest used frequency and on the velocity range of the model. Not sufficient exact chosen parameters leads to dispersion effects in space and time, typically high frequency oscillations in the wavefield (Alford et al., 1974). Due to the high discontinuities at the rock-air interface, an application of higher-order spatial FD-operators is not reasonable. The FD-scheme is only stable for second-order spatial FD-operators. For all modellings we used FD_ORDER=2 (Cunha, 1993).

Thus, only the neighbouring grid point is taken into account for updating the velocity and stress values. The minimum and maximum occurring velocity in the random media model is $c_{\min} = 5000\,\mathrm{m/s}$ and $c_{\max} = 7000\,\mathrm{m/s}$. For a max frequency of 2000 Hz (Figure 4.3), the minimum wavelength $\lambda_{\min}$ is thus, 2.5 m (Equation (2.12)). With $\lambda_{\min}/dh \geq 12$ we satisfy the required number of grid points per minimum wavelength with approximately 21. Also the criteria for $dt = \frac{dh}{\sqrt{2}*7000\,\mathrm{m/s}} = 1.22 * 10^{-5}$ (Equation (2.13)) is fulfilled with DT=$5 * 10^{-6}$ s.
The FD-code is parallelised and could be run on several CPUs at the same time. FD-schemes with a regular grid can be parallelised reasonably well. "The parallelisation is based on domain decomposition, i. e., each processing element updates the wavefield within his portion of the grid" (Bohlen et al., 2012). For the decomposition, the number of processors in each direction has to be specified with NPROCX and NPROCY.
We also have to make use of the absorbing frame implemented in DENISE (Section 2.2.3). At three sites of our model we have a natural reflector, the rock-air interface. This is represented in our model. In reality, at the top end, the gneiss block is extended several hundreds of meter (Figure 3.3a). For this, we have to add an absorbing boundary at the top end of the model, so that no reflections can occur. We used the already by Köhn (2011) implemented convolutionary perfectly matched layers, or CPMLs (Section 2.2.3). This formulation is an effective way to get rid of unwanted boundary reflections. The width of the absorbing frame is set by the parameter FW. Some other parameters have to be adjusted with respect to the occurring velocities and frequencies. For all inversion tests we used a width of 20 grid points.As the CPMLs surround the whole model along all four boundaries, we have to make sure that their are at least 20 grid points, beginning from the last grid point of the gneiss block to the boundary of the model. To get an impression how the wavefield propagates

Table 5.2: Parameters for the forward modelling.

Parameter	Value	Explanation
NPROCX x NPROCY	12 x 8	Number of processors in each direction
FD_ORDER	2	Order of the FD-operator
NX x NY	468 x 664	Number of grid points in each direction
DH	0.12 m	Grid spacing
TIME	0.030 s	Recording length
DT	$5 * 10^{-6}$ s	Time stepping
FW	20 grid points	Width of CPMLs

within the model, we saved some snapshots at specific time steps for Shot 1 (Figure 5.3). The wavefield is approximately separated in the S-wave and P-wave (Dougherty and Stephen, 1988). The colour scale does not change for all snapshots but differs for the P- and S-wave. As a source wavelet, we used a low-pass filtered Klauder wavelet with a corner frequency of 400 Hz (Figure 4.3). For better visualisation, DH was reduced. The gallery walls are indicated with black lines. The source direction is chosen perpendicular to the gallery wall similar to the field survey (Section 3.4). So, we have to split the force density on the x- and y-component which is described in more detail in Section 2.2.3. The actual time T is shown between the S- and P-wave models. Below, with a thin black line, the source wavelet is shown. The part of the wavelet which was already fed in the FD-scheme is highlighted in blue.
Initially at T = 0.00810 s we can already see some wave propagating in the model, also the Klauder wavelet has a quite flat shape from the beginning. In the S-wave snapshot, we can

see converted phases in front of the actual wave front which are caused by the permanent scattering of the P-wave due to the random velocity distribution. At T = 0.01350 s, the radiation pattern of the source is illustrated very nice. Later, at T = 0.01500 s, the maximum amplitude is fed in the FD-scheme. In the next snapshot, note the different wavelength of the P- and S-wave due to the different velocities. At T = 0.02010 s, the first P-wave arrives at the receivers in the transmission geometry at the *Wilhelm Stehender Süd* and is afterwards reflected at the rock-air interface. Along the gallery walls of the *Richtstrecke*, the tunnel surface wave propagates at the rock-air interface. At T = 0.25950 s also the P-wave is reflected at the *Quergang* and interferes with the propagating S-wave and the reflections from the *Wilhelm Stehender Süd*. The tunnel surface wave has a significant higher amplitude than the P-wave. In the last snapshot, the tunnel surface wave has reached the corner at the *Richtstrecke*. The direct S-wave front is still propagating in the media. This is not crucial because we do not invert for the S-wave (Section 4.3.3).
When the P-wave reflection at the rock-air interface occurs, a small part of energy is transmitted into the air because we set $v_{\mathrm{P}} = 300\,\mathrm{m/s}$ for the part of the model which is filled with air. The same effect could be noticed in the measurement by standing on the opposite site of the source. It sounds like the noise came "out of the rock".

The corresponding wavefield for the x-component which has been recorded at the receiver positions is shown in Figure 5.4 as black-grey seismograms in the background. The appearance of the wavefield is comparable to Figure 4.10 where the different visible wave types are explained for the field data. We want to test the influence of different grid spacing DH in order to investigate whether we have to deal with dispersion effects even though the FD-simulation is stable. The other parameters and the velocity model is kept constant.

The seismograms were computed with the mentioned parameters in Table 5.2. To test if the chosen grid spacing is accurate enough for our purpose, we halve DH to 0.06 m. That means, the overall number of grid points have been increased by a factor of four. The absolute dimension of the model is, thus, the same. Due to the different spatial discretisation of the model, first the scattering points within the random model are getting smaller and second, the dispersion characteristic along the gallery walls changes. We expect a different waveform for the tunnel surface waves for long offset receivers where the dispersion has a greater impact but only marginal changes for the body waves due to the used relatively long wavelength.
In Figure 5.4, in red dashed, the seismograms for the modelling with DH = 0.06 m are shown. Both, the black-grey seismograms in the background and the red dashed seismograms are amplitude normalised trace by trace. In green, the difference seismograms with true amplitude are shown. As expected, for the Receiver 1 - 13, the tunnel surface waves differ more with larger offset. For Receivers 16 - 27 which are in an optimal transmission geometry, especially for the first-arrival P-wave phase, the difference seismograms have a very small amplitude. Also for Receivers 28 - 30 the first arrival still matches well, but the coda is affected by different reflections characteristic. Thus, as we will only use the first arrival of the P-wave by time windowing and mute seismograms with tunnel surface waves, the grid spacing in Table 5.2 is accurate for the used frequency content.

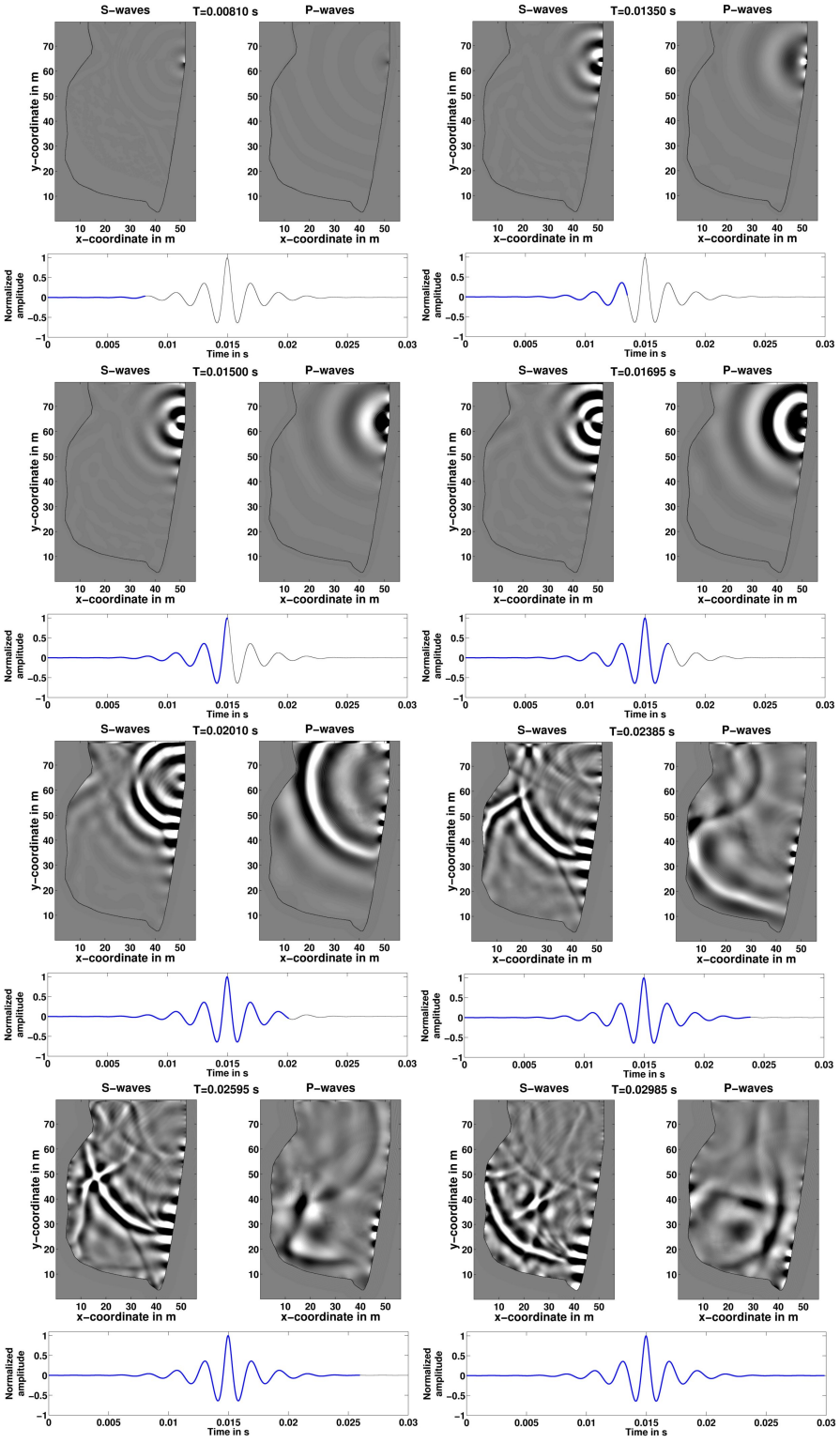

Figure 5.3: Snapshots of the propagation of the P- and S-wave for different time steps. The actual time T is shown between the S- and P-wave models. The used model was obtained with the travel-time tomography of the random model (Section 5.1.2). Beneath, in blue, the already excited part of the source wavelet is shown.

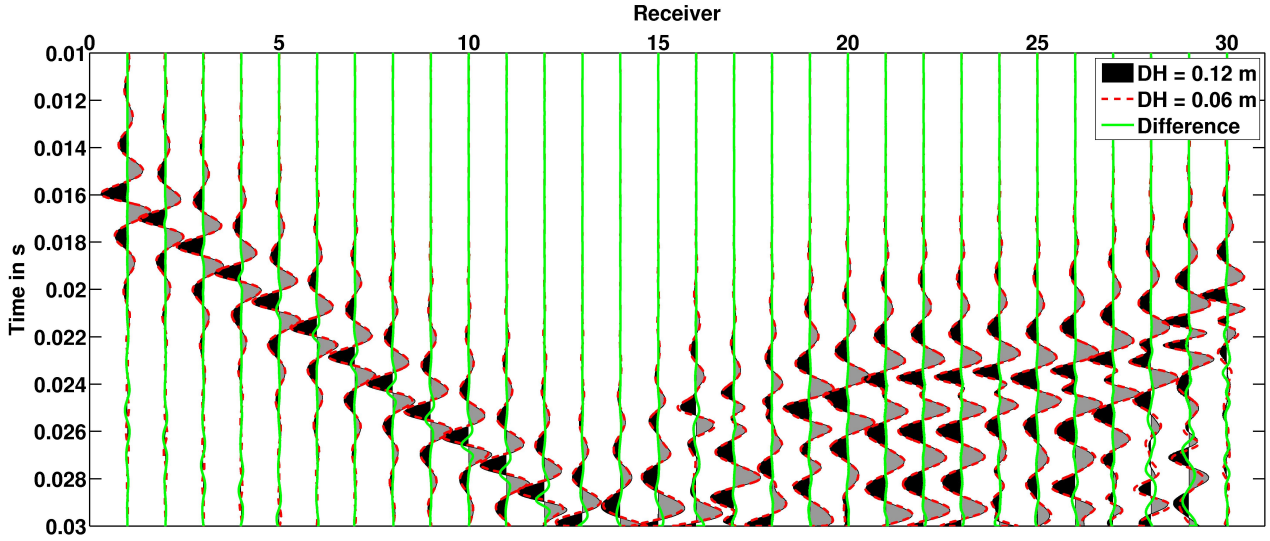

Figure 5.4: Comparison of two different grid spacings DH. For Shot 1, In black and grey, the seismograms with a grid spacing of 0.12 m and in red dashed, the seismograms for a grid spacing of 0.06 m are shown. Both are normalised separately trace by trace. In green, the difference seismograms are shown with its true amplitude.

5.3 Inversion Parameters

In this section the necessary parameters used for an inversion are explained. Some parameters have a significant influence on the inversion result and have to be chosen accurately. The preprocessing steps which are applied to the field data have to be applied to the synthetic data, too. Especially, the influence of the parameters on the inversion result used for the preprocessing are investigated with synthetic case studies.
The most basic parameters for the inversion and an explanation for each parameter are summarised in Table 5.3. The LNORM defines the used misfit function. As the FWI aims to minimise the difference between synthetic and observed data, we have to define a minimisation criteria. In Crase et al. (1990) some well-known criteria like the L1-norm, the L2-norm, the Cauchy or sech function are described. For the synthetic test we apply the widely-used L2-norm (LNORM=2). In addition, as we only use approximately one wavelengths of the first-arrival P-wave, we normalise the amplitude (NORMALIZE=1). The contribution for far and near offset traces to the misfit function is equal. The residual seismograms are directly used as adjoint sources (Section 2.3.2).
In Section 4.9, as we use a 2D inversion code, we described the necessary preprocessing steps for the field data. For the synthetic data, the same preprocessing steps are required. With TRKILL=1, we can control which traces contributes to the gradient calculations by generating a matrix with the dimension numbers of sources times number of receivers. For our application, this is a very important tool because we cannot consider all receivers for every source and thus have to mute some traces. For the synthetic tests, it would be possible to take all waveforms into account, because the observed data are also modelled with the 2D code. But we want to imitate the conditions for the field data inversion as good as we can. If nothing else is mentioned, the number of muted traces were nearly the same as we will use in the field data (Figure 4.9). With TIMEWIN=1, travel times for each receiver and every shot could be read in the inversion code. The parameters TWLENGTH_PLUS and

TWLENGTH_MINUS control the length of the time window where the taper coefficient are equals one and GAMMA controls the slope of the flanks.

Table 5.3: Necessary parameters for the FWI inversion.

Parameter	Value	Explanation
LNORM	2	Specifies the misfit function
NORMALIZE	1	Amplitude normalisation
TRKILL	1	Trace muting
TIMEWIN	1	Time windowing
TWLENGTH_PLUS	0.0015 s	Length of time window after the picked time
TWLENGTH_MINUS	0.0015 s	Length of time window before the picked time
GAMMA	1000000	Slope of the flanks

In addition to the parameters described in Table 5.3, we have to precondition the gradient which is used for updating the velocity model (Section 2.3.3). First, the gradient is tapered around the source positions individually for every source. This ensure that the entire model receives an update and not only in the vicinity of the source (see Figure 2.4 Groos, 2013, p. 25). For the synthetic tests, a radius around the sources of 2.4 m was used.
In addition to the taper around the sources, we used a second taper function for the already summed up gradient. This is common practise in the marine FWI where an update within the water layer is forbidden (Przebindowska, 2013). We used this technique to allow only an update within the gneiss block. Although at the very strong rock-air interface, only a small part of the seismic energy is transmitted (Section 5.2), we would like to ensure that no model update is taken place outside of the gneiss block. The gradient is therefore multiplied with a matrix which consists of ones within the gneiss block and zero values for all other grid points. For the step length estimation we use three test shots (Shot 15, 40 and 65) as the synthetic data is consistent with one another.

5.4 Influence of Inversion Parameters

For the inversion we need several parameters which are explained in the previous section. These parameters need to be tested in synthetic studies investigate the effect and the influence on the inversion results. We use two different synthetic models which are described in Section 5.1.1. As the trace muting and time windowing was required for the inversion of the field data, we implemented these features into DENISE and did several analysis on those parameters (Section 5.4.2 and 5.4.3). With the parameter TRKILL we can decide which source-receiver combinations, respectively which seismogram is used for the calculation of the gradient. The residual seismogram which is back-propagated in time from the receiver position is simply set to zero. So, it has no influence on the correlation coefficients of the forward- and back-propagated wavefield. Also for the misfit calculation the muted traces are not taken into account. The time windowing is already explained in Section 4.3.3. Furthermore, we tested the influence of wrong coordinates for the receivers. As already mentioned in Section 3.4, we cannot measure the error of the source and receiver coordinates. Therefore, we want to test, which deviation could be handled by the inversion (Section 5.4.4). Those test are performed with the random distributed velocity model.

The checkerboard model is used for a different kind of study. We want to investigate the possible resolution and its limits related to the used source frequency and the size of the squares of the checkerboard (Section 5.4.5). Also the accuracy of the starting model is tested with the checkerboard model by increasing the velocity perturbation and by using the same starting model.
In Section 5.4.7, a common used method to get a more stable inversion by a simplification of the misfit function is presented and tested. Afterwards, in Section 5.4.8, the role of v_S and the density in the inversion is investigated. We vary both and study the influence on the v_P inversion result in which we are mainly interested. In general, the inversion stops, if the algorithm is not able to reduce the misfit between synthetic and observed data anymore by updating the models. The misfit converges and could not be longer reduced. This results in a different number of iterations for the various tests.

To evaluate the results of the synthetic tests for the random model not only by eye, we calculate the error of the starting model, respectively of the inverted models, relative to the true model for v_P. This is appropriate because we do not have straight boundaries, sharp velocity contrasts or anomalies within the model. For the checkerboard model, the results are evaluated by eye.
For the error ϵ we calculated the relative error for every grid point, summed up the absolute errors and took the mean over all grid points within the gneiss block, like in the following equation:

$$\epsilon = \frac{1}{\sum \text{grid points}} * \sum_{\text{grid points}} \left| \frac{\text{true model} - \text{test model}}{\text{true model}} \right|_{\text{grid point}} \tag{5.1}$$

In the Tables 5.4 and 5.6, all inversion tests are summarised which were calculated with the random velocity model. The parameter of interest is highlighted in grey. The error is colour-coded. The overview of the checkerboard tests can be seen in Table 5.5.

5.4.1 Reference Inversion and Error Calculation

We discussed in Section 4.3.3 how the data have to be preprocessed. In the following sections, we are going to study the influence of the preprocessing parameters. As we do synthetic tests, the preprocessing is not necessary because we calculate the observed data with the same code as we invert it. Therefore, we want to calculate a reference inversion result (REF) for the random distributed velocity model described in Section 5.1.1. This should be the levelling rule for all other inversion results.
With the data, no preprocessing steps or other constraint are done. That means, that P- and S-waves and tunnel surface waves were taken into account in the inversion. The starting model for P-wave velocity model is a smoothed version of the travel-time tomography result and is described in Section 5.1.2. The v_S model is obtained by the $\frac{v_P}{v_S} = \sqrt{3}$ criteria and the density is assumed to be known with a homogeneous pattern and a value of $2550\,\mathrm{kg/m^3}$. The parameters for the inversion can be found in Table 5.3. In Figure 5.5, from left to right in the first column, the starting model, the true model and the inversion results and in the second column the difference between true and starting model, respectively true and inverted model are shown for all three elastic parameters. The starting, the true model and the difference of both for the v_P and v_S model looks the same because the colour scales were

adjusted with the $\sqrt{3}$ criteria, too. First we will describe the inversion results (Figure 5.5c, 5.5h and 5.5m) and afterwards we will focus on the difference models.
In the inverted models, the large scale structures could be reconstructed very well. Even inside the high and low velocity areas, many detailed velocity distributions are similar to the true model. In the upper most part, the inversion did not update the models because of zero ray coverage. Almost no artefacts occur at the receiver positions. For the shot positions, we applied a preconditioning described in Section 5.3. Due to the shorter wavelength of the S-wave, the inverted model is even closer to the true model (Figure 5.5h). The density model which was actually correct has only changed little. The included structures have nothing in common with the velocity distribution (Figure 5.5m). As we only allow an update within the gneiss block, the velocity around the block is fixed to 300 $\mathrm{m/s}$ for the v_P model, approximately 0 $\mathrm{m/s}$ for the v_S model and 1.25 $\mathrm{kg/m^3}$ for the density model.
To get a better impression of the effect of the inversion, the difference models for true minus the starting model (Figure 5.5d, 5.5i and 5.5k) and the difference for the true minus the inverted models are plotted (Figure 5.5e, 5.5j and 5.5p). In Figure 5.5d and 5.5i, the size of the residual structures for the not explained velocity perturbations are approximately in the range of a few meters to a couple of ten meters. For the density model, the residual model is equals zero.

The error ϵ of the starting relative to the true model is the same for the v_P and v_S model with $\epsilon = 3.09\,\%$ and $0\,\%$ for the density model as we used the true one. In Figure 5.5e, the true model minus the inverted model is shown for v_P. The size of the not reconstructed structures have a maximum size of 3 m and is in the range of the smallest wavelength, especially in the upper part of the model. In general, the gained resolution is very good. But, little footprints of the geometry can be seen. Most of the ray paths are parallel to the x-axis. Hence, the resolution in the y-direction is less good as in the x-direction. This is indicated by the unresolved larger structures parallel to the y-axis in the middle of the model. In the difference plot, we can also clearly see the low ray coverage in the upper part with the high velocity residuals. The relative error decreases from 3.09 % to 1.70 %. At a first glance, this is not quite much, but looking at the velocity models, the FWI did an impressive job. The S-wave due to the lower velocity has a shorter wavelength compared to the P-wave. This leads to an even better inversion result (Figure 5.5j). The error drops from 3.09 % to 1.46 %. The residual structures are even smaller than for the v_P model. The footprint of the geometry is still visible. The density has been set free in the inversion. That means, although the true and starting model were the same, the inversion was allowed to update the model. The error increased from 0.00 % to 0.76 %. The influence of the density on the inversion results is obviously not that strong, because the difference model shows no clear pattern. Even in the upper part were the sensitivity is very low, the values have the same range as in the centre of the gneiss. The influence of the density is analysed in more detail in Section 5.4.8.

The above inversion should show to us the potential of the FWI by using all wavetypes, respectively the entire data. However, this proceeding is not realistic for field data.
In the following sections, the inversion parameters are chosen more realistically, considering the field data. In each case, one of many parameters is varying to test its influence. In the various sections, one model is necessity always inverted with the same parameters. In each case, this model is marked with a red star, e. g., Figure 5.7f or 5.9d and Table 5.4 and 5.6.

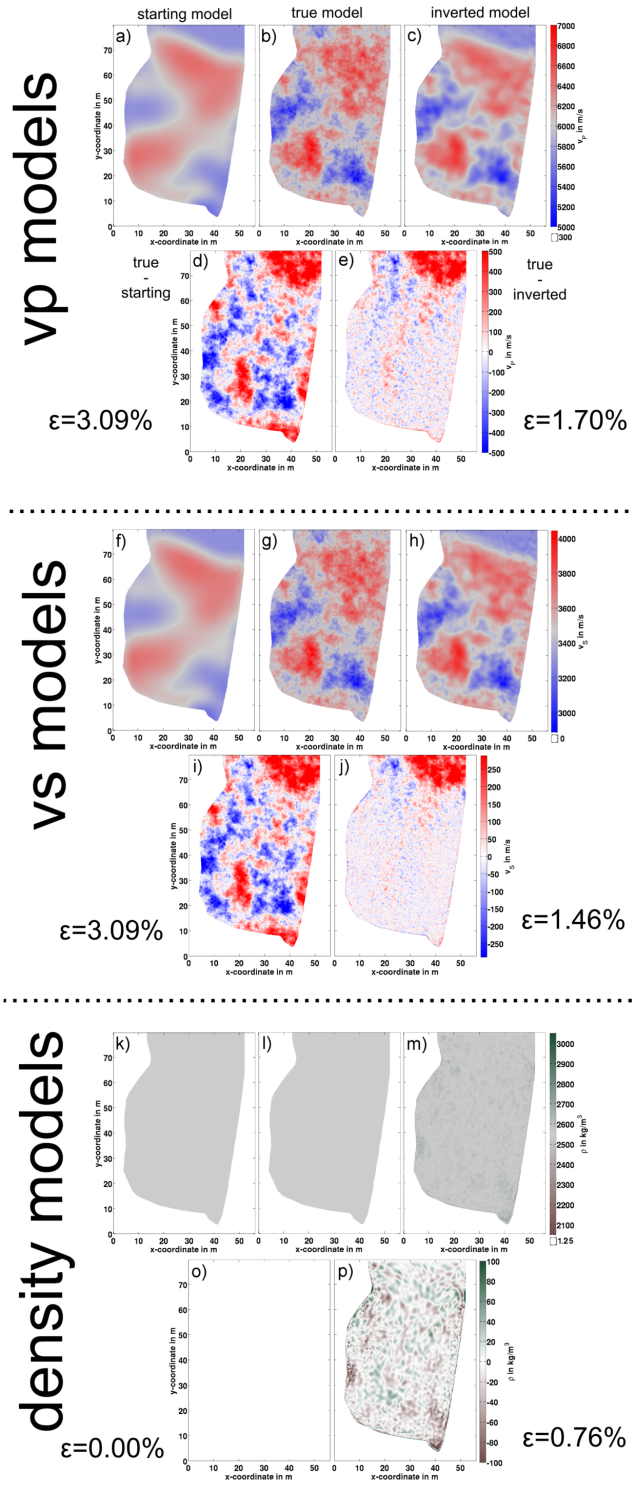

Figure 5.5: Reference inversion result for all three elastic parameters. From left to right in the first column, the starting model, the true model and the inversion result and in the second column the difference between true and starting model, respectively true and inverted model are shown for each parameter. The error ϵ of the starting and inverted model relative to the true model is calculated with Equation (5.1).

Table 5.4: Overview of the various synthetic inversion tests. TM and TW in the header means trace muting and time windowing, respectively. The parameters which we vary are highlighted with grey. The error value is colour-coded. The red star behind some figures indicates the model which is necessity always inverted with the same parameters. Further tests by not changing the inversion parameters itself but the starting and true model, respectively, can be found in Table 5.6

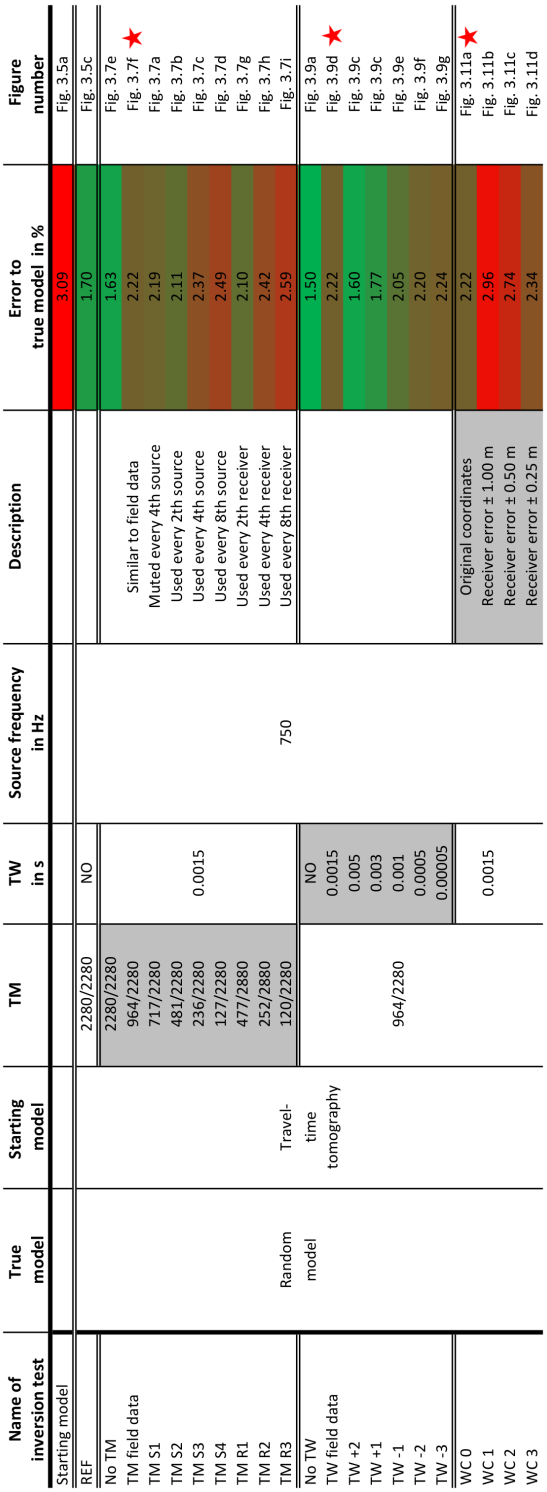

Name of inversion test	True model	Starting model	TM	TW in s	Source frequency in Hz	Description	Error to true model in %	Figure number
Starting model							3.09	Fig. 3.5a
REF			2280/2280	NO			1.70	Fig. 3.5c
No TM			2280/2280				1.63	Fig. 3.7e
TM field data			964/2280			Similar to field data	2.22	Fig. 3.7f ★
TM S1			717/2280			Muted every 4th source	2.19	Fig. 3.7a
TM S2			481/2280			Used every 2th source	2.11	Fig. 3.7b
TM S3			236/2280	0.0015		Used every 4th source	2.37	Fig. 3.7c
TM S4			127/2280			Used every 8th source	2.49	Fig. 3.7d
TM R1			477/2880			Used every 2th receiver	2.10	Fig. 3.7g
TM R2			252/2880			Used every 4th receiver	2.42	Fig. 3.7h
TM R3	Random model	Travel-time tomography	120/2280		750	Used every 8th receiver	2.59	Fig. 3.7i
No TW				NO			1.50	Fig. 3.9a
TW field data				0.0015			2.22	Fig. 3.9d ★
TW +2				0.005			1.60	Fig. 3.9c
TW +1				0.003			1.77	Fig. 3.9c
TW -1			964/2280	0.001			2.05	Fig. 3.9e
TW -2				0.0005			2.20	Fig. 3.9f
TW -3				0.00005			2.24	Fig. 3.9g
WC 0						Original coordinates	2.22	Fig. 3.11a ★
WC 1				0.0015		Receiver error ± 1.00 m	2.96	Fig. 3.11b
WC 2						Receiver error ± 0.50 m	2.74	Fig. 3.11c
WC 3						Receiver error ± 0.25 m	2.34	Fig. 3.11d

5.4.2 Source and Receiver Muting

In this section we want to investigate if the used number of sources and receivers are adequate for the geometry and what is the minimum number of traces for a satisfactorily inversion result. At best, such a study should be carried out prior to the measurement.
For the FWI for each source position a forward modelling and backward modelling must be calculated. Therefore, more receivers than sources are normally used because of the reduction of the computational time. In our measurement, all existing boreholes are equipped with receiver anchors. The maximum number of receivers is thus fixed to 30. The sources can be applied to the gallery walls around the block in an arbitrary position. 76 shot positions spaced almost equidistantly (spacing about 2 m) around the block, were recorded at total. By testing different combinations of less sources or fewer receivers, we want to investigate at which number the FWI is no longer able to reconstruct the true model. In addition, with this analysis, we want to test whether the number of sources or the number of receivers have an influence on the accuracy of the inverted model.
Since it does not make sense to use more sources and receivers as in the field survey, we limited the synthetic study by reducing the number of sources and receivers. At first, all sources and receivers are used (No TM). This is quite unrealistic, because, as described in Section 4.3.3, we cannot use all traces due to the used 2D code. The next inversion is the most realistic one by using the number of sources and receivers which we are going to use for the field data (TM field data). The next step is to mute every 4th and to use every 2nd, every 4th and every 8th source (TM S1 - TM S4) and just using every 2nd, every 4th and every 8th receiver (TM R1 - TM R3), respectively. In the most extreme cases (TM S4 and TM R3), only 10 of 76 shots and 3 of 30 receivers are left. The tests are summarised in Table 5.4 and visualised in Figure 5.6. For TM R1 / S2, TM R2 / S3 and TM R3 / S4, we almost used the same number of traces.

In Figure 5.7, all inversion results are plotted. The number of iterations varies for all tests. The colour scale is valid for all models. In the row in the middle, the inversion results for no trace muting (No TM) and for the trace muting as it will be performed in the field data is shown (Figure 5.7e and 5.7f). For no trace muting (No TM), we got by far the best resolution. For this case also tunnel surface wave have been inverted which are not yet clearly separated from the P-wave in time. The error to the true model was calculated to 1.63% and is, in contrast to the error of the starting model, very low (Table 5.4). It is even lower than the reference inversion. This shows the complexity of the inversion scheme. Even for synthetic tests, the resolution is not linear to the used traces. For the trace muting like we use it in the field data, we get a reasonable result, also the velocity perturbation inside the low and high velocity areas are not perfectly recovered. Nevertheless, in contrast to the starting model, the resolution was improved and the errors are reduced.
On the left row, the inversion results for neglecting specific sources are shown (TM S1 - S4). Also from Figure 5.7a - 5.7d, the number of used sources is decreasing dramatically, the inversion results looks very similar. For TM S1 and S2 the error between inverted model and true model are even a little bit smaller than for the TM field data. Again, the resolution within the low and high velocity areas is very well. In general the velocity models are comparable to similar trace muting as in the field data in Figure 5.7f. The computational cost decreases by approximately the ratio of the muted sources to the total number of sources. For S3 and S4 the error is getting higher even this is not clearly visible in the inversion result. In the right row (Figure 5.7g - 5.7i), the inversion results by using less receivers are

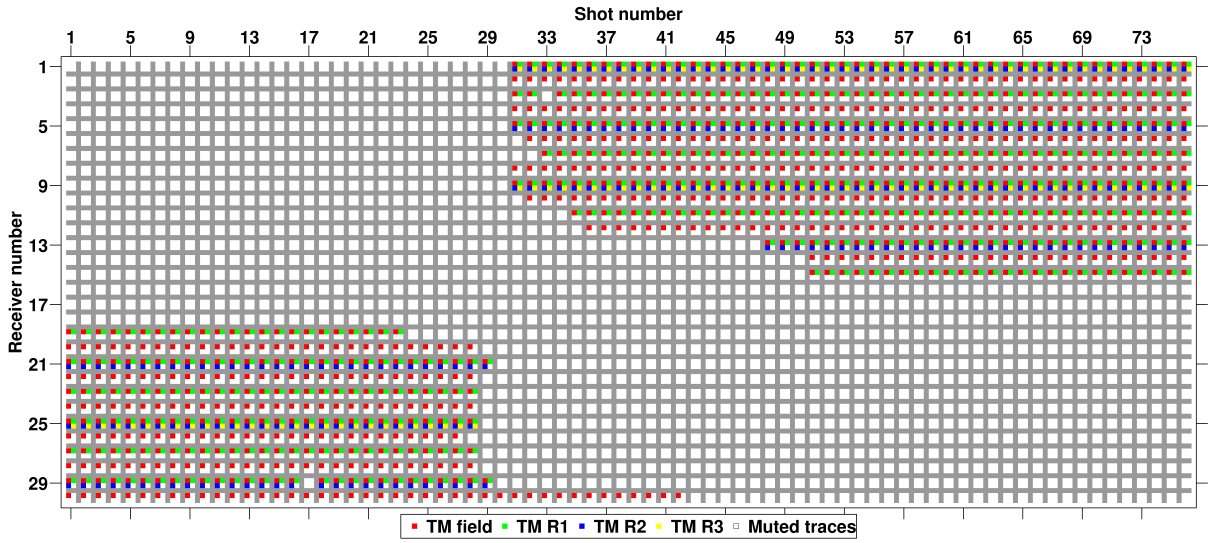

(a) TM field data, TM R1 - TM R3

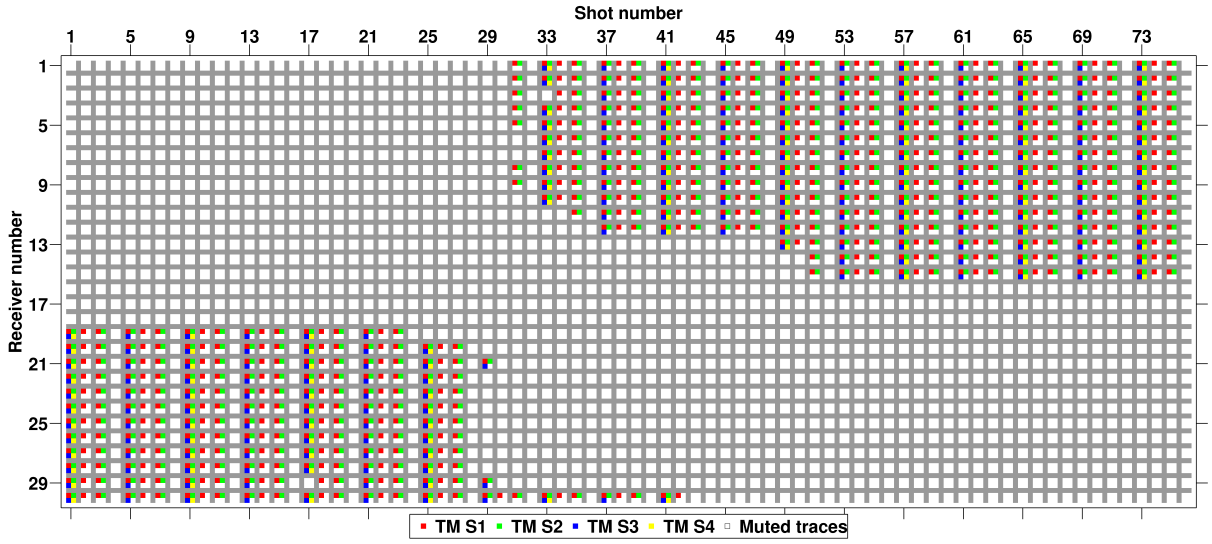

(b) TM S1 - TM S4

Figure 5.6: Colour-coded matrix for the various inversion tests. Each filled out element of the matrix represents one in the inversion used source-receiver pair. Empty elements are excluded a priori because of reasons described in Section 4.3.3. The overall number of used source-receiver pairs can be seen in Table 5.4.

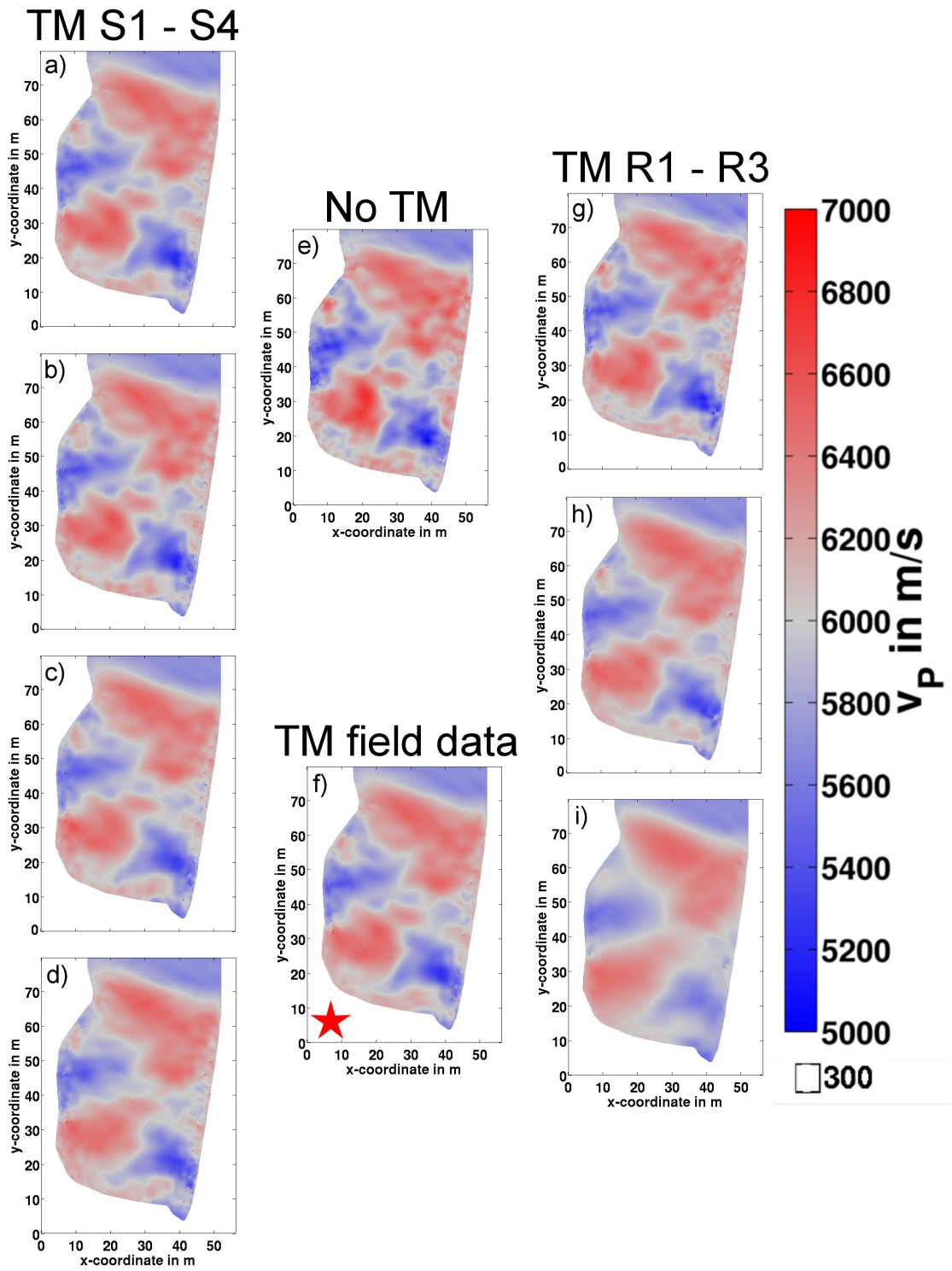

Figure 5.7: v_P inversion results for the trace muting analysis. The exact number of used traces and the corresponding error to the true random model can be found in Table 5.4. In order to have an optimum inversion result, for No TM all source and receiver combinations were used. In the inversion TM field data approximately those receivers and sources were used as we do in the field data inversion. For TM S1 -S4, the number of sources were reduced and for TM R1 -R3, the number of receivers respectively. The red star marks the model which could be rediscovered in the later analysis.

shown. In these tests, the resolution drops drastically for less used traces. Also for TM R1, the error is again smaller than for the TM field data. As mentioned above, the number of used traces for TM S4 and TM R3 is almost the same. Nevertheless, the resolution of the inverted velocity model differs.
In general, the number of used receivers is more importance than the number of sources. Using less sources but the same quantity of receivers has a smaller effect on the inversion result as vice versa. For the field measurement, the receiver and source number is sufficient for a reasonable result, also we should take care to use as much receivers as possible.

Also, the v_S model reacts similar as the v_P model, even though the resolution is not as good as for the v_P model. The density which was assumed to be known was left free in the inversion. The structures in the inverted density models have nothing common with the existing velocity structures. We will focus on the v_S and density inversion later on in Section 5.4.8.

5.4.3 Time Window Length

The length of the time window is an essential parameter for the inversion. As described in Section 4.3.3, we have to cut out a time window around the picked time of the first arrival because we only want to invert the first-arrival P-wave, as it is the most dominant phase. This also implies a simplification of the misfit function (Brossier et al., 2009). This approach is also very common in the FWI because converted phases in the later part of the seismograms are not considered in the inversion (Sheng et al., 2006; Zhang et al., 2012) and the inversion gets more stable (Pratt and Worthington, 1988). The used taper function, respectively time window is shown in Figure 4.11. The parameters of the time window are described in Section 5.3. We test different lengths of the time window and its influence on the inversion result. Afterwards we can state which length of the P-wave contributes most to the inversion accuracy. The aim is to use a window as short as possible, because otherwise the containing noise in the field data will contribute and have an impact on the results. Nevertheless, the length of the window must be adapted to the used frequency content of the source signal. It is assumed that for longer windows, the resolution will be improved in the synthetic case. The windows are symmetrical to the picked first-arrival time, since the source wavelet is zero-phase. γ (GAMMA) describes the steepness of the flanks is kept constant for all tests (Table 5.3).
We start with no time windowing (NO TW) and decrease the length of the taper until almost any more coefficients equals one occur. In Figure 5.8 one seismogram tapered with different time windows, the corresponding length of each time window where the taper coefficients are equals one and the picked first-arrival time for Shot 60 and Receiver 4 is shown. We named the tests with NO TW by using no time window, TW field data for the window length we were expecting to use in the field data inversion and TW +1 and TW +2, respectively TW -1 to TW -3 for longer and shorter time windows relative to TW field data. In Table 5.4, the corresponding lengths of the windows can be found. For the shortest time window the amplitude of the neighbouring side lobes is heavily truncated. This effect decreases for longer time windows. For all other synthetic studies, we use a time window of 0.015 s.
By using no time windowing we expect the best results in the synthetic tests. Nevertheless, this is not realistic because in contrast to the field data, no noise or other disturbances are present in the observed data.

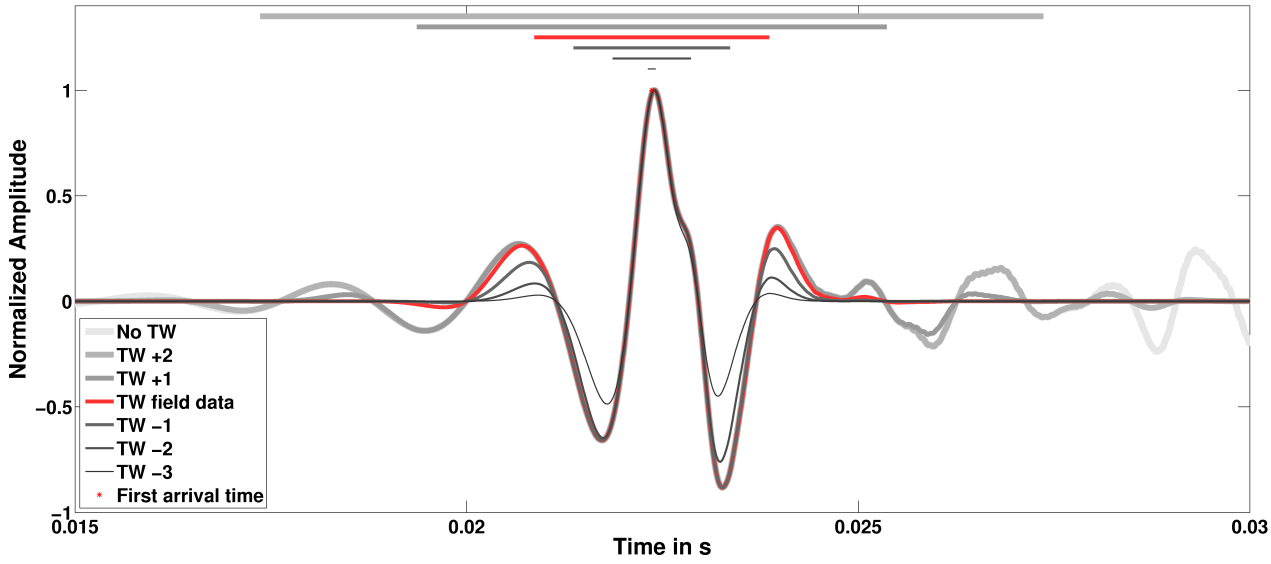

Figure 5.8: Seismogram of Shot 60 and Receiver 4 with different lengths of the time window. All traces are normalised. The exact value of the length of the window can be found in Table 5.4.

The global maximum and the first and second side lobe of the P-wave, which looks similar to the Klauder wavelet and which has the best signal to noise ratio, are almost not changed in its amplitude. After that, the amplitude is tapered by the taper function.

In Figure 5.9 the inversion results for the v_P model for the different length of the time window are shown. In Table 5.4 the error of the models relative to the true model can be found. As expected, the best resolution could be achieved by using no time window (Figure 5.9a). Many small velocity perturbations could be reconstructed within the low and high velocity zones. This is the best result relating to the calculated error ϵ we have achieved. Compared to the reference inversion (REF) the error relative to the true model gets smaller by using less sources and receivers. Again, this shows the high non-linearity of the inversion scheme. Also the two tests TW +2 and TW +1 (Figure 5.9b and 5.9c) show a very accurate reconstruction of the model. For the time window we aim to use for the field data, the resolution is less. The third side lobe is not used anymore. By shorten the window length (Figure 5.9e - 5.9g) we still get reasonable results which only differ in details, also the error for TW -1 is smaller. So, the main phase of the Klauder wavelet contains most of the information about the velocity distribution, since the phase also has the largest amplitude. However, the side lobes are also of importance for further details.
Also the S-phase is not directly included in the inversion because the first arrival of the S-wave is after the time window (Section 5.2) the v_S model is also well reconstructed for TW +2 and TW +1. This is first because some scattered and converted waves are within the time window and second the v_P model makes a footprint in the v_S model. For shorter time windows, the v_S model gets worse. We will focus on the influence of the v_S model in Section 5.4.8.
For the field data inversion, in contrast to our first suggestion, we choose a length of 0.001 s for the time window because first, the length provides a well reconstructed velocity distribution and second, we will use higher frequencies and, thus, more narrow wavelets.

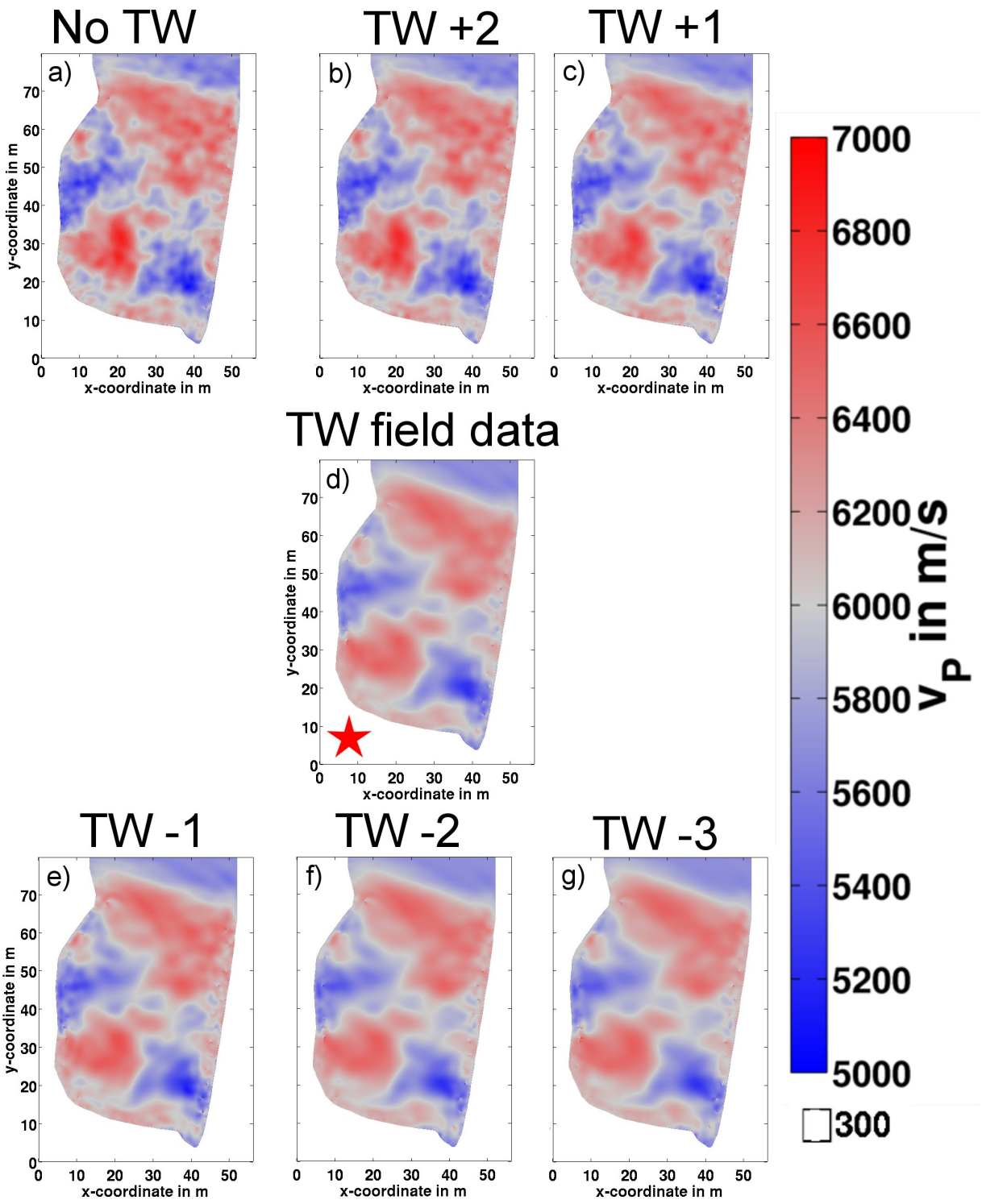

Figure 5.9: Inversion results with different lengths of the time window. The exact value of the length of the window can be found in Table 5.4. In a) the result without any time window is shown. In d) the length we want to consider in the inversion can be seen. TW + means a longer window and TW - a shorter window.

5.4.4 Impact of Wrong Coordinates

To investigate the influence of not precise coordinates in the field measurement, we tested different randomly misplaced receiver coordinates. As in nature the error is not systematically, we generated random numbers in different ranges, from ± 0.25 m, ± 0.5 m to ± 1 m. The random values are added to the x- and y-component of each receiver. In Figure 5.11, the deviation from the original receiver coordinates are shown for all 30 receivers. The colour-coded crosses at the centre indicate the standard deviation. As described in Section 3.3 we assume that the boreholes for the receiver anchors are drilled perpendicular to the host rock. With a 2 m long anchor, a deviation of 0.25 m leads to a variation of $\pm 7.13\,^{\circ}$ in the direction of the vertical axis which is quite small. So, the deviation values is a realistic guess for the error of the receiver coordinates. The coordinates of the sources have not been changed.

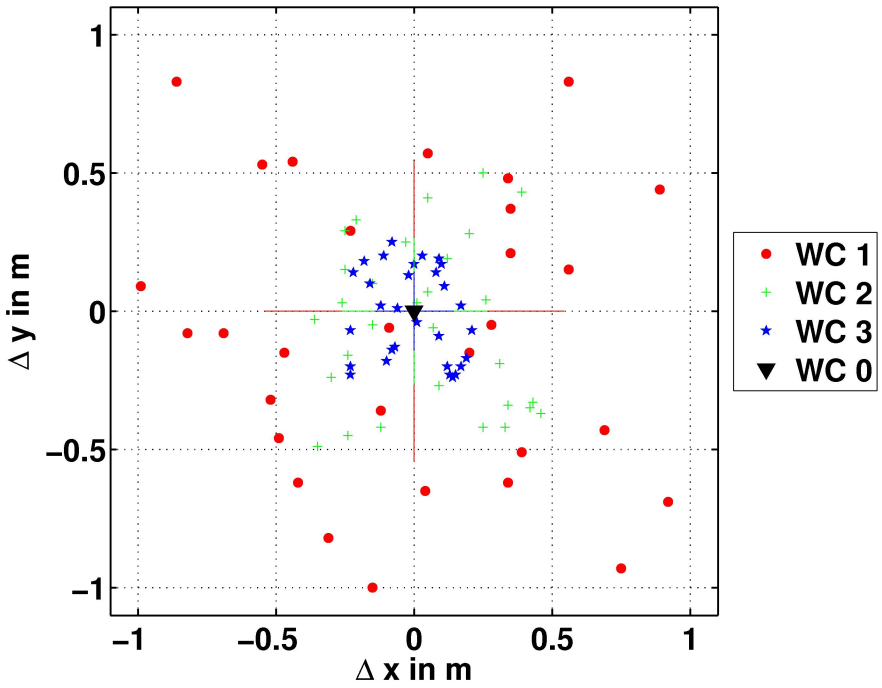

Figure 5.10: The deviation from the original receiver coordinates for the three tests WC 1 to WC 3 are shown. For all 30 receivers, a random number is added to its original x- and y-coordinate. The maximum deviation for WC 1 was ± 1 m, for WC 2 ± 0.5 m and for WC 3 ± 0.25 m. The colour-coded crosses at the centre indicate the standard deviation.

We want to compare the results of the inversion with the random model (Figure 5.1.1b). We used the low-pass filtered Klauder wavelet at a corner frequency of 750 Hz and as a starting model the smoothed version of the travel-time tomography model (Figure 5.2c). The spectra of the source signal is shown in Figure 4.3d. Assuming the corner frequency of the filter of 750 Hz of the source signal and $v_{\mathrm{P}} = 6000\,\mathrm{m/s}$, the wavelengths is 8 m. The ratio of the maximum coordinate deviation to the wavelength for the main frequency is in the range from 8 to 32.
Figure 5.11 shows the FWI result for the v_{P} model for the original coordinates and the three scenarios with added errors. In the inversion, the parameters from Table 5.3 are used for

the preprocessing. Compared to the true random model, the inversion with the original receiver coordinates is satisfactory (Figure 5.11). Almost no artefacts at the receivers occur. Also, the starting model already contains the low and high velocity zones, the inversion was able to reconstruct many details of the true model within the model. In the upper most part, the inversion did not update the model because of zero ray coverage. In Figure 5.11b to 5.11d, the inversion results for different wrong placed receiver coordinates are shown. In Figure 5.11b, the maximum deviation was ± 1 m. The inversion was not able to reconstruct any detail. Even the artefacts at the receivers are quite small compared to Figure 5.11b. This indicates, that the misfit between the observed data and modelled data could not be reduced significantly, because the random deviation of the receiver coordinates forces the model into the opposite direction. Almost the same happens in Figure 5.11c for Receivers with a deviation of ± 0.5 m. Here, the inversion creates strong artefacts at the receiver positions and only a small improvement of the velocity structure. In Figure 5.11d, the velocity structure is comparable to 5.11a with additional receiver artefacts. The errors relative to the true model can be found in Table 5.4.

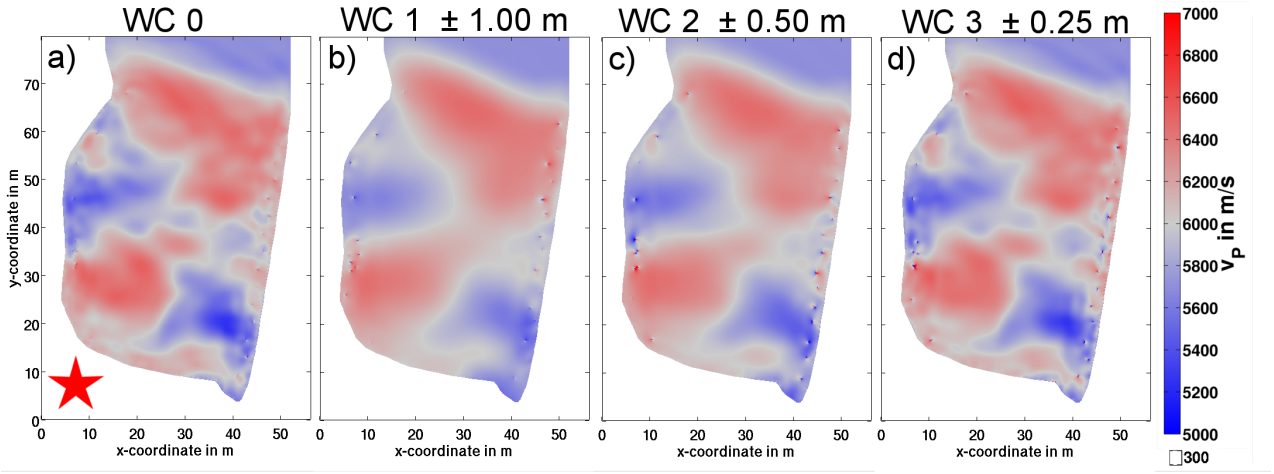

Figure 5.11: Inversion results for the v_P model for the different deviations of the receiver coordinates. The inversion parameter and the corresponding error can be found in Table 5.4.

In this study, we just investigated deviations of receiver coordinates, but, it is safe to say, that also the source coordinates will have a certain error. By reciprocity (Section 4.3.1), it is adequate to state the error only to one coordinate. If the cumulative errors of source and receiver coordinates is about 0.25 m at a wavelength of 8 m, the inversion can resolve the velocity structures, but artefacts at the source and receiver positions will arise. For a deviation of 0.5 m, the resolution is significantly reduced and furthermore, the inverted model shows mainly the structures of the starting model.

5.4.5 Resolution Study

In order to test which resolution could be achieved with the FWI, we performed several synthetic inversion tests with the synthetic checkerboard model (Rao et al., 2006). In this model only one well defined structure size is exists. By using the same acquisition geometry as in the previous tests, we first test different edge length, and second we alter the frequency

Table 5.5: Overview of the synthetic inversion tests with the checkerboard model. We vary the size of the checkerboard blocks by using a constant source frequency, increasing the source frequency by using a constant block size and vary the velocity perturbation. The parameters which are varied are highlighted with in grey. For these models, we do not state an error because the strong interfaces would tamper the relative error.

Name of inversion test	True model: Checkerboard size in m	True model: velocity perturbation in %	Starting model	Source frequency in Hz	Figure number
CB 1m	1	5.00	Homogeneous model	750	Fig 3.12a
CB 2m	2	5.00	Homogeneous model	750	Fig 3.12b
CB 4m	4	5.00	Homogeneous model	750	Fig 3.12c
CB 6m	6	5.00	Homogeneous model	750	Fig 3.12d
CB 8m	8	5.00	Homogeneous model	750	Fig 3.12e
CB 10m	10	5.00	Homogeneous model	750	Fig 3.12f
SF 400Hz	4	5.00	Homogeneous model	400	Fig 3.12g
SF 750Hz	4	5.00	Homogeneous model	750	Fig 3.12c
SF 1000Hz	4	5.00	Homogeneous model	1000	Fig 3.12h
SF 1250Hz	4	5.00	Homogeneous model	1250	Fig 3.12i
SF 1500Hz	4	5.00	Homogeneous model	1500	Fig 3.12j
VP 2.5%	4	2.50	Homogeneous model	750	Fig 3.12k
VP 5.0%	4	5.00	Homogeneous model	750	Fig 3.12c
VP 7.5%	4	7.50	Homogeneous model	750	Fig 3.12l
VP 10.0%	4	10.00	Homogeneous model	750	Fig 3.12m
VP 12.5%	4	12.50	Homogeneous model	750	Fig 3.12n
CB 2m SF 1500Hz	2	5.00	Homogeneous model	1500	Fig 3.12o

content of the source wavelet. Additionally, these studies give us a hint which parts of the model are well resolved and we can identify footprints of the geometry. The used velocity model for our investigations, the checkerboard model, is described in Section 5.1.1. Often, the perturbations are overlaid to a background velocity model (Zhao et al., 1992; Ghose et al., 1998), but to see the pure resolution, we just use the checkerboard pattern on a homogeneous model. The inversion parameters are summarised in Table 5.5. For these tests, we do not state an error because the strong interfaces would tamper the relative error. Also, the results can rather be assessed by eye much better than by the random model.

First, we vary the size of the squares of the checkerboard pattern in order to determine the smallest structure the FWI is able to invert. The length of the edges of the blocks are getting continuously smaller starting at 10 m, 8 m, 6 m, 4 m, 2 m to 1 m. All other parameters are kept constant for the inversion and are shown in Table 5.3 and 5.5. As the source wavelet we used the low-pass filtered version of the Klauder wavelet with a corner frequency of 750 Hz (Section 4.2.2). The starting model is a homogeneous velocity model with $v_\mathrm{P} = 6000\,\mathrm{m/s}$, the corresponding v_S model with $\frac{v_\mathrm{P}}{v_\mathrm{S}} = \sqrt{3}$ and a homogeneous density with $2550\,\mathrm{kg/m^3}$ which coincident with the true density. Assuming the homogeneous model, the wavelength of the source signal is 8 m.
In Figure 5.12a - 5.12f, the results for the six different block sizes can be seen from left to right (CB 1 m to CB 10 m). In Figure 5.12p, for comparison, the true checkerboard pattern with a block size of 4 m is shown. The colour scale is valid for all results without a colour scale in this section.

In general, due to the band limited frequency content of the source signal, the sharp edges of the checkerboard pattern could not be inverted as in the true models. For both, the pattern of CB 10 m and CB 8 m checkerboard models are very well resolved. Almost no artefacts at the receiver positions are noticeable. Only at the top end of the checkerboard, the squares could not be resolved as the geometry of sources and receivers do not allow this. Due to the neglected Receivers 16 - 19 at the bottom of the gneiss, we expect a higher sensitivity in the x-direction because of a lower ray coverage in the y-direction. Nevertheless, no significant resolution differences in the y-direction in contrast to the x- direction are observable. For smaller checkerboard pattern of 6 m (CB 6 m) and 4 m (CB 4 m), the pattern is still very good resolved. The size of the squares are already below the wavelength for an assumed frequency of 750 Hz but could still be recovered accurately. For the two smallest checkerboard pattern of 1 m and 2 m, the limitations in the resolution for the inversion is reached. For the 2 m model, the velocity structure near the gallery walls could be guessed, for the 1 m block size model, the inversion fails completely. This was not surprising, because the size of the checkerboard pattern is almost one magnitude smaller than the wavelength. Generally, the geometry has no visible specific footprint besides in the upper part of the model. In contrast to the *Richtstrecke*, the sources and receivers on the *Wilhelm Stehender Süd* are used until the upper end. This leads to a streaky sensitivity in the upper part.

A second study deals with the same topic but have a different approach. We take the model with the block size of 4 m and now vary the frequency content of the source. This study should show at which frequencies we can expect a sudden resolution. Later, this will help us in the interpretation of the inversion results of the field data inversion. We chose different corner frequencies for the low-pass filter of 400 Hz, 750 Hz, 1000 Hz, 1250 Hz and 1500 Hz with the knowledge of the frequency content of the field data (Section 4.4.1). For the first three wavelets, the spectra have already been shown in Figure 4.3, respectively. Again

assuming the velocity of the homogeneous starting model, the wavelength ranges from 15 m to 4 m. All other parameters for the inversion remain again constant. In Figure 5.12c and 5.12g - 5.12j, from top to bottom, the inversion results are shown (SF 400 Hz to SF 1500 Hz). In the SF 400 Hz inversion, the checkerboard pattern could only be recovered in parts. Again, due to the higher sensitivity at the gallery walls, the checkerboard pattern is immediately apparent in that area. In Figure 5.12h - 5.12j, only very small improvements of the pattern are visible. As a further test, we inverted the a checkerboard block size of 2 m with a filtered source wavelet with the corner frequency of 1500 Hz. As the 750 Hz wavelet was not able to reconstruct the checkerboard pattern, with higher frequencies it is possible, also the checkerboards are little blurred (Figure 5.12o).

The synthetic study shows the potential of the FWI related to the source frequency and the used geometry. With a source wavelet which was filtered with a low-pass filter with a corner frequency of 750 Hz the inversion was able to reconstruct a block size of 4 m. The wavelength of the source signal was 8 m. In the second test, the block size was set to 4 m and the source frequency varies. With a frequency of 400 Hz, the FWI succeeded only partly. Especially, the area in the middle of the block could only poorly reconstructed. With increasing frequencies, starting at 750 Hz, the results were satisfactory. From 1000 Hz, with the naked eye no more differences can be observed.

5.4.6 Importance of the Starting Model

In this section, we will show the importance of an accurate starting model and will illustrate the limits. In the previous section we used a homogeneous starting model which was able to invert the checkerboard models with a velocity perturbation of 5 % and a frequency of source wavelet of 750 Hz up to an edge length of 4 m. Now, we want to light up the issue of choosing an accurate starting model with a different approach. We will change the true model and not the starting model. We will again use the checkerboard model with a block size of 4 m but with different velocity perturbations. We will increase the perturbation from 2.5 % to 12.5 % which is effectively a velocity perturbation of $\pm 150\,\mathrm{m/s}$ to $\pm 750\,\mathrm{m/s}$. That means, not the structure of the model is changed, but the absolute velocity deviation of the true model to the starting model. This has an effect on the waveforms, especially the reflections on the edges of the blocks are getting stronger and the information of the model is found in the coda after the first-arrival P-wave. Due to the chosen time window which is quite short, we expect a loss in resolution for high perturbation values because the coda is truncated. In Table 5.5, the parameters are summarised. In Figure 5.12c and 5.12k - 5.12n the inversion results for different velocity perturbation are shown (VP 2.5 % to VP 12.5 %). The colour scales correspond to the minimum and maximum values of the true model. With 2.5 % and 5 % velocity perturbation in contrast to the homogeneous starting model, the checkerboard pattern could be well recovered. Starting at 7.5 % the resolution of the absolute values and of the pattern is getting worse. For 12.5 % which means a velocities range of $\pm 750\,\mathrm{m/s}$ referring to the starting model, the model is only reconstructed at the gallery walls due to the higher sensitivity in this area. In general, the checkerboard is not recognisable. So, with the used frequency of 750 Hz, the maximum velocity perturbation for the used geometry could be $\pm 450\,\mathrm{m/s}$.

In the introduction of Section 5.4, the random model is compared to the starting model. This should give us a hint, how accurate the starting model is. Also the minimum and maximum

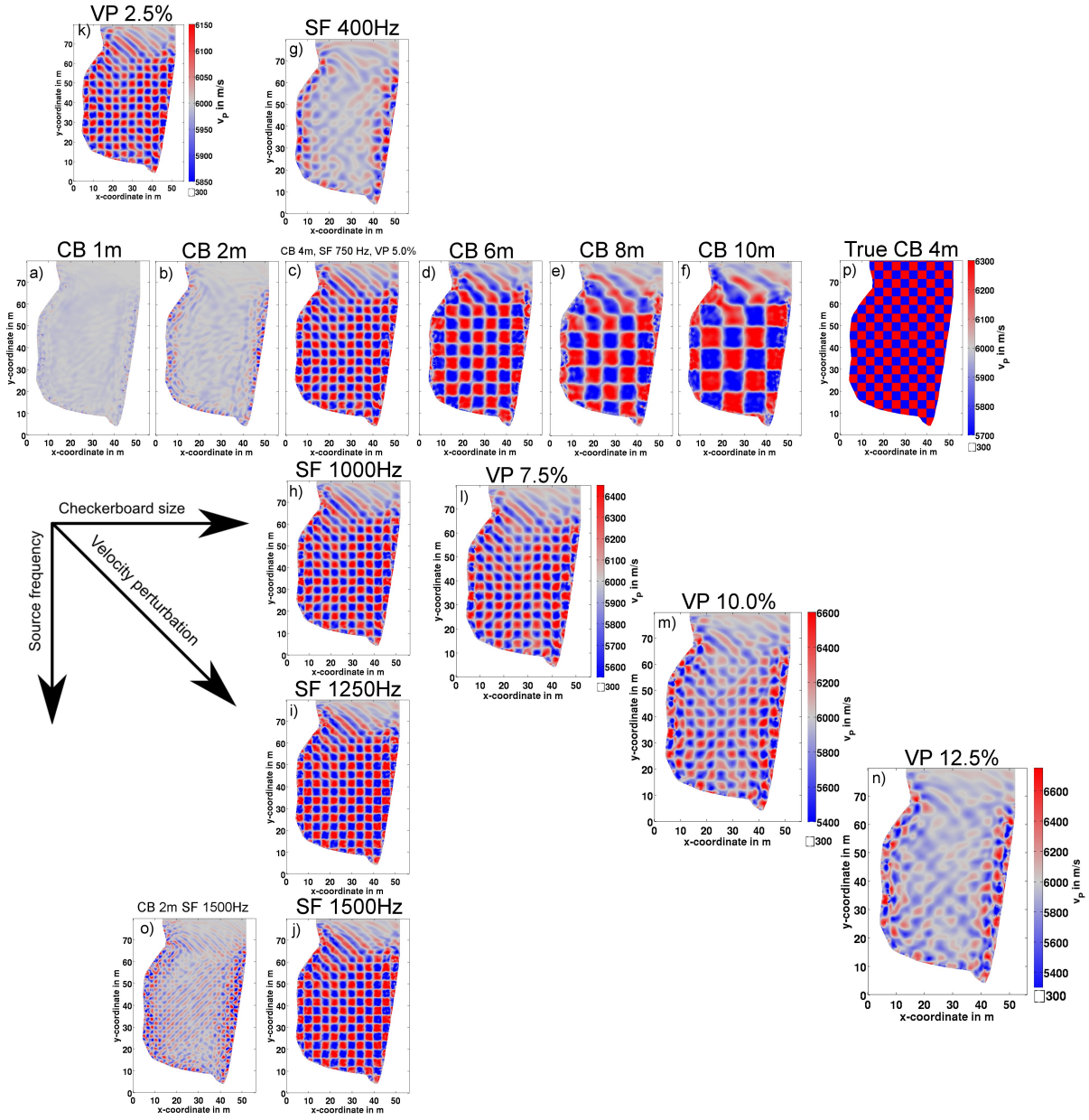

Figure 5.12: Inversion results for the v_{P} model for all tests carried out with the checkerboard model. The colour scale in p) corresponds to all models without colour scales. The three arrows indicate the direction of the various tests. All inversion parameters can be found in Table 5.3 and 5.5.

difference value is smaller and greater, respectively, than $\pm 450\,\mathrm{m/s}$, the mean values are much smaller in the range of 2.5 %. That means, the starting model is accurate for the FWI in terms of the velocity perturbations. We also expect such a maximum perturbation for the field data.
As we will see in the next chapter, this study strongly depends on the used frequency of the source wavelet.

5.4.7 Multi-Scale Approach - Frequency Filtering

In the previous section, we have referred how accurate the starting model has to be and how big the maximum absolute deviations may be with the synthetic checkerboard model, respectively. In this test, we return to the more realistic random distributed velocity model (Figure 5.13b) and demonstrate an approach, the so called multi-scale inversion, that is widely-used to reduce the ambiguities of the FWI (Bunks et al., 1995). It is used, if the starting model is not able to explain the full frequency content of the data at once. The misfit function of the inversion gets therefore very complex and the inversion will not find the global minimum. Also it can avoid cycle-skipping.
If we apply the multi-scale inversion, the FWI starts with low frequencies and further on, more and more high frequency content of the data is added. Due to the low frequency content at the beginning, the complexity of misfit function can be simplified. With this approach we can avoid local minimum in which the inversion would otherwise has ended. In contrast to an inversion in the frequency domain where also single frequencies could be inverted, in the time-domain we automatically have the whole range of frequencies beginning from the lowest to the corner frequency of the low-pass filter (Brossier et al., 2009; Sourbier et al., 2009). To demonstrate this approach, we no longer use the travel-time tomography as the starting model but a homogeneous model (Figure 5.13a). In contrast to the other tests, for the source frequency we chose 1500 Hz. Both, the worse starting model as well as the higher frequencies for the source contribute to a more complex misfit function and makes it harder for the inversion not to get stuck in a local minimum.
If we proceed as in the previous tests, that means, we do not apply a multi-scale approach, the inversion fails (MS 0, Figure 5.13c). The general high and low velocity areas are somehow reconstructed but the detailed structure as well as the absolute velocities are missing or are wrong, respectively. The shape of the misfit functions must be very complex and the inversion starts at an unfavourable point and is trapped in a local minimum, respectively. However, after applying the multi-scale approach by starting at 500 Hz and increasing the frequency of the data in steps of 100 Hz to 1500 Hz, the inversion could find a path in a deeper minimum and the model could be reconstructed satisfactorily (MS 1, Figure 5.13d). Most of the structures and also the absolute velocity values are much better resolved as in MS 0. In Table 5.6, the error of both inversion results relative to the true model is shown. The error of the inversion result of MS 0 is even higher than for the travel-time tomography. As we use higher frequencies, the error for MS 1 is also even smaller than the best result so far.
For all former analysis, this approach was not necessary because we had an accurate starting model, respectively we do not use such a large frequency band for tests with the random model. Therefore, as the individual misfit values have no meaning, we do not interpret them. According to the mathematical concept, the curve has to decrease. By adding gradually new data, i. e., adding new information into the inversion scheme, also the shape of the misfit

Table 5.6: Overview of the various synthetic inversion tests by applying a different inversion strategy (MS) and changing the starting and true model, respectively (VS and DENS). The error value is colour-coded and only comparable for the VS and DENS tests. The red star behind some figures indicates the model which is necessity always inverted with the same parameters.

Name of inversion test	True model vp	True model vs	True model density in kg/m³	Poisson ratio	Starting model vp	Starting model vs	density in kg/m³	Source frequency in Hz	Error to true model in %	Figure number
MS 0	Random model	Random model	2550	0.250	Homogeneous model		2550	1500	3.24	Fig 3.13c
MS 1									1.95	Fig 3.13d
VS -3	Random model	vp / 1.56		0.150	Traveltime tomography			750	2.85	Fig 3.14i
VS -2		vp / 1.63		0.200					2.24	
VS -1		vp / 1.67		0.225					2.37	
VS 0		vp / 1.73		0.250					2.22	
VS +1		vp / 1.80		0.275					2.07	
VS +2		vp / 1.87		0.300					2.37	
VS +3		vp / 2.08		0.350					2.85	
DENS -3		Random model		0.250			2100		2.20	Fig 3.15e
DENS -2							2250		2.22	
DENS -1							2400		2.22	
DENS 0							2550		2.22	
DENS +1							2700		2.21	
DENS +2							2850		2.07	
DENS +3							3000		2.20	

curve is changing. We forced the inversion to change the frequency band not before 10 iterations per frequency. This leads to a stable inversion scheme. The frequency is changed if the inversion could not found a proper step length for updating the model or after the model has not changed by 0.01 % referring to the second to last one.
In Figure 5.14 the shape of the misfits for both tests is shown (MS 0 and MS 1). The misfits are normalised together to the highest occurring value. For the test MS 0, the misfit decreases until iteration 20. Afterwards the inversion could not update the model to reduce the misfit. The inversion is trapped in a local minimum. The misfit curve of MS 1 is separated into the different frequencies. Generally the misfit starts in contrast to MS 0 at a smaller value because of the lower frequencies. Also within a frequency band, the misfit is increasing. This is because we only use three test shots for the estimation of the step length as explained in Section 2.3.4. At some point, the misfit is reduced for the three shots but increased for all shots. Most of the time, afterwards the misfit decreased again. So, this is not crucial. After adding more data to the inversion, the misfit is always getting little higher. This is because new information is added to the data and is not yet explained by the model. At a frequency of 600 Hz, the inversion could reduce the misfit most. At 1000 Hz, the misfit is only decreasing very slowly and most of the data is already explained by the current velocity model. The occurring peaks at iteration 78 and 184 are due to a not accurate estimated step length but do not affect the inversion in general. After 211 iterations at the maximum frequency of 1500 Hz, the inversion was not able to minimise the misfit anymore and stops. As an increment we chose 100 Hz, from 500 Hz to 1500 Hz. One the one hand by choosing a smaller increment, we expect an even better convergence but also more iterations which leads to a higher computational time. On the other hand, if the step between two frequencies is too large, the misfit could become too complex and the inversion will fail. A guideline for choosing optimal frequency bands is proposed by Sirgue and Pratt (2004). As in DENISE only a linear frequency stepping is implemented, we could not test the proposed strategy.

The multi-scale inversion approach can also be applied automatically. In the field data, however, in a not synthetic case, we have to do a quality check after each frequency range.

5.4.8 Role of v_S and the Density

First we want to consider the influence of a wrong v_P to v_S ration for the starting model to the inversion results, by changing the v_S model. In the previous analysis, the v_P to v_S ratio for both, the starting and the true velocity models was equal $\sqrt{3}$ which corresponds to a the Poisson ratio of $\sigma_P = 0.25$. For sub-crustal rocks the ratio vary between 0.25 and 0.3 (Shearer, 1999). With the relation from Aki and Richards (2002)

$$\frac{v_P}{v_S} = \left[\frac{2(1-\sigma_P)}{1-2\sigma_P}\right]^{\frac{1}{2}} \tag{5.2}$$

we calculate the v_P to v_S ratio for different Poisson ratio from 0.15 to 0.35 (Table 5.7). Since we cannot be sure how the value of the ratio really is for the field data, in the following analysis, we vary the ratio for the true models and kept it constant throughout the entire gneiss (Figure 5.15d and 5.15f). The starting model remains the same with the common v_P to v_S ratio of $\sqrt{3}$, as nothing else is known for the field data (Figure 5.15a and 5.15b). Please note the extended range of the colour scales for v_S. We consider the impact of the wrong v_P

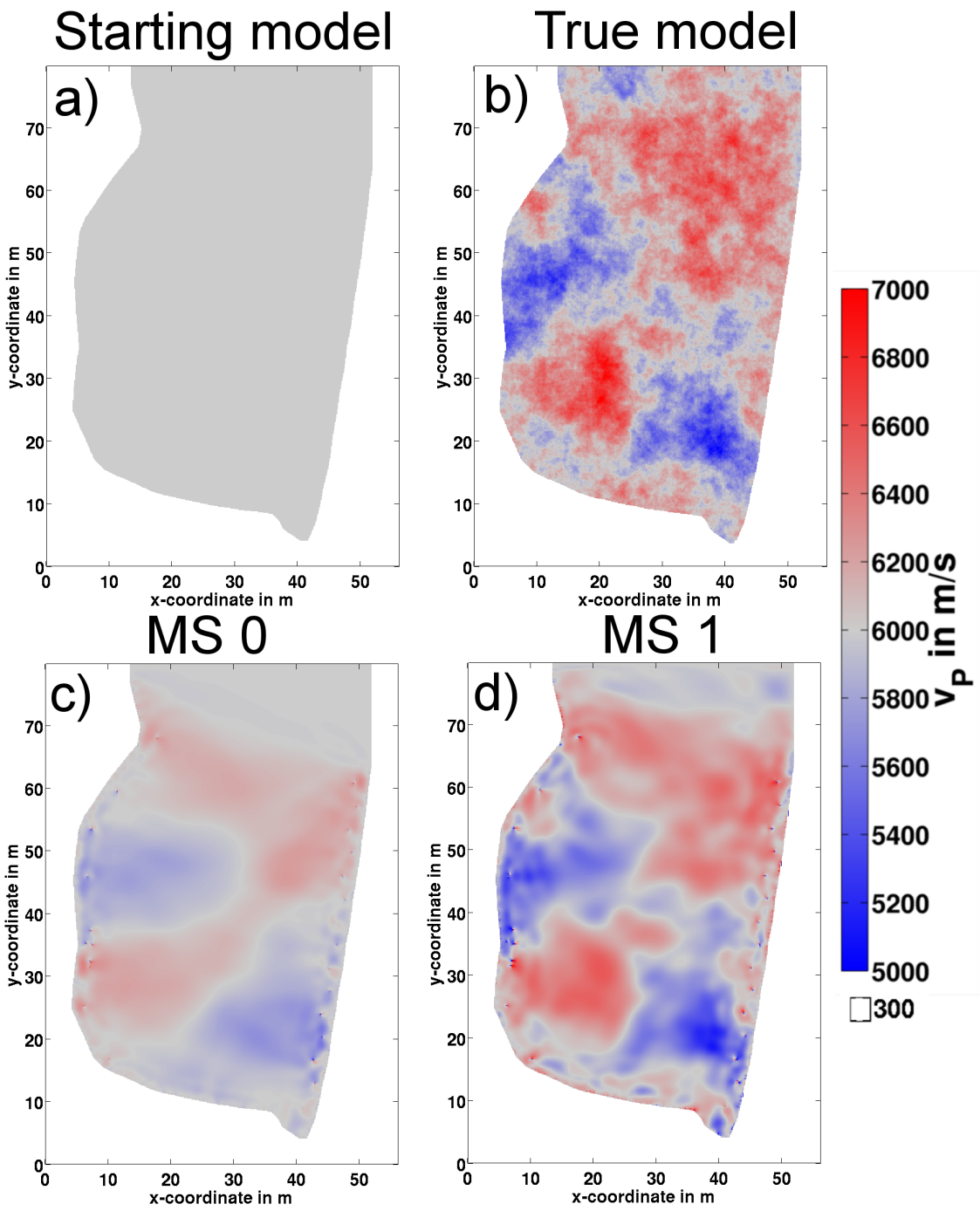

Figure 5.13: Starting, true and inverted v_P models for two different strategies. For this analysis, the starting model in a) was chosen homogeneous. In b), the true model is shown. For the inversion result in c), the entire frequency content was inverted at once. For the velocity model in d) which is very well resolved, we started with low frequencies and increased the bandwidth. The errors of both approaches relative to the true model can be found in Table 5.6.

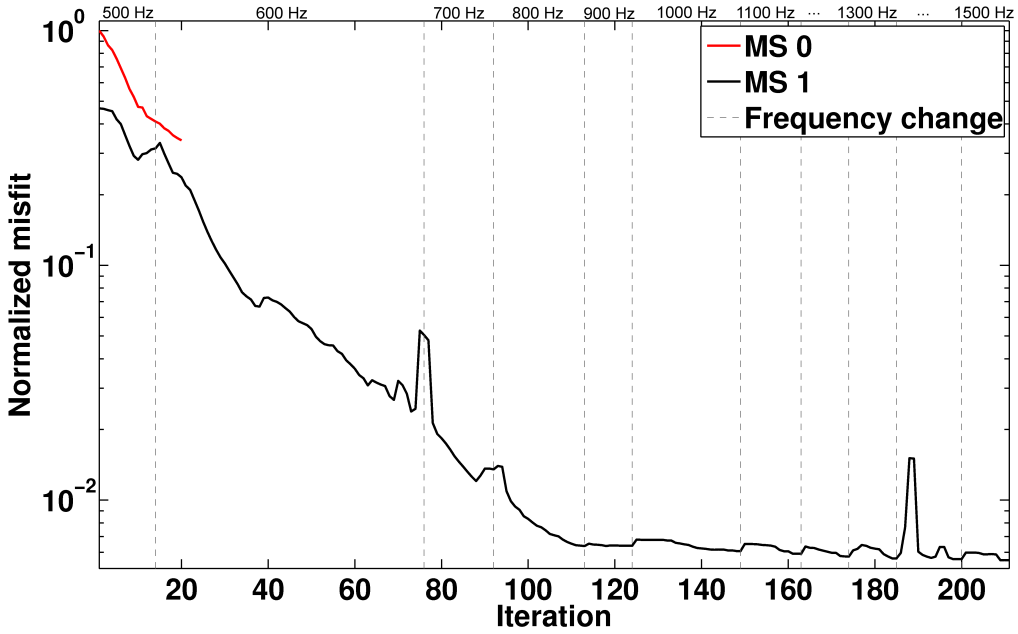

Figure 5.14: The curve of the misfit for both inversions are shown. The black line is for MS 0 and the red for MS 1. The amplitude is normalised together to its maximum value. The frequency jumps are only valid for MS 1.

to v_S ratio of the starting model on the inversion results. Primarily we want to investigate the influence on the v_P models. The density is assumed to be known. The influence of a wrong starting model for the density is systematically investigated in the next part. All further parameters for the inversion can be found in Table 5.3 and 5.6.

Table 5.7: The name of the inversion tests, the Poission ratio σ_P and the corresponding v_P to v_S ratio.

Name	VS -3	VS -2	VS -1	VS 0	VS +1	VS +2	VS +3
Poisson ratio σ_P	0.15	0.2	0.225	0.25	0.275	0.3	0.35
v_P/v_S ratio	1.53	1.63	1.67	$\sqrt{3} = 1.73$	1.80	1.87	2.08

The inversion results for the v_P and v_S models are shown in Figure 5.15h and 5.15i and the ratio of both can be seen Figure 5.15g. For a better visual comparison, the difference model between true and the inverted models are shown. In Figure 5.15c, the difference between true and starting model for the v_P model is shown to rate the inversion results more easily. For VS 0, the correct v_P to v_S ratio of the starting models was chosen. Here, the v_P as well as the v_S model are well recovered. This was expected and already shown in several tests before. Compared to Figure 5.15c, the velocity residuals of the v_P model are much smaller in its extension and in its absolute values. In Figure 5.15g, also the inverted v_P to v_S ratio has approximately the right value and is relatively homogeneous. For smaller ratios like VS -1 or VS -2, the difference v_P models are relatively constant, for the v_S models, the resolution gets worse. Also, the value of the v_P to v_S ratio is well resolved and fits to the true ratio. For VS -3 the inversion result for the v_S model is very poor, also the v_P model is bad resolved. This leads to a high error value of 2.85% (Table 5.6). Having larger v_P to v_S ratio values, the picture is nearly the same. Again the v_P model for VS +1 and VS +2 differs only little from

VS 0 and for VS +3, the inversion result is comparable to VS -3. Even for VS +1, the error is less than for the true Poission ratio. Again, this shows us the dependency and the influence of the elastic parameters from each other. For the v_S inversion, the picture is different. The inversion already failed to reconstruct the v_S model for VS +2 and also for VS +3. This can be emphasised by the v_P to v_S ratio. The values for VS +2 and VS +3 have nothing in common with the true values.
For the field data we will use the common ratio for the Poisson ratio of 0.25. The true ratio could change by ± 0.05 without major reductions of the resolution for the v_P model. We will further have look at the v_P to v_S ratio relating to its homogeneity.

For all previous synthetic test a homogeneous distribution of the density with a value of 2550 kg/m^3 was assumed to be known, but left free in the inversion. The FWI could update the density values as it likes. Now, in the second part, the influence of different starting models for the density on the inversion result is considered. Kopf et al. (2008) determined a density of 2550 kg/m^3 for the gneiss. However, this is just one density value for the whole gneiss block and could be vary within the observed area. The true model for the density remains at 2550 kg/m^3 (Figure 5.16a) and the already known random distributed v_P and v_S models are used (Figure 5.16c and 5.16f). In contrast to the v_S tests in the first part, we modify the starting density value. The density is increased from 2100 kg/m^3 to 3000 kg/m^3 in steps of 150 kg/m^3 (DENS -3 to DENS +3). For the v_P models, the starting model was obtained with a travel-time tomography shown in Figure 5.16d (Section 5.1.2). The parameters for the inversion are summarised in Table 5.3 and 5.6.

The inverted v_P and v_S models are, as a first approximation, very similar for all inversions, both for the true density as well as for all other densities (Figure 5.16e and 5.16h). Therefore only the inversion result for DENS 0 is shown. The errors to the v_P true model are listed in Table 5.6 and remain almost the same. The resolution is the same as for previous tests. If we now subtract the used starting model for the density and the inverted density model, the resulting model is the same for all different starting models (Figure 5.16b). The absolute values of the inverted models for the density differ, but this is only the case because of the various starting models. It appears, that the absolute values for the density do not play any role, only the inserted structures are of importance for the inversion. However, most of the structures are mainly at the edges and have nothing in common to the structures in the velocity model. Köhn (2011) also investigated that the density inversion is completely independent of the velocity inversion.

The inversion approach as we use it is inverting the whole waveform that means phase and amplitude. As we normalise the amplitude both, for the observed as well as for the synthetic data trace by trace, only the amplitude decay within one trace is considered. The amplitude information between different traces is neglected. Due to the short used time window, mainly the main phase with the dominant amplitude of the waveform is inverted. Obviously, the influence of the density model on the phase of the waveforms must be rather small because the inversion results are similar and do not depend on the starting density model (Köhn, 2011). Nevertheless, we will have a close look at the density in the field data inversion.

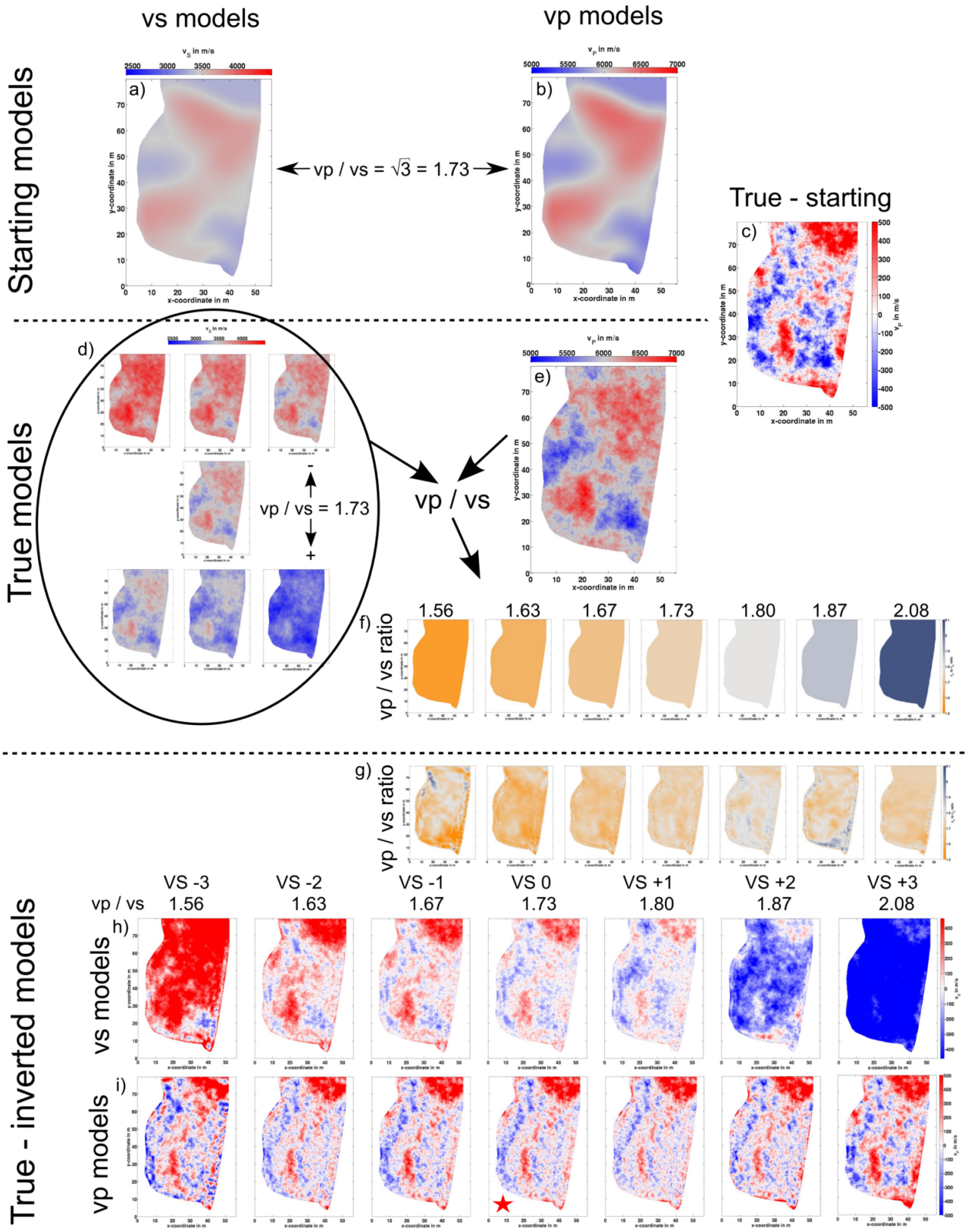

Figure 5.15: Overview of the starting, true and difference models for v_P and v_S between true and inverted models for different Poission ratios. The error of the inverted v_P models relative to the true model could be found in Table 5.6.

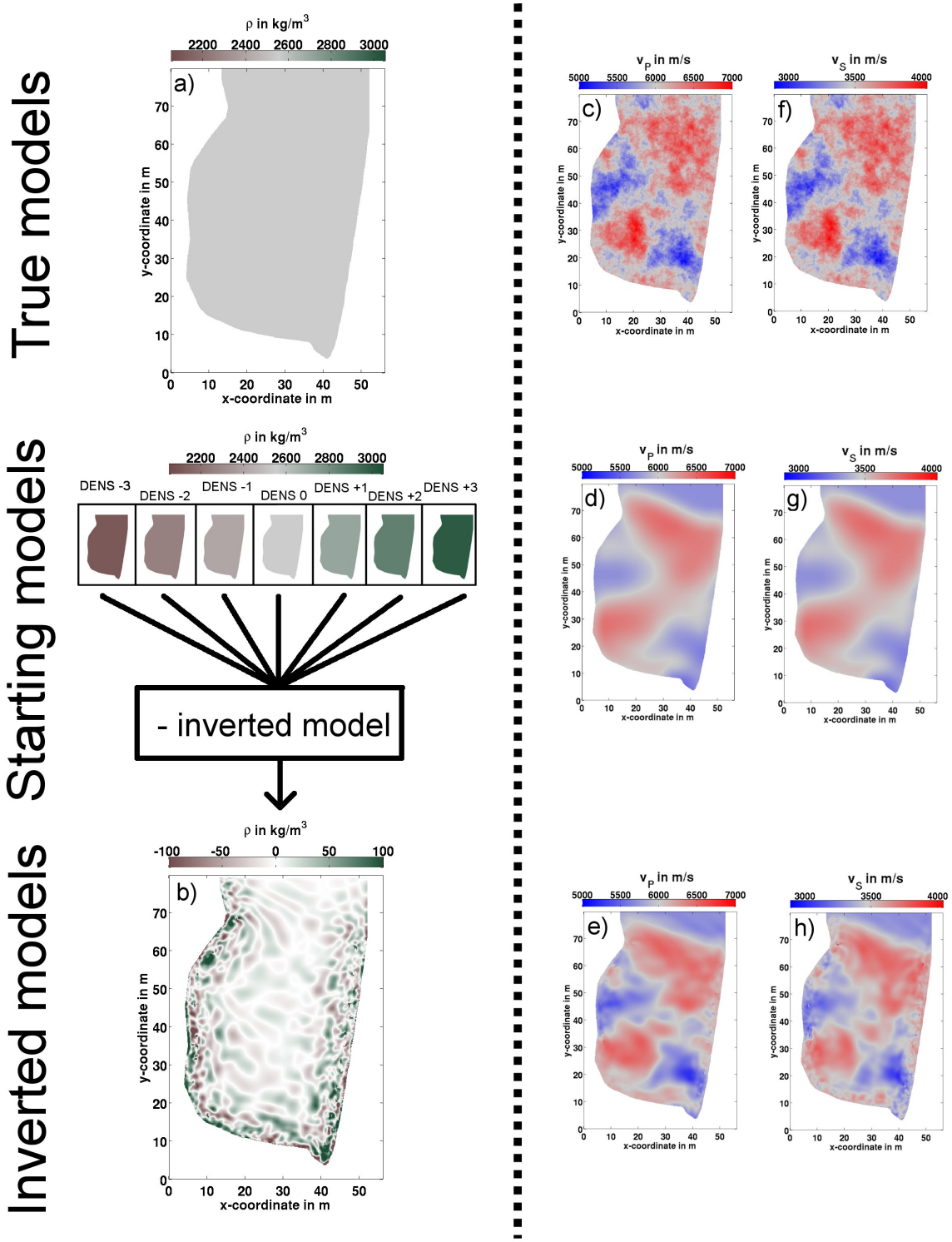

Figure 5.16: Overview of the starting, true and inverted models for all three elastic parameters. Also only the inverted v_P and v_S models for DENS 0 are shown, the error for all v_P models relative to the true model can be found in Table 5.6. The inversion does not depend on the density for this setup. The difference between the starting and the inverted density in b) is almost the same for all tests.

5.5 3D vs 2D: Semblance Analysis

Since now, we used a 2D modelling and inversion code. However, the recorded data itself has 3D characteristics, although the geometry in the measurement is 2D. Thus, as described in Section 4.3.4, the data is transformed with a 3D/2D transformation to simulate a line source, which corresponds to the 2D modelling scheme. For synthetic data which is modelled with a 2.5D velocity model with a 3D code, the transformation works very well (Figure 4.12). Also the inversion result for the 3D/2D transformed data is nearly the same compared to true 2D synthetic data.
In reality, however, we do not have a 2.5D model where the gallery walls are extended in the third dimension (Figure 4.8). In contrast, we have rectangular three dimensional galleries. By calculating the observed data with the 3D velocity model with the 3D code and applying a 3D/2D transformation afterwards, the inversion fails. We think, this is mainly because of the different reflection characteristics of the gallery walls. On the one hand, all seismic energy is reflected (2.5D model), on the other hand, only a small part of the energy is reflected (3D) (Figure 4.8). The inversion is not able to handle this discrepancy. This is a crucial point, because the field data should be most comparable to the 3D modelled data. Therefore, the 3D/2D transformation is not sufficient. Definitely, we have to take very much care about the different reflection characteristics of the different models.
To investigate the characteristics of the reflection in more detail, we have to find a strategy to evaluate how big the reflections from the gallery walls are. Similar to the field data (Section 4.4.3), we perform a semblance analysis for different scenarios for the synthetic data and compare the results with the field data. Five different scenarios are considered with the random velocity model (Table 5.8). In the first scenario (SEM 1) we use a 2D model with galleries like in all previous synthetic tests. In the second scenario (SEM 2) we do not include the gallery walls. These two models are pure 2D models and are modelled with the 2D code. The third, respectively fourth scenario (SEM 3 and SEM 4) consists of a 2.5D model without and with plane gallery walls perpendicular to the propagation plane. In the last scenario (SEM 5) we simulate a real 3D model with three dimensional rectangular galleries. Although the velocity model is not the same for the synthetic scenarios and for the field data, respectively, the influence of the velocity distribution is negligible in contrast to the occurring ghost reflections at the gallery walls.

Table 5.8: Overview over the various scenarios. The 2.5D model means, that the model is extracted in the third dimension without changing the model properties.

Scenario	Model	Galleries	Used Code
SEM 1	2D	no	2D
SEM 2	2D	yes	2D
SEM 3	2.5D	no	3D
SEM 4	2.5D	yes - planar plane	3D
SEM 5	3D	yes - rectangular galleries	3D

For all scenarios we consider the semblance analysis for the first-arrival P-wave. The data is preprocessed similar to the field data. We used Equation (4.4) for calculating the semblance value. We also investigate, like we did with the field data, the influence of different frequencies. The data was modelled with a source wavelet which was filtered with

a low-pass filter with a corner frequency of 750 Hz. Anyhow, we have a close look at the unfiltered data, data filtered with 750 Hz and 400 Hz in order to have a better comparison with the field data.

In Figure 5.17, the semblance for the five different scenarios (columns) and for three different frequencies (rows) in the CRG domain are shown. Scenario SEM 1 and SEM 3 and scenario SEM 2 and SEM 4 have exactly the same semblance values. As described before, with the 3D/2D transformation we can invert the data from SEM 4 and get almost the same inversion result as for the data of SEM 2.

Again, the two most important areas for all plots are in the left upper and right lower part. For these seismograms, most of the shots and receivers are close to each other and on the same side of the investigated gneiss block. Also, in these parts the total number of correlations is much higher for nearby shots and receivers. For some shot and receiver combinations, no semblance could be calculated due to muted traces or the semblance value is below 0.4.

In SEM 1 and SEM 3, with the 2D / 2.5D model with no galleries, no ghost reflections from the rock-air interface are observable because no interfaces exist (Figure 5.17a, 5.17d and 5.17g). The seismic waves are travelling straight through the media. This results in a very high and similar summed up semblance value for all frequencies. In SEM 2 and SEM 4, with the 2D / 2.5D model with planar planes perpendicular to the acquisition plane, the checkerboard pattern is very clear observable for R1 - R15 for the original data (Figure 5.17b). Also R25, which has a different depth in contrast to its neighbouring receivers, the different waveforms and different semblance values, respectively, stick out of the matrix. This effect is reduced for lower frequencies but still observable in the data. Also the waveforms for Receiver 25 fits better to its direct neighbours (Figure 5.17e and 5.17f). For the 3D model with rectangular galleries (SEM 5, Figure 5.17c, 5.17f and 5.17i), the checkerboard pattern is also obvious but not that dominant as in Figure 5.17b for all frequencies. So, the rectangular galleries reduce the ghost reflection effect because not all of the seismic energy is reflected. Especially for lower frequencies the waveforms are very similar on both sides of the gneiss block. To quantify the results, for all models and frequencies the sum and the maximum possible sum is written in the title.
In Figure 5.18 three seismograms of the synthetic data for SEM 1, SEM 2 and SEM 5 for two neighbouring receivers (R4 and R5, Figure 3.6) with two different frequency ranges are shown. The data is preprocessed as described before and the amplitude is normalised for each trace separately, but not filtered in Figure 5.18a and filtered with 400 Hz in Figure 5.18b. The source was directly on the opposite site of the gallery in a transmission geometry (SP60, Figure 3.6). The two receivers are drilled in the host rock with different depths: Receiver 4 is drilled with a depth of 1 m and Receiver 5 with a depth of 2 m.
For the original, respectively not filtered data, the grey seismograms modelled with no galleries are almost identical with only a small time shift which is not considered in the semblance analysis. In contrast, the seismograms with a planar plane or the rectangular galleries differ from each other. For both, the ghost reflections lead to a second positive peak. The amplitude of the reflection for the planar plane at R5 is even as large as the first arrival. For R4 the two peaks are blurred into each other. These different resulting reflections leads to the above discussed checkerboard pattern. For the zero-phase low-pass filtered data with a corner frequency of 400 Hz (Figure 5.18b), the effect of the ghost reflection is reduced for receiver R5 for both models, respectively is almost no more visible for R4. This leads to a

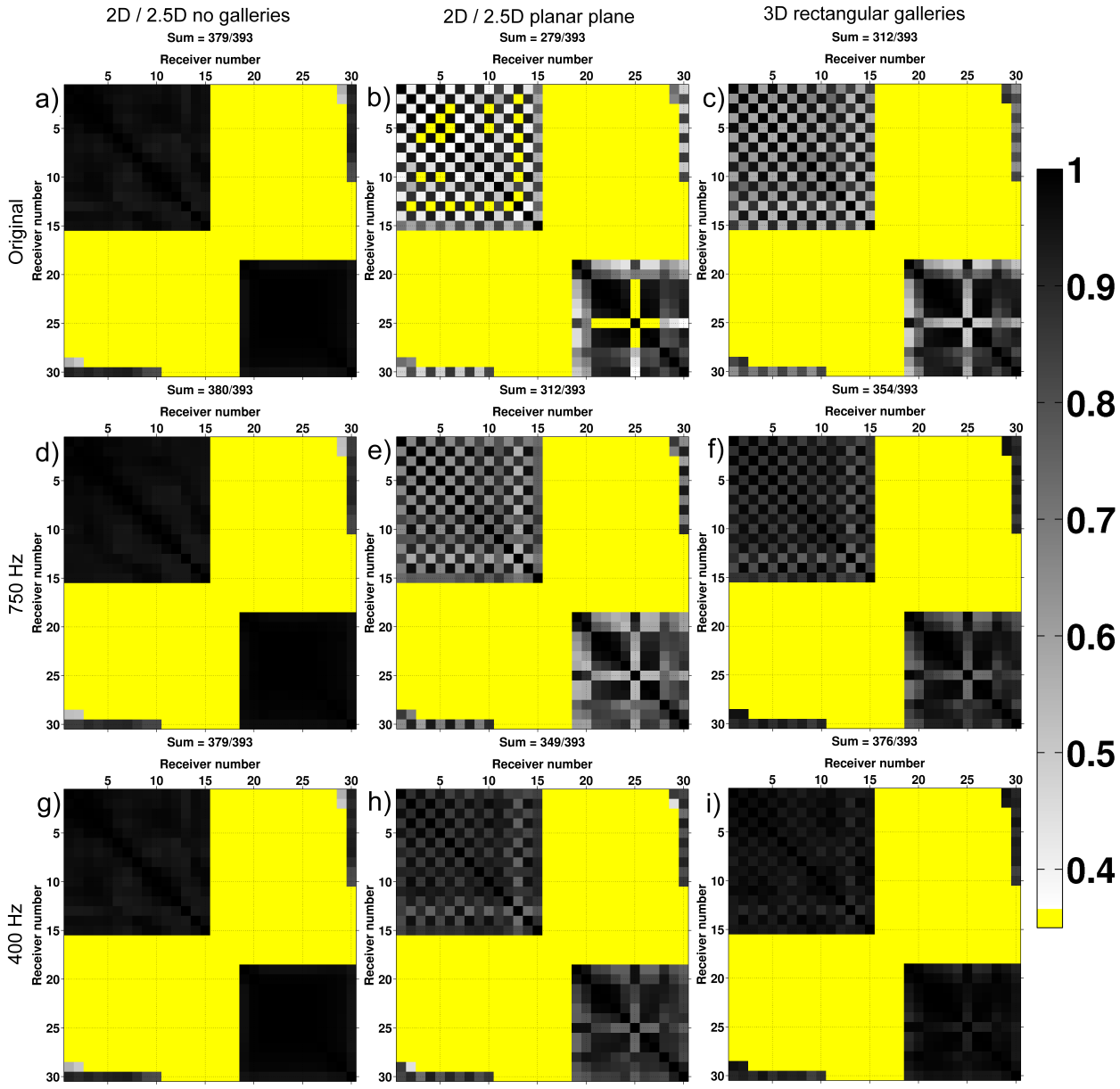

Figure 5.17: Semblance values for the five different scenarios in the CRG domain. From a) to c) the data not filtered, from d) to f) the data is low-pass filtered with corner frequencies of 750 Hz and from g) to i) with a corner frequency of 400 Hz. The colour scale has the same range for all figures. In the title, the summed up SEM value and the maximum possible value is shown.

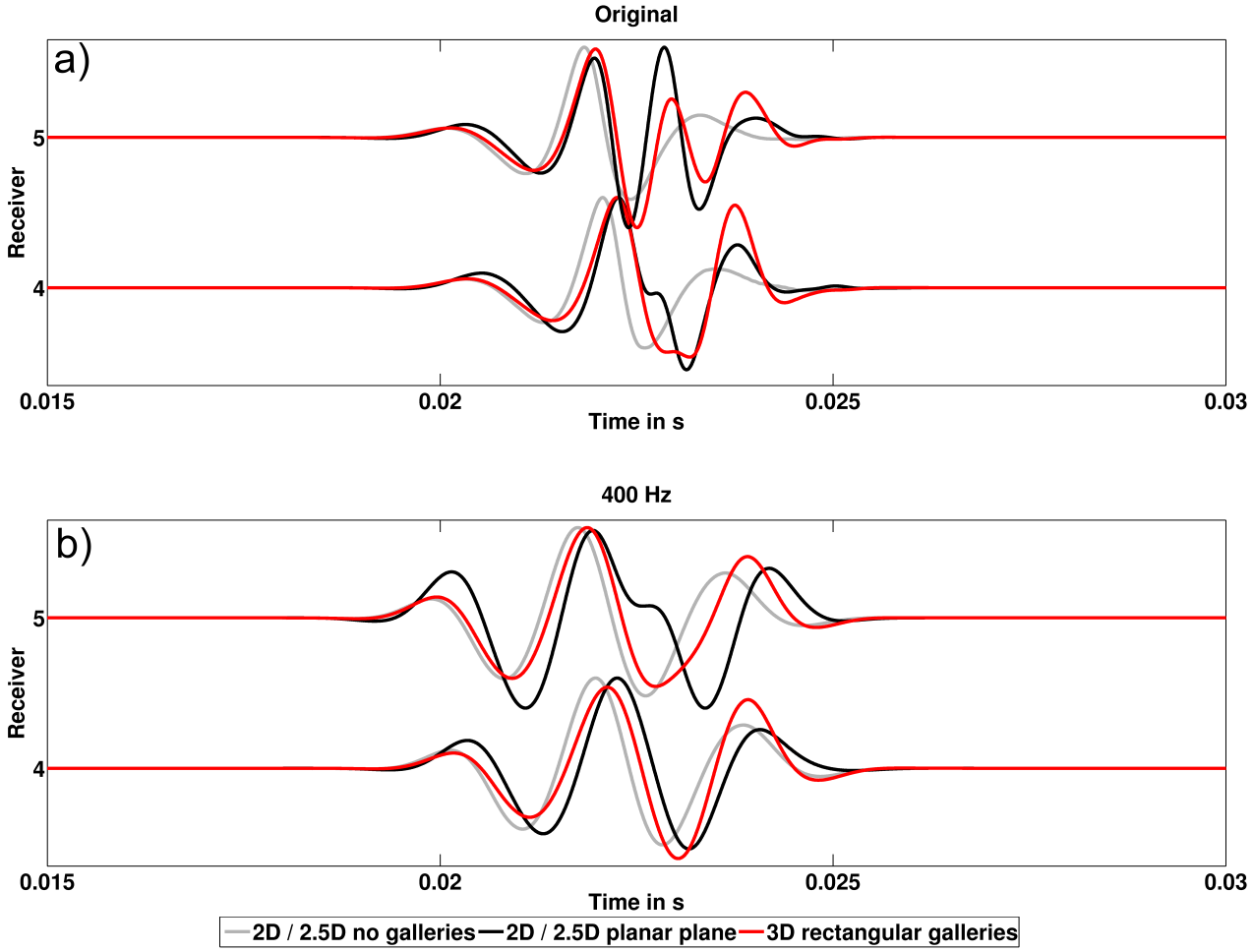

Figure 5.18: Original seismograms and filtered seismograms with 400 Hz for Receiver 4 in 1 m depth and Receiver 5 in 2 m depth for the three different modellings.

much higher semblance values.

After calculating the semblance values for the synthetic data, we want to compare them with the field data (Figure 4.18). For both, synthetic and field data, the maximum summed up semblance value differs because of a slightly different number of used traces. However, the most important parts of the plots, the upper left and lower right part are comparable. First of all, the frequency dependency which was observable for the field data is also valid for the synthetics. In order to model and invert the ghost reflection properly, we would have to us a 3D code. However, at the moment, this is computationally very expensive and with the used geometry, it does not justify the computational costs. At the same time, it will be very difficult, to invert the field data with the 2D code and with the galleries where strong ghost reflections occur. We will investigate the following approach. By not considering the gallery walls in the starting model and making some constraints with the preconditioning, the ghost reflections can be best explained in its behaviour. In addition, we will start with the lowest possible frequencies, which also give us a benefit as we have already shown.

5.6 Chapter Conclusion

In this chapter, at the beginning, we have presented two synthetic models with those all further studies were carried out. First, we used a random distributed velocity model adapted from the typical properties of the a crystalline rock. The occurring velocities are almost Gaussian distributed and the size of the structures varies in the order of several meters. Secondly, we have chosen a checkerboard model in which both, the edge length of the checkerboard pattern and the velocity perturbations can be set individually. The random model is used to determine the influence of various parameters on the inversion result, with the checkerboard pattern the resolution potential for different edge lengths and different source frequencies can be shown. The starting model for the random model was obtained with a travel-time tomography. A block size of 2 m turned out to be a stable parameter. The receiver array along the *Wilhelm Stehender Süd* has virtually no influence on the appearance of the velocity model. The velocity model was then smoothed in order to remove the predefined interfaces introduced by the chosen block size. For the starting model of the checkerboard model we have chosen a homogeneous model, which was the basis for the checkerboard pattern. By varying the grid spacing DH, it was shown that the spatial discretisation of the gallery walls of the gneiss block is sufficient for our concerns. Subsequent, some inversion parameters were varied to study its influence on the inversion result. In order to be able to describe the inversion result quantitatively, an error value was calculated for the models of the random velocity model. We calculated the mean of the absolute error of the inverted to the true model for each grid point. But often it is only hardly possible to reduce the result on a single number. So, the interpretation is usually a combination of both, the visible result and the quantitative value.

In general, the full-waveform inversion approach is strongly non-linear. In order to determine a minimum number of source and receiver which the FWI requires for a proper result with the preprocessed data, we even obtain a better result with a lower number of used source-receiver combinations in contrast to the use of all combinations. Nevertheless, we investigated, that a lower number of receivers lead to a larger error of the inverted model compared to a lower number of sources. Also, e. g., comparing the inversion results

for different length for the time window, the error has no linear behaviour. So, for our special geometry and preprocessing, we have to chose the parameters for the inversion very carefully. As we cannot be very sure how accurate the coordinates of source and receivers are, we found out that up to a deviation of ± 0.25 m, the inversion can still resolve the velocity model very well. For larger errors, this is not possible anymore.

Continuing to investigate the resolution potential of the FWI, for the checkerboard model, the length of the edges was varied. With a frequency of 750 Hz an edge length of 10 m to 4 m could be reconstructed very well. For edge length of 2 m and less, the inversion failed. For higher source frequencies of up to 1500 Hz, for an edge length of 4 m, the edges could be further sharpened. By varying the velocity perturbation of the model while using the homogeneous starting model, the inversion could handle a perturbation of up to 7.5%. For a perturbation of 12.5% or higher, the inversion is not able to reconstruct the velocities and the structures correctly.

Further, a common approach has been tested, which can increase the convergence of the inversion approach. For this purpose, also a homogeneous starting model for the random model was used. The source wavelet was filtered with a corner frequency of 1500 Hz. If we us the entire frequency range from the beginning, the shape of the misfit function is very complex, and the inversion fails to invert the structures. It is obvious that the inversion get stuck in a local minimum. By adding gradually higher frequencies to the inversion, the low frequencies at the beginning can smooth the misfit function and the convergence to the true model can be increased. We started at a frequency of 400 Hz and inverted up to 1500 Hz in steps of 100 Hz. We forced the inversion to change the frequency range not before 10 iterations per frequency, respectively if the FWI failed to decrease the misfit. We will also use this approach in the field data by starting with low frequencies.
Furthermore, the influence of different true v_S models were tested on the inversion results. The true v_P model and the starting models remained the same, but the Poisson ratio was systematically varied between 0.15 and 0.35 for the true v_S model. For a Poisson ratio between 0.2 and 0.3, the v_P model could be well reconstructed. So, the wrong v_S starting model has only a small effect on the v_P model in a certain range. For the density, we tested different starting models. The density does not affect the inversion result of v_P and v_S.

Then, similar to the field data, a semblance analysis for five different scenarios and different frequencies were calculated. It turned out, that the ghost reflections at the rock-air interface differ due to the different depths of the receivers and due to different models with a planar rock-air interface and with a three dimensional gallery, respectively. For lower frequencies the effect of the ghost reflection is reduced and comparable to the field data.
In the following chapter, we will deal with the field data and its difficulties by always keeping the synthetic tests and its results in mind.

6 Application to Field Data

Finally, in this chapter we apply a FWI with the field data presented in Chapter 3 and 4 and include the gained experience of the synthetic tests from Chapter 5. First we perform a travel-time tomography using first arrivals to obtain an accurate v_P starting model. Based on the v_P model we estimate a v_S and density model as well. (Section 6.1). Afterwards, we have to determine the source time function for the field data (Section 6.2). In order to test the optimal FWI parametrisation, we first introduce the parameters and second perform an inversion for only single sources. Afterwards, the simultaneous inversion using all shots are presented and the inversion results are discussed in Section 6.3.

6.1 Starting Model Generation

Similar to the synthetic data, we performed a travel-time tomography with the picked first-arrival times of the field data. Pratt and Goulty (1991) showed that a starting model obtained from a travel-time tomography can be sufficient for FWI. The theoretical background of the travel-time tomography can be found in Section 2.5. The obtained velocity model is used as a starting model for FWI and should be able to explain the waveforms within a temporal shift of less than half a wavelength (Sun and McMechan, 1992), otherwise cycle-skipping occurs (Section 2.3.6).

The picking of the first-arrival times had already been described in Section 4.3.2. We only picked traces with a distinct first break - since we consider a vibroseis source - with a distinct shape of the Klauder wavelet. The picks are already used for anisotropy analysis in Section 4.4.2 and for the preprocessing of the field data for the semblance analysis in Section 4.4.3. As done in the synthetic case, different block sizes were tested to obtain the best tomography result. With the experience gained from the random model (Section 5.1.2), we only tested three different block sizes of 1 m, 2 m and 4 m. In the following, the galleries are named according to Figure 3.6. The entire receiver array along the *Wilhelm Stehender Süd* was taken into account in the tomography (Section 5.1.2). As a starting model for the travel-time tomography, a homogeneous velocity model of 4714 $\mathrm{m/s}$ was estimated from the used software GeoTomCG. In Figure 6.1a - 6.1c the three inverted v_P models, interpolated to a grid size of DH $= 0.12$ m, can be seen. In grey the position of the galleries are shown.
In general, the three velocity models represent the same structures. At the top end of the model, a high velocity area occurs. Beneath, a zone of lower velocities in the range of 4500 $\mathrm{m/s}$ to 4700 $\mathrm{m/s}$ almost continuous from left to right can be seen. Along the *Wilhelm Stehender Süd* at the receiver array, an area with little higher velocities which decrease to the *Richtstrecke* occurs. Another small area of high velocities is present at the corner of the *Richtstrecke* and the *Quergang*.
In Figure 6.1d the ray density, respectively the number of rays travelling through one block is shown for the 2 m block size result. In the vicinity of the rock-air interface, the number of

rays per cell is less than 50, at the receiver array along the *Wilhelm Stehender Süd*, the number increases to 450 rays per block. In general, almost no single ray paths are observable for 4 m in the v_P model and for and 2 m in both, the v_P model and the ray density image. For the starting model of the FWI, we chose the block size of 2 m. For 4 m the model is still very blocky and for 1 m we can already recognise the individual ray paths very clearly which indicates an insufficient ray coverage. In order to avoid artificial structures due to the used block size, we additionally smoothed the model (Figure 6.1e). After smoothing with an operator length of 6 m, the velocity model in Figure 6.1e has mainly the same characteristics as the not smoothed model in Figure 6.1b and is used as the v_P starting model for the FWI. Finally, we want to compare the obtained v_P model with the results of the already described velocity models in Section 3.3.2.2, as the same dataset has been used. Similarities as well as differences occur. The high velocity zone at the upper end of the model and the low velocity zone beneath can be seen in Richter (2010) and Krauss (2013), too. The velocity pattern at the lower part of the model is more similar to Krauss (2013) as does the model generally matches this model better. Nevertheless, in the previous tomographies the overall velocity values are much higher. The travel-time tomographies had been performed using different software. However, the higher velocities are mainly due to the different picked travel times as shown in Figure 4.7.
In Section 6.3.1 we will study the general topic of the rock-air interface and which part of the model should be updated.

The v_S model was calculated by the classical ratio of $v_P/v_S = \sqrt{3}$. Through synthetic tests we have already shown that even with an inaccurate v_S model, the v_P model is still reconstructed sufficiently accurate (Section 5.4.8). Similar to the synthetic tests, the density is set to a spatially constant value of $2550\,\mathrm{kg/m^3}$ after Kopf et al. (2008).

In the following section, we determine the source time function and compare it to the primarily assumed Klauder wavelet.

6.2 Source Time Function Inversion

The residuals between synthetic and field data are caused by first, the difference of the true velocity structure of the gneiss and the starting model and second, due to the differences in the source wavelet and the receiver response, respectively receiver coupling. The latter influence, mainly the difference in the source wavelet, could be corrected with a source time function inversion suggested by Pratt (1999). The theory of the inversion can be found in Section 2.4. Even if we used a sweep signal in the field measurement and, therefore, should actually know the shape of the source wavelet, there might be a change in the source signal by different couplings of the vibrators at different source positions. Also, as already mentioned, the coupling of the receiver anchors could influence the waveforms (Maurer et al., 2012) which could be corrected up to a certain amount with the source time function inversion if the coupling effect is similar for all receivers. The semblance analysis (Section 4.4.3) has identified receivers which differs strongly in its waveforms regarding their direct neighbours and also corrupt receivers. We do not use this receivers, because they would influence the source time function inversion.

Without the intention of anticipating, the FWI fails if we do not perform a source time function inversion. Even though, the FWI could reduce the misfit, the artefacts around the

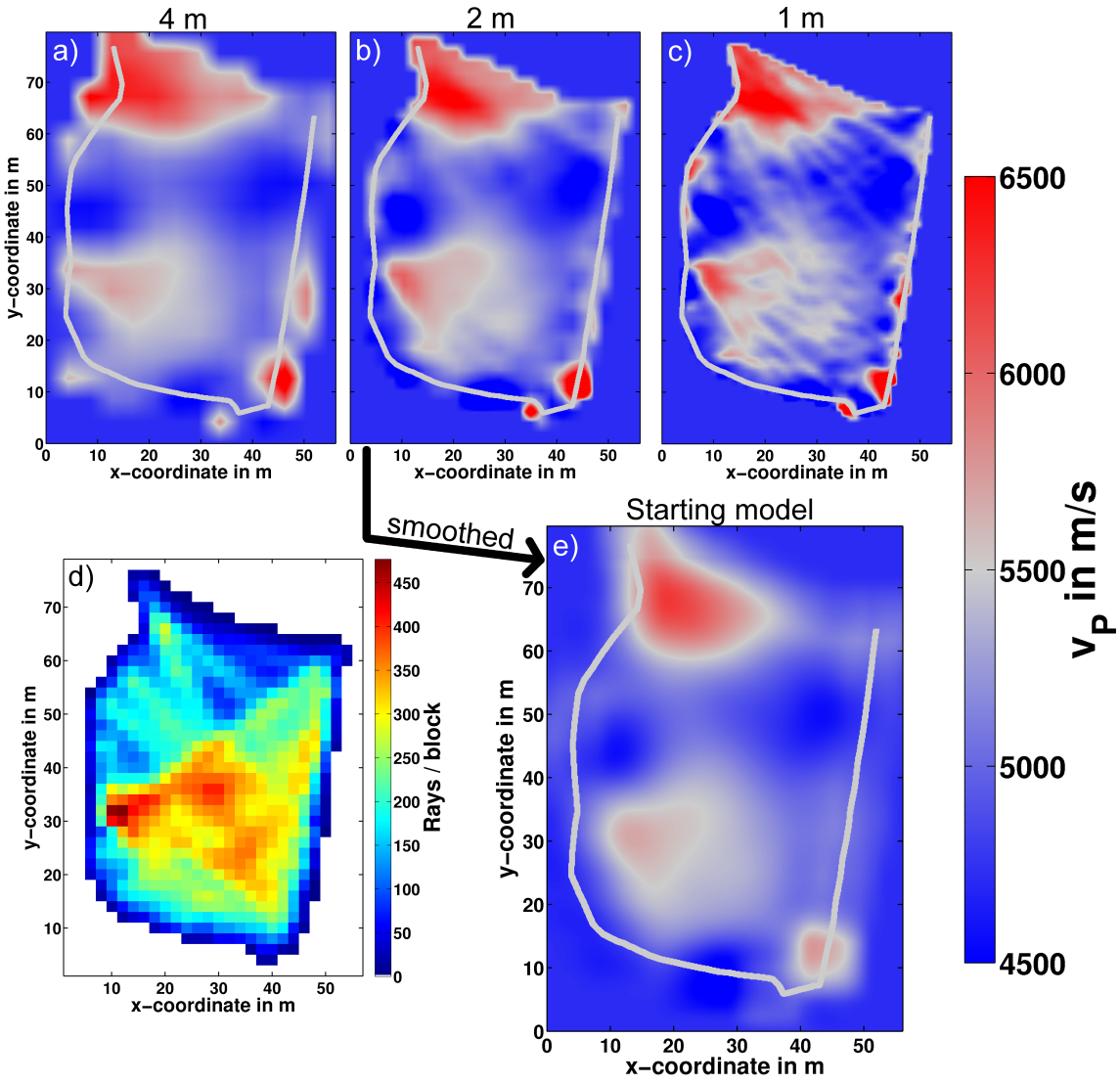

Figure 6.1: a) - c) Results of the travel-time tomography of the field data for the different block sizes (title). All three results are interpolated to DH = 0.12 m. For better orientation, the grey line represents the galleries. In d) the number of rays per cell for a block size of 2 m is shown. In e), the smoothed velocity model which is further the starting model for the FWI is plotted.

receivers and in the entire model are huge with large velocity contrasts. Thus, we need to invert for the source time function.

The synthetic data should have a broader frequency spectrum as the field data for the source time function inversion. Otherwise, the inversion has to adapt frequencies which could cause ringing in the inverted source wavelet. To satisfy this, we do not use the Klauder wavelet extracted from the field data (300 - 3000 Hz) but use an analytical wavelet with a frequency content of 200 - 1500 Hz (Appendix B). So, the lower frequency limit is set to some lower frequencies. In addition, we neglected the high frequencies because, first they are only included sparely in the field data (Section 4.4.1) and second the computational costs would be higher due to the adjusted FD-parameters.
As described in Section 5.4.7, we use the multi-scale approach starting at a frequency of 400 Hz. The synthetic data is based on the already shown starting model. Afterwards the synthetic and the field data are preprocessed similar to the synthetic tests (Section 4.3.3). In addition, the field data is filtered with a low-pass filter of 400 Hz.
Usually, e. g., for measurements at the surface, only the near offset traces are used for the source time function inversion, because the waveforms are not that strongly influenced by the velocity model as for far offset traces (Groos, 2013). Due to the preprocessing, we can only use receivers which are in transmission geometry. Nevertheless, also Pratt (1999) who suggested the source time function inversion approach, uses receivers in a transmission geometry. But as we cannot avoid this constrain, we have to keep it in mind.

In Figure 6.2 the inverted source wavelets for all shots from black to light grey and for comparison the Klauder wavelet which we extract from the field data filtered within the appropriate frequency range, are shown. The Klauder wavelet and the wavelets from the source time function inversion are similar in their appearance. The maxima for every source wavelet of the field data are each slightly shifted from the Klauder wavelet. Also the amplitudes of the side lobes differ slightly. The time shifts may be caused by an inappropriate starting model. So, the source time function could project model features into the wavelet. In order to test, whether the time shifts are primarily caused by the velocity structure, we shifted the maximum of the wavelets at one point in time (0.015 s) and performed a FWI with the shifted source wavelets. This corresponds nearly to the FWI with the original Klauder wavelet, which has its maximum also at the same point in time for all shots. However, now, the shape of the wavelets differs for each shot. As a result, again, the inversion can reduce the misfit, however, artefacts and strong velocity contrasts arises in the entire model. This shows to us that the phase shift in the source wavelets is needed to obtain a smoother inversion result without artefacts.

In the next section, first we will use the FWI for inverting single shots to make sure that the inversion scheme can explain the field data. Before, we describe the used parameters in the inversion.

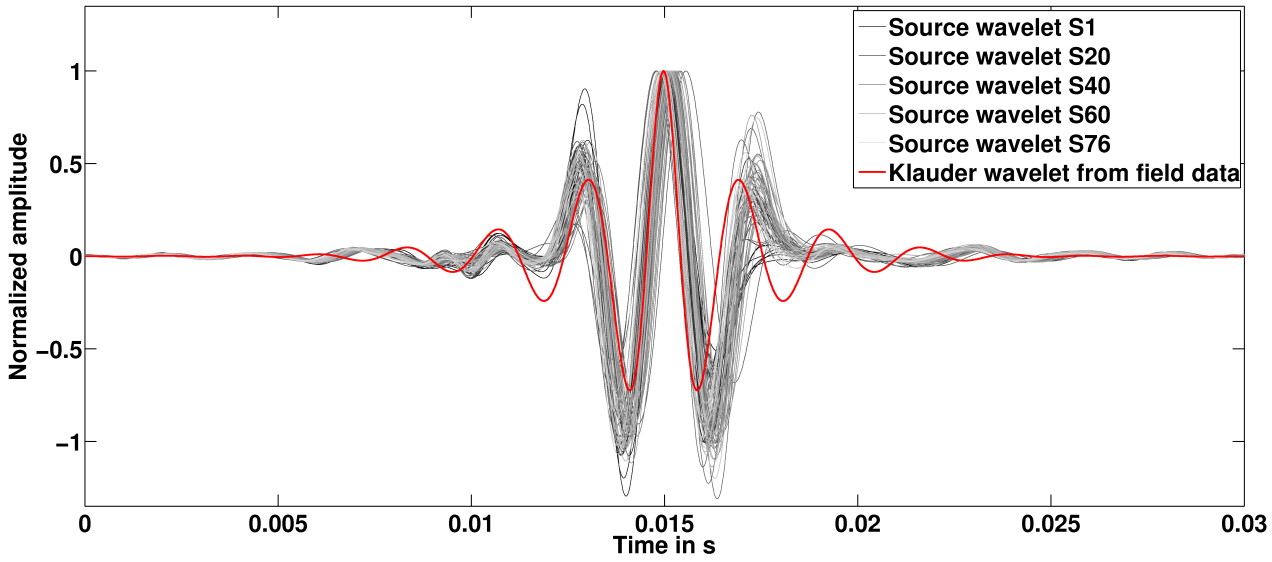

Figure 6.2: The determined source time functions for all shots up to 400 Hz are plotted from black to light grey. Also the Klauder wavelet which was extracted from the field data with the same frequency range is plotted in red. The amplitudes are normalised separately to the largest positive value.

6.3 Full-Waveform Inversion with Field Data

6.3.1 Inversion Parameters and Preconditioning

In order to get the inversion running, we have to specify the parameters for the FWI, so they are in agreement with the field data. As already mentioned above, we will conduct a multi-scale inversion which starts at a frequency of 400 Hz. Due to the lowest frequency we use, we can neglect the various ghost-reflections at the rock-air interface in the field data. In Section 4.4.3 and 5.5 this is shown with a semblance analysis which was carried out with first, the field data and afterwards with the synthetic data for various types of velocity models (with and without a rock-air interface). In the field data we could identify some receivers which obviously differ from the other due to their coupling. These receivers are not used in the inversion. Though, the most noticeable feature of both data sets was some kind of checkerboard pattern for R1 to R15. This is due to the different, alternating depth of the receivers. The checkerboard pattern decreases with lower frequencies. But, especially in the synthetic case, for a velocity model with a transition from rock to air, the pattern is still dominant and differs strongly to the field data. Therefore, we do not include the rock-air interface in the starting model. For all performed inversions, only the interior of the gneiss block is allowed to be updated (Section 6.3.3).

In the synthetic tests (Chapter 5), we applied the widely-used L2-norm as objective function and normalised the wavefields in advance. In the ongoing work, Choi and Alkhalifah (2012) proposed a global correlation norm which is a zero-lag cross-correlation of the normalised synthetic and observed data and is therefore insensitive to the geometrical spreading (Section 2.3.2). This coincides with our preprocessing (Section 5.3). Comparing the global correlation norm to the L2-norm, the back-propagated adjoint sources differs only little (Przebindowska, 2013). In the used inversion code DENISE, the misfit calculation for the global correlation

norm is slightly different implemented as suggested by Choi and Alkhalifah (2012). In addition, the misfit value is normalised by the energy of the normalised field seismograms (Section 2.3.2). In the following, we used the global correlation norm as implemented in DENISE to obtain a meaningful misfit value.

For the length of the time window to only invert the first-arrival P-phase, we chose 0.01 s, in contrast to the synthetic test (Section 5.4.3). We shortened the time window because of two reasons. First, we will end up at a higher frequency compared to the synthetic tests. That means, the shape of the Klauder wavelet is narrower. And second, we want to be sure that only the main phase with the largest amplitude is used in the inversion.

In the inversion, mainly the seismograms for sources and receivers in the transmission geometry are used. The P-wave is polarised in the x-direction and thus, the main energy of the phase is recorded on the x-component. On the y-component only little energy of the P-wave arrives, as we already showed in Figure 4.10. The dominant wavetype on the y-component is the S-wave which we do not consider in the inversion. Thus, in the field data inversion, we only use the x-component. This provides are more stable result, as on the y-component due to the smaller amplitudes, the signal to noise ratio is decreased which will produce artefacts in the velocity model. The maximum spatial resolution as determined in the synthetic tests will not decrease dramatically by neglecting the y-component. For surface waves such an analysis has already been carried out by Romdhane et al. (2011).
The muted traces which are not considered in the inversion have been shown in Figure 4.9. Receiver 16 - 18 at the bottom of the gneiss along the *Quergang* are neglected. They are not in a transmission geometry and thus, the amplitude of the P-wave on the x-component is very small. In Section 4.3.3 and 4.4.3 the appearance of the matrix is explained. For testing the step length for scaling the gradient, respectively updating the velocity model, we use every 5th source position. In the synthetic tests we used only three shots because the individual shots are consistent with one another. For the field data we cannot expect this fact.

For the multi-scale approach, we start at a maximum frequency of 400 Hz. The minimum frequency is limited to the lowest frequency of the sweep signal to 300 Hz. We gradually increase the frequency in steps of 100 Hz until 900 Hz. The source time function inversion is determined as described in Section 6.2. After each frequency change, we calculate a new source time function on the current velocity model.

The preconditioning of the gradient in the synthetic tests was described Section 5.3. The gradient around the sources is tapered with the shape of a Gauss error function and only updates of the velocity model within the gneiss block are allowed. Now, we adjust these preconditioning to the field data inversion. The gradient before updating the velocity model is slightly smoothed with a median filter (Section 5.1.2). The filter length is only five gridpoints. The filter reduces the very strong velocity contrasts directly around the source and receiver positions. If we do not smooth the gradient, the inversion becomes unstable after a few iterations, since the used FD-modelling parameters are not chosen for very high or very low velocities. In addition, similar to the synthetic tests, we precondition the gradient around the sources with the shape of a Gauss error function and only allow updates of the velocity model within the gneiss block (Section 6.3.3).
After each frequency change, the velocity model was also smoothed with a median filter because of the still occurring high and low velocity areas in the vicinity of the receiver positions. To smooth the velocity model similar to the gradient during the inversion after each iteration would be only possible without the preconditioning. Otherwise the occurring

edges in the velocity model due to the used taper would be shifted after each smoothing. The inversion runs until the misfit converges and the FWI cannot find a velocity model which reduces the misfit.

6.3.2 Single Shot FWI

For a first investigation, we just invert single sources individually to see whether the preprocessing and the chosen parameters are reasonable for the field data. We expect a very good fit of the synthetic data to the field data, because by using one single source, the velocity model can be updated without any constrains. The v_P, v_S and the density starting models are described in Section 6.1 and the v_P starting model is shown in Figure 6.1e. Velocity models for the separately inverted shots should not be interpreted in the sense of existing velocity structures. Representative, we selected three shots, Shot 10 along the *Richtstrecke*. Shot 39 along the *Quergang* and Shot 60 at the *Wilhelm Stehender Süd* and have a closer look at the seismograms and the resulting velocity models.
The maximum frequency of the inverted data ranges only to 400 Hz. We will start with this frequency range also for the inversion for all shots. The misfit between synthetics and field data is getting continuously smaller: For Shot 10 from 38.4 % to 0.9 %, for Shot 39 from 38.8 % to 0.3 % and for Shot 60 from 48.1 % to 0.6 %. That means, the final velocity model can explain the seismograms of the field data very well.
Intentionally, in Chapter 5, no seismograms were shown. In the synthetic case, the FWI was almost always able to fit the seismograms very well. This is because they based on the same physical and numerical principles and the data was consistent with one another. For the field data, the degree of the fit of the seismograms is one indication if we considered the physics right.
The seismograms for the field data, the starting seismograms and the inverted seismograms for the final velocity model are shown in Figure 6.3 for the three sources. Due to the preprocessing only the seismograms which were used in the inversion are plotted. Especially for Shot 10, the waveform of Receiver 27 and for Shot 60 the waveform of Receiver 3 are not well explained by the starting model. Nevertheless, the starting model fits most of the receivers already very well. We do not have any problems with cycle-skipping. As described above, the FWI can handle the relatively huge discrepancy for some receivers and could fit the waveforms to the field data. The final v_P models for the three shots are shown in Figure 6.4.

Now, we want to explain how the inversion has changed the velocity models. An update of the velocity model is only allowed within the boarder of the gneiss block (Section 6.3.3). Generally, the change of the seismograms is nicely reflected in the model. For Shot 10, the starting seismograms matches well to the field data. Only for the Receivers 25, 28, 30 and in particular 27, differences occur in the travel time. For Receiver 25 and 30 the model have to be updated with higher velocities in order to ensure an earlier arrival time of the P-wave, for Receivers 27 and 28 the other way round. Especially for Receiver 27 the model shows a significant decrease in the velocity between Shot 10 and Receiver 27. At almost all receiver positions typical artefacts occur. Such artefacts with very low and high velocity in the vicinity of the receiver positions are also visible in the synthetic tests, e. g., for the wrong coordinates analysis in Figure 5.4.4. However, the artefacts do not necessarily have its basis from incorrect coordinates. For Shot 39, receivers are used along both galleries.

For Receiver 1, the velocity should be increased slightly. For Receiver 3 and also for the following, the velocity must be reduced. The tendency to increase the velocity of Receiver 30 is the same case as for Shot 10. This is also visible in the model (Figure 6.4b). For shot 60, only the receiver along the *Richtstrecke* are used. The effect of the various reflections because of the alternating depths of the receiver in the field data is negligible due to the used low frequencies. For the starting seismograms, also no reflections occur because in the model the galleries are not included. The picture of the increased, respectively decreased velocities fits also very well to Shot 60. Again, the velocity of the model must be increased for Receiver 1 and decreased for Receiver 3.
Comparing the areas of high and low velocities which are captured in the starting model, they fit well to the areas in which the velocity is increased and decreased by the FWI. Hence, the used parameters for the FWI are able to find a velocity models which explain the field data for single sources.

In the next section we will invert for all shots simultaneously. We will investigate whether the sources are consistent to each other. In addition, the resultant velocity models are then interpretable.

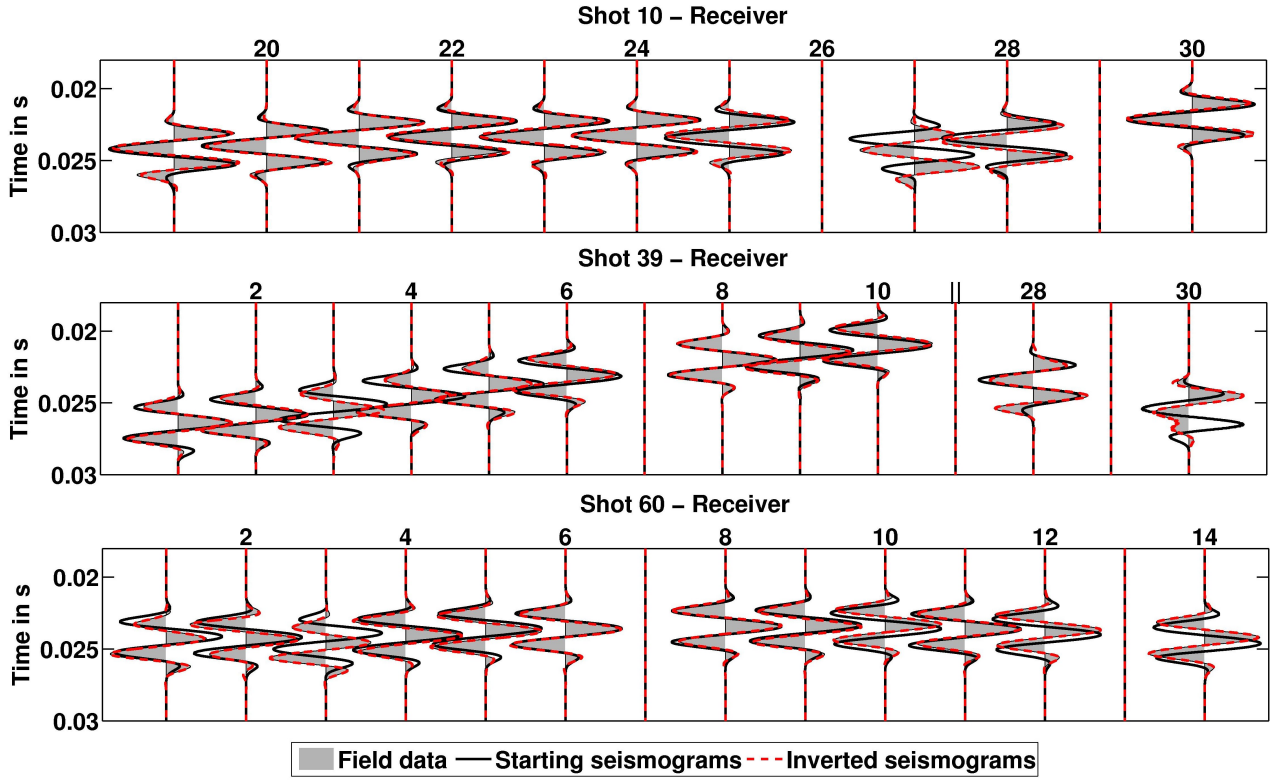

Figure 6.3: The field data in the background in grey, the starting seismograms with determined source time function in solid black and the inverted seismograms based on the final velocity models in dashed red are shown. The FWI was performed individually for the three Shots 10, 39 and 60. Only the traces which were used in the inversion are shown. The time axis is equal for all three plots.

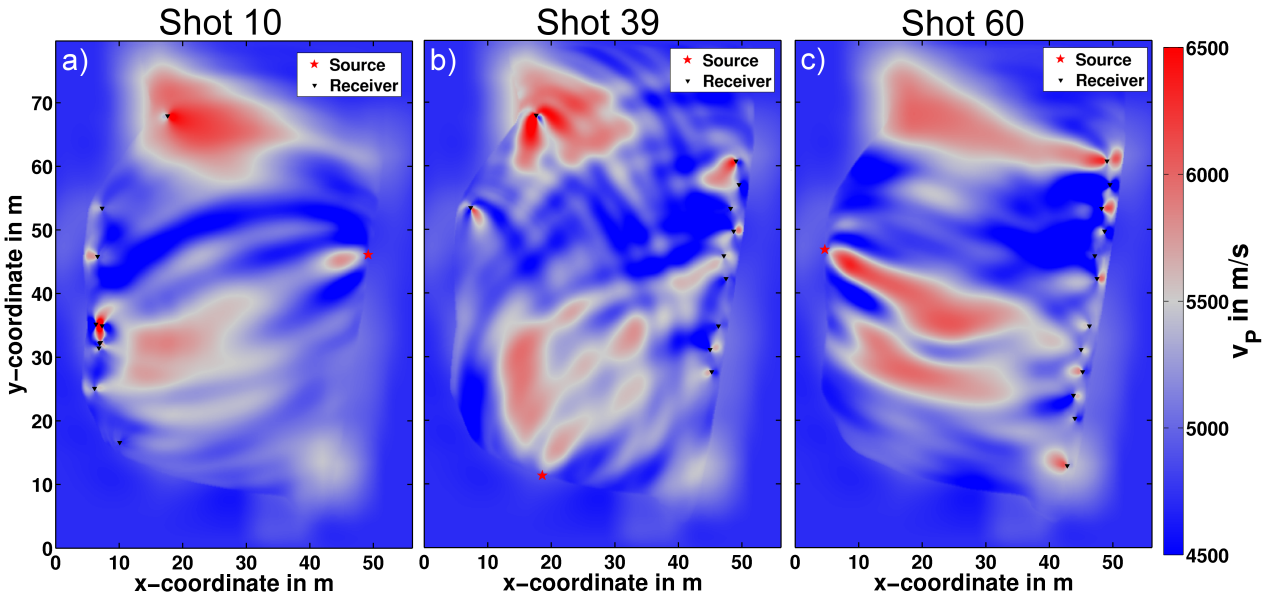

Figure 6.4: Final v_P model for the single shot FWI for Shots 10, 39 and 60. The source position is marked with a red star, the receiver positions which were used in the inversion with black triangles. Only an update of the velocity model within the boarder of the gneiss block was allowed.

6.3.3 Multiple Shot FWI

In contrast to the previous section, all shots are inverted simultaneously now. The inversion and thus, the velocity model has not only to satisfy one shot, but all shots.
As described in Section 5.4.7, we will conduct a multi-scale inversion and start with low-pass filtered data with a corner frequency of 400 Hz.

In addition to the multi-scale approach, we allow the inversion only to update the interior of the gneiss. This is the most realistic approach comparing to the field survey because the waves can only travel within the gneiss block. If the FWI requires an update of the model outside of the gneiss to explain the field data, we do not allow the update due to none physical reasons. In addition, we successfully used the same approach in all performed synthetic tests (Section 5.3).

In Figure 6.5 the contribution to the overall misfit for each shot and each receiver in respect to the starting model (Figure 6.1e) and to the final model for a maximum frequency of 400 Hz (Figure 6.9b) is shown. The grey areas are receivers which are neglected in the inversion (Section 4.3.3). The sum of all misfit values is equal to the starting value and to the value at the last iteration for the first frequency range in Figure 6.7, respectively. As already seen in the previous section, Receiver 3 and Receiver 27 have a large time shift which is reflected in the misfit value for the starting model (Figure 6.5a). The colour scale is clipped especially for these two receivers. Furthermore, the misfit for the other shots and receivers is not systematically distributed. In Figure 6.5b the misfit for the final model for a maximum frequency of 400 Hz is shown. In general, the misfit could be reduced for almost all shots and receivers, although some misfit is left. The FWI was able to find a velocity model which explains most of the used seismograms and is consistent to almost all shots and receivers.

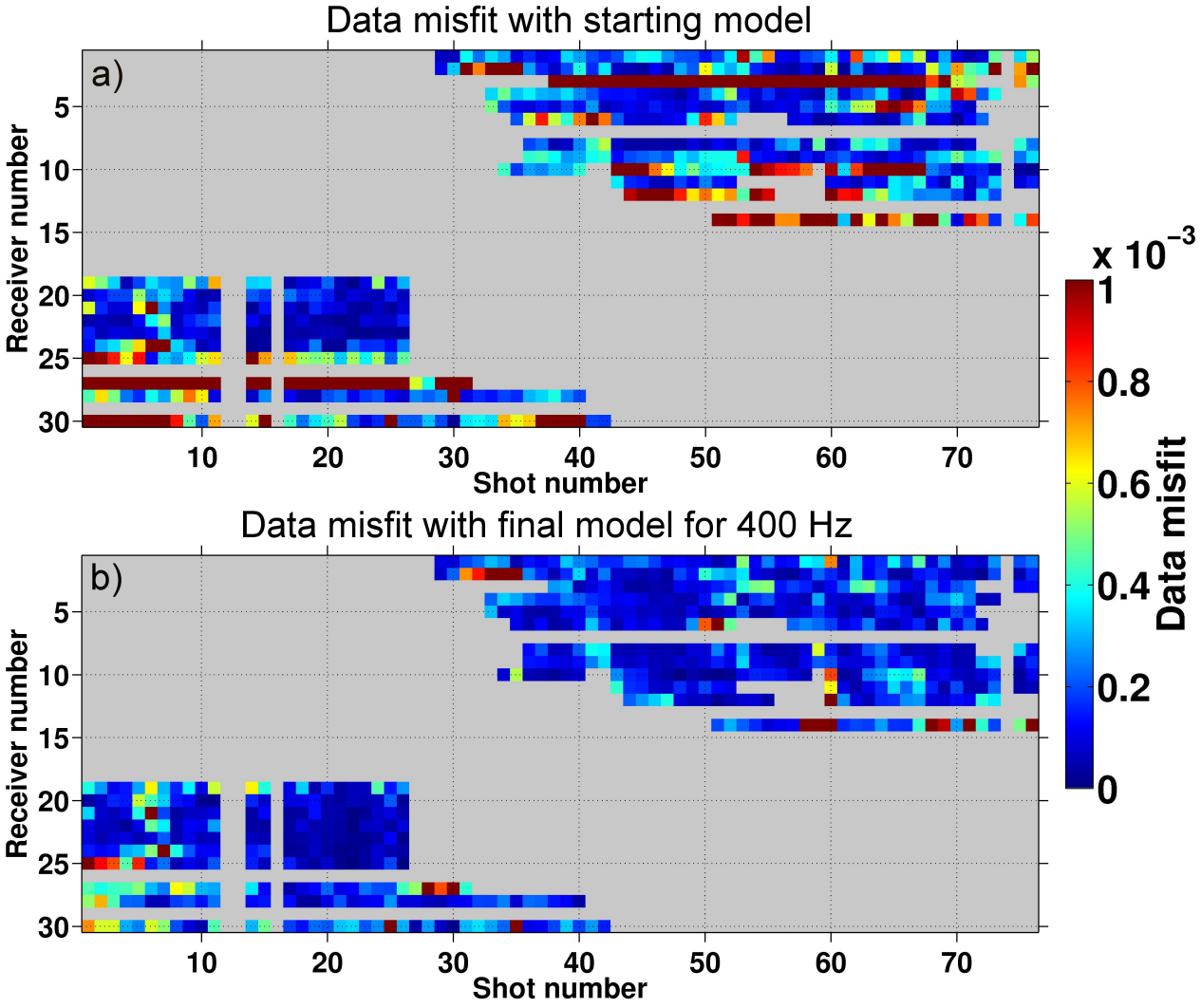

Figure 6.5: In a) the contribution to the data misfit between the field data and the seismograms for the starting model and in b) for the final model up to 400 Hz (Figure 6.9b) is shown. Grey shot-receiver combinations were not used in the inversion. The colour scale is clipped especially for Receiver 3 and Receiver 27. The sum of the misfit in a) and in b), respectively, result in the total data misfit shown in Figure 6.7 for 400 Hz.

We will now go on by increasing the frequency range of the field data. In contrast to the synthetic test, where the inversion automatically increased the frequencies, we perform a visual quality check of the velocity models and the data before starting the next inversion manually.
In the following, we explain the applied approach for the frequency range of 500 Hz exemplary. Afterwards, the final inversion result up to a frequency of 900 Hz is shown. In the next frequency range we used the velocity model obtained from the previous frequency stage and apply a smoothing to reduce the strong velocity contrasts at the receiver positions which occur despite of the gradient smoothing. This is necessary to remove small-scale artefacts and for a stable FD-modelling. But we do not change reliable structures in the inversion results. The used filter length is different for each frequency range and is summarised in Appendix D. In addition, based on the smoothed model, new source time functions are calculated to update both, the frequency content as well as the shape of the wavelets. Afterwards, the inversion is again started, with the velocity model obtained from the previous frequency stage as the starting model, new source time functions and with a field data that has a broader frequency content.

In Figure 6.6a and 6.6c the inverted source time function of Shot 10 and 60 for all frequency ranges are shown. The general shape is almost the same for all frequencies. This a quality feature for a stable inversion (Brenders, 2011; personal communication: Jean Virieux). If the source time functions would differ for higher frequencies and for different shot positions that would indicate that the inversion is not on a straight path to a minimum of the misfit function, although for higher frequencies, the symmetry of the Klauder wavelet is reduced. The second side lobe after the global maximum is getting smaller. This could be due to the rising influence of the reflection at the rock-air interface in the field data (Section 4.4.3).

On the right side in Figure 6.6b and 6.6d, the corresponding frequency spectra are shown. Adding higher frequencies to the inversion is only plausible up to 900 Hz because in the field data no higher frequencies occur (Section 4.4.1). This is also reflected in the frequency content of the source time function. Comparing the source time function of 800 Hz and 900 Hz, the frequency content is almost the same. We stop the inversion at this frequency.

In Figure 6.7, the misfit curve for all frequency ranges is plotted. The number of iterations differs for different frequency ranges. In Appendix D the exact number of iterations and the maximum and minimum misfit value for each frequency can be found. The data misfit with the unit %, is specified with respect to the unexplained energy of the energy normalised field data. Within one frequency band the misfit decreases steadily until no model update can be found which reduces the misfit. After the jump to a higher frequency content of the field data, the misfit is increased for two reasons. First, due to the newly added higher frequencies and therefore further information. And second, since the model is smoothed before each frequency change, this also contributes little to the misfit. For the last frequency range of 900 Hz, the final misfit as well as the velocity model does only change slightly. As explained above, the frequency content of the field data is almost exploited, no information could further improve the velocity model.

In Figure 6.8 the fit of the final seismograms to the field data for the first frequency range up to 400 Hz can be seen, again for Shot 10, 39 and 60. We show this frequency range because the misfit could be reduced most. The starting seismograms are already very well fitted to the field data, and for many traces almost no more misfit is observable. The seismograms calculated with the final inverted model of 400 Hz are fitted very well and the misfit drops.

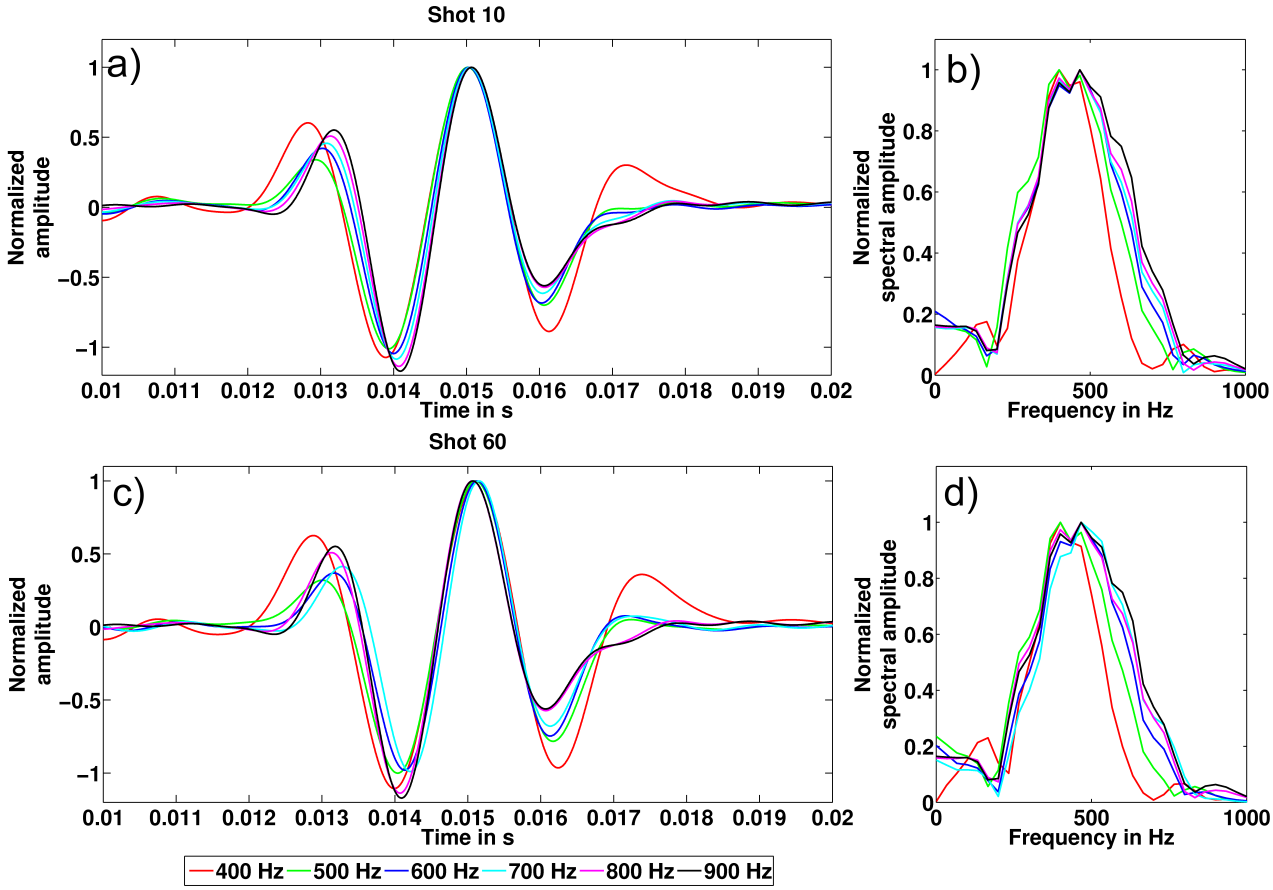

Figure 6.6: Source time functions for all frequency ranges with its corresponding frequency spectrum for Shot 10 and Shot 60. The source wavelets as well as the frequency spectra are normalised separately.

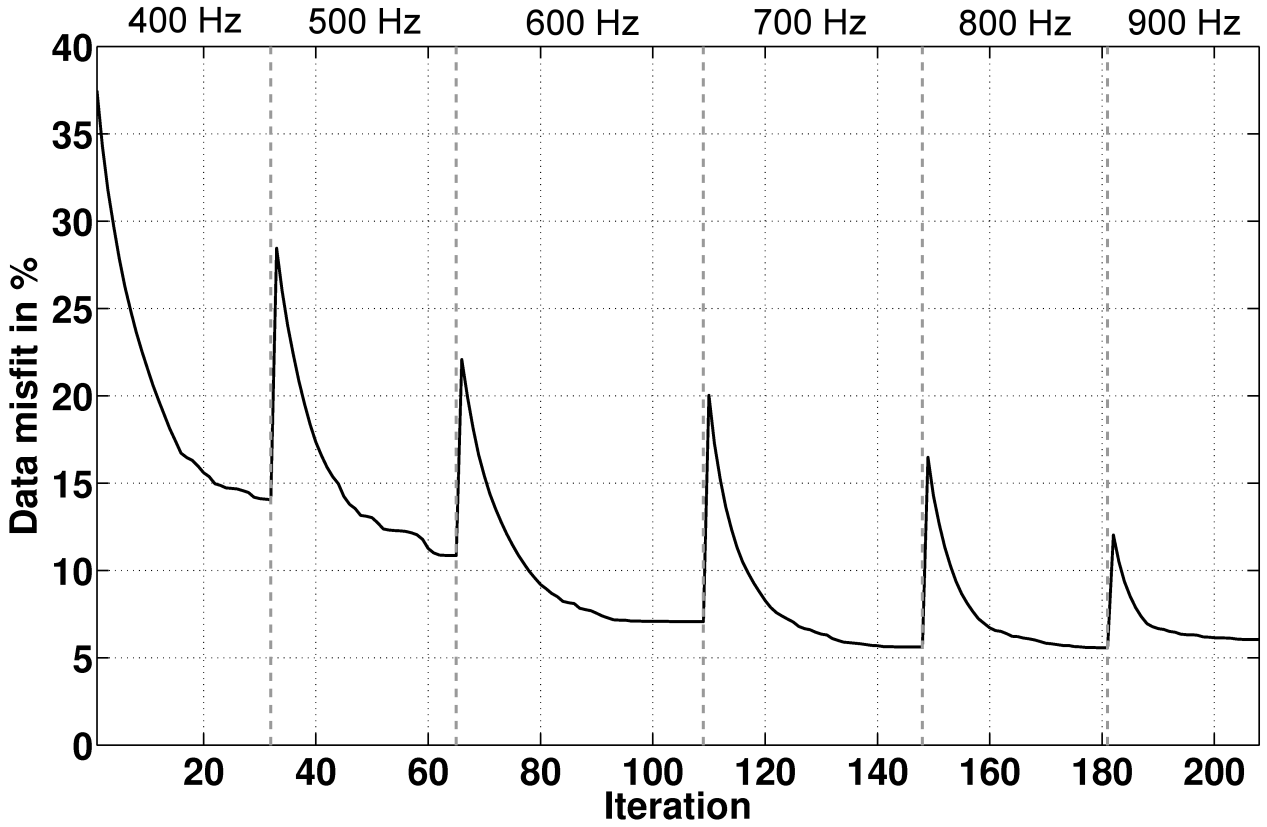

Figure 6.7: The evolution of the overall data misfit. The data misfit with the unit % is specified in respect to the unexplained energy of the energy normalised field data. The vertical dashed lines indicate jumps to the next frequency range. In Appendix D, the number of iterations per frequency range and the exact values at the first and last iteration for every frequency range can be found.

In comparison to Figure 6.3 where only single shots were inverted, certainly the fit for an inversion with all shots is worse. For some traces, the inversion is not able to explain the seismograms by changing the velocity model.

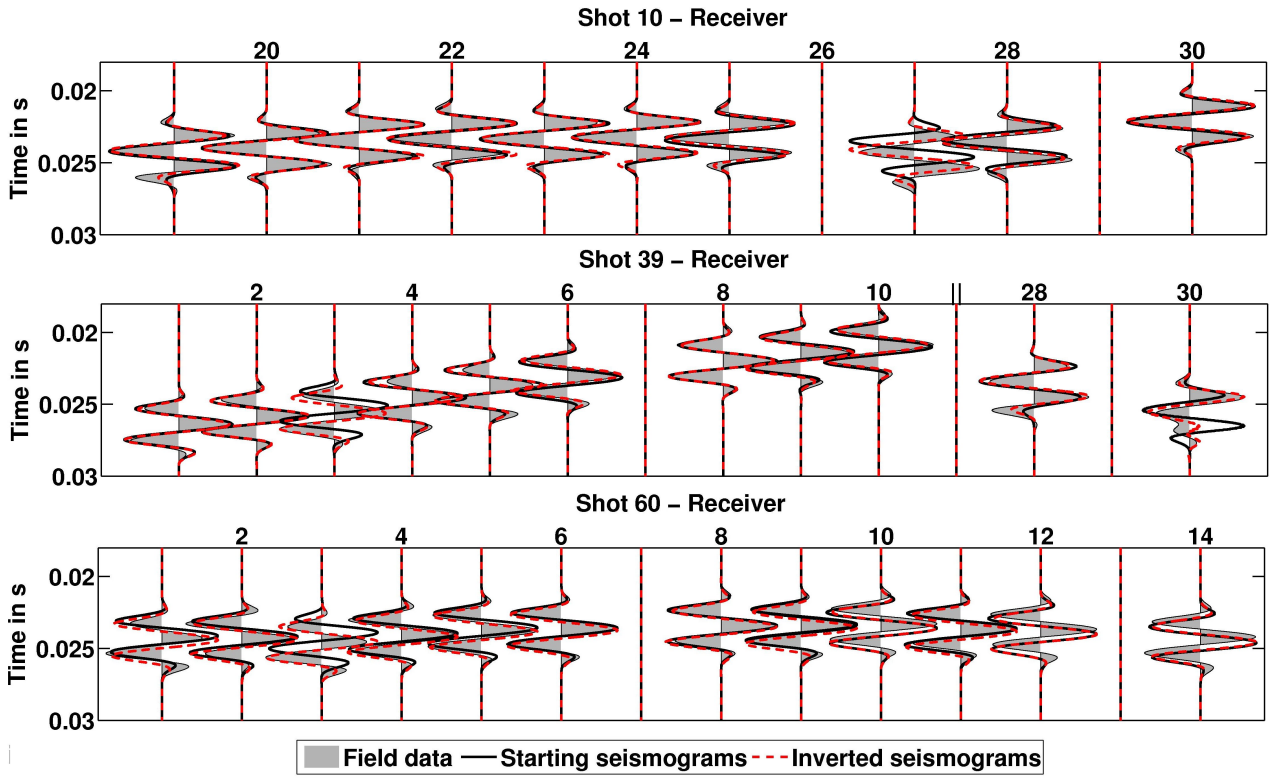

Figure 6.8: The field data in the background in grey, the starting seismograms with determined source time function in solid black and the inverted seismograms based on the final velocity models in dashed red for 400 Hz are shown. In contrast to Figure 6.3, the FWI was performed simultaneously for all shots. Only the traces which were used in the inversion are shown. The time axis is equal for all three plots.

In Figure 6.9 the final inverted models for the highest inverted frequency of 900 Hz as well as for 600 Hz for all three elastic parameters and for the v_P to v_S ratio is shown. The v_P model for 600 Hz has already more structures than the starting model (Figure 6.9a). Especially in the vicinity of the receivers and at the edge of the preconditioning taper, some artefacts with strong velocity contrasts occur. The low velocity zone at the top of model from left to right has some more structure as well as the high velocity zone at the bottom along the *Wilhelm Stehender Süd*. After the inversion up to 900 Hz, the velocity model is even more heterogeneous (Figure 6.9e). The artefacts at the edge of the gneiss get stronger. In Figure 6.10 the v_P models for all frequencies are shown. We will discuss the structures and containing velocity values in more detail later on.

In the v_S model for both frequencies the artefacts around the receivers are different to the v_P model (Figure 6.9b and 6.9f). Also the structures in the v_S model are only little comparable to the v_P model. As we only invert the first-arrival P-wave, the sensitivity is much higher for the v_P model as for the v_S model. By comparing the synthetic seismograms in Section 5.4.8 with different v_S models, the varying v_S does have an influence on the shape of the first-arrival P-wave, anyway not as big as a varying v_P model. The inversion has a trade-off

between the S-wave and P-wave velocity. In DENISE the gradients of each parameter is individual scaled (Section 2.3.4). In Groos (2013) the same problematic occur the other way round: "However, in each iteration the update of each model parameter is a percentage of the maximum value of the corresponding model parameter in the current model, independent of the absolute amplitude of the gradients for the different model parameters. This could cause a too large update of the P-wave velocity which then influences also the update of the S-wave velocity in the following iteration steps." (Groos, 2013, p. 104). The synthetic tests in Section 5.4.8 showed that the v_P model could still be resolved even though v_S model is incorrect to a certain degree. The v_P to v_S ratio for the starting model was constant with 1.73 which corresponds to a Poisson ratio of $\sigma_P = 0.25$. At the edge of the gneiss, the v_P to v_S ratio is blurry and the ratio drops below 1.41 which corresponds to $\sigma_P = 0$ for both frequencies (Figure 6.9d and 6.9h). Negative Poisson values means that if a tension is applied to the material, it will expand in the other directions. This is possible, but we do not expect such materials within the gneiss. The negative σ_P is not physically feasible. However, in the middle of the gneiss, the ratio is almost constant with approximately 1.8 for 600 Hz. For 900 Hz the ratio gets little more irregular. Comparing to the synthetic tests the homogeneity indicates that the starting models are accurate for the inversion. In the area of the low velocity zone, also the ratio drops which is an indication for the low v_P value. In future inversion, we should spend more attention to the v_P to v_S ratio and implement a routine which avoids negative Poisson numbers.

The density model is mainly updated at the edge of the gneiss block (Figure 6.9c and 6.9g). The structures do not correlate to the velocity models and are very heterogeneous. We almost see similar effects in the synthetic tests we carried out to investigated the influence of the density in the inversion (Section 5.4.8). So, as it is not well constrained by the field data, we will not interpret the density model. By modelling synthetic seismograms with the final inverted v_P and v_S but using the density of the starting model, almost no difference in the seismograms occur.

In Figure 6.10 the evolution of the v_P model beginning at the starting model to 900 Hz is shown. We show all v_P models for every frequency range because the inversion is mainly sensitive for v_P. For all frequency ranges, almost the same artefacts around the receivers occur. The are between the edge of the preconditioning taper and the receivers should not be over-interpreted. The size of the structures within the gneiss which are continuously added to the velocity models as well as the minimum and maximum velocities are increasing to higher frequencies, although the size of the additionally small-scale structures is in the range of the smallest wavelength. As investigated in Section 5.4.5, the size of the structures are within the possible resolution. Especially starting at 700 Hz, the contrast between the structures get very strong. The misfit could be reduced for every frequency range and the synthetic data fits better and better to the field data. The general pattern from the starting model, the low velocity zone from left to right in the upper part of the model likewise the two high velocity zones still exist and have a finer structure as in the starting model.

6.4 Chapter Conclusion and Discussion

In this chapter a FWI for a field data set which we acquired in the GFZ U-Lab in a hard rock regime was presented. We mainly used the sources and receivers which are in a transmission

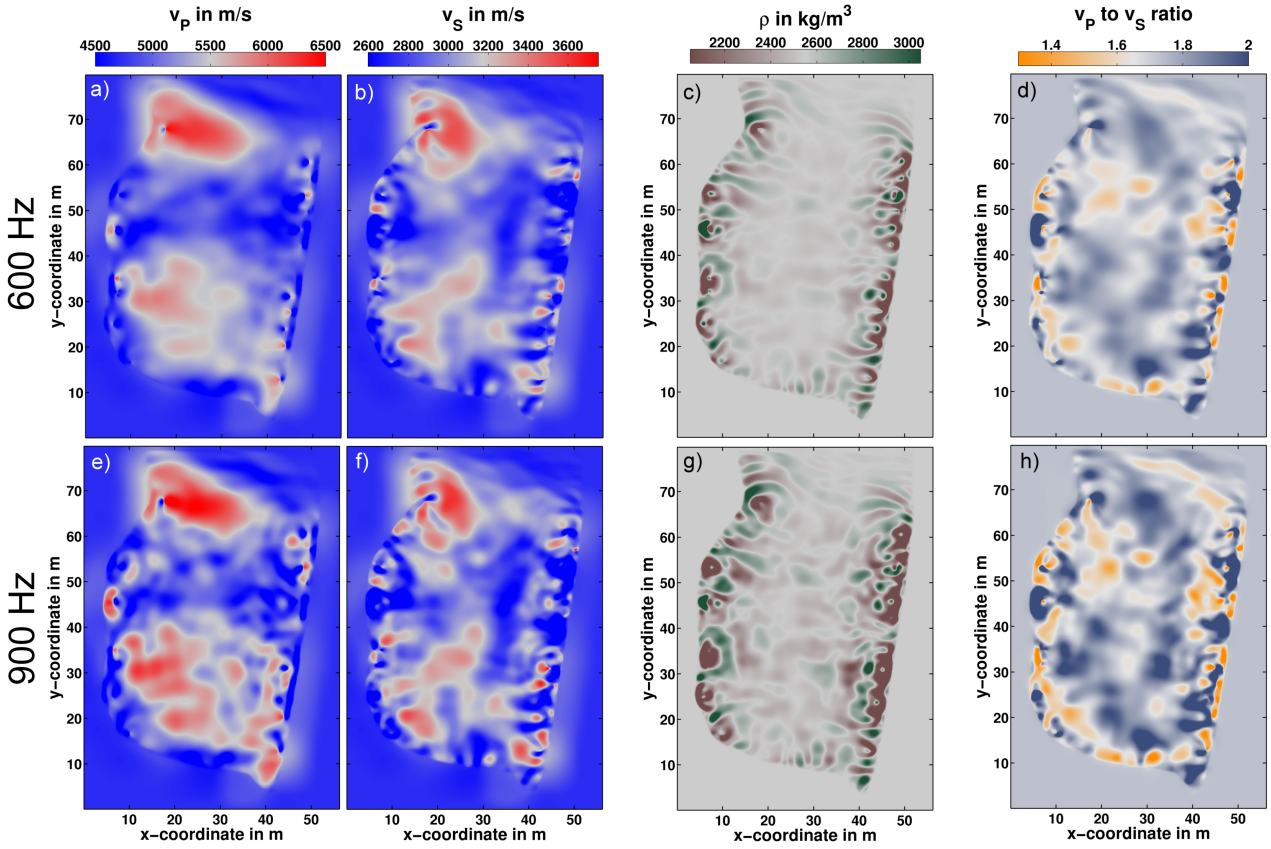

Figure 6.9: Inversion result for all three elastic parameters and the v_P and v_S ratio for two different frequencies ranges. The colour scale at the top is used for both frequencies.

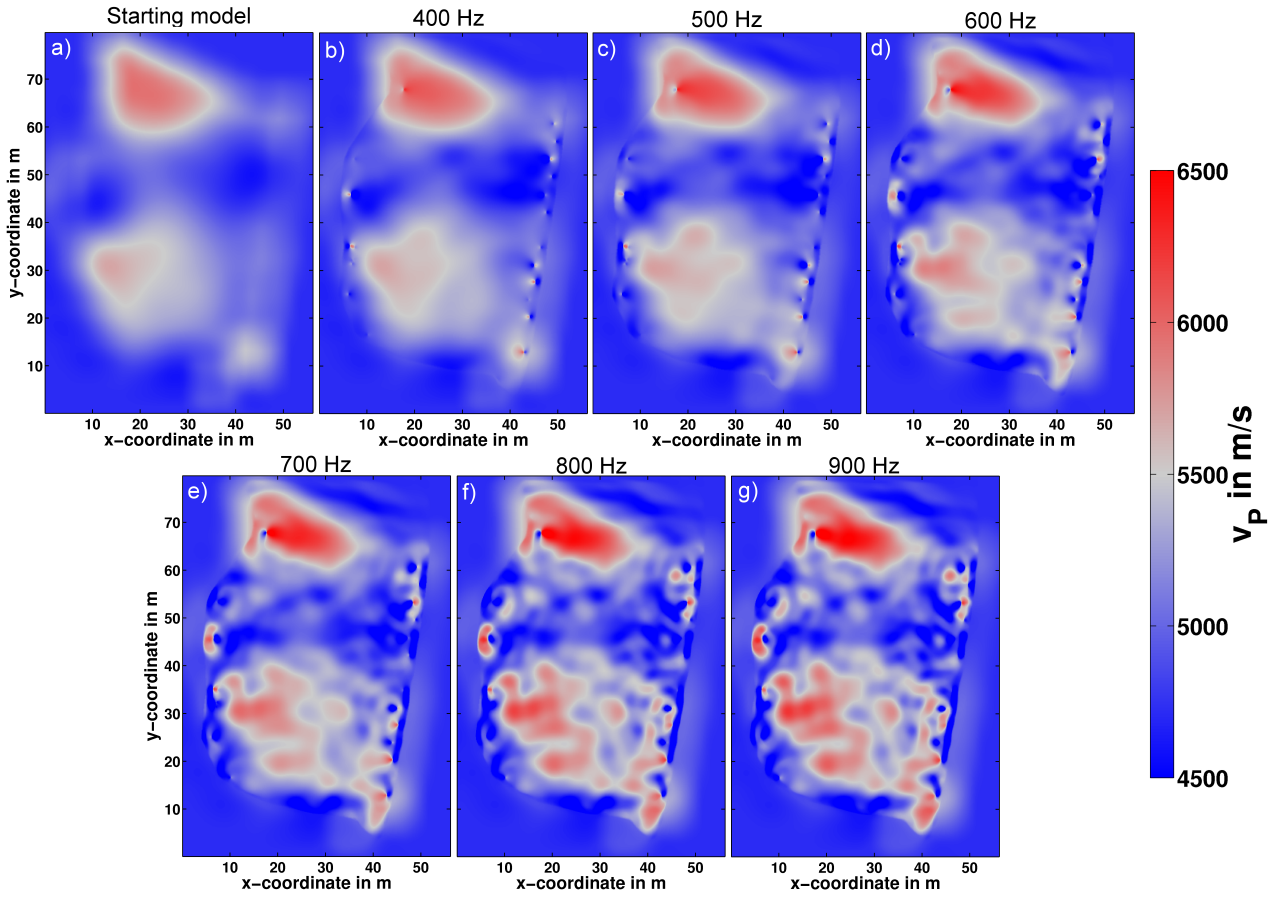

Figure 6.10: Evolution of the v_P model from the starting model to 900 Hz. Only an update of the velocities within the gneiss block is allowed. Always the final model of each frequency range is shown.

geometry for the inversion. The starting model was obtained with a travel-time tomography. With the used parameters, the misfit between the field and the synthetic data could be reduced significantly. The resulting velocities and density model fits the field data much better than the starting model. The inverted v_P models after each frequency stage are very consistent in its development. The three dominant areas in the starting model, the low velocity zone from left to right and the two high velocity zones above and on the left gallery along the *Wilhelm Stehender Süd*, are still observable in the inverted model although smaller structures are added especially for higher frequencies.
In the vicinity of the receivers and at the edge of the preconditioning taper, strong velocity contrasts which are treat as artefacts occur and should not be interpreted. The size of the additional structures is in the range of the minimum wavelength. The determined source time functions for different frequency ranges in the inversion do only differ little. Both are indications for a stable run of the inversion with a good convergence.
The v_S and the density model is not interpreted. The sensitivity of the inversion was restricted to the v_P model due to the preprocessing of the field data. With the data used in the inversion, also an acoustic inversion would be imaginable. As the the survey was designed for an elastic inversion due to the used sources which excited a force with a specific radiation pattern and geophones which recorded the ground velocity, the aim was to perform an elastic inversion. For a future application with including S-waves or even tunnel surface waves, we laid the foundation for a successful application in the future.

7 Summary and Conclusion

The aim of this thesis was to perform a seismic measurement in a hard rock environment below ground and, in particular, to invert the field data with the full-waveform inversion (FWI) approach.
The measurement took place at the GFZ-Underground-Laboratory (GFZ U-Lab) in the research and education mine *Reiche Zeche* of the Freiberg University of Mining and Technology (TU BAF). The field data was acquired with a high frequency magnetostrictive vibrator source and three-component receivers. With synthetic tests, the data preprocessing, the magnitude of the influence of various inversion parameters on the inversion results, the resolution potential and inversion strategies were investigated. Finally, an inversion of the field data with a 2D elastic FWI code was shown.

In Chapter 2, the underlying theory of the approaches applied in this thesis is explained in detail. We use a 2D elastic full-waveform inversion code called DENISE which uses the conjugated gradient method. The forward modelling and back-propagation of the wavefields is realised with the finite-difference (FD) scheme. With respect to the field data application, we focused on the source implementation, the choice of the objective function, the preconditioning and scaling of the gradient, and on a multi-scale approach with frequency filtering.
In order to imitate the source direction in the field measurement, we implemented sources in arbitrary directions which split the force density within the FD-scheme between the x- and y-component. The implementation was verified by a forward modelling with different source angles and by an evaluation of the corresponding radiation pattern of the P- and S-wave.

In Chapter 3 and 4, we introduce the performed seismic survey in hard rock conditions at the GFZ U-Lab and characterise the field data. The U-Lab provides the necessary equipment for performing seismic measurements. The test site encloses a gneiss block almost 50 m wide and 80 m long, surrounded by three galleries in a depth of approximately 150 m.
Previous projects and publications have already characterised the gneiss very well. We used a high frequency magnetostrictive vibrator source to excite a sweep signal from 300 - 3000 Hz at 76 positions spaced almost equidistantly (about 2 m). The actual source wavelet is the autocorrelation of the sweep signal, the so-called Klauder wavelet. With FD-modellings, we confirmed the zero-phase characteristics. That means, the first-arrival time corresponds to the maximum or minimum amplitude, respectively, which is important for picking the travel time.
30 three-component receivers mounted with anchors in the rock to avoid the influence of the excavation damage zone were used to record the seismic wavefield. All anchors are located in one horizontal plane along the galleries. Along one of these galleries the anchor depth is alternating between 1 m and 2 m, which we exploit to investigate ghost reflection phenomena. The dominant wavetypes are the tunnel surface wave, which travels at the rock-air interface along the galleries, and the direct P-wave for a transmission geometry.

S-wave arrivals are also observable, although they are often influenced by the coda of the P-wave.

In order to ensure comparability with simulated waveforms, the entire wavefield were rotated into the coordinate system of the FD-scheme. Afterwards, a 3D/2D transformation of the field data was applied. These are basic processing steps which are independent of the geometry and application purpose.
Due to the 2D acquisition geometry in one horizontal plane and the predominant perpendicular direction of the faults resulting from the geological mapping, we employed a 2D inversion. However, the remaining differences after the 3D/2D transformation between the modelling in 2D and the measurement in 3D result from an inaccurate modelling of tunnel surface waves. Thus, we focused on the inversion of the P-waves which required an appropriate preprocessing. First, we applied a trace muting of near offset receivers where the P-wave and the tunnel surface wave are not separated. Secondly, we applied a time windowing around the first-arrival time. This preprocessing was performed for nearly all synthetic tests as well as for the field data inversion.
We determined the maximum frequency in the field data to approximately 1000 Hz, although the source excited a maximum frequency of 3000 Hz. The drop of the spectral amplitude at higher frequencies may be caused by attenuation. However, this was not considered in this thesis. We could not find any evidence for anisotropy by investigating an angle dependency of the first-arrival times for the P-wave, at least within the horizontal plane. With a semblance analysis which is sensitive to differences in the waveforms in a common shot and a common receiver gather (CSG and CRG), we can conclude two facts. First, the varying depth of the receivers results in different reflection characteristics (ghost effect) for reflections at the rock-air interface. In the CRG we observed a checkerboard pattern for the alternating depth. For lower frequencies the pattern is reduced, the waveforms are more coherent. Secondly, we identified sources in the CSG and receivers in the CRG which have significantly different waveforms compared to their neighbours. Apparently, this is due to an imperfect coupling of or corrupt receivers. Consequently, we can only use 703 of 2280 possible source-receiver combinations.

In Chapter 5, the influence of different preprocessing parameters, the resolution potential and strategies for a better convergence of the FWI was tested in synthetic case studies. As a source wavelet, the Klauder wavelet extracted from the field data was used. We adopted the acquisition geometry from the field survey. For synthetic velocity models, we generated a random distributed velocity model which represents the crystalline rock and a velocity model with a checkerboard pattern. As a starting model, we used the result of a travel-time tomography for the random model and a homogeneous model for the checkerboard model, respectively.
A reference inversion result was calculated by applying no preprocessing to the data, i. e., no trace muting and no time windowing. On the one hand, we compared all further results to the reference P-wave velocity model and, on the other hand, by varying one parameter we compared it amongst each other. We quantified the differences of the inverted P-wave velocity model to the true model by calculating the absolute mean deviation. The parameter study showed the high non-linearity of the inversion. The perturbation of the parameters and the error of the inverted model have no linear behaviour.
Also we can only use 703 of 2280 possible source-receiver combinations, in synthetic tests we varies the number in both directions by taking approximately 250 to 1000 combinations into account. Above 500 combinations, the error between inverted and true model vary

little without a clear trend around an average value of 2.15 %. By a reduction to 250 of 2280 combinations, the error increased to 2.45 %. In addition, in this work, a lower number of receivers lead to a larger error of the inverted model compared to a lower number of sources. For the time windowing, we chose different window lengths between 0.005 s and 0.00005 s. The error between inverted model and true model increased linearly with an increasing time window length, except for 0.0015 s. The window length for the field data was set to 0.001 s to ensure to invert as little noise as possible but still have a reasonable P-phase.
To summarise, the preprocessing by only using the first P-wave arrivals provides very promising inversion results for the parameters we will use in the field data application. Starting from a model obtained by a first-arrival travel-time tomography, most of the structures of the true model were recovered.
For the coordinates of the sources and receivers in the field survey, we cannot state an exact error regarding their position. To investigate the influence of wrong coordinates, we added a random number with a maximum value of ± 0.25 m, ± 0.50 m and ± 1.00 m to the x- and y-coordinate, respectively. For all tests, the inversion creates artefacts in the vicinity of the receiver positions and only for a maximum perturbation of 0.25 m the inversion can reconstruct a proper model. This corresponds to the estimated error in the field measurement.
To evaluate the resolution potential of the FWI, we used the checkerboard model which has a defined structure size. We varied the size and the velocity perturbation of the blocks, and the maximum frequency of the source. The FWI was able to recover structures with the size of about half a wavelength. This means for the field data, that we can smooth the model with a proper filter to remove small-scale artefacts without changing reliable structures in the inversion result. The maximum velocity perturbation of ± 7.5 % which could be inverted is quite large. For the field data inversion we expect a much smaller value.
Next, we discussed the multi-scale approach with frequency filtering for a poor starting model. We demonstrate the approach with the random distributed velocity model as the true model and a homogeneous starting model. By adding continuously higher frequencies from 500 Hz to 1500 Hz to the inversion, the convergence increased dramatically. Comparing the inversion results with and without frequency filtering, the gain in resolution with filtering is enormous. This is an important approach for the field data because the inversion is able to converge with a poor starting model.
Next, the influence of the S-wave velocity by changing the Poission ratio of the true model from 0.15 to 0.35 is investigated. The typical Poission ratio for hard rock of 0.25 was used for the starting model. In the range of a Poission ratio of 0.20 to 0.30, the inversion was able to reconstruct the P-wave velocity model with an average error of 2.20 %. The error increased to 2.85 % for Poission ratios of 0.15 and 0.35. The test showed the trade-off between the S-wave and P-wave velocity model, even only P-waves are considered. For the field data inversion, we will use the typical Poission value of 0.25 as we have no further information on the S-wave velocity structure. A subsequent test, varies the density of the starting model between 2100 kg/m^3 and 3000 kg/m^3 with a constant density of 2550 kg/m^3 for the true model. For the synthetic inversion results, the starting density value has no influence on the velocity models, even though the inversion must be allowed to change the density model.
Similar to the field data, with a semblance analysis for different modelling scenarios we can observe that the intensity of the ghost reflections is frequency dependent with a smaller effect for low frequencies. For a 2D modelling with a rock-air interface, the transition zone acts like an infinitesimally extended interface where all seismic energy is reflected. For a 3D modelling with a real 3D gallery the reflected energy is less and matches better to the the

field data. Nevertheless, we conclude to invert the field data in 2D with a gallery-free model without the rock-air interface which fits the behaviour of the field data best.

Finally, in Chapter 6, we performed a full-waveform inversion with the acquired field data in the GFZ U-Lab. At first, we used the travel-time tomography software GeoTomCG to obtain a P-wave starting velocity model. The starting model for the S-wave velocity was calculated via a Poission ratio of 0.25 and the density was chosen homogeneous with 2550 kg/m^3.
In the FWI, the multi-stage approach with frequency filtering starting at 400 Hz was applied. Before the first iteration, we had to determine the source time functions for each source based on the starting model. The shape of the inverted wavelets is very similar to the expected Klauder wavelet, although it differs in the amplitude of the sidelobes. For all sources, the source time function has a similar shape. By comparing forward modelled seismograms with the actually determined source wavelets on the starting velocity model, in the majority, the waveforms already match very well for most of the receivers. Nevertheless, some arrival times are inaccurate. As we used a sweep as a source signal, we are supposed to know the shape of the source wavelet. However, without the source time function inversion, the inversion produces significant artefacts in the velocity model.
In a first investigation, we inverted only for single sources to get an impression how the FWI changes the velocity model. For each source, the inversion is able to converge to velocity models which explain the field data perfectly. Nevertheless, the inverted velocity models are not interpretable regarding the velocity distribution. Consequently, we inverted all sources simultaneously.

We only used the x-component because most of the energy of the P-wave is recorded on this component for a transmission geometry. An update of the gallery-free velocity model is only allowed within the gneiss because, as in the field survey, the seismic waves can only travel within the block. The frequency in the inversion is increased by 100 Hz if the FWI failed to decrease the misfit. After adding higher frequencies, the source time function is recomputed with the current velocity model. We stopped the inversion at 900 Hz.
The general velocity distribution of the P-wave velocity model is consistent for all frequency ranges. We could achieve a small-scale velocity distribution of the gneiss block. Nevertheless, 3D effects could influence the result which we cannot proof. Although the inversion added small-scale details to the velocity model, the dominant structures of the starting model remain the same. Indeed, the influence of the receiver artefacts is very strong. Both, the S-wave velocity and the density model do not coincide in their structures with the P-wave velocity model. By only inverting the P-phase, the FWI is also just sensitive for the P-wave velocity model. Nevertheless, the realistic P- and S-wave velocity ratio around the centre of the gneiss block indicates a stable and trustful inversion result. However, at the gallery walls negative Poission ratios occur due to the strong artefacts.
The general shape of the source time functions is similar within the different frequency ranges. This is also an evidence for a consistent inversion. Changes in the source time functions for different frequencies indicate an alternating and inconsistent update of the model and the source time function.

With the shown preprocessing the inversion is mostly sensitive to the P-wave. Thus, we only interpret the P-wave velocity model. With the data used in the inversion, also an acoustic inversion would be imaginable. Nevertheless, the original survey geometry and equipment was designed for an elastic inversion. We used sources which excited a force with a specific radiation pattern and geophones which recorded the ground velocity in three directions.

The expectancy was to have a clear P- and S-wave arrival and to invert for both wavetypes. But, it turned out, that the S-wave arrival is influenced by the P-wave coda. At first, we decided to only invert the relatively clear P-wave arrivals but still with an elastic code and the intention to invert both phases later on. The effort to investigate the preprocessing to invert only the P-wave with a 2D code but having 3D data and 3D effects was very large. The complexity of the misfit function would increase dramatically by adding the S-wave. Therefore, we concluded not to use the S-wave explicitly in this thesis. We only interpreted the S-wave velocity model according to the experiences of the synthetic tests but not in detail. Nevertheless, we presented some essential steps towards an elastic inversion in hard rock conditions.

We showed a successful inversion of field data in a hard rock regime at the GFZ U-Lab. With the used measurement equipment and the characterisation and preprocessing of the data, also other applications are possible. With the highly regulated magnetostrictive double vibrator, we have the potential to measure small changes in the host rock for permanent installations for monitoring developments in service. To identify receivers and sources which have differences in the coupling or are corrupt, the semblance analysis is an approach which should be performed before the full-waveform inversion. In addition, the inversion strategy neglecting the rock-air interface and only allowing updates within the host rock was also necessary and successful and can be transferred to other surveys below ground. Regarding computational resources, 3D inversions are highly demanding and are thus not feasible in the near future.

For future surveys in underground developments, we suggest to involve a larger number of receivers, also we know that this is a difficult task. The number of sources must be aligned to the number of receivers to ensure a sufficient illumination. For the source, we suggest to try an impulsive source for a larger signal to noise ratio. The receivers should be mounted with anchors in the host rock to avoid influences by the excavation damage zone.

Although the FWI is a complex multi-parameter problem, we recommend its application in hard rock regimes, e. g., for seismic imaging around a tunnel to identify rock changes during the construction period or to monitor the rock conditions between two tunnels to obtain a high resolution image.

Bibliography

Aki, K. and Richards, P. G. (2002). *Quantitative Seismology*. University Science Books, Sausalito, CA., 2nd edition.

Alford, R. M., Kelly, K. R., and Boore, D. M. (1974). Accuracy of finite-difference modeling of the acoustic wave equation. *Geophysics*, 39(6):834–842.

Auer, L., Nuber, A. M., Greenhalgh, S. A., Maurer, H., and Marelli, S. (2013). A critical appraisal of asymptotic 3D-to-2D data transformation in full-waveform seismic crosshole tomography. *Geophysics*, 78(6):R235–R247.

Barnes, C., Charara, M., and Tsuchiya, T. (2008). Feasibility study for an anisotropic full waveform inversion of cross-well seismic data. *Geophysical Prospecting*, 56(6):897–906.

Bauer, K., Pratt, R. G., Weber, M. H., Ryberg, T., Haberland, C., and Shimizu, S. (2005). Mallik 2002 cross-well seismic experiment: project design, data acquisition, and modelling studies. In Dallimore, S. R. and Collett, T. S., editors, *Scientific Results from Mallik 2002 Gas Hydrate Production Research Well Program*. Geological Survey of Canada Bulletin 585, Mackenzie Delta, Northwest Territories, Canada.

Bayer, M. (1999). *Die Himmelfahrt Fundgrube: Ein Führer durch das Lehr- und Besucherbergwerk der TU Bergakademie Freiberg*. Der Rektor der TU Bergakademie Freiberg, https://katalog.ub.tu-freiberg.de/Record/0003192504 (last access: 02.04.2014).

Bleibinhaus, F., Lester, R. W., and Hole, J. A. (2009). Applying waveform inversion to wide-angle seismic surveys. *Tectonophysics*, 472(1-4):238–248.

Bohlen, T. (1998). Viskoelastische FD-Modellierung seismischer Wellen zur Interpretation gemessener Seismogramme. PhD thesis, Kiel University.

Bohlen, T. (2002). Parallel 3-D viscoelastic finite difference seismic modelling. *Computers & Geosciences*, 28(8):887–899.

Bohlen, T., De Nil, D., Köhn, D., and Jetschny, S. (2012). *User Guide: SOFI2D - seismic modeling with finite differences - elastic and viscoelastic version*. Karlsruhe Institute of Technology, http://www.gpi.kit.edu/downloads/guide_sofi2D.pdf (last access: 08.05.2014).

Boonyasiriwat, C., Schuster, G. T., Valasek, P., and Cao, W. (2010). Applications of multiscale waveform inversion to marine data using a flooding technique and dynamic early-arrival windows. *Geophysics*, 75(6):R129–R136.

Borm, G., Barth, M., Krüger, K., Mielitz, S., and Mikulla, S. (2008a). *Seismische Quelle mit adaptiver Regelung und entsprechendes Verfahren*. Specification DE102007013413A1, Date: 09.10.2008.

Borm, G. and Giese, R. (2003). Geophysical investigations: integrated seismic imaging system for geological prediction during tunnel construction. In Kolymbas, D., editor, *Rational Tunnelling Summerschool*, Innsbruck. Advances in geotechnical engineering and tunnelling 8, Logos Verlag, 225-234.

Borm, G., Giese, R., Maushake, B., Otto, P., and Paul, R. (2008b). *Verankerungseinrichtung für eine Sensoreinrichtung zur Erfassung von seismischen Signalen in geologischen Strukturen oder Bauwerken*. Specification DE102006007474B4, Date: 31.07.2008.

Borm, G., Schmidt-Hattenberger, C., Giese, R., Mielitz, S., and Bribach, J. (2003). *Verankerungseinrichtung mit seismischem Sensor*. Specification DE000019852455C2, Date: 24.12.2003.

Bozdağ, E., Trampert, J., and Tromp, J. (2011). Misfit functions for full waveform inversion based on instantaneous phase and envelope measurements. *Geophysical Journal International*, 185(2):845–870.

Brenders, A. J. (2011). Strategies for waveform tomography for long-offset, 2-D exploration seismic data. PhD thesis, The University of Western Ontario, Canada.

Brossier, R., Operto, S., and Virieux, J. (2009). Seismic imaging of complex onshore structures by 2D elastic frequency-domain full-waveform inversion. *Geophysics*, 74(6):WCC105–WCC118.

Bunks, C., Saleck, F., Zaleski, S., and Chavent, G. (1995). Multiscale seismic waveform inversion. *Geophysics*, 60(5):1457–1473.

Butzer, S., Kurzmann, A., and Bohlen, T. (2013). 3D elastic full-waveform inversion of small-scale heterogeneities in transmission geometry. *Geophysical Prospecting*, 61(6):1238–1251.

Causse, E., Mittet, R., and Ursin, B. (1999). Preconditioning of full waveform inversion in viscoacoustic media. *Geophysics*, 64(1):130–145.

Choi, Y. and Alkhalifah, T. (2012). Application of multi-source waveform inversion to marine streamer data using the global correlation norm. *Geophysical Prospecting*, 60(4):748–758.

Costain, J. K. and Coruh, C. (2004). *Basic Theory in Reflection Seismology*. Handbook of Geophysical Exploration: Seismic Exploration. Elsevier Science, Amsterdam, The Netherlands.

Courant, R., Friedrichs, K., and Lewy, H. (1928). Über die partiellen Differenzengleichungen der mathematischen Physik. *Mathematische Annalen*, 100(1):32–74.

Courant, R., Friedrichs, K., and Lewy, H. (1967). On the partial difference equations of mathematical physics. *IBM Journal of Research and Development*, 11(2):215–234.

Crase, E., Pica, A., Noble, M., McDonald, J., and Tarantola, A. (1990). Robust elastic nonlinear waveform inversion: Application to real data. *Geophysics*, 55(5):527–538.

Cunha, C. (1993). Elastic modeling in discontinuous media. *Geophyiscs*, 58(12):1840–1851.

Dickmann, T. and Sanders, B. K. (1996). Drivage-Concurrent Tunnel Sesmic Prediction (TSP). *Felsbau*, 14:406–411.

Dougherty, M. and Stephen, R. (1988). Seismic energy partitioning and scattering in laterally heterogeneous ocean crust. *Pure and Applied Geophysics*, 128(1-2):195–229.

Fichtner, A. (2011). *Full Seismic Waveform Modelling and Inversion*. Advances in Geophysical and Environmental Mechanics and Mathematics. Springer.

Fichtner, A., Kennett, B. L. N., Igel, H., and Bunge, H.-P. (2009). Full seismic waveform tomography for upper-mantle structure in the Australasian region using adjoint methods. *Geophysical Journal International*, 179(3):1703–1725.

Forbriger, T., Groos, L., and Schäfer, M. (2014). Line-source simulation for shallow-seismic data. Part 1: Theoretical background. *Geophysical Journal International*, 198(3):1387–1404.

Geyer, R. L. (1989). *Vibroseis*. Geophysics Reprint Series, No 11. Society of Exploration Geophysicists.

Ghose, S., Hamburger, M. W., and Virieux, J. (1998). Three-dimensional velocity structure and earthquake locations beneath the northern Tien Shan of Kyrgyzstan, central Asia. *Journal of Geophysical Research: Solid Earth*, 103(B2):2725–2748.

Giese, R., Klose, C., and Borm, G. (2005). In situ seismic investigations of fault zones in the Leventina Gneiss Complex of the Swiss Central Alps. In Harvey, P. K., Brewer, T. S., Pezard, P., and Petrov, V. A., editors, *Petrophysical Properties of Crystalline Rocks*. Geological Society, London, Special Publications, 240:15-24.

Goff, J. A. and Jordan, T. H. (1988). Stochastic modeling of seafloor morphology: Inversion of sea beam data for second-order statistics. *Journal of Geophysical Research: Solid Earth*, 93(B11):13589–13608.

Gradstein, F. M., Ogg, J. G., Schmitz, M., and Ogg, G. (2012). *The Geologic Time Scale 2012*. Elsevier Science & Technology Books, 1st edition.

Groos, L. (2013). 2D full waveform inversion of shallow seismic Rayleigh waves. PhD thesis, Karlsruhe Institute of Technology.

Groos, L., Schäfer, M., Forbriger, T., and Bohlen, T. (2014). The role of attenuation in 2D full-waveform inversion of shallow-seismic body and Rayleigh waves. *Geophysics*, GEO-2013-0462.

Heider, S., Jetschny, S., Bohlen, T., and Giese, R. (2012). Towards an application of an elastic FWI for a measurement below ground in a crystalline environment. In *SEG Technical Program Expanded Abstracts*.

Hofmann, J. (1965). *Zur Petrotektonik des Graugneiskomplexes von Freiberg*. TU Bergakademie Freiberg. Freiberger Forschungsheft C292. Dt. Verlag für Grundstoffindustrie, Leipzig.

Hurtig, E. (1967). Zum Problem der Anisotropie petrophysikalischer Parameter in geologischen Körpern. Habilitation, Leipzig University.

Ikelle, L. T. and Amundsen, L. (2005). *Introduction to Petroleum Seismology*. Society of Exploration Geophysicists.

Jetschny, S. (2010). Seismic prediction and imaging of geological structures ahead of a tunnel using surface waves. PhD thesis, Karlsruhe Institute of Technology.

Kirk, P. (1981). Vibroseis processing. In Fitch, A., editor, *Developments in Geophysical Exploration Methods*, The Developments Series, pages 37–52. Springer Netherlands.

Kneib, G. (1995). The statistical nature of the upper continental crystalline crust derived from in situ seismic measurements. *Geophysical Journal International*, 122(2):594–616.

Kneib, G., Kassel, A., and Lorenz, K. (2000). Automatic seismic prediction ahead of the tunnel boring machine. *First Break*, 18(7):295–302.

Köhn, D. (2011). Time domain 2D elastic full waveform tomography. PhD thesis, Kiel University.

Köhn, D., De Nil, D., Kurzmann, A., Groos, L., Schäfer, M., and Heider, S. (2013). *DENISE - User manual*. Kiel University and Karlsruhe Institute of Technology, http://www.gpi.kit.edu/downloads/manual_DENISE.pdf (last access: 08.05.2014).

Köhn, D., De Nil, D., Kurzmann, A., Przebindowska, A., and Bohlen, T. (2012). On the influence of model parametrization in elastic full waveform tomography. *Geophysical Journal International*, 191(1):325–345.

Kolymbas, D. (1998). *Geotechnik - Tunnelbau und Tunnelmechanik: Eine systematische Einführung mit besonderer Berücksichtigung mechanischer Probleme*. Springer.

Komatitsch, D. and Martin, R. (2007). An unsplit convolutional perfectly matched layer improved at grazing incidence for the seismic wave equation. *Geophysics*, 72(5):SM155–SM167.

Koop (1962). *Blatt Freiberg 24/1 : Sohlengruppen-Grundriss*.

Kopf, M., Rechlin, A., Reinhardt, J., Michael, S., and Wenke, A. (2008). *Protokoll zur Untertagekartierung im Lehr- und Forschungsbergwerk Reiche Zeche der TU Bergakademie Freiberg*. http://www.geo-t.de/downloads/endbericht_spwd_geot.pdf (last access: 05.05.2014).

Krauss, F. (2013). Seismic attenuation tomography in the education and research mine Reiche Zeche and at the GFZ-Underground-Lab. Master's thesis, TU Bergakademie Freiberg.

Krauss, F., Giese, R., Alexandrakis, C., and Buske, S. (2014). Seismic travel-time and attenuation tomography to characterize the excavation damaged zone and the surrounding rock mass of a newly excavated ramp and chamber. *International Journal of Rock Mechanics and Mining Sciences*, 70:524–532.

Kurzmann, A. (2012). Applications of 2D and 3D full waveform tomography in acoustic and viscoacoustic complex media. PhD thesis, Karlsruhe Institute of Technology.

Kurzmann, A., Köhn, D., Przebindowska, A., Nguyen, N., and Bohlen, T. (2009). 2D acoustic full waveform tomography: performance and optimization. In *71th EAGE Conference and Technical Exhibition*. Extended Abstract.

Lay, T. and Wallace, T. (1995). *Modern Global Seismology*. International Geophysics. Elsevier Science.

Lehmann, B. (2007). *Seismic Traveltime Tomography for Engineering and Exploration Applications*. EAGE publications.

Levander, A. R. (1988). Fourth-order finite-difference P-SV seismograms. *Geophysics*, 53(11):1425–1436.

Lüth, S., Bohlen, T., Giese, R., Heider, S., Hock, S., Jetschny, S., Polom, U., Wadas, S., and Rechlin, A. (2014). Seismic Tomography and Monitoring in Underground Structures: Developments in the Freiberg Reiche Zeche Underground Lab (Freiberg, Germany) and Their Application in Underground Construction (SOUND). In Weber, M. and Münch, U., editors, *Tomography of the Earth's Crust: From Geophysical Sounding to Real-Time Monitoring*, Advanced Technologies in Earth Sciences, pages 115–133. Springer International Publishing.

Lüth, S., Buske, S., Goertz, A., and Giese, R. (2005). Fresnel-volume migration of multicomponent data. *Geophysics*, 70(6):S121–S129.

Lüth, S., Giese, R., Otto, P., Krüger, K., Mielitz, S., Bohlen, T., and Dickmann, T. (2006). Seismic investigations of the Piora Basin using S-wave conversions at the tunnel face of the Piora adit (Gotthard Base Tunnel). *International Journal of Rock Mechanics and Mining Sciences*, 45:86–93.

Lytle, R. and Lawrence Livermore Laboratory (1978). *Electromagnetic cross-borehole survey of a site proposed for an urban transit station*. Department of Energy [Office of the Assistant Secretary for Defense Programs], Lawrence Livermore Laboratory.

Manukyan, E. (2011). Seismic monitoring and elastic full waveform inversion investigations applied to the radioactive waste disposal issue. PhD thesis, ETH.

Maurer, H., Greenhalgh, S. A., Manukyan, E., Marelli, S., and Green, A. G. (2012). Receiver-coupling effects in seismic waveform inversions. *Geophysics*, 77(1):R57–R63.

Mora, P. (1987). Nonlinear two-dimensional elastic inversion of multioffset seismic data. *Geophysics*, 52(9):1211–1228.

Murawski, H. and Meyer, W. (2010). *Geologisches Wörterbuch*. Spektrum Akademischer Verlag, Heidelberg, 12th revised and extended edition.

Nocedal, J. and Wright, S. (1999). *Numerical Optimization*. Springer series in operations research and financial engineering. Springer.

Peterson, J. E., Paulsson, B. N. P., and McEvilly, T. V. (1985). Applications of algebraic reconstruction techniques to crosshole seismic data. *Geophysics*, 50(10):1566–1580.

Petronio, L., Poletto, F., and Schleifer, A. (2007). Interface prediction ahead of the excavation front by the tunnel-seismic-while-drilling (TSWD) method. *Geophysics*, 72(4):G39–G44.

Pica, A., Diet, J. P., and Tarantola, A. (1990). Nonlinear inversion of seismic reflection data in a laterally invariant medium. *Geophysics*, 55(3):284–292.

Pratt, R. G. (1999). Seismic waveform inversion in the frequency domain; Part 1, Theory and verification in a physical scale model. *Geophysics*, 64(3):888–901.

Pratt, R. G. and Goulty, N. R. (1991). Combining wave-equation imaging with traveltime tomography to form high-resolution images from crosshole data. *Geophysics*, 56(2):208–224.

Pratt, R. G., Hou, F., Bauer, K., and Weber, M. H. (2005). Waveform tomography images of velocity and inelastic attenuation from the Mallik 2002 cross-hole seismic surveys. In Dallimore, S. R. and Collett, T. S., editors, *Scientific Results from Mallik 2002 Gas Hydrate Production Research Well Program*. Geological Survey of Canada Bulletin 585, Mackenzie Delta, Northwest Territories, Canada.

Pratt, R. G. and Shipp, R. M. (1999). Seismic waveform inversion in the frequency domain; Part 2; Fault delineation in sediments using crosshole data. *Geophysics*, 64(3):902–914.

Pratt, R. G. and Worthington, M. H. (1988). The application of diffraction tomography to cross-hole seismic data. *Geophysics*, 53(10):1284–1294.

Przebindowska, A. (2013). Acoustic full waveform inversion of marine reflection seismic data. PhD thesis, Karlsruhe Institute of Technology.

Rao, Y. and Wang, Y. (2011). Crosshole seismic tomography including the anisotropy effect. *Journal of Geophysics and Engineering*, 8(2):316.

Rao, Y., Wang, Y., and Morgan, J. V. (2006). Crosshole seismic waveform tomography - II. Resolution analysis. *Geophysical Journal International*, 166(3):1237–1248.

Richter, H. (2010). Hochauflösende seismische Tomographie zur Charakterisierung eines Gebirgsblocks im Lehr- und Forschungsbergwerk Reiche Zeche - Freiberg unter Verwendung von Strecken- und Bohrlochmessdaten. Master's thesis, University of Potsdam.

Romdhane, G., Grandjean, G., Brossier, R., Rejiba, F., Operto, S., and Virieux, J. (2011). Shallow-structure characterization by 2D elastic full-waveform inversion. *Geophysics*, 76(3):R81–R93.

Sebastian, U. (2013). *Die Geologie des Erzgebirges*. Springer Spektrum, Berlin, Heidelberg.

Shearer, P. (1999). *Introduction to Seismology*. Cambridge University Press.

Sheng, J., Leeds, A., Buddensiek, M., and Schuster, G. T. (2006). Early arrival waveform tomography on near-surface refraction data. *Geophysics*, 71(4):U47–U57.

Sheriff, R. (2002). *Encyclopedic Dictionary of Exploration Geophysics*. Geophysical references series. Society of Exploration Geophysicists.

Sirgue, L. and Pratt, R. G. (2004). Efficient waveform inversion and imaging: A strategy for selecting temporal frequencies. *Geophysics*, 69(1):231–248.

Sourbier, F., Operto, S., Virieux, J., Amestoy, P., and L'Excellent, J.-Y. (2009). FWT2D: A Massively Parallel Program for Frequency-domain Full-waveform Tomography of Wide-aperture Seismic data - Part 2. *Computers & Geosciences*, 35(3):496–514.

Sun, R. and McMechan, G. A. (1992). 2-D full-wavefield inversion for wide-aperture, elastic, seismic data. *Geophysical Journal International*, 111(1):1–10.

Tarantola, A. (1984). Linearized inversion of seismic reflection data. *Geophysical Prospecting*, 32(6):998–1015.

Trampert, J. and Leveque, J.-J. (1990). Simultaneous iterative reconstruction technique: Physical interpretation based on the generalized least squares solution. *Journal of Geophysical Research: Solid Earth*, 95(B8):12553–12559.

Tromp, J., Tape, C., and Liu, Q. (2005). Seismic tomography, adjoint methods, time reversal and banana-doughnut kernels. *Geophysical Journal International*, 160(1):195–216.

Tweeton, D. (2011). *Installing and running the three-dimensinal tomography program GEOTOMCG*. Apple Valley, MN 55124, USA, http://dev.geotom.net/ (last access: 13.04.2014).

Virieux, J. (1986). P-SV wave propagation in heterogeneous media; velocity-stress finite-difference method. *Geophysics*, 51(4):889–901.

Virieux, J. and Operto, S. (2009). An overview of full-waveform inversion in exploration geophysics. *Geophysics*, 74(6):WCC1–WCC26.

Wagenbreth, O. and Steiner, W. (1985). *Geologische Streifzüge : Landschaft und Erdgeschichte zwischen Kap Arkona und Fichtelberg*. Deutscher Verlag für Grundstoffindustrie, Leipzig, 2nd edition.

Wang, Y. (2011). Seismic anisotropy estimated from P-wave arrival times in crosshole measurements. *Geophysical Journal International*, 184(3):1311–1316.

Yilmaz, Ö. (2001). *Seismic Data Analysis: Vol.1*. Society of Exploration Geophysicists, Tulsa.

Zhang, F., Juhlin, C., Cosma, C., Tryggvason, A., and Pratt, R. G. (2012). Cross-well seismic waveform tomography for monitoring CO2 injection: a case study from the Ketzin Site, Germany. *Geophysical Journal International*, 189(1):629–646.

Zhao, D., Hasegawa, A., and Horiuchi, S. (1992). Tomographic imaging of P and S wave velocity structure beneath northeastern Japan. *Journal of Geophysical Research: Solid Earth*, 97(B13):19909–19928.

Zhou, C., Schuster, G. T., Hassanzadeh, S., and Harris, J. M. (1997). Elastic wave equation traveltime and waveform inversion of crosswell data. *Geophysics*, 62(3):853–868.

List of Figures

List of Tables

Appendix A

Correlograms for Shot 1, 20, 40, 60 and 76

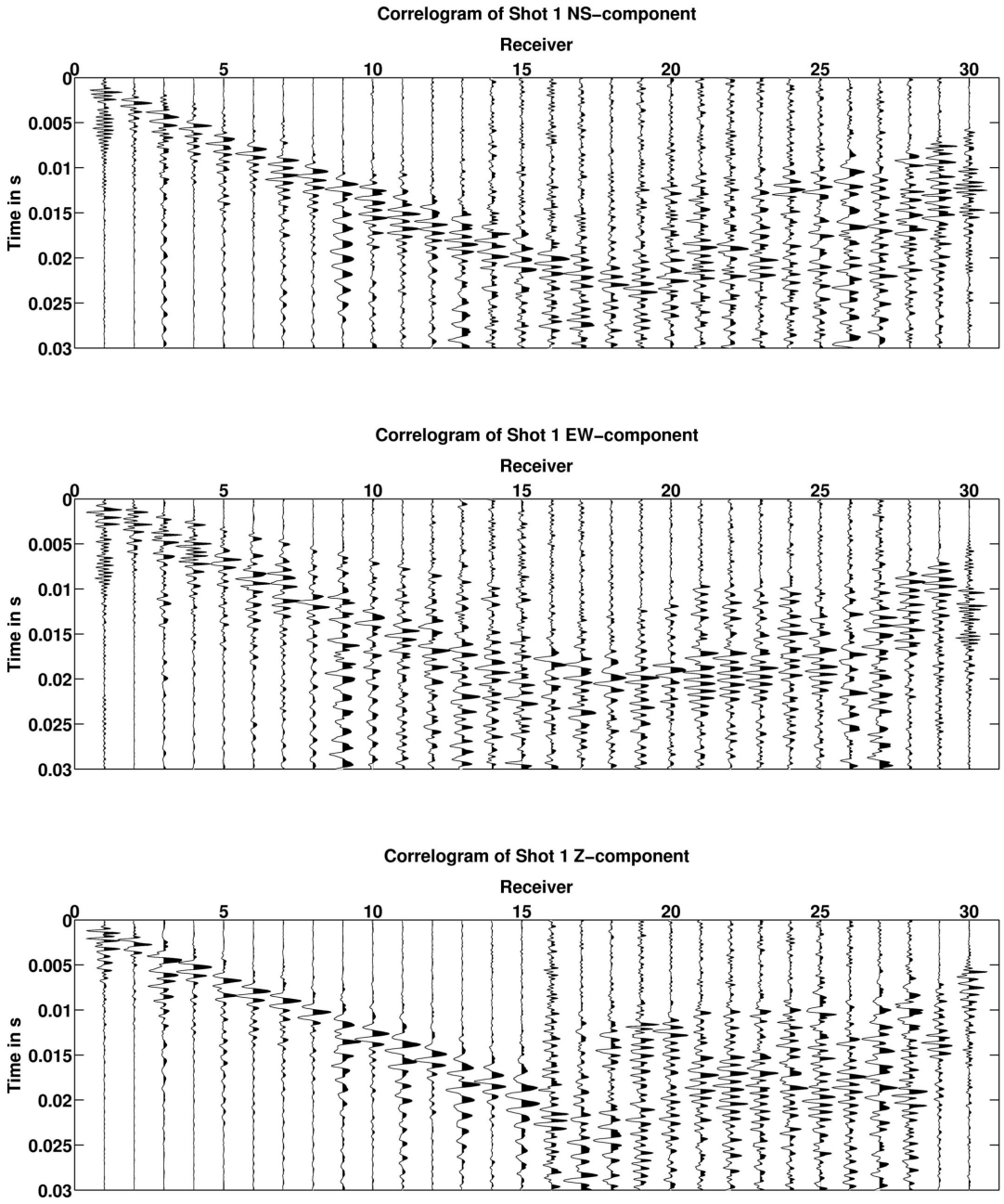

Figure A.1: Correlograms of the field data for Shot 1.

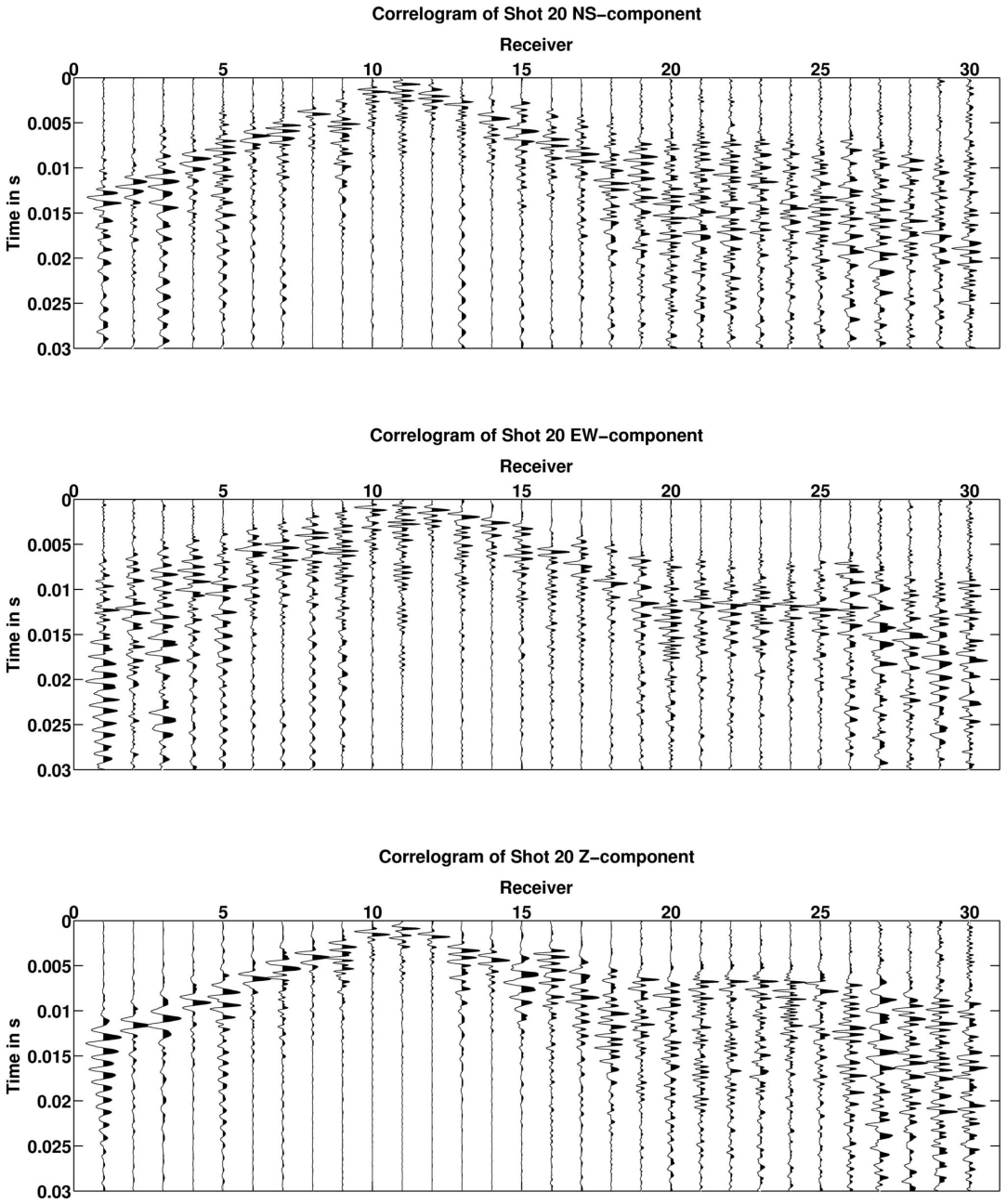

Figure A.2: Correlograms of the field data for Shot 20.

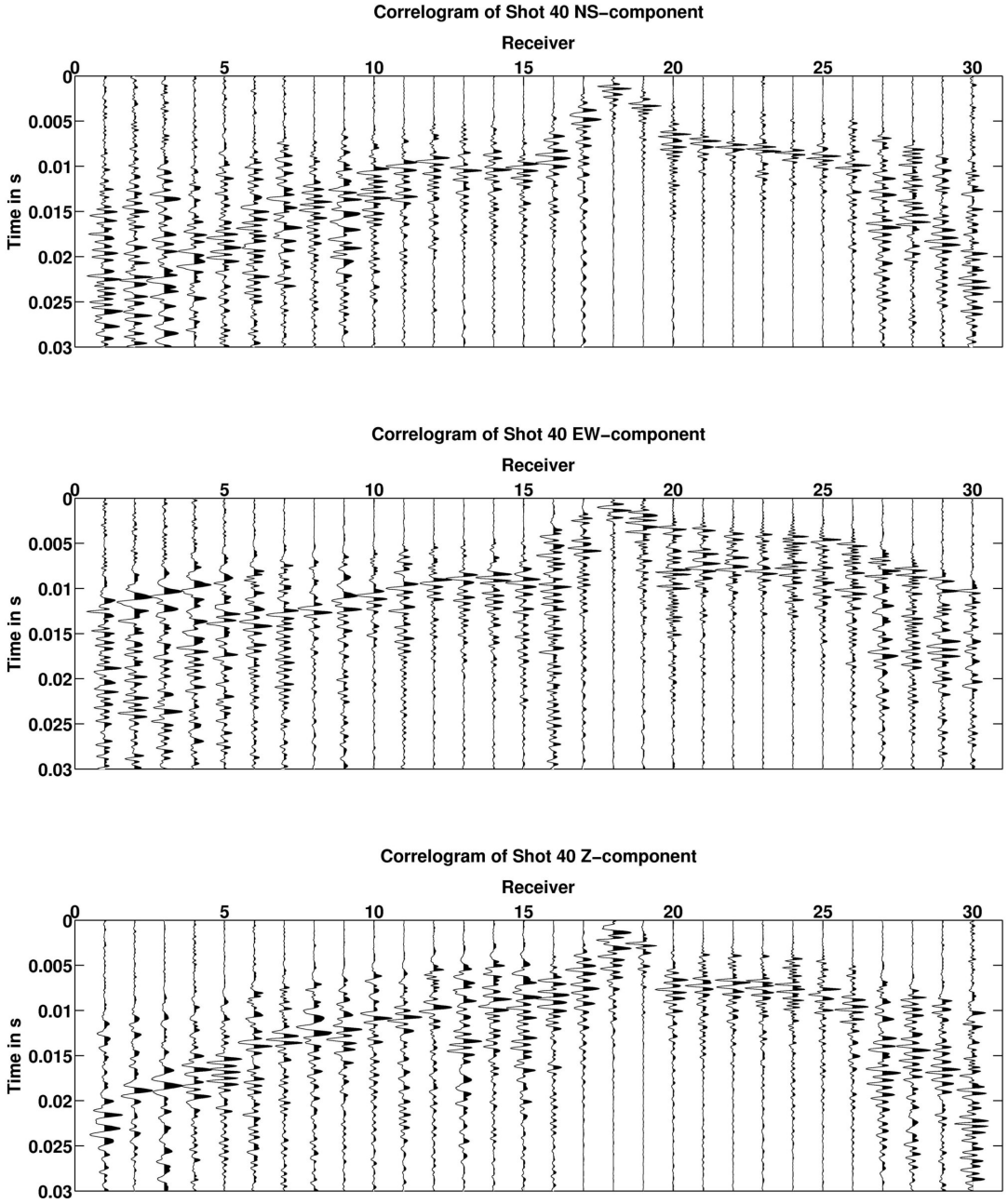

Figure A.3: Correlograms of the field data for Shot 40.

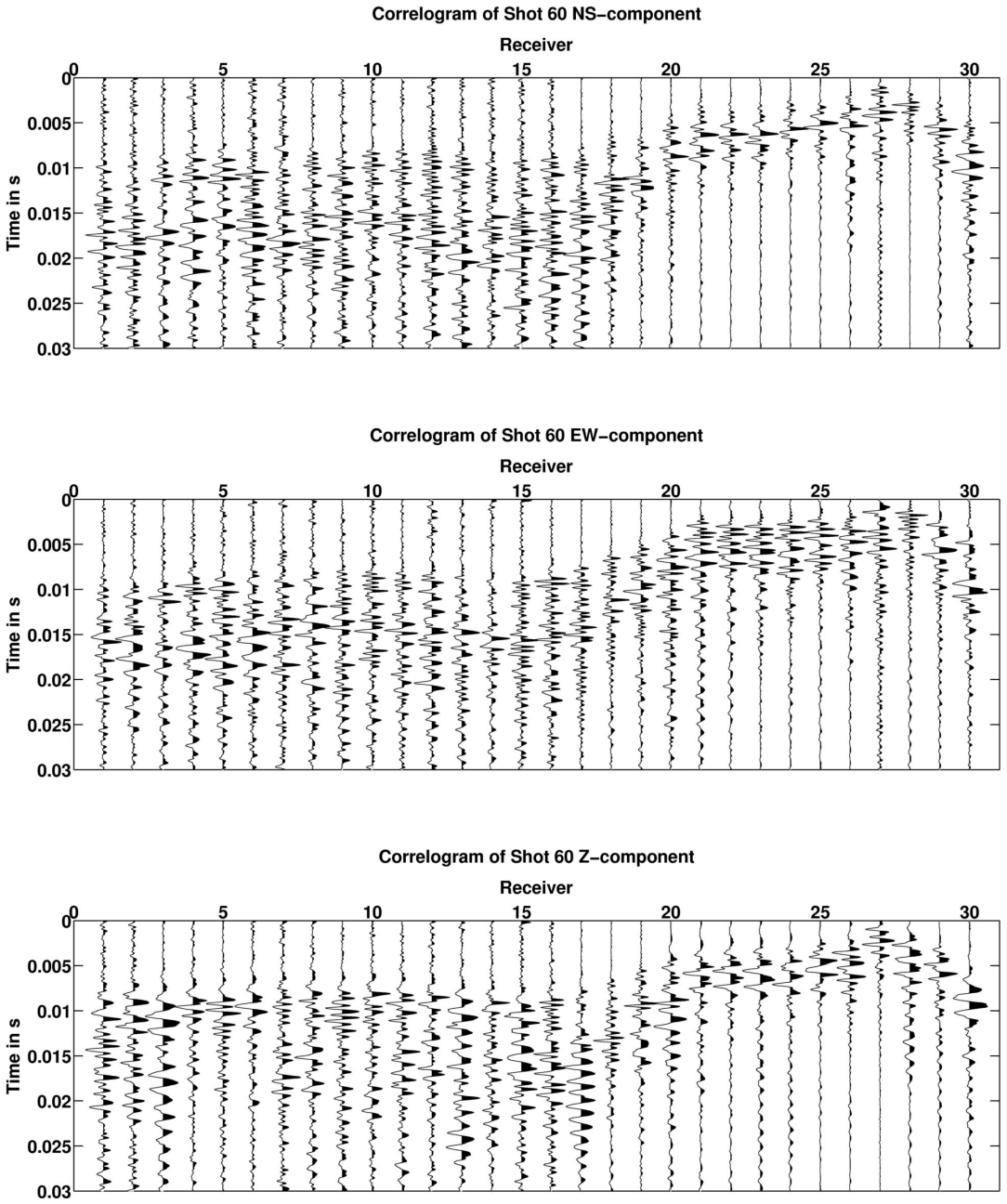

Figure A.4: Correlograms of the field data for Shot 60.

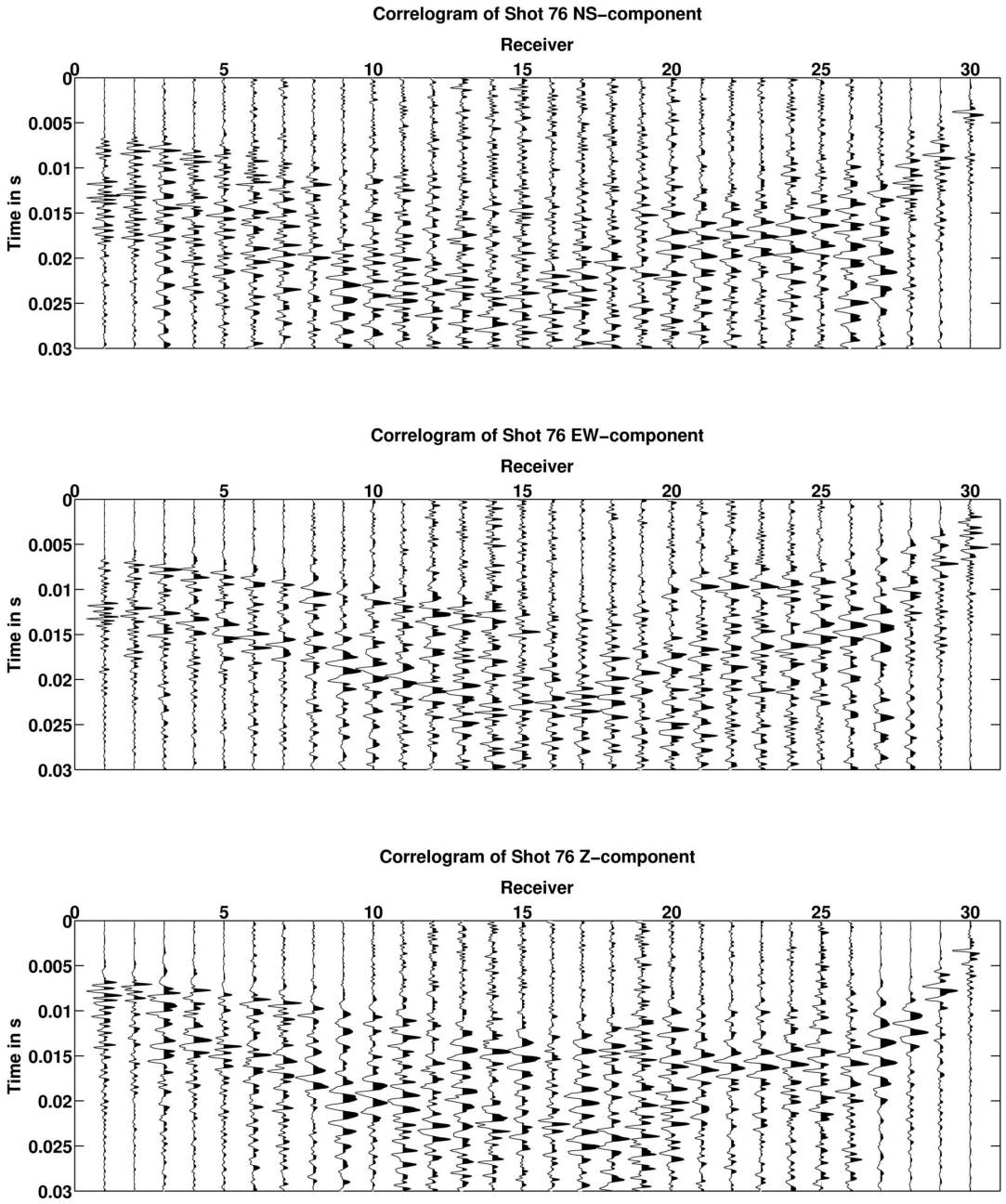

Figure A.5: Correlograms of the field data for Shot 76.

Appendix B

Analytical Klauder Wavelet

The analytical Klauder wavelet $K(t)$ is extracted from Costain and Coruh (2004):

$$K(t) = \frac{(sin[(L-t)B] * cos(Pt)}{BL}, \tag{B.1}$$

where $P = \pi(f_1 + f_2)$, $A = \pi\frac{f_2 - f_1}{L}$, and $B = At$. The frequencies f_1 and f_2 are the start and end frequencies of the vibroseis sweep in Hz, respectively, and L is the length of the sweep in seconds. As the equation (B.1) starts at time zero, this represents only the positive time of the wavelet. We have to flip $K(t)$ to get the symmetrical and zerophase Klauder wavelet.

Appendix C

Rotation Angle of the Receivers

Table C.1: Rotating angle for the 30 receivers. The angle must be applied clockwise.

Receiver	Angle in °	Receiver	Angle in °	Receiver	Angle in °
1	82	11	81	21	277
2	83	12	80	22	284
3	83	13	80	23	276
4	82	14	77	24	265
5	80	15	77	25	262
6	81	16	339	26	266
7	81	17	350	27	268
8	81	18	338	28	250
9	80	19	325	29	264
10	81	20	275	30	270

Appendix D

Field Data Inversion Parameters

Table D.1: The number of iterations, the drop of the misfit, the minimum wavelength of the P-wave and the used filter length for smoothing the velocity model with a median filter after each frequency stage for all frequencies. The minimum wavelength of the P-wave was estimated with a constant velocity of 4500 $^{m}/_{s}$. The misfit curve is shown in Figure 6.7.

Frequency band in Hz from 300	Number of iterations	Misfit decrease from - to in %	Minimum wavelength of P-waves in m	Filter length for velocity models in m
to 400	32	37.5 to 14.0	11.25	2.40
to 500	33	28.4 to 10.9	9.00	1.92
to 600	44	22.1 to 7.1	7.50	1.92
to 700	39	20.0 to 5.6	6.42	1.44
to 800	33	16.5 to 5.6	5.63	1.44
to 900	27	12.0 to 6.0	5.00	0.96

Appendix E

Used Software and Hardware

Software

All full-waveform inversion (FWI) results were computed with 2D FWI code DENISE (subwavelength DEtail resolving Nonlinear Iterative SEismic inversion). DENISE was originally developed by Daniel Köhn (Köhn, 2011) and further extended by Lisa Groos, Martin Schäfer, and myself. The code is freely available from
`http://www.gpi.kit.edu/Software.php` under the terms of the GNU General Public License.

Most of the preprocessing of the data, as well as the analysis of the inversion results were done with `The MathWorks MATLAB®` R2009b for Linux, version 7.9.0.529. In particular, the toolbox `Large Data in MATLAB: A Seismic Data Processing Case Study` by Stuart Kozola was used to read in SEG2 files to `MATLAB®`. For the inversion of the source time function, we used the program `soutifu`. This code was provided by Thomas Forbriger. It is part of the `TFSoftware` package.
Most of the figures were created with `MATLAB®`and modified with `GIMP`, version 2.6.8 and `Inkscape` version 0.46. The thesis is written in LaTeX 2_ε with `Kile`, version 2.0.83.

Hardware

The data preprocessing and the analysis were performed on a Intel® Core™ i7 CPU 950 @ 3.07GHz, 11.8 GB RAM and an nVidia GeForce 9500 GT with openSUSE 11.2 and KDE 4.3.5.

The inversion results were calculated on several high-performance-computing (HPC) systems. We would like to mention and acknowledge the used facilities:

- The authors gratefully acknowledge the computing time granted by the John von Neumann Institute for Computing (NIC) and provided on the supercomputer JUROPA at Jülich Supercomputing Centre (JSC).
- This work was performed on the high-performance computer InstitutsCluster II (IC2) at Steinbuch Centre for Computing at Karlsruhe Institute of Technology.
- This work was performed on the computational resource bwUniCluster funded by the Ministry of Science, Research and Arts and the Universities of the State of Baden-Württemberg, Germany, within the framework program bwHPC.

Appendix F

Project SOUND

Project Description

The shown results were calculated within the framework of the SOUND project (Seismic Observations for UNderground Development). For an overview of the topics within the project, we refer to Lüth et al. (2014) and to the website of the GFZ
`http://www.gfz-potsdam.de/en/research/organizational-units/scientific-infrastructures/scientific-drilling/projects/completed-projects/sound/` (last access: 20.05.2014).

Many collaboration partners and scientists were involved in the results such as the German Research Centre for Geosciences (GFZ) in Potsdam with Rüdiger Giese, Stefan Lüth, Aissa Rechlin and Silke Hock and the Leibniz Institute for Applied Geophysics (LIAG) in Hannover with Ulrich Polom and Sonja Wadas.
Some material presented in this thesis has been already published or will be published in scientific journals. Therefore, I generally use the term "we" instead of "I" to refer to the originators throughout all chapters. Nevertheless, the thesis represents the work which I did.

Acknowledgements

This work was funded within the GEOTECHNOLOGIEN program by the Federal Ministry of Education and Research (BMBF) and German Research Foundation (DFG), Grant 03G0738C (Project: SOUND). It was also kindly supported by the sponsors of the Wave Inversion Technology (WIT) Consortium, Germany.

Danksagung

Nach so vielen Seiten ist nun noch Platz für das eine oder andere persönliche Wort an all jene, die mich in den letzten dreieinhalb Jahren in der Zeit meiner Promotion begleitet haben.

Danke an Thomas Bohlen für die Übernahme des Referats, für die vielen Freiheiten, die du mir beim Schreiben der Arbeit gabst und für die durchgängige, gesicherte Finanzierung.

Vielen Dank an Friedemann Wenzel für die Übernahme des Korreferates.

Ein sehr großes Dankeschön an Stefan Jetschny. Des Öfteren, vor allem am Anfang der Promotion, hast du mir geholfen, die richtige Richtung einzuschlagen. Auch für das Korrekturlesen unzähliger Texte, was der Qualität sicherlich nicht schadete, ein riesiges Dankeschön. Neben dem Universitären war es mir, bis zu deinem Weggang, auch immer eine große Freude so einiges Privates mit dir und deiner Familie zu unternehmen.

Danke an die gesamte Arbeitsgruppe der Angewandten Geophysik in Karlsruhe: Anna, Lisa, Anja, Ines, Eva, Laura, Stefan, André, Martin und Niklas. Die Zusammenarbeit mit euch hat mir immer sehr viel Spaß gemacht.

Dir, Anja, gehört nochmal ein besonderes Dankeschön. Dein fundamentales geophysikalisches Wissen hat so manche Diskussion überflüssig gemacht. Die Zeit mit dir im Büro war immer sehr angenehm. Auch für die gemeinsamen Aktivitäten außerhalb der Wissenschaft möchte ich dir danken.

Danke an alle Mitarbeiter des Geophysikalischen Instituts am KIT. Ihr haltet den Laden am laufen!

Bei dir, Claudia, möchte ich mich ganz besonders bedanken. Du hast einem immer den Rücken frei gehalten und bei so manch einer Dienstreiseabrechnung geholfen.

Besonders bei Martin, Stefan und André möchte ich mich für das Korrekturlesen der Arbeit bedanken. Eure Anmerkungen und Vorschläge haben die Arbeit sicher ein erhebliches Stück verbessert.

Ein großer Dank geht an die Mitarbeiter des Deutschen GeoForschungsZentrums in Potsdam: Rüdiger Giese, Aissa Rechlin, Andreas Jurczyk, Stefan Mikulla und Felix Krauß. Danke an alle weiteren SOUND-Projektpartner. Danke an Daniel Köhn für die Bereitstellung seines 2D FWI Code DENISE.

Auch vielen Dank an meinen Mitbewohner, Trauzeugen und Freund Michael “Biomichl” Bachmann. Es war eine tolle Zeit mit dir! Das wir schon wie ein altes Ehepaar sind, stimmt natürlich nicht :).

Vielen, vielen Dank an meine Frau Tanja, die mich in der gesamten Zeit zu 100 % unterstützte und, vor allem im letzten halben Jahr, die eine oder andere Entbehrung hin nahm. Lieb dich!

Vielen lieben Dank an meine Eltern Wolfgang und Monika für die finanzielle Unterstützung während des Studiums und das uneingeschränkte Vertrauen in den dreieinhalb Jahren danach. Danke euch!